A model reduction approach in space and time for fatigue damage simulation

Mainak Bhattacharyya

ÉCOLE DOCTORALE
Sciences mécaniques et énergétiques, matériaux et géosciences (SMEMAG)

ViVaCE „Virtual Materials and their Validation: German-French School of Computational Engineering" - IRTG 1627

Mainak Bhattacharyya

A model reduction approach in space and time for fatigue damage simulation

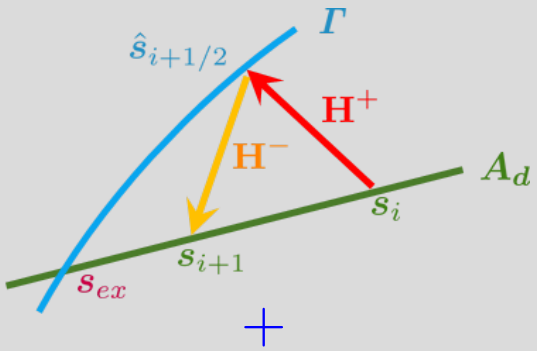

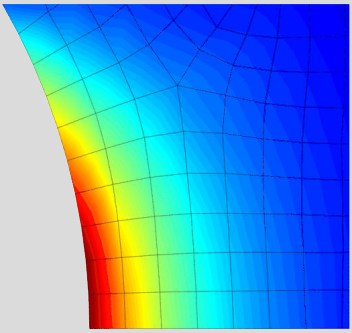

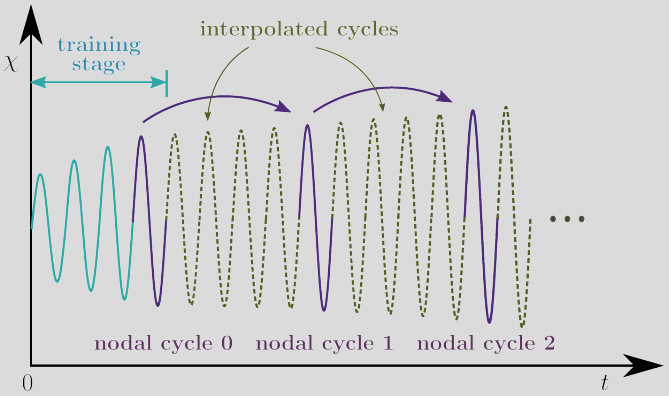

école normale supérieure paris-saclay
université PARIS-SACLAY
Leibniz Universität Hannover
ibnm

NNT: 2018SACLN019 ISBN: 978-3-935732-47-5

A model reduction approach in space and time for fatigue damage simulation

A joint doctoral thesis between

Université Paris Saclay

prepared at

École normale supérieure Paris-Saclay

under École doctorale n°579

Sciences mécaniques et énergétiques, matériaux, géosciences- SMEMAG

for the degree of

Docteur

with specialisation in

Mécanique des solides

and

Gottfried Wilhelm Leibniz Universität Hannover

in

Fakultät für Bauingenieurwesen und Geodäsie

prepared at

Institut für Baumechanik und Numerische Mechanik

for the degree of

Doktor-Ingenieur

by

Mainak Bhattacharyya

The thesis was presented and defended in Hannover on May 8, 2018

Members of the jury:

Mr. David Dureisseix	Professor, INSA Lyon	(Reviewer and President)
Ms. Stefanie Reesse	Professor, RWTH Aachen	(Reviewer)
Mr. Guillaume Puel	Professor, Centrale Supélec Paris	(Examiner)
Mr. Michael Beer	Professor, LU Hannover	(Examiner)
Mr. Peter Schaumann	Professor, LU Hannover	(Examiner and Chairman)
Ms. Amélie Fau	Research associate, LU Hannover	(Co-Supervisor)
Mr. Pierre Ladevèze	Professor Emeritus, ENS Paris-Saclay	(Co-Supervisor)
Mr. David Néron	Professor, ENS Paris-Saclay	(Supervisor)
Mr. Udo Nackenhorst	Professor, LU Hannover	(Supervisor)

Editors: Prof. Dr.-Ing. Udo Nackenhorst, Prof. Dr. habil. David Néron

The researchwork was funded by the German Research Foundation (DFG) in the framework of the International Research Training Group (IRTG) 1627. Further financial support has been provided by the Franco-German University (FGU) for the enactment of the Cotutelle procedure.

Ces travaux de thèse ont été financés dans le cadre du collège doctoral international ≪ International Research Training Group (IRTG) 1627 ≫ par la Fondation allemande pour la recherche (DFG). Cette thèse a également fait l'objet d'un soutien financier de l'Université franco-allemande (UFA) pour la mise en œuvre de la cotutelle.

Diese Forchungsarbeiten wurden im Rahmen des Internationalen Graduiertenkolleg „International Research Training Group (IRTG) 1627 "von der Deutsche Forschungsgemeinschaft (DFG) gefördert. Eine weitere finanzielle Förderung hat die Deutsch-Französischen Hochschule (DFH) für die Durchführung des Cotutelle-Verfahrens bereitgestellt.

Contact

Institut für Baumechanik und Numerische Mechanik,
Gottfried Wilhelm Leibniz Universität Hannover,
Appelstr. 9a,
30167 Hannover, Germany.
Tel: +49 511 762 3219
Fax: +49 511 762 19053

École normale supérieure Paris-Saclay,
Université Paris Saclay,
61 Avenue du Président Wilson,
94235 Cachan Cedex, France.
Tel: +33 1 47 40 24 02
Fax: +33 1 47 40 27 85

ISBN 978-3-935732-47-5 NNT 2018SACLN019

Abstract

The motivation of the research project is to predict the life time of mechanical components that are subjected to cyclic fatigue phenomena. The idea herein is to develop an innovative numerical scheme to predict failure of structures under such loading. The model is based on classical continuum damage mechanics introducing internal variables which describe the damage evolution. The challenge lies in the treatment of large number of load cycles for the life time prediction, particularly the residual life time for existing structures.

Traditional approaches for fatigue analysis are based on phenomenological methods and deal with the usage of empirical relations. Such methods consider simplistic approximations and are unable to take into account complex geometries, and complicated loadings which occur in real-life engineering problems. A thermodynamically consistent continuum-based approach is therefore used for modelling the fatigue behaviour. This allows to consider complicated geometries and loads quite efficiently and the deterioration of the material properties due to fatigue can be quantified using internal variables. However, this approach can be computationally expensive and hence sophisticated numerical frameworks should be used.

The numerical strategy used in this project is different when compared to regular time incremental schemes used for solving elasto-(visco)plastic-damage problems in continuum framework. This numerical strategy is called Large Time Increment (LATIN) method, which is a non-incremental method and builds the solution iteratively for the complete space-time domain. An important feature of the LATIN method is to incorporate an on-the-fly model reduction strategy to reduce drastically the numerical cost. Proper generalised decomposition (PGD), being a priori a model reduction strategy, separates the quantities of interest with respect to space and time, and computes iteratively the spatial and temporal approximations. LATIN-PGD framework has been effectively used over the years to solve elasto-(visco)plastic problems. Herein, the first effort is to solve continuum damage problems using LATIN-PGD techniques.

Although, usage of PGD reduces the numerical cost, the benefit is not enough to solve problems involving large number of load cycles and computational time can be severely high, making simulations of fatigue problems infeasible. This can be overcome by using a multi-time scale approach, that takes into account the rapid evolution of the quantities of interest within a load cycle and their slow evolution along the load cycles. A finite element like description with respect to time is proposed, where the whole time domain is discretised into time elements, and only the nodal cycles, which form the boundary of the time elements, are calculated using LATIN-PGD technique. Thereby, classical shape functions are used to interpolate within the time element.

This two-scale LATIN-PGD strategy enables the reduction of the computational cost remarkably, and can be used to simulate damage evolution in a structure under fatigue loading for a very large number of cycles.

Keywords: LATIN method, damage mechanics, (visco)plasticity, metal fatigue, model order reduction, PGD, multi-temporal scale

Zusammenfassung

Das Ziel des Forschungsprojektes ist es, die Lebensdauer mechanischer Tragwerke unter zyklischen Ermüdungsphänomenen vorherzusagen. Die zugrunde liegende Idee ist, ein innovatives numerisches Schema zu entwickeln, um das Versagen der Strukturen unter bestimmten Belastungen zu berechnen. Für das Kontinuumsmodell werden innere Variablen eingeführt, um die Entwicklung der Materialermüdung zu beschreiben. Die Herausforderung liegt dabei in der numerischen Behandlung der Belastungszyklen für die Voraussage der Lebensdauer, insbesondere für die Voraussage der Restlebensdauer der Strukturen.

Traditionelle Ansätze zur Ermüdungsanalyse basieren auf phänomenologischen Methoden welche aus emperischen Beobachtungen abgeleitet werden. Solche Verfahren berücksichtigen einfache Annäherungen und können komplexe Geometrien und komplizierte Belastungen, die in realen technischen Problemen auftreten, nicht abbilden. Zur Modellierung des Ermüdungsverhaltens wird daher ein thermodynamisch konsistenter kontinuumsbasierter Ansatz verwendet. Dieser ermöglicht es, komplizierte Geometrien und Lasten recht effizient zu betrachten, und die Verschlechterung der Materialeigenschaften aufgrund von Ermüdung kann unter Verwendung interner Variablen quantifiziert werden. Dieser Ansatz kann jedoch numerisch teuer sein und daher sollten effiziente numerische Techniken entwickelt werden.

In diesem Projekt wird eine innovative numerische Strategie basierend auf einer nicht-zeitinkrementellen Lösung von elasto-(visko)plastischen Schädigungsproblemen in der Kontinuumsmechanik vorgestellt. Diese numerische Strategie basiert auf der sogenannten LATIN Methode (Large Time Increment method). Bei dieser nicht-inkrementellen Methode wird iterativ im vollständigen Zeit-Raum Bereich eine Lösung gesucht. Eine wichtige Eigenschaft der LATIN Methode ist eine ad hoc Modellsreduktionsstrategie um die Rechnenkosten zu reduzieren. Die Proper Generalised Decomposition (PGD) ist eine a priori Modellreduktionsstrategie, die in Raum und Zeit die Variablen in zwei unabhängige Teile auftrennt, einen zeitabhängigen und einen raumabhängigen. Iterativ wird eine Approximation dieser beiden Anteile gesucht. Die Effektivität des LATIN-PGD Verfahrens ist seit Jahren für die Lösung von elasto-(visko)plastischen Problemen nachgewiesen. Der erste Teil dieses Projektes zielt auf die Erweiterung dieser Methode für Schädigungsmodelle ab.

Obwohl die Anwendung des LATIN-PGD Verfahrens die numerischen Kosten reduziert, ist die Ersparnis nicht groß genug, um Probleme mit vielen Belastungszyklen lösen zu können. Dieses Problem soll mit einem Mehrskalenansatz in der Zeit gelöst werden. Damit können schnelle Entwicklung der Variablen während eines Belastungszyklus erfasst und ihre langsame Evolution während vielen Zyklen abgebildet werden. Der Zeitbereich wird dabei mit diskontinuierlichen Finiten Elementen diskretisiert, während die Knotenzyklen, die die Grenzen der Zeitelemente bilden, mit der LATIN-PGD Technik beschrieben werden. Dafür werden klassische Ansatzsfunktionen benutzt, um die Variablen innerhalb der Zeitelemente zu interpolieren.

Mit dieser innovativen Strategie werden die Rechnenkosten signifikant reduziert und die Simulation von Ermüdungsbelastung unter großen Lastzyklenzahlen ermöglicht.

Stichworte: LATIN Methode, Schädigungsmechanik, (Visko)Plastizität, Metallermüdung, Modellreduktion, PGD, Mehrskalenansatz in der Zeit

Résumé

L'objet de ce projet de recherche est de prédire la durée de vie d'éléments mécaniques qui sont soumis à des phénomènes de fatigue cyclique. L'idée est de développer un schéma numérique novateur pour prédire la rupture de structures sous de tels chargements. Le modèle est basé sur la mécanique des milieux continus qui introduit des variables internes pour décrire l'évolution de l'endommagement. Le défi repose dans le traitement des cycles de chargement pour la prédiction de la durée de vie, particulièrement pour la prédiction de la durée de vie résiduelle de structures existantes.

Les approches traditionnelles de l'analyse de la fatigue sont basées sur des méthodes phénoménologiques utilisant des relations empiriques. De telles méthodes considèrent des approximations simplificatrices et sont incapables de prendre en compte aisément des géométries ou des charges complexes associées à des problèmes d'ingénierie réels. Une approche basée sur la description de l'évolution thermodynamique d'un milieu continu est donc utilisée pour modéliser le comportement en fatigue. Cela permet de considérer efficacement des problèmes d'ingénierie complexe et la détérioration des propriétés du matériau due à la fatigue peut être quantifiée à l'aide de variables internes. Cependant, cette approche peut être numériquement coûteuse et, par conséquent, des approches numériques sophistiquées doivent être utilisées.

La stratégie numérique sur laquelle ce projet est basé est singulière par rapport aux schémas incrémentaux en temps usuellement utilisés pour résoudre des problèmes élasto-(visco)plastique avec endommagement dans le cadre de la mécanique des milieux continus. Cette stratégie numérique appelée méthode LATIN (Large Time Increment method) est une méthode non-incrémentale qui recherche la solution de manière itérative sur l'ensemble du domaine spacio-temporel. Une importante innovation de la méthode LATIN est d'incorporer une stratégie de réduction de modèle adaptative pour réduire de manière très importante le coût numérique. La Décomposition Propre Généralisée (PGD) est une stratégie de réduction de modèle a priori qui sépare les quantités d'intérêt spacio-temporelles en deux composantes indépendantes, l'une dépendant du temps, l'autre de l'espace, et estime itérativement les approximations de ces deux composantes. L'utilisation de l'approche LATIN-PGD a montré son efficacité depuis des années pour résoudre des problèmes élasto-(visco)plastiques. La première partie de ce projet vise à étendre cette approche aux modèles incorporant de l'endommagement.

Bien que l'utilisation de la PGD réduise les coûts numériques, le gain n'est pas suffisant pour permettre de résoudre des problèmes considérant un grand nombre de cycles de chargement, le temps de calcul peut être très conséquent, rendant les simulations de problèmes de fatigue intraitables même en utilisant les techniques LATIN-PGD. Cette limite peut être dépassée en introduisant une approche multi-échelle en temps, qui prend en compte l'évolution rapide des quantités d'intérêt lors d'un cycle et leur évolution lente au cours de l'ensemble des cycles. Une description type éléments finis en temps est proposée, où l'ensemble du domaine temporel est discrétisé en éléments temporels, et seulement les cycles nodaux, qui forment les limites des éléments, sont calculés en utilisant la technique LATIN-PGD. Puis, des fonctions de forme classiques sont utilisées pour interpoler les quantités d'intérêt à l'intérieur des éléments temporels.

Cette stratégie LATIN-PGD à deux échelles permet de réduire le coût numérique de manière significative, et peut être utilisée pour simuler l'évolution de l'endommagement dans une structure soumise à un chargement de fatigue comportant un très grand nombre de cycles.

Mots clés : méthode LATIN, mécanique de l'endommagement, (visco)plasticité, fatigue des métaux, réduction d'ordre de modèle, PGD, échelle multi-temporelle

Contents

List of figures

List of tables

List of abbreviations

CA	constant amplitude
CDM	continuum damage mechanics
CPU	central processing unit
DLDR	double linear damage rule
EPFM	elastic plastic fracture mechanics
FE	finite element
GP	Gauss point
GTN	Gurson-Tvergaard-Needleman
H-L	high-to-low
HCF	high cycle fatigue
KLE	Karhunen Loève expansion
L-H	low-to-high
LATIN	large time increment
LCF	low cycle fatigue
LDR	linear damage rule
LEFM	linear elastic fracture mechanics
MFM	micro-structural fracture mechanics
MOR	model order reduction
MR	model reduction
NLDR	non-linear damage rule
ODE	ordinary differential equation
PCA	principal component analysis
PGD	proper generalised decomposition
POD	proper orthogonal decomposition
ROB	reduced order basis
ROM	reduced order model
RVE	representative volume element
SVD	singular value decomposition
VA	variable amplitude
VHCF	very high cycle fatigue
VLCF	very low cycle fatigue

Introduction

Failure of structures have been a major consideration among engineers, over the decades. Failure in a general sense can be defined as rupture or excessive deformation. Among many different loading phenomena that induce failure of structures, such as static loading or monotonic loading, one important phenomenon is cyclic loading or fatigue loading, where the load is lower than the static strength but causes failure due to repetition. Fatigue forms one of the most important failure mechanisms for civil, mechanical, aviation and automotive components. It is believed that 50-90 % of all the mechanical failures especially for metallic structures occur due to fatigue (see Sobczyk and Spencer, 1992). The failure mechanism for structures subjected to cyclic fatigue is complicated in a sense that failure does not happen instantaneously, but material is degraded over a period of time and this degradation is often not apparent and in many cases structures may fail without any prior warning.

Although, the experimental studies of fatigue had been under progress for a long time, these experimental investigations, in general are very time consuming and restricted to specimens suitable for laboratory conditions. Thereby, a lot of attentions were focused on numerical studies of fatigue later on. The initial numerical studies of fatigue made in the 20th century, were empirical in nature, and could only simulate very simple cases. In the later part of the century, thermodynamically consistent models were utilised to describe the phenomenological aspects of fatigue. This idea gave a better description of the physical behaviour of the problem, which also paved the way for efficient time integration schemes to simulate large number of cycles. A major boost in the numerical modelling of fatigue process was in the late 20th century, when continuum damage mechanics (CDM), a branch of continuum mechanics, was used to model fatigue behaviour. This branch of continuum mechanics, essentially quantifies the degradation of material properties, in terms of a separate internal variable, called the damage variable. A lot of developments have been proposed from the first usage of continuum damage mechanics in Chaboche and Lesne (1988) to predict fatigue, both in the aspects of modelling different types of fatigue processes, and also on different improved numerical schemes to handle large number of cycles.

The goal of this thesis is to provide a novel simulation approach to compute fatigue damage using continuum damage mechanics. The challenge in this case is obviously to handle the temporal part of the problem, which involves a large number of cycles (e.g. 10^5 cycles). Therefore, instead of using a traditional time incremental scheme, the large time increment (LATIN) method is used. The advantage of LATIN method is that it separates the difficulties into a part where only the linear global admissibilities are solved and another where the local non-linear constitutive relations can be solved. The solution can be built over the whole space-time domain, and is improved successively, with each iteration between the linear and local stages. This kind of description allows the user to introduce a model reduction strategy in space and time which not only allows reduction in numerical expenditure, but also incorporates separate treatment of the temporal part, which is necessary to tackle large number of cycles.

The invention and popularity of model order reduction (MOR) or model reduction (MR) techniques stem from the fact that simulation of full physical models consisting of thousands of degrees of freedom with structural evolutions spanning for a large time interval, can be extremely expensive. In simple words, the idea of MOR is to reduce a complete high fidelity model into several low-fidelity models which are relatively less expensive to solve. One of the most widely used model reduction methods is to find through a training or learning phase, the full solution of the problem at hand and then perform singular value

decomposition (SVD) of the full solution to extract the relevant modes that can be used to approximate it as much as possible. The learning phase can sometimes be computed for a certain short interval of time and the spatial basis functions that are extracted are reused to approximate the solution over a larger time interval by only recomputing the temporal basis. Otherwise, if the learning phase is for the whole time domain, the space-time bases can be reused to solve a similar problem but with certain changes, for instance small changes in boundary conditions or material parameters. This kind of model reduction method is *a posteriori* technique that relies on the solution of the full model and is popularly referred to as proper orthogonal decomposition (POD), Karhunen Loève expansion (KLE) or principal component analysis (PCA). However it is desirable to build an *a priori* method which does not rely on the complete solution of the full model. The proper generalised decomposition (PGD) is one of such techniques, which does not require the knowledge of the full model, but build, "on the fly" separable approximation of the problem. The governing equations are separated into equations depending on the number of independent variables to be considered (in most classical cases space and time are the two independent variables), and then these separated equations are solved independently using fixed point method. If the approximation is not satisfactory, a new basis vector can be added spontaneously. This method is very helpful and flexible as no training phase is required.

PGD was first introduced in the LATIN framework by Ladevèze (see Ladevèze, 1989, 1985a,b) as the "radial loading approximation" to solve the global equilibrium. PGD basically separates the quantities of interest into space and time which leads to sovereign time and space problems that can then be solved using a staggered algorithm. There have been many versions of LATIN method over the years, to solve (visco)plasticity, viscoelasticity, contact problems, however all of them have the two key features: separation of difficulties, and separation of variables using PGD.

Therefore the innovation of this research is divided into two parts:

- The first part is to incorporate CDM in LATIN framework. Although there have been certain strategies proposed in the past to solve CDM using LATIN method, a unique way to include CDM in LATIN-PGD method is suggested in this thesis.
- The next part is to introduce an innovative multi-temporal scheme so that a large number of cycles can be computed. The model reduction strategy that is used in the LATIN framework enables the temporal quantities to be treated using this time scheme. Similar strategy has been used in the past for cyclic visco-plasticity. This strategy incorporates a massive reduction in numerical expenditure.

The structure of the thesis is described in the following paragraphs.

Chapter 1 introduces the definition and classification of fatigue. A brief history of fatigue over the past two centuries is given and different methods of fatigue calculations from traditional till current developments are also detailed.

In the current work, the focus is on continuum damage mechanics (CDM), developed out of classical continuum mechanics, where the deterioration of material properties is represented in terms of internal variables in a thermodynamically consistent framework. Chapter 2 introduces the fundamental ideas of continuum mechanics, (visco)plasticity, and damage. It also highlights a few methods that have been developed over the years to incorporate CDM in fatigue problems.

The most challenging part in the solution of thermodynamic based mechanical problem is the numerical expense that arises while solving a full model having a large spatial degrees of freedom for the complete temporal domain. For fatigue simulation this issue is accentuated due to the enhancement of the temporal domain which involves large number of cycles. To solve this issue, model reduction techniques may be used which can reduce the numerical cost drastically by separating the spatial and temporal part and tackling them independently. Chapter 3 gives a brief overview of different model reduction techniques that are available and their numerical importance. Chapter 3 also gives a brief introduction of large time increment (LATIN) method, a non-incremental technique which is used as a solution framework in this research.

The usage of LATIN has been extensive over the years for the solution of non-linear problems such as plasticity or visco-plasticity, however a novel approach has been adopted in this research to solve CDM problems using LATIN method. The numerical modification in the LATIN method to include CDM is

portrayed in chapter 4 along with certain academic examples, depicting the numerical robustness of the approach.

The simulation of large number of cycles for fatigue problems is an obvious numerical challenge and has been addressed within the framework of LATIN technique in chapter 5. This approach uses the idea of two separate time discretisation schemes, one within a cycle and the other along the cycles. Several numerical examples are presented to depict the efficiency of the two-time scale formulations.

Chapter 6 finally summarises the important discoveries in the research and provides a foresight on the future scope and development.

Chapter 1

Fatigue: an overview

Fatigue simulation being the goal of this research, a classification of fatigue, and established approaches are presented here. It has to be noted that no novel approaches are presented in this chapter. The only purpose here is to provide the readers with a brief but comprehensive overview of fatigue. The chapter begins with a concise historical perspective of fatigue, leading on to different forms of fatigue and their engineering importance. Thereafter, the mechanism of fatigue and the classical numerical approaches towards it are reviewed.

The term "fatigue" originating from the Latin word *fatigare*, meaning "to tire", has been used extensively in engineering to describe the degradation of materials subjected to fluctuating loads (see Suresh, 2001). Fatigue in a generic mechanical sense can be defined as the "change in properties" of materials under the influence of time-varying loading. This "change in properties" leads to the detoriation of the materials which ultimately culminates into the inability of the structure to sustain the intended loading. The most noteworthy feature of fatigue is that failure at macro-scale does not occur immediately, but happens after a certain number of load fluctuations has taken place (see Cui, 2002).

1.1 History of fatigue

The first study of metal fatigue was done by a German mining engineer named Albert around 1829 who studied fatigue effect of conveyor chains (see Albert, 1838). The most noticeable activity in record after Albert was from a British railway engineer named Rankine. Although he became more famous in the field of thermodynamics, around 1842 he discussed the importance of stress concentration in the fatigue strength of railway axles (see Rankine, 1842). The first idea of "safe life concept" in perspective of railway coaches was given by a French engineer named Morin (see Morin, 1853). The credit of coining the term "fatigue" to describe cracking of metals under repeated loading goes to a British researcher named Braithwaite (see Braithwaite, 1854). The most important name in that era however was of a German engineer named Wöhler, who conducted systematic experiments on fatigue failure of railway axles and found that the fatigue strength is much below the static strength (see Wöhler, 1860, 1870). His self designed machines were able to perform rotating-bending as well as combined bending and torsion fatigue. His experimental results were plotted first by his successor, another German engineer named Spangenberg (see Spangenberg, 1879), which came to be known as S-N curves or "Wöhler curves" since 1936. Gerber and Goodman studied the effect of mean stress in the late 19th century (see Gerber, 1874, Goodman, 1899). Another important contribution in the late 19th century was by another German researcher named Bauschinger (see Bauschinger, 1886), who discovered the difference in the elastic limits of metals between reverse and monotonic loadings. This was one of the earliest investigations on cyclic hardening and softening phenomenon.

In the early 20th century, first important research contribution was from a British researcher named Erwing, who along with his colleagues investigated the crack nucleation and propagation mechanism in

polycrystalline materials (see Ewing and Humfrey, 1903, Ewing and Rosenhain, 1900). The American engineer Basquin also became famous in the early 20th century, after his proposal of empirical laws to characterise S-N curves in 1910. He discovered that in a logarithmic scale the stress has a linear relationship with number of fatigue cycles over a large stress range (see Basquin, 1910). The early part of the 20th century was dominated by the British and American engineers, with notable contributions from Smith (1908), Haigh (1912), Gough (1924), Griffith (1920), Inglis (1913), Kommers (1915), Moore (1919), and many more. The most important of them was Griffith, who with his investigations on glass, laid the foundation of fracture mechanics. By the early quarter of the century, fatigue became one of the most important fields of study. Another noteworthy contribution of the period was from a Swedish scientist named Palmgren who investigated and proposed a theory on accumulation of damage in material during fatigue, especially for variable amplitudes. His contribution (see Palmgren, 1924) was extended and formulated by the American scientist Miner (see Miner, 1945), who developed what is now called the famous "Palmgren-Miner linear damage rule". Another landmark in this period was by the Swedish engineer Weibull, who extended his theory of static strength to fatigue and conducted several tests to obtain numerical data of number cycles to failure, to quantify his proposed distribution, which later on became famous as "Weibull distribution" (see Weibull, 1939). One of the most important German researchers of this era was Thum, who pioneered the idea of "Gestaltfestigkeit", which according to Thum was "*a strength value which depends on the magnitude and type of loading as well as on the material, and especially on the component's shape*" (see Schütz, 1996). He had a major contribution in the area of fatigue and his studies in the areas of corrosion fatigue, hardenings, residual stresses, fretting and such others were revolutionary (see Thum, 1939). The concept of fatigue stress concentration factor was developed by him. Another important personality during this time was the German engineer Gassner who was the pioneer in variable amplitude fatigue tests (see Gassner, 1941). The idea of "Betriebsfestigkeit", which translates to *operational fatigue strength* was first formulated by him. Another important scientist of this time was a German engineer named Neuber, who published the first comprehensive book (see Neuber, 1937) about the theoretical calculations of stress concentration factors. He was one of the first to study notch effects on fatigue. The next landmark came in the later half of the century, when two American engineers Coffin and Manson, independently investigated the dependency of plasticity on cyclic damage (see Coffin, 1954, Manson, 1954). Their works were the first efforts in the investigations of low cycle fatigue and led to the strain-based measurements, compared to the stress-based measurements that had been used traditionally. The ideas of Griffith used for brittle materials were extended by Irwin (see Irwin, 1957) for ductile materials, giving the concept of stress singularity using stress intensity factor. Paris, with his co-workers in the 1960s found that the fatigue crack growth rate can be related to the stress intensity factor range (see Paris and Erdogan, 1963, Paris et al., 1961). Japanese researchers Matsuishi and Endo developed a method in 1968 to represent a non-cyclic loading in equivalent number of cycles (see Matsuishi and Endo, 1968). This method became famous as rainflow counting. During the similar time frame, a German scientist named Elber, experimentally found out that under cyclic tensile loading, crack closes before the load reaches zero (see Elber, 1968). His proposed "crack closure" ideas has paved the way for crack-growth hypotheses since his discovery. A notable person during this period was the Dutch scientist Schijve, who greatly contributed to the fatigue studies of aircraft, even for variable loading (see Schijve and Brock, 1962, Schijve and Hoeymakers, 1971). A contemporary British scientist Pearson was the first to identify the "short crack problem", which later on became an important are in fatigue crack growth (see Pearson, 1975). During the late 70s and early 80s, an Indian scientist named Suresh along with his co-workers investigated various types of crack growth and crack closure mechanisms (see Ritchie et al., 1980, Suresh and Ritchie, 1982). The numerical simulation of fatigue got a boost when researchers began using continuum damage mechanics to model and simulate fatigue phenomena. The onset of continuum damage mechanics although happened in 1958 through a Russian scientist named Kachanov (see Kachanov, 1958), the usage of CDM for fatigue modelling and simulations took place a lot later. The initial usage of CDM for fatigue computation started during late 80s and early 90s. Two French scientists, Lemaitre (see Lemaitre, 1985, Lemaitre and Doghri, 1994) and Chaboche (see Chaboche and Lesne, 1988) were pioneers in the usage of damage mechanics in the prediction of fatigue life. Later on a Japanese researcher named Murakami, who also played a part in the development of CDM in the

70s (see Murakami and Ohno, 1978), used damage mechanics for fatigue computation (see Tanaka et al., 1998). Thereafter a new idea of cycle jumping methods has been proposed to compute fatigue. Initially in Lesne and Savalle (1989) and later on in Lemaitre and Desmorat (2005), jump-in-cycles method has been used extensively in the 90s and 2000s. Fish and his colleagues since the early 2000s have used an alternative method to simulate fatigue with CDM (see Fish and Oskay, 2005, Oskay and Fish, 2004a,b) using the temporal homogenisation technique developed by a French scientist called Aubry in the late 80s (see Guennouni and Aubry, 1986).

Although, the complete history of fatigue was not covered, only certain landmarks are highlighted, which according to the author are most significant. For more comprehensive historical perspective on fatigue, Schütz (1996), Suresh (2001) are suggested.

1.2 Different forms of fatigue in the engineering world

The driving factor of fatigue is cyclic or fluctuating stresses or strains, which can arise due to many factors in real-life engineering structures. One of the most classical form is the **mechanical fatigue**, in which the internal repetitive stresses occurs under the fluctuations of externally applied mechanical loading (forces or displacements). Most of the civil structures like bridges, dams, and such others, or mechanical components like machine tools, pumps, vibration dampers etc. are susceptible to mechanical fatigue. **Thermal fatigue** occurs under the influence of fluctuating temperature. This induces internal fluctuating stresses and strains which result into fatigue failure. This can happen in high temperature super heaters, nuclear reactors, and such others. A fluctuation of both mechanical and thermal quantities, for instances in internal combustion engines, steam or gas turbines, results into **thermo-mechanical fatigue**. **Electrical fatigue** occurs generally for electro-active materials such as piezoelectrics under the influence of fluctuating electric field. This kind of materials produces fluctuating internal mechanical stresses or strains due to electromechanical coupling resulting into fatigue of the material. **Thermo-electrical fatigue** and **electro-mechanical fatigue** occurs for electro-active materials when electrical fatigue is combined with thermal and mechanical fatigue respectively. **Creep fatigue** takes place when a structure is subjected to mechanical fatigue at high temperature. **Corrosion fatigue** occurs at chemically aggressive environment. There can still be further different varieties depending on the different forms of loading.

1.3 Phases of fatigue life

Irrespective of the type of loading, fatigue phenomenon is considered to be originating from local yielding of the material (see Cui, 2002, Schijve, 2008, Sobczyk and Spencer, 1992). Due to local stress concentration at grain level of a material, dislocations or invisible micro-cracks occur in slip bands. These dislocations, under the influence of cyclic stress, migrate and coalesce to form a micro-crack. The micro-cracks grow to form macro-crack. This macro-crack then propagates through the structure, generally perpendicular to the maximum principal stress direction, which ultimately leads to the failure of the structure (see Cui, 2002, Ottosen et al., 2008, Schijve, 2008, Sobczyk and Spencer, 1992). Thereby the initiation and propagation of macro-crack are the two paramount stages of fatigue process.

Various steps of fatigue life within the two principal stage as mentioned in Oller et al. (2005), Schijve (2008), Sobczyk and Spencer (1992) are concisely depicted in fig. 1.1. The two principal stages and the physical phenomena behind them are herein detailed in brief (see Schijve, 2008, Sobczyk and Spencer, 1992, for more details).

Crack initiation phase of fatigue is a surface phenomenon. Plasticity, being a local phenomenon, for initial cycles, is restricted to a small number of grains and can occur more effectively if there are no surrounding grains to hinder the plastic deformation, i.e. at the surface. This micro-plasticity is a consequence of cyclic slip originating from cyclic shear stress, which is not homogeneous but varies from grain to grain. Cyclic loading creates a non-reversible slip band on parallel slip planes. The first initiation of a micro-crack is experienced to develop along a slip band in the form of intrusion or extrusion (see Schijve, 2008, Suresh, 2001, for more details). These micro-defects will be initiated depending on

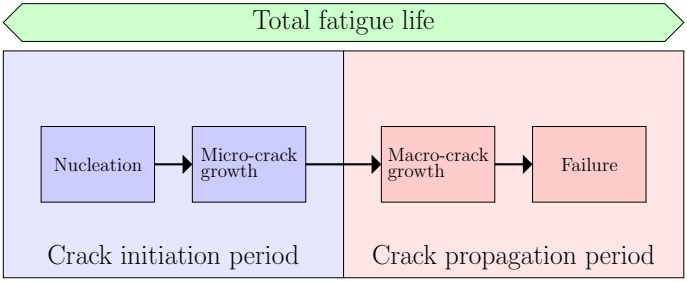

Figure 1.1: Different stages of fatigue process

surface imperfections, inherent material defects, geometric discontinuities, high stress concentrations, and such other conditions that facilitate cyclic slip. These micro-cracks grow into adjacent grains with the growth directions deviating from initial slip band orientations with the grain boundaries providing resistance against growth. When the number of grains along the micro-crack front becomes sufficiently large, the growth happens continuously with the growth rate depending on the crack growth resistance of the material. The completion of the crack initiation phase is assured when the growth of the micro-crack becomes independent of surface conditions.

Crack propagation phase starts when the growth of crack is controlled by the crack growth resistance which is a bulk property and not a surface phenomenon. The crack generally grows perpendicular to the direction of the maximum principal stress through the structure until it fails completely. For brittle materials the propagation can be rapid, however for ductile material it is slower and accompanied by local plastic zones around the crack tip which provides crack growth resistance.

The percentage of total life that is contributed by these two phases depends on the type of material along with loading itself. This total life can be used as quantity that classifies different forms of fatigue.

1.4 Different domains of fatigue

The classical way to split the domains of fatigue is with respect to the number of cycles to failure (see Kazymyrovych, 2009). Structures that are subjected to low amplitude loading such that the induced stress range is below the yield stress, are macroscopically elastic. However, plasticity and damage can occur at the micro-scale. In such cases, the number of load cycles to failure is generally more than 10^6 (see Kazymyrovych, 2009), and this is referred to as *high cycle fatigue (HCF)*. For high amplitude loading, however, the induced stresses exceed the elastic limit and the dominating mechanism is plasticity at the macro-scale. In these cases, the number of cycles is relatively low and generally below 10^6 and they are called *low cycle fatigue (LCF)*. These demarcations are also relative to the authors, as for instance, Pook (2007) considers LCF if number of cycles to failure $N_f < 10^4$ and above that it is HCF, Davoli (1999) however introduces 10^5 as the demarcation point between LCF and HCF. Lemaitre and Desmorat (2005) on the other hand considers LCF if $N_f < 10^4$ and HCF if $N_f > 10^5$ and in between either of them can be considered depending on the particular case.

Apart from these distinctions, if the number of cycles to failure is extremely high, it is referred to as *very high cycle fatigue (VHCF)*. The demarcation point in this case is also debatable, Kazymyrovych (2009) considers it to be more than 10^8, but Pyttel et al. (2011) considers VHCF if $N_f > 10^7$. In this context there also exist what is called *very low cycle fatigue (VLCF)*, also referred to as extremely or ultra low cycle fatigue. This is applicable when N_f is extremely low. Skrzypek and Ganczarski (1999) defines N_f to be less than 10, however according to Xue (2008) this is less than 100. Irrespective of these variable demarcations, it is universally agreed that LCF and VLCF are governed by macro-plasticity and HCF and VHCF are governed by macro-elasticity (especially for metals). It has to be noted that VLCF

and VHCF are subsets of LCF and HCF respectively, and the differentiation is based more on the number of cycles instead of any difference in the governing physical phenomena.

Although fatigue can be classified with respect to number of cycles, however for many practical cases "the cycles" prescribed by the load history are not well defined. Hence it is necessary to introduce different forms of load fluctuations.

1.5 Different types of load fluctuations

It is necessary at this point to introduce the different types of fluctuations or the load forms that are generally considered for fatigue studies. The most primitive form is **constant amplitude (CA)** loads where the loads are completely repetitive after certain time instances called the time period. All the cycles in such type of loading are identical (see Pook, 2007). The loading in such cases is defined in general by certain terminologies which are classical in CA fatigue. Considering for instance a stress-controlled case where the loading is between maximum stress σ_{max} and minimum stress σ_{min}, the stress amplitude is then $\sigma_a = \frac{\sigma_{max}-\sigma_{min}}{2}$ and the mean stress is $\sigma_m = \frac{\sigma_{max}+\sigma_{min}}{2}$. The stress range S or $\Delta\sigma$ is defined as $\Delta\sigma = 2\sigma_a = \sigma_{max} - \sigma_{min}$. The loading may also be expressed in terms of the stress ratio $R = \frac{\sigma_{min}}{\sigma_{max}}$, and the amplitude ratio $A = \frac{\sigma_a}{\sigma_m}$. Certain types of CA loadings are shown in fig. 1.2. Although, these terminologies are classically used for stress-based loading, similar expressions exist in terms of strains as well (see Lemaitre and Desmorat, 2005).

Variable amplitude (VA) loading however does not have a fixed definition, but encompasses everything which does not fall under CA loading (see Schijve, 2009). Schijve (2009) states that the most simple form of VA loading is when several blocks of CA loadings are applied. Similarly, loadings that have constant amplitude but variable mean stress or loadings which have constant mean values but variable amplitudes also fall under VA loading. Richard and Sander (2016) include arbitrary non-periodic loading and also overloading and underloading, shown in fig. 1.3 as VA loading.

Pook (2007) however categorises VA loading into *narrow band random loading*, where individual cycles can be distinguished and *broad band random loading*, where the individual load cycles cannot be distinguished. These are shown in fig. 1.4.

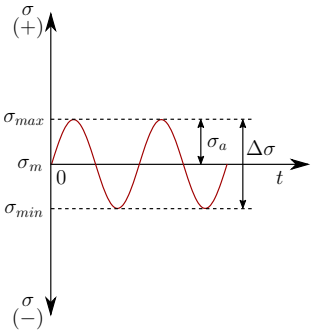

(a) Fully reversed cycle, $R = -1$ and $A = \infty$

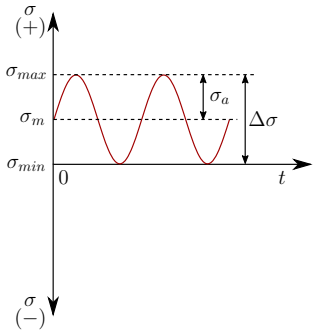

(b) Repeated cycle with positive mean stress, $R = 0$ and $A = 1$

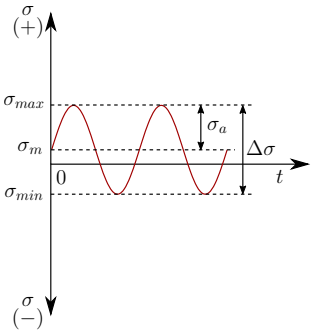

(c) Partially reversed cycle with positive mean stress, $-1 < R < 0$ and $\infty > A > 1$

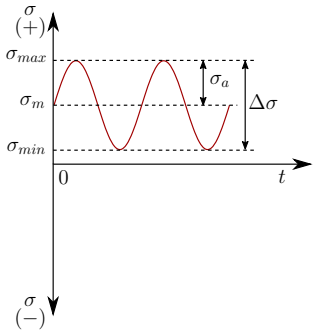

(d) Fluctuating cycle with positive mean stress, $R > 0$ and $A < 1$

Figure 1.2: Different types of constant amplitude loading

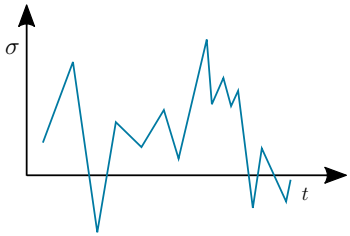

(a) Arbitrarily non-periodic loading

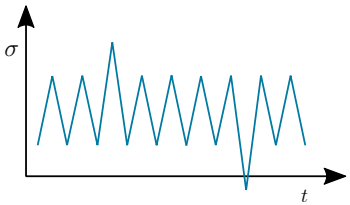

(b) Overload and underload in a mostly periodic loading

Figure 1.3: Different types of variable amplitude loading according to Richard and Sander (2016)

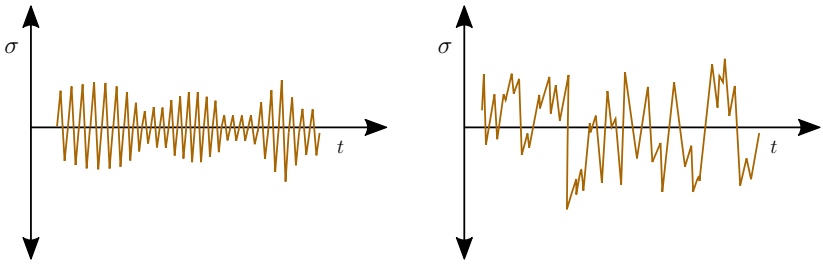

(a) Narrow band random loading (b) Broad band random loading

Figure 1.4: Different types of variable amplitude loading according to Pook (2007)

1.6 Existing fatigue approaches

Various authors over the years have used different ways of classifying different methods that have been developed for fatigue. In Suresh (2001), the methods have been grouped under "total-life approaches" and "defect-tolerance approaches". However, in Cui (2002), the methods have been grouped under "cumulative fatigue damage theories" and "fatigue crack propagation theories". All the approaches where crack behaviour is not taken into consideration, or to be more specific, all the approaches which do not consider a pre-existing crack can be categorised under "cumulative fatigue damage theories", because essentially these methods quantify the deterioration of material properties without involving fracture mechanics. "Fatigue crack propagation theories" or "defect-tolerance approaches" both essentially indicate those methods which assume the presence of macroscopic flaws and compute the number of cycles needed to propagate them. The "total-life approaches" described in Suresh (2001) encompass all the phenomenological continuum-based approaches where the total life is expressed as a function of measurable quantities like stress or strain range. The total life in this case is the time to initiate a dominant crack and the time to propagate the rupture to failure.

It is perhaps important at this point to introduce what is known as "safe-life" and "fail-safe" design approaches for fatigue. These concepts came into existence in the 1950s for the design of aircraft components (see Schütz, 1996). In the case of safe-life approach, the component in question is subjected to a load spectrum that mimics the actual service conditions and a fatigue life is obtained which is invariably modified using a factor of safety. Several tests can be considered using various influential factors to get an idea of the useful fatigue life. The component is thereby rejected from service when it reaches its "safe life", even though there is no failure. The "fail-safe" concept however stems from the idea that even if an individual component fails, the other components should have enough structural integrity so that the whole structure can operate safely. Periodic inspections of individual components are mandatory in this design philosophy, such that damaged members can be repaired or replaced (see Suresh, 2001).

The following classification uses the designation attributed by Cui (2002).

1.6.1 Cumulative fatigue damage theories

The basic idea behind these theories is the fact that the inherent microscopic parameters governing the damage of the material is related to macroscopic quantities like stress or strain. Different damage theories have been developed over the years based on different macroscopic quantities.

1.6.1.1 Stress-based approach or stress life approach

This was first introduced by Wöhler in 1860. The basic idea of this method is to generate what is called the S-N curves. The specimen is loaded at specified cyclic stresses till the specimen ruptures completely, and the number of cycles to failure (N_f) is observed. The stress range ($\Delta\sigma$) or the stress amplitude (σ_a) is plotted with respect to the number of cycles to failure to obtain what is called the S-N curve (fig. 1.5). The concept of endurance limit or fatigue limit (σ_e) is an outcome of the asymptotic behaviour of the S-N curves, which signifies that if the specimen is loaded with a stress amplitude below the endurance limit (σ_e) then it will have infinite life.

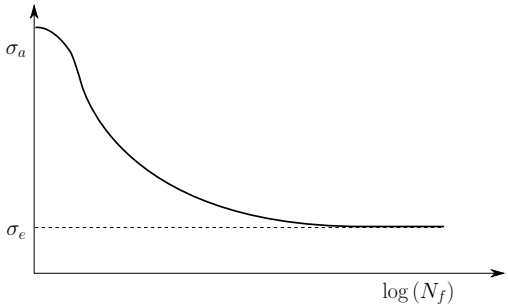

Figure 1.5: A typical S-N curve

The numerical formulation of the S-N curves is given by the Basquin's equation as

$$\sigma_a = \sigma'_f \left(2N_f\right)^b, \tag{1.1}$$

where σ'_f is the fatigue strength coefficient and b is the fatigue strength exponent. However, the Basquin's equation can not predict the complete S-N curve especially for the low cycle regime. A relatively new reformulation of the Basquin's was made in Kohout and Vechet (1999) to describe the complete S-N curve. The S-N curve is influenced by a lot of factors such as frequency of loading, ambient temperature, notches in the specimens, and such others. The most important influencing factor is the "mean stress effect", where with the increase in the mean stress, the number of cycles to failure decreases for a given stress amplitude. The classical way of representing the "mean stress effect" is by using constant life diagrams (fig. 1.6). The most important mean stress models used are developed in Gerber (1874), Goodman (1899), and Soderberg (1939). Although these diagrams do not provide any information on the number of cycles to failure, they can predict any potential to fatigue failure. These diagrams basically depict the maximum mean stress that can be achieved for a given stress amplitude without fatigue failure. The Basquin's equation has been modified in Morrow (1964) to include mean stress effect as,

$$\sigma_a = \left(\sigma'_f - \sigma_m\right)\left(2N_f\right)^b. \tag{1.2}$$

The next important consideration in stress-based approaches is to deal with multiaxial cyclic stresses. The most easy way to analyse multiaxial fatigue is to consider effective stresses. For instance, if $\sigma_{i,a}$ are the amplitudes of the principal stresses σ_i, with $i = 1, 2, 3$, the effective stress amplitude can be computed using the von Mises criterion as

$$\sigma_{e,a} = \frac{1}{\sqrt{2}}\sqrt{\left(\sigma_{1,a} - \sigma_{2,a}\right)^2 + \left(\sigma_{2,a} - \sigma_{3,a}\right)^2 + \left(\sigma_{3,a} - \sigma_{1,a}\right)^2}. \tag{1.3}$$

This effective stress can be used in the Basquin's equation to obtain the number of cycles to failure. In the same way the effective mean stress can be calculated which can then either be used in constant life

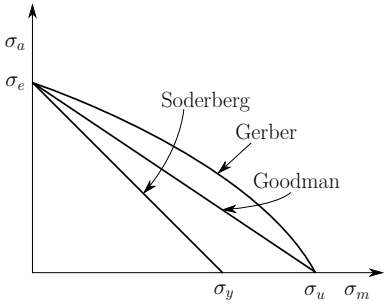

Figure 1.6: Constant life diagram

approach or in Morrow's equation. One of the major drawbacks of this type of effective stress approach is the fact that the effect of tension and compression might not be adequately captured. Thereby the critical plane approach is generally used. Critical plane for multiaxial fatigue can be loosely defined as the plane on which damage and subsequently cracks will occur. Although, the orientation of the critical plane for general multiaxial and non-proportional stress state is not straightforward, several simplified theories have been proposed over the years for multiaxial loading. The first one was from Crossland (1956) who proposed a safety criterion based on effective stress,

$$\sqrt{J_{2,a}} + \bar{\alpha}\sigma_{H,max} \leq \bar{\beta}. \tag{1.4}$$

$J_{2,a}$ is the amplitude of the second invariant of the deviatoric stress and $\sigma_{H,max} = \sigma_{H,m} + \sigma_{H,a}$, with $\sigma_{H,m}$ and $\sigma_{H,a}$ being the mean and amplitude of the hydrostatic stress. $\bar{\alpha}$ and $\bar{\beta}$ are material parameters. This criterion was modified by Sines (1959) to use the mean hydrostatic stress instead of the maximum hydrostatic stress,

$$\sqrt{J_{2,a}} + \bar{\alpha}\sigma_{H,m} \leq \bar{\beta}. \tag{1.5}$$

Several other theories exist especially in Dang Van (1973) with the maximum shear stress and instantaneous hydrostatic stress, and in Papadopoulos et al. (1997) where volume averaged stress quantities are used.

1.6.1.2 Strain-based approach or strain life approach

The idea of stress-based analysis is mainly restricted to elastic deformation. However, for practical cases, structures generally undergo localised plastic deformation, therefore it is more appropriate under these circumstances, to consider a strain-based analysis. The first formulated idea of strain-based analysis is given by the Coffin-Manson relationship,

$$\varepsilon_a^p = \varepsilon_f' \left(2N_f\right)^c, \tag{1.6}$$

where, ε_f' is the fatigue ductility coefficient, ε_a^p is the plastic strain amplitude, and c is the fatigue ductility exponent. Considering additive strain decomposition relation

$$\varepsilon_a = \varepsilon_a^e + \varepsilon_a^p, \tag{1.7}$$

with ε_a and ε_a^e being the total and elastic strains respectively, and the linear elastic law

$$\varepsilon_a^e = \frac{\sigma_a}{E}, \tag{1.8}$$

with E being the modulus of elasticity, the Basquin's equation and the Coffin-Manson rule can be combined to give

$$\varepsilon_a = \frac{\sigma'_f}{E}\left(2N_f\right)^b + \varepsilon'_f\left(2N_f\right)^c. \tag{1.9}$$

This equation can be plotted as ε-N curves as shown in fig. 1.7. This figure defines a transition life $N_{f,t}$ which is the fatigue life when elastic and plastic strain amplitudes are equal.

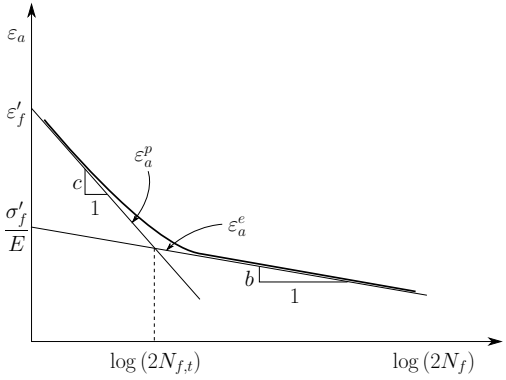

Figure 1.7: A typical ε-N curve

Many modifications have been proposed for the Coffin-Manson relation to replicate accurately experimental ε-N curves, initially in Manson (1965) and later on in Roessle and Fatemi (2000).

In cases of multiaxial loading, similar to the stress-based analysis, the simplest way is to calculate an effective strain amplitude as

$$\varepsilon_{e,a} = \frac{1}{\sqrt{2}\,(1+\nu)}\sqrt{(\varepsilon_{1,a}-\varepsilon_{2,a})^2 + (\varepsilon_{2,a}-\varepsilon_{3,a})^2 + (\varepsilon_{3,a}-\varepsilon_{1,a})^2}, \tag{1.10}$$

with ν being the Poisson's ratio, $\varepsilon_{i,a}$ the principal strain, and $i = 1, 2, 3$. This can then be used in eq. (1.9). Similar criterion can be derived using Tresca theory. However these effective strain measures do not capture the mean stress effect, hence an energy-based criterion was proposed in Smith et al. (1970),

$$\sigma_{max}\varepsilon_a = \frac{\left(\sigma'_f\right)^2}{E}\left(2N_f\right)^{2b} + \varepsilon'_f\sigma'_f\left(2N_f\right)^{b+c}. \tag{1.11}$$

1.6.1.3 Cumulative damage rules

The first damage rule is the linear summation of fatigue damage that is being accumulated with load level. If n_i is the number of cycles for which a load level of $\sigma_{a,i}$ is applied in a sequence of m load levels, the Palmgren-Miner linear damage rule (LDR) states that,

$$D = \sum_{i=1}^{m} r_i = \sum_{i=1}^{m} \frac{n_i}{N_{f,i}}, \tag{1.12}$$

where D is the damage variable, $N_{f,i}$ is the number of cycles to failure for load level $\sigma_{a,i}$ which can be obtained from S-N curves, and r_i is the cycle ratio corresponding to load level $\sigma_{a,i}$. The assumption of

LDR is that at each load level the damage is accumulated in the form of cycle ratio and failure occurs if

$$\sum_{i=1}^{m} r_i = 1. \tag{1.13}$$

This theory does not take into account the order of the load levels $\sigma_{a,i}$, and does not comply with experimental findings.

The first important modification of the LDR was in Marco and Starkey (1954), where non-linear damage rule (NLDR) is represented by a power relationship,

$$D = \sum_{i=1}^{m} r_i^{x_i} = \sum_{i=1}^{m} \left(\frac{n_i}{N_{f,i}} \right)^{x_i}, \tag{1.14}$$

where x_i is an exponent depending on load level $\sigma_{a,i}$. This power law mimics the experimental behaviour of $\sum_{i=1}^{m} r_i < 1$ for high-to-low (H-L) loading and $\sum_{i=1}^{m} r_i > 1$ for low-to-high (L-H) loading. The comparison of LDR and NLDR for H-L and L-H loadings is shown in fig. 1.8.

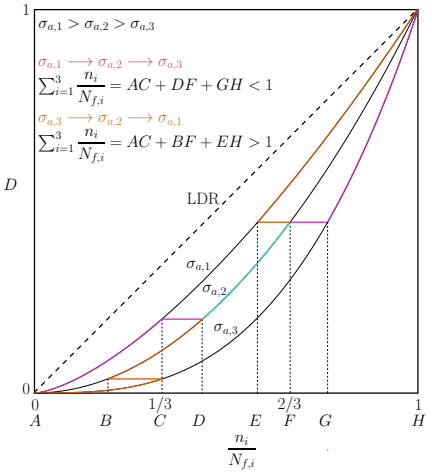

Figure 1.8: Comparison between LDR and NLDR

Another important cumulative damage theory is the two stage linear damage theory developed by the combined work of Langer and Grover (see Grover, 1960, Langer, 1937). The idea is basically to separate the damage process into crack initiation, $N_I = \alpha N_f$; and crack propagation, $N_P = (1 - \alpha) N_f$; where α is a life fraction factor. The LDR can then be applied to either stage. Manson (1965) provided the double linear damage rule (DLDR) through which the equations can be separated into

$$N_I = N_f - P N_f^{0.6}, \tag{1.15a}$$

$$N_P = P N_f^{0.6}, \tag{1.15b}$$

where P is a fatigue life coefficient. The LDR can be applied thereby one for the initiation of crack

$$\sum_{i=1}^{m} \frac{n_i}{N_{I,i}} = 1, \tag{1.16}$$

and another for propagation,

$$\sum_{i=1}^{m} \frac{n_i}{N_{P,i}} = 1. \tag{1.17}$$

The graphical representation of the DLDR is shown in fig. 1.9, which, similar to NLDR, also correctly predicts $\sum_{i=1}^{m} r_i < 1$ for H-L loading and $\sum_{i=1}^{m} r_i > 1$ for L-H loading.

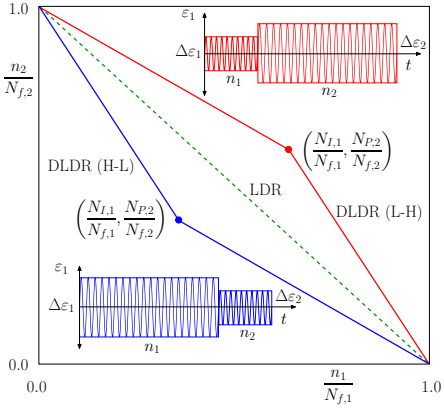

Figure 1.9: Comparison between LDR and DLDR

1.6.1.4 Energy-based damage models

The connection between the hysteretic area and fatigue behaviour, first discovered by Inglis (see Inglis, 1927), has led to a lot of research in describing cumulative damage variables in terms of energy-based parameters. Energy-based damage models can predict the damage accumulation in notched specimen, based on Glinka's rule; which basically states that, if the plastic zone around a notch is surrounded by elastic zone, the elasto-plastic strain energy is approximately equal to the strain energy if the material is assumed to be completely elastic. Energy-based models are able to take mean stress effects and multiaxial behaviour into account. One of the earliest energy-based model was in Kujawski and Ellyin (1984), where plastic strain energy density as a parameter was used. Later on it was found that mean stress effect can not be directly incorporated using plastic strain energy. To rectify this problem, a total strain energy-based approach was introduced in Golos and Ellyin (1988). Irrespective of the type of model used, the main idea is to formulate a power law similar to the Basquin's equation to obtain energy-life relation (see Fatemi and Yang, 1998). Another important development was in Leis (1988), where the damage parameter similar to Smith (eq. (1.11)) was linked as

$$D = \frac{4\sigma_f'}{E}\left(2N_f\right)^{2b_1} + 4\varepsilon_f'\sigma_f'\left(2N_f\right)^{b_1+c_1}, \tag{1.18}$$

with b_1 and c_1 being obtained from instantaneous strain hardening exponent. It is found in Niu et al. (1987) that the strain hardening coefficient tends to change while the strain hardening exponent remains the same during cyclic process. Thereby, a damage function was proposed as

$$D = r^{1/(n'+\alpha)}, \tag{1.19}$$

where $\alpha = (\Delta\sigma\Delta\varepsilon_p/4)^{2b}\sqrt{a}$ with a and b being constants, and n' is the cyclic strain hardening exponent. Another important method was postulated in Kliman (1984), who proposed a damage model for repeated blocks of harmonic load cycles. Considering W_b is the hysteretic energy for a block and $W_{f,b}$ is the energy at fracture for the block, the damage fraction for the block is given by

$$D = \frac{W_b}{W_{f,b}}. \tag{1.20}$$

1.6.1.5 Continuum damage mechanics (CDM) theories

The mechanics of damage is the study, through mechanical variables, of the mechanisms involved in the deterioration when the materials are subjected to loading. The idea of degradation of material being quantified by internal variable in a thermodynamically consistent continuum framework was first developed by Kachanov (1958, 1986). This is a relatively new branch, which is an extension of the classical continuum mechanics. The first usage of CDM for fatigue computation was in Chaboche and Lesne (1988). The proposed damage law is of the form

$$D = 1 - \left(1 - r^{1/(1-\alpha)}\right)^{1/(1+\beta)}, \tag{1.21}$$

where, β is a material parameter, α is a function of the stress state, and r is the cycle ratio. Many notable works have followed since, and well-established continuum damage mechanics theories can be found in Lemaitre (1996), Lemaitre and Desmorat (2005), Murakami (2012). CDM will be dealt in details in Chap. 3.

1.6.2 Fatigue crack propagation theories

Although many authors (see Fatemi and Yang, 1998) do not distinguish between fatigue damage theories and crack propagation theories, a distinction between damage mechanics and fracture mechanics concepts following the demarcation from Cui (2002), Suresh (2001) has been made here. However the counter argument in Fatemi and Yang (1998) is also valid as crack is initiated at the very beginning of the loading and the entire life of the structure is spent in propagating the crack. The initiation and propagation phase can be distinguished from the length of the crack (which is again not fixed). However based on classical fracture mechanics theories, a distinction is made on the fact that crack propagation theories are based on the presence of a pre-crack in the structure.

Based on the theories explained in Cui (2002), Fatemi and Yang (1998), Suresh (2001), it can be divided into three parts based on the crack length.

1.6.2.1 Long crack growth

The first law about fatigue crack growth is based on the findings of Paris and Erdogan (see Paris and Erdogan, 1963). Paris-Erdogan law basically equates the crack growth rate with the stress intensity factor range at the tip of a long crack, i.e.

$$\frac{\mathrm{d}a}{\mathrm{d}N} = A\left(\Delta K\right)^n, \tag{1.22}$$

with $\frac{\mathrm{d}a}{\mathrm{d}N}$ being the growth rate of crack length a with respect to the number of cycles N, n and A being the material constants, and the stress intensity factor being

$$\Delta K = Y\Delta\sigma\sqrt{\pi a}, \tag{1.23}$$

where Y depends on crack geometry. Later on it was discovered that Paris-Erdogan law is only applicable for stable crack propagation region. Thereby the crack growth region was divided into three parts; *Region*

I- initiation and threshold, *Region II- stable crack growth*, and *Region III- unstable crack growth*. The crack growth relation for the threshold region was given in Donahue et al. (1972),

$$\frac{\mathrm{d}a}{\mathrm{d}N} = C\left(\Delta K - \Delta K_{th}\right)^m, \tag{1.24}$$

where ΔK_{th} is the threshold factor below which there will be no crack growth, and C and m are material parameters. For the region of unstable crack growth, the growth rate is extremely high leading to either brittle fracture or ductile tearing. A relation expressing unstable crack growth rate is proposed in Forman and Kearney (1967) as,

$$\frac{\mathrm{d}a}{\mathrm{d}N} = \frac{C\left(\Delta K\right)^m}{\left(1-R\right)K_c - \Delta K}, \tag{1.25}$$

where K_c is the fracture toughness and R is the load ratio. These three regions are schematically represented in fig. 1.10.

Other works include the contribution of Elber (see Elber, 1970) who introduced crack closure concepts which was later on improved in Donald and Paris (1999), Hertzberg et al. (1988), Vasudevan et al. (1994) and especially in Kujawski (2001), where the concept of partial crack closure was introduced.

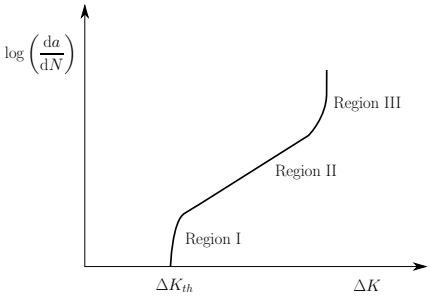

Figure 1.10: Crack growth rate curve showing different regions

The main ideas and developments about long crack growths are based on linear elastic fracture mechanics (LEFM).

1.6.2.2 Physically small crack growth

The growth of physically small cracks is governed by elastic plastic fracture mechanics (EPFM). The first idea of EPFM was proposed in Tomkins (1968), who equated the crack growth rate as a function of the plastic strain, for high strain fatigue, i.e.

$$\frac{\mathrm{d}a}{\mathrm{d}N} = B\left(\Delta\varepsilon_p\sqrt{\pi a}\right)^m - \Xi, \tag{1.26}$$

where B and m are material parameters and Ξ is the threshold condition. Many theories have been proposed especially by modifying the long crack growth laws to include plastic deformation. They were able to predict different EPFM processes quite effectively. One such is the model proposed in McEvily et al. (1999) which matched quite well with experimental findings.

1.6.2.3 Microstructurally small crack growth

This method was developed to measure crack growth at the level of microstructure. The first idea of micro-structural fracture mechanics (MFM) was first introduced in Hobson et al. (1986) and later on in Navarro and de los Rios (1988). The concept of MFM is also based on EPFM and the growth of the crack can be expressed as

$$\frac{\mathrm{d}a}{\mathrm{d}N} = B\left(\Delta\gamma\right)^{\alpha}\left(d-a\right), \tag{1.27}$$

where B and α are material parameters, $\Delta\gamma$ is range of shear strain, and d is a microstructural dimension. As both microstrually small crack (MSC) and physically small crack (PSC) are governed by EPFM, Miller and Hobson (see Hobson, 1986, Miller, 1992) proposed combined laws which are of the form

$$\frac{\mathrm{d}a}{\mathrm{d}N} = B\left(\Delta\gamma\right)^{\alpha}\left(d-a\right), \text{for MSC}, a_0 \leq a \leq a_t, \tag{1.28a}$$

$$\frac{\mathrm{d}a}{\mathrm{d}N} = A\left(\Delta\gamma\right)^{\beta} a - C, \text{for PSC}, a_t \leq a \leq a_f, \tag{1.28b}$$

where a_0 is the initial defect size, a_t is the transition crack length, a_f is the final crack length, A and α are material parameters, C is the crack growth rate at threshold condition.

Although several other methods exist, only the most popular techniques of traditional or contemporary approaches have been covered. For a more extensive review, Cui (2002), Fatemi and Yang (1998) are suggested.

1.7 Cyclic elasto-(visco)plasticity

Structures when subjected to cyclic elasto-(visco)plasticity, three typical phenomena may occur (see Maugin, 1992, Weiß et al., 2004). One of the behaviour corresponds to the case where the stress-strain response curve does not close and the strain increases with each cycle to induce a *ratcheting* effect (see fig. 1.11a). Otherwise, the response curve may end up in a stable hysteresis loop leading to *plastic shakedown* or accumulation (see fig. 1.11b). It is also possible in some instances where this stable loop can completely flatten such that the structure behaves elastically, generating *elastic shakedown* or adaptation (see fig. 1.11c).

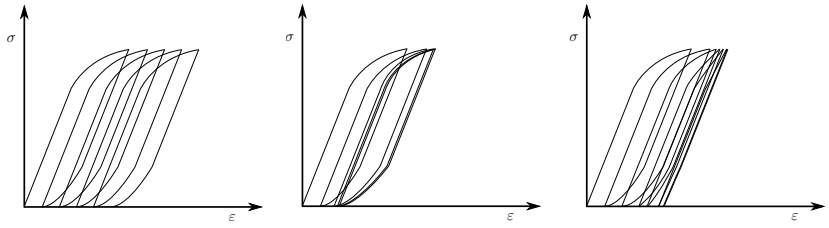

(a) Ratcheting (b) plastic shakedown (c) elastic shakedown

Figure 1.11: Cyclic elasto-(visco)plastictic behaviour

In many cases the idea is to find the stabilised cycle, and thereafter the Coffin-Manson rule can be utilised to find the number of cycles to failure. The search for the stable loop however can be expensive, and hence some sophisticated numerical methods are used to accelerate the simulation. In general these acceleration techniques are divided into three groups (see Nasri, 2017)

– Methods where the evolutions of the quantities of interest are estimated at each point of the structure, e.g. direct cyclic method, cycle skip method, Zarka method, LATIN method;
– Methods where the evolutions of the quantities of interest are estimated only at the critical points of the structure, e.g. Neuber type methods;
– Methods based on model reduction approaches.

The direct cyclic method as introduced in Pommier (2003) is based on calculation of a single cycle with imposed periodic condition. The global admissibilities and local behaviour laws are iteratively calculated until convergence is achieved. Cycle skip methods, for plasticity, essentially deal with the fact that full blocks of cycles can be skipped by successive extrapolations (Saï, 1993). The Zarka method basically considers a structural transform parameter to find the stabilised cycle from the history of its elastic state, both for elastic and plastic shakedown (see Zarka and Caiser, 1979, for details). The variant of the LATIN method as introduced in Cognard and Ladevèze (1993) used temporal model reduction technique to simulated large number of cycles for elasto-viscoplastic materials. The Neuber method is similar to the energy-based approach where most of the structure is considered elastic and Neuber correction is applied only on the local plastic zones (see Lemaitre and Desmorat, 2005). Nasri (2017) used several PGD-based model reduction methods to obtain the stabilised cycle.

1.8 Concluding remarks

From all the methods that have been discussed, the S-N curve, or ε-N curve approaches might seem straightforward, but they are extremely time consuming. Experimental S-N or ε-N curves are generally built using uniaxial tests, for simple specimens. In practical cases involving mixed loading, with localised plasticity with hardening or softening behaviour, therefore resulting in the stress or strain amplitude being depended on space and time, making the S-N or ε-N curves irrelevant. The cumulative damage theories, like the LDR, NLDR, or DLDR although seem to be efficient, rely on the information of S-N or ε-N curves, which for practical structures are not available. Although, NLDR and DLDR give better approximations for block loadings than LDR, the damage variable for all these cases is a function of the cycle ratio and does not represent the physical mechanism of fatigue damage. Energy-based approaches although are thermodynamically consistent models, the damage variable is calculated as a post process of the hystertic area, and not in the form of internal variable. CDM however considers damage to be an intrinsic variable in the fundamental lemmas of thermodynamics, and thereby provides a thermodynamically consistent quantification of the degradation of the material due to fatigue. Fracture mechanics, although provides a consistent framework to model and simulate the crack propagation phase, especially with the advent of the J integral and EPFM, which takes into account crack tip plasticity, is beyond the scope of this research. The focus of this research is to use a novel approach for CDM simulation such that the crack initiation phase can be predicted. A brief review of CDM especially in the context of fatigue loading is presented in the next chapter.

Chapter 2

Continuum damage mechanics

This chapter inherently discusses about the basic theory and modelling of quasi-static evolution of structures satisfying the momentum balance, the energy balance, and the entropy balance. No new formulations are presented here but classical theories of modelling elasto-plastic processes involving damage as an internal variable are discussed, details of which can be found in Lemaitre (1996), Lemaitre and Desmorat (2005). Lastly certain innovations based on damage mechanics to tackle fatigue processes are highlighted.

2.1 Continuum mechanics: an overview

To obtain the global admissibility conditions, it is necessary that a reference problem is introduced in a spatial domain Ω, as shown in fig. 2.1. The region Ω has a boundary $\partial\Omega$, which is subdivided into $\partial\Omega_1$ and $\partial\Omega_2$, such that $\partial\Omega = \partial\Omega_1 \cup \partial\Omega_2$. The body is subjected to specified surface force per unit surface area $\vec{F}_d$ on $\partial\Omega_2$ and to specified displacement $\vec{U}_d$ on $\partial\Omega_1$. The outward normal vector $\vec{n}$ is defined at any material point M on the boundary $\partial\Omega$. The body is also subjected to body force per unit volume $\vec{f}_d$. The evolution of the structure is considered to be quasi-static within time $t \in [0, T]$, with T being the total time.

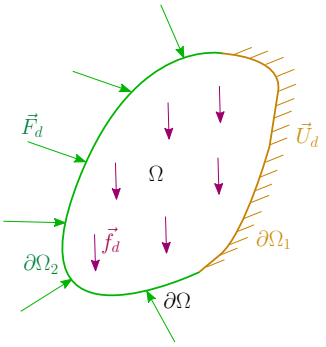

Figure 2.1: Reference problem in domain Ω

2.1.1 Admissibility conditions

In this thesis, infinitesimal deformation is considered, with no distinction between Lagrangian and Eulerian description. Considering $\vec{u}(\vec{x},t)$ is the displacement field of the body Ω, with $\vec{x}$ representing the position vector, the velocity field can be written as $\vec{v}(\vec{x},t) = \dot{\vec{u}}(\vec{x},t)$, and the corresponding strain tensor is $\boldsymbol{\varepsilon}$. If the body is subjected to a virtual displacement field $\delta\vec{u}$, the total internal virtual power can be written as (see Lemaitre and Chaboche, 1990)

$$W_i = -\int\limits_{\Omega\times[0,T]} \boldsymbol{\sigma} : \delta\dot{\boldsymbol{\varepsilon}}\mathrm{d}V\mathrm{d}t, \tag{2.1}$$

where $\delta\dot{\boldsymbol{\varepsilon}}$ is the virtual strain rate corresponding to the virtual velocity $\delta\dot{\vec{u}}$ such that

$$\delta\dot{\boldsymbol{\varepsilon}} = \frac{1}{2}\left[\nabla\left(\delta\dot{\vec{u}}\right) + \left(\nabla\delta\left(\dot{\vec{u}}\right)\right)^T\right], \tag{2.2}$$

and $\boldsymbol{\sigma}$ is the Cauchy stress tensor. The external virtual power is given by

$$W_e = \int\limits_{\Omega\times[0,T]} \vec{f_d}\cdot\delta\dot{\vec{u}}\,\mathrm{d}V\mathrm{d}t + \int\limits_{\partial\Omega_2\times[0,T]} \vec{F_d}\cdot\delta\dot{\vec{u}}\,\mathrm{d}S\mathrm{d}t. \tag{2.3}$$

From the virtual work principle, it can be established that

$$\begin{aligned} &W_i + W_e = 0, \\ \implies &-\int\limits_{\Omega\times[0,T]} \boldsymbol{\sigma} : \delta\dot{\boldsymbol{\varepsilon}}\mathrm{d}V\mathrm{d}t + \int\limits_{\Omega\times[0,T]} \vec{f_d}\cdot\delta\dot{\vec{u}}\,\mathrm{d}V\mathrm{d}t + \int\limits_{\partial\Omega_2\times[0,T]} \vec{F_d}\cdot\delta\dot{\vec{u}}\,\mathrm{d}S\mathrm{d}t = 0. \end{aligned} \tag{2.4}$$

It has to be noted that $\delta\vec{u}$ is kinematically admissible, i.e.

$$\boldsymbol{\varepsilon} = \frac{1}{2}\left[\nabla\vec{u} + (\nabla\vec{u})^T\right], \text{ in } \Omega, \tag{2.5a}$$

$$\vec{u} = \vec{U_d}, \text{ i.e. } \delta\vec{u} = 0 \text{ on } \partial\Omega_1. \tag{2.5b}$$

Using these conditions, along with the divergence theorem, eq. (2.4) can be re-written as

$$\int\limits_{\Omega\times[0,T]} \left(\nabla\cdot\boldsymbol{\sigma} + \vec{f_d}\right)\cdot\delta\dot{\vec{u}}\,\mathrm{d}V\mathrm{d}t + \int\limits_{\partial\Omega_2\times[0,T]} \left(\vec{F_d} - \boldsymbol{\sigma}\cdot\vec{n}\right)\cdot\delta\dot{\vec{u}}\,\mathrm{d}S\mathrm{d}t = 0,\ \forall\delta\dot{\vec{u}}. \tag{2.6}$$

Equation (2.6) or eq. (2.4) is known as the static admissibility condition. From eq. (2.6), the static equilibrium equation and the static boundary condition are obtained as

$$\nabla\cdot\boldsymbol{\sigma} + \vec{f_d} = 0, \text{ in } \Omega, \tag{2.7a}$$

$$\vec{F_d} = \boldsymbol{\sigma}\cdot\vec{n}, \text{ on } \partial\Omega_2. \tag{2.7b}$$

In the previous case, the variation principle was applied to the rates of displacements. If similar formulations are performed on stress, complementary virtual work can be obtained (see Wunderlich and

Pilkey, 2002). The principle of complementary virtual work is dual to the principle of virtual work. If Ω is subjected to a virtual stress field $\delta\boldsymbol{\sigma}$, the internal complementary virtual power can be written as

$$W_i^c = -\int\limits_{\Omega\times[0,T]} \delta\boldsymbol{\sigma} : \dot{\boldsymbol{\varepsilon}}\ \mathrm{d}V\mathrm{d}t. \tag{2.8}$$

Considering a virtual force $\delta\vec{F_u}$ is acting on the boundary $\partial\Omega_1$ such that

$$\delta\vec{F_u} = \delta\boldsymbol{\sigma}\cdot\vec{n}, \text{on } \partial\Omega_1, \tag{2.9}$$

the external complementary virtual power can be written as,

$$W_e^c = \int\limits_{\partial\Omega_1\times[0,T]} \delta\vec{F_u}\cdot\dot{\vec{u}}\ \mathrm{d}S\mathrm{d}t = \int\limits_{\partial\Omega_1\times[0,T]} \delta\boldsymbol{\sigma}\cdot\vec{n}\cdot\dot{\vec{U}}_d\ \mathrm{d}S\mathrm{d}t. \tag{2.10}$$

Similar to the previous case, the principal of complementary virtual work states,

$$\begin{aligned} &W_i^c + W_e^c = 0, \\ &\implies -\int\limits_{\Omega\times[0,T]} \delta\boldsymbol{\sigma} : \dot{\boldsymbol{\varepsilon}}\ \mathrm{d}V\mathrm{d}t + \int\limits_{\partial\Omega_1\times[0,T]} \delta\boldsymbol{\sigma}\cdot\vec{n}\cdot\dot{\vec{U}}_d\ \mathrm{d}S\mathrm{d}t = 0. \end{aligned} \tag{2.11}$$

It has to be noted at this point, that $\delta\boldsymbol{\sigma}$ has to be statically admissible, i.e.

$$\delta\left(\nabla\cdot\boldsymbol{\sigma}\right) = 0, \text{ in}\,\Omega, \tag{2.12a}$$

$$\boldsymbol{\sigma}.\vec{n} = \vec{F_d} \quad \text{i.e.} \quad \delta\boldsymbol{\sigma}\cdot\vec{n} = 0 \text{ on } \partial\Omega_2. \tag{2.12b}$$

Equation (2.11) is called the kinematic admissibility condition (see Wunderlich and Pilkey, 2002). Similar to the static admissibility condition, it is possible to obtain the corresponding strong form, i.e. the strain-displacement relationship and the kinematic boundary condition from eq. (2.11). These can be written as,

$$\boldsymbol{\varepsilon} = \frac{1}{2}\left[\nabla\vec{u} + (\nabla\vec{u})^T\right], \text{ in}\,\Omega, \tag{2.13a}$$

$$\vec{u} = \vec{U_d}, \text{ on}\,\partial\Omega_1. \tag{2.13b}$$

2.1.2 Constitutive relations

Apart from the admissibility conditions described before, the structure also needs certain local laws which describe the material properties and are called constitutive relations. The starting point of any constitutive relation is the first law of thermodynamics, or the conservation of energy. Without going into the details of thermodynamics, it is possible to write the first law in the form,

$$\rho\dot{e} = \boldsymbol{\sigma} : \dot{\boldsymbol{\varepsilon}} + w - \nabla\cdot\vec{q}, \tag{2.14}$$

where ρ is the mass density of the material, e is the specific internal energy, w is the volumetric density of the internal heat production, and $\vec{q}$ is the heat flux vector.

The next is the second law of thermodynamics, which states that the total entropy production rate is always greater than or equal to the rate of heating divided by the temperature $\mathcal{T}$. This can be written as

$$\rho \frac{\mathrm{d}s}{\mathrm{d}t} - \frac{w}{\mathcal{T}} + \nabla \cdot \frac{\vec{q}}{\mathcal{T}} \geq 0, \tag{2.15}$$

where s is the specific entropy.

Equation (2.14) can be used to rewrite eq. (2.15) as

$$\rho \left(\mathcal{T} \frac{\mathrm{d}s}{\mathrm{d}t} - \frac{\mathrm{d}e}{\mathrm{d}t} \right) + \boldsymbol{\sigma} : \dot{\boldsymbol{\varepsilon}} - \vec{q} \cdot \frac{\nabla \mathcal{T}}{\mathcal{T}} \geq 0. \tag{2.16}$$

The next step is to define Helmholtz specific free energy $\Psi = e - \mathcal{T}s$, to rewrite eq. (2.16) as

$$\boldsymbol{\sigma} : \dot{\boldsymbol{\varepsilon}} - \rho \left(\dot{\Psi} + s\dot{\mathcal{T}} \right) - \vec{q} \cdot \frac{\nabla \mathcal{T}}{\mathcal{T}} \geq 0. \tag{2.17}$$

This equation is called the Clausius-Duhem inequality. It has to be considered now, that the thermodynamic state of a material medium at a given point and instant is completely defined by the knowledge of certain variables at that particular point and instant. These variables are called the state variables, and the physical phenomena they describe will be thermodynamically admissible if the Clausius-Duhem inequality is satisfied. Certain state variables can be measured directly and are called observable variables, e.g. the total strain $\boldsymbol{\varepsilon}$ and the temperature $\mathcal{T}$. Also, for dissipative phenomena, the current state depends on the past history, which is represented by the values at each instant of certain other variables called internal variables. Restricting to infinitesimal strain theories, the strain can be decomposed additively, into two internal variables,

$$\boldsymbol{\varepsilon} = \boldsymbol{\varepsilon}^e + \boldsymbol{\varepsilon}^p. \tag{2.18}$$

where $\boldsymbol{\varepsilon}^p$ is the plastic or permanent strain, and $\boldsymbol{\varepsilon}^e$ is the elastic strain. To describe dissipative phenomena other than plasticity, e.g. damage or hardening, other internal variables have to be introduced. The choice of the type or number of internal variables is not restricted. However, they are dictated by the physics of the phenomena that these variables are intended to describe. For the time being, let $\Upsilon_i, i \in \mathbb{Z}$, be the set of all internal variables used for the following formulation. The concepts of plasticity along with other internal variables that dictates the dissipative phenomenon will be dealt later on.

The general choice of Helmholtz free energy should be such that

$$\Psi = \Psi \left(\boldsymbol{\varepsilon} - \boldsymbol{\varepsilon}^p, \mathcal{T}, \Upsilon_i \right) = \Psi \left(\boldsymbol{\varepsilon}^e, \mathcal{T}, \Upsilon_i \right), \tag{2.19}$$

which gives

$$\frac{\partial \Psi}{\partial \boldsymbol{\varepsilon}^e} = \frac{\partial \Psi}{\partial \boldsymbol{\varepsilon}} = -\frac{\partial \Psi}{\partial \boldsymbol{\varepsilon}^p}. \tag{2.20}$$

Thereby, using

$$\dot{\Psi} = \frac{\partial \Psi}{\partial \boldsymbol{\varepsilon}^e} : \dot{\boldsymbol{\varepsilon}}^e + \frac{\partial \Psi}{\partial \mathcal{T}} \dot{\mathcal{T}} + \frac{\partial \Psi}{\partial \Upsilon_i} \dot{\Upsilon}_i, \tag{2.21}$$

the Clausius-Duhem inequality can be rewritten as

$$\left(\boldsymbol{\sigma} - \rho \frac{\partial \Psi}{\partial \boldsymbol{\varepsilon}^e} \right) : \dot{\boldsymbol{\varepsilon}}^e + \boldsymbol{\sigma} : \dot{\boldsymbol{\varepsilon}}^p - \rho \left(s + \frac{\partial \Psi}{\partial \mathcal{T}} \right) \dot{\mathcal{T}} - \rho \frac{\partial \Psi}{\partial \Upsilon_i} \dot{\Upsilon}_i - \vec{q} \cdot \frac{\nabla \mathcal{T}}{\mathcal{T}} \geq 0. \tag{2.22}$$

Considering uniform and constant temperature conditions (no thermal effects), the Clausius-Duhem inequality reduces to

$$\left(\boldsymbol{\sigma} - \rho \frac{\partial \Psi}{\partial \boldsymbol{\varepsilon}^e} \right) : \dot{\boldsymbol{\varepsilon}}^e + \boldsymbol{\sigma} : \dot{\boldsymbol{\varepsilon}}^p - \rho \frac{\partial \Psi}{\partial \Upsilon_i} \dot{\Upsilon}_i \geq 0. \tag{2.23}$$

As eq. (2.23) is valid for any $\dot{\boldsymbol{\varepsilon}}^e$, the elastic state law can be written as

$$\boldsymbol{\sigma} = \rho \frac{\partial \Psi}{\partial \boldsymbol{\varepsilon}^e}. \tag{2.24}$$

Equation (2.20) along with eq. (2.24) can be combined to give

$$\boldsymbol{\sigma} = \rho \frac{\partial \Psi}{\partial \boldsymbol{\varepsilon}^e} = \rho \frac{\partial \Psi}{\partial \boldsymbol{\varepsilon}} = -\rho \frac{\partial \Psi}{\partial \boldsymbol{\varepsilon}^p}. \tag{2.25}$$

This defines the stress tensor $\boldsymbol{\sigma}$ as the associated or conjugate variable of $\boldsymbol{\varepsilon}^e$, $\boldsymbol{\varepsilon}$, and $-\boldsymbol{\varepsilon}^p$. In a similar manner, thermodynamic forces associated with the set of the internal variables Υ_i can be defined as

$$\Lambda_i = \rho \frac{\partial \Psi}{\partial \Upsilon_i}. \tag{2.26}$$

Using the state laws (eq. (2.24) and eq. (2.26)), the Clausius-Duhem inequality (eq. (2.23)) can be rewritten as

$$\boldsymbol{\sigma} : \dot{\boldsymbol{\varepsilon}}^p - \Lambda_i \dot{\Upsilon}_i \geq 0, \tag{2.27}$$

which basically states that the internal intrinsic dissipation is positive. In order to define the laws related to the dissipation process, a dissipation potential is defined of the form

$$\Phi = \Phi \left(\dot{\boldsymbol{\varepsilon}}^p, \dot{\Upsilon}_i \right). \tag{2.28}$$

This function Φ is a positive convex function with zero at the origin of the space of the flux variables $\left(\dot{\boldsymbol{\varepsilon}}^p, \dot{\Upsilon}_i \right)$ (see de Souza Neto et al., 2011, Lemaitre and Chaboche, 1990). The complementary laws are thereby defined as

$$\boldsymbol{\sigma} = \frac{\partial \Phi}{\partial \dot{\boldsymbol{\varepsilon}}^p}, \tag{2.29a}$$

$$\Lambda_i = -\frac{\partial \Phi}{\partial \dot{\Upsilon}_i}. \tag{2.29b}$$

However, it is more convenient to express the complementary laws as functions of the dual variables. To achieve that, a dissipation pseudo-potential $\Phi^* \left(\boldsymbol{\sigma}, \Lambda_i \right)$ is obtained through Legendre-Fenchel transformation of the dissipation potential $\Phi \left(\dot{\boldsymbol{\varepsilon}}^p, \dot{\Upsilon}_i \right)$. This pseudo-potential Φ^*, being the dual of Φ, helps to write the complementary laws in the form

$$\dot{\boldsymbol{\varepsilon}}^p = \frac{\partial \Phi^*}{\partial \boldsymbol{\sigma}}, \tag{2.30a}$$

$$\dot{\Upsilon}_i = -\frac{\partial \Phi^*}{\partial \Lambda_i}. \tag{2.30b}$$

These equations are called the evolution equations of the flux variables as functions of the dual variables. It can be seen in eq. (2.30) that the rates of change of the flux variables are normal to the surface Φ^*. This normality rule is obeyed by all generalised standard materials. The only difficulty hereby is to define the pseudo-potential Φ^*. For behaviour independent of velocity, Φ^* becomes non-differentiable, and the normality rule can then be written in terms of another potential function F as

$$\dot{\boldsymbol{\varepsilon}}^p = \dot{\lambda} \frac{\partial F}{\partial \boldsymbol{\sigma}}, \tag{2.31a}$$

$$\dot{\Upsilon}_i = -\dot{\lambda} \frac{\partial F}{\partial \Lambda_i}, \tag{2.31b}$$

where $\dot{\lambda}$ is the Lagrange multiplier which is obtained from the consistency condition eq. (2.33). For associative flow rules, the potential F is taken to be the plastic yield function f^p, and in such cases the loading-unloading criterion is given by the Karush-Kuhn-Tucker condition

$$\dot{\lambda} \geq 0, f^p \leq 0, \dot{\lambda} f^p = 0. \tag{2.32}$$

The consistency condition is given by

$$\dot{\lambda} \dot{f}^p = 0. \tag{2.33}$$

2.2 General constitutive behaviour

The most primitive form of constitutive behaviour is the linear elastic state law. To define a linear elastic state law, the elastic free energy function Ψ^e is written as,

$$\rho \Psi^e = \frac{1}{2} \boldsymbol{\varepsilon}^e : \mathbf{C} \boldsymbol{\varepsilon}^e, \tag{2.34}$$

where $\mathbf{C}$ is called Hooke tensor or elasticity tensor. This helps to rewrite eq. (2.24) as

$$\boldsymbol{\sigma} = \mathbf{C} \boldsymbol{\varepsilon}^e. \tag{2.35}$$

However, such phenomenon is completely reversible and is valid till there are no permanent deformations of the structure. Certain materials, especially brittle materials, can be completely quantified using elastic stress-strain relationships, which fail without any permanent deformations. For ductile materials, e.g. metals, however, there are appreciable permanent deformations before rupture and the material behaviour are non-linear and dissipative after the *elastic limit* is reached. Such behaviour is essentially deemed to be plastic.

2.2.1 Concept of plasticity

The most idealistic plastic behaviour is perfect plasticity, which rarely happens for metals in practical scenario. Perfect plasticity or ideal plasticity results in infinite deformations after the elastic limit is reached, or in other words the load carrying capacity is completely lost after the elastic limit is crossed. Strain hardening, however in general, results in a non-linear increase in stress with respect to the strain after yielding. Due to hardening, the material does not loose the load carrying capacity at the onset of yielding. The stress-strain relationship is complicated and can in the most simplified case be defined in terms of hardening modulus which is a function of total or plastic strain, or can be described as power law, e. g. the classical case of Ramberg-Osgood equation (see Ramberg and Osgood, 1943). Perfect plasticity and strain hardening are illustrated in fig. 2.2.

However, Ramberg-Osgood type equations do not capture the stress-strain behaviour accurately, especially for cyclic plasticity. For an accurate description of hardening, it is more convenient to use separate internal variables. Classically, hardening can be classified into kinematic and isotropic. For isotropic hardening, the radius of the yield surface (the surface of elastic limit) in the principal stress space increases. In this case the yielding during tension and compression is considered to be the same. This kind of hardening fails to take into account Bauschinger effect, which indicates the loss of isotropy and lower strength during compression, prevalent mostly in metals. Thereby, kinematic hardening is introduced, where the yield surface only translates in the principal stress space without any change in radius. These phenomena are shown in fig. 2.3. For metals, in general, either pure kinematic hardening or mixed hardening model is used. It has to be noted that reverse phenomena called softening also exist, which have been detailed in Lemaitre and Chaboche (1990).

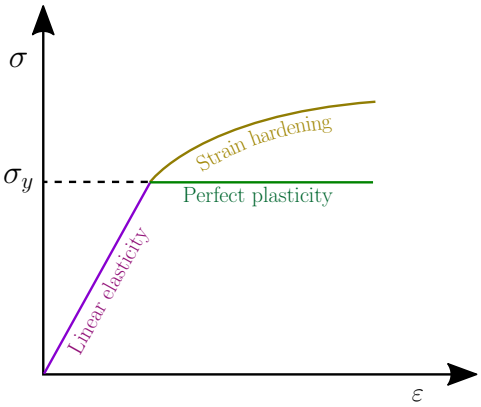

Figure 2.2: Stress-strain relationship for hardening and perfect plasticity

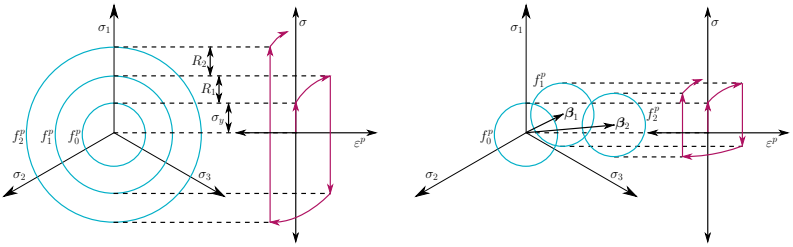

(a) Isotropic hardening

(b) Kinematic hardening

Figure 2.3: Representation of strain hardening in stress space and in tension-compression

2.2.2 Rate-independent plasticity

As the name suggests rate-independent plasticity or often referred as just "plasticity", is confined to those cases where the rate of loading does not have any influence. Before beginning any description of constitutive relations it is necessary to define the accumulated or cumulative plastic strain p as a non-decreasing quantity, i.e.

$$\begin{aligned} \dot{p} &= \left(\frac{2}{3}\dot{\boldsymbol{\varepsilon}}^p : \dot{\boldsymbol{\varepsilon}}^p\right)^{1/2}, \\ \implies p &= \int_0^t \left(\frac{2}{3}\dot{\boldsymbol{\varepsilon}}^p : \dot{\boldsymbol{\varepsilon}}^p\right)^{1/2} \mathrm{d}\tau. \end{aligned} \tag{2.36}$$

Now, the free energy function mentioned in eq. (2.19), can be decoupled into parts, one with respect to elasticity and the other one with respect to hardening,

$$\Psi = \Psi^e\left(\boldsymbol{\varepsilon}^{\boldsymbol{e}}\right) + \Psi^p\left(\boldsymbol{X}\right), \tag{2.37}$$

where Ψ^e is the contribution from elasticity and Ψ^p gives the contribution from the set of hardening variables $\boldsymbol{X} = \{\boldsymbol{\alpha}, r\}$, with $\boldsymbol{\alpha}$ being the flux variable for kinematic hardening and r being the flux variable for isotropic hardening. It is convenient at this point to use the Gibbs specific free enthalpy Ψ^*, by a partial Legendre transformation of Ψ on the strain (see Lemaitre and Desmorat, 2005). This gives

$$\Psi^* = \Psi^{*,e}(\boldsymbol{\sigma}) + \frac{1}{\rho}\boldsymbol{\sigma} : \boldsymbol{\varepsilon^p} - \Psi^p(\boldsymbol{X}). \tag{2.38}$$

The elastic state law can be obtained then by differentiating the Gibbs free enthalpy with respect to the associated variable (stress tensor), i.e.

$$\begin{aligned} \boldsymbol{\varepsilon} = \rho\frac{\partial\Psi^*}{\partial\boldsymbol{\sigma}} &= \rho\frac{\partial\Psi^{*,e}}{\partial\boldsymbol{\sigma}} + \boldsymbol{\varepsilon}^p, \\ \implies \boldsymbol{\varepsilon}^e &= \rho\frac{\partial\Psi^{*,e}}{\partial\boldsymbol{\sigma}}. \end{aligned} \tag{2.39}$$

The other state laws for the hardening variables are obtained as

$$\boldsymbol{Z} = -\rho\frac{\partial\Psi^*}{\partial\boldsymbol{X}} = \rho\frac{\partial\Psi^p}{\partial\boldsymbol{X}}, \tag{2.40}$$

with $\boldsymbol{Z}$ being the set of thermodynamic forces, $\boldsymbol{Z} = \{\boldsymbol{\beta}, R\}$, which are conjugate to $\boldsymbol{X}$. In the most classical case, $\Psi^{*,e}$ is defined as

$$\rho\Psi^{*,e} = \frac{1}{2}\boldsymbol{\sigma} : \mathbf{C}^{-1}\boldsymbol{\sigma}. \tag{2.41}$$

This gives the elastic state equation to be

$$\boldsymbol{\varepsilon}^e = \mathbf{C}^{-1}\boldsymbol{\sigma}. \tag{2.42}$$

As far as the state laws for the hardening variables are concerned, mostly, the kinematic relation is taken to be linear and the isotropic relation is considered to be exponential. This is achieved by using Ψ^p as

$$\rho\Psi^p = \frac{1}{2}\boldsymbol{\alpha} : \mathbf{Q}\boldsymbol{\alpha} + g(r) \tag{2.43}$$

with $\mathbf{Q}$ being tensor of material parameters similar to the Hooke tensor and g being a function depending on r such that

$$g'(r) = R_\infty(1 - \exp(-\gamma r)), \tag{2.44}$$

where R_∞ and γ are the material parameters. The tensor $\mathbf{Q}$ in Voigt matrix notation will be a diagonal matrix with equal diagonal terms Q. This would give the equations of state as

$$\boldsymbol{\beta} = \mathbf{Q}\boldsymbol{\alpha}, \tag{2.45a}$$

$$R = R_\infty(1 - \exp(-\gamma r)). \tag{2.45b}$$

Equation (2.45a) shows a linear kinematic state law and eq. (2.45b) shows a non-linear (exponential) isotropic state law (see Cognard and Ladevèze, 1993). These are commonly used formulations, however either non-linear kinematic law or linear isotropic law can also be used (see Lemaitre and Desmorat, 2005). The choice of the type of law just has to be consistent with the real physical behaviour of the material it mimics.

At this point it is necessary to introduce what is called the plastic yield function f^p. This is basically a surface that demarcates the elastic state and the plastic flow. The most classical form of yield function that is used for metals is of the von Mises type,

$$f^p = \sqrt{3J_2(\boldsymbol{\sigma} - \boldsymbol{\beta})} - R - \sigma_y, \tag{2.46}$$

with σ_y being the initial yield stress and J_2 being the second invariant of the deviatoric part of $\boldsymbol{\sigma} - \boldsymbol{\beta}$. Considering, $\boldsymbol{\beta}$ to be completely deviatoric, eq. (2.46) can be re-written as

$$f^p = \sqrt{\frac{3}{2}\left[(\boldsymbol{\sigma}^D - \boldsymbol{\beta}) : (\boldsymbol{\sigma}^D - \boldsymbol{\beta})\right]} - R - \sigma_y, \tag{2.47}$$

where $\boldsymbol{\sigma}^D$ is the deviatoric stress tensor. The idea of plasticity is that this function cannot be greater than zero. If $f^p < 0$, it is considered to be in the elastic regime; if $f^p = 0$ and $\dot{f}^p = 0$, plastic flow is said to occur; and if $\dot{f}^p < 0$ with $f^p = 0$, it is considered to be elastic unloading. The evolution equations (eq. (2.31)) can then be written as

$$\dot{\boldsymbol{\varepsilon}}^p = \frac{3}{2}\frac{\left(\boldsymbol{\sigma}^D - \boldsymbol{\beta}\right)}{\sqrt{\frac{3}{2}\left[(\boldsymbol{\sigma}^D - \boldsymbol{\beta}) : (\boldsymbol{\sigma}^D - \boldsymbol{\beta})\right]}}\dot{\lambda}, \tag{2.48a}$$

$$\dot{\alpha} = \frac{3}{2}\frac{\left(\boldsymbol{\sigma}^D - \boldsymbol{\beta}\right)}{\sqrt{\frac{3}{2}\left[(\boldsymbol{\sigma}^D - \boldsymbol{\beta}) : (\boldsymbol{\sigma}^D - \boldsymbol{\beta})\right]}}\dot{\lambda}, \tag{2.48b}$$

$$\dot{r} = \dot{\lambda}. \tag{2.48c}$$

It is evident from eqs. (2.48a) to (2.48b) that for von Mises associative plasticity, the plastic strain and the back strain are the same, and the plastic multiplier and the isotropic internal variable are the same. Equation (2.48a) can be used to rewrite eq. (2.36) as

$$\dot{p} = \dot{\lambda}, \tag{2.49}$$

which basically gives

$$\dot{r} = \dot{p} = \dot{\lambda}. \tag{2.50}$$

Remaining challenge is to calculate the plastic multiplier $\dot{\lambda}$, such that $\dot{\lambda} = 0$ when $f^p < 0$ or $\dot{f}^p < 0$; and $\dot{\lambda} \neq 0$ when $f^p = 0$ or $\dot{f}^p = 0$, for which $\dot{\lambda}$ can be calculated from the consistency condition $\dot{f}^p = 0$.

Although, yield surface of von Mises type has been considered here, other forms such as Tresca yield surface, Mohr-Coulomb yield surface, Drucker-Prager yield surface are also possible (see Lemaitre and Desmorat, 2005). However for metals, von Mises yield function is the standard. Many variations of the von Mises type visco(plasticity) models exist, one of the most important is the Marquis-Chaboche visco(plasticity) model (see Cognard and Ladevèze, 1993) which includes an extra softening term in the yield function, i.e.

$$f^p = \sqrt{\frac{3}{2}\left[(\boldsymbol{\sigma}^D - \boldsymbol{\beta}) : (\boldsymbol{\sigma}^D - \boldsymbol{\beta})\right]} + \frac{a}{2}\left[\boldsymbol{\beta} : \mathbf{Q}^{-1}\boldsymbol{\beta}\right] - R - \sigma_y. \tag{2.51}$$

2.2.3 Viscoplasticity

This is a more general case, where the evolution equations depend on the rate of loading. This is more profound in metals at high temperature (e.g. creep). In the case of viscoplasticity the plastic domain is given by $f^p > 0$, which is of course not possible for plasticity; and the elastic domain is given by $f^p \leq 0$. Plasticity can be interpreted as a limiting case of viscoplasticity (see Ladevèze, 1999). For the formulation of viscoplasticity, the equations of state remain the same as given in eq. (2.42) and eq. (2.45). The only change that needs to be incorporated is in the evolution equations. In the case of visco-plasticity,

the pseudo-dissipation potential Φ^* introduced in eq. (2.30) has a closed form and is differentiable. The most common is to introduce a pseudo potential of the form

$$\Phi^* = \frac{k}{n+1} \langle f^p \rangle_+^{n+1}, \tag{2.52}$$

where k and n are viscosity parameters. Thereby, eq. (2.48a) can be re-written as

$$\dot{\boldsymbol{\varepsilon}}^p = k \langle f^p \rangle_+^n \left[\frac{3}{2} \frac{\left(\boldsymbol{\sigma}^D - \boldsymbol{\beta}\right)}{\sqrt{\frac{3}{2} \left[(\boldsymbol{\sigma}^D - \boldsymbol{\beta}) : (\boldsymbol{\sigma}^D - \boldsymbol{\beta}) \right]}} \right]. \tag{2.53}$$

In a similar manner, the evolution equation for the hardening variable can also be written as

$$\dot{\alpha} = k \langle f^p \rangle_+^n \left[\frac{3}{2} \frac{\left(\boldsymbol{\sigma}^D - \boldsymbol{\beta}\right)}{\sqrt{\frac{3}{2} \left[(\boldsymbol{\sigma}^D - \boldsymbol{\beta}) : (\boldsymbol{\sigma}^D - \boldsymbol{\beta}) \right]}} \right], \tag{2.54a}$$

$$\dot{r} = k \langle f^p \rangle_+^n. \tag{2.54b}$$

Comparing these equations with eq. (2.48), the term $k \langle f^p \rangle_+^n$ can be interpreted as the viscoplastic multiplier and according to the definition of $\langle \square \rangle_+$ this viscoplastic multiplier $\dot{\lambda} = k \langle f^p \rangle_+^n > 0$ when $f^p > 0$ and zero otherwise. Equations (2.53) to (2.54) are known as Norton's law, and although there exist a lot of other viscoplastic laws (see Lemaitre and Chaboche, 1990), it remains one of the most popular.

2.2.4 Concept of damage

The concept of damage as a continuum variable was first introduced by Kachanov (see Kachanov, 1958), considering a representative volume element (RVE) on which all properties were represented by homogenised variables. Damage, especially for metals, is always related to plastic strain or plastic dissipation, either at mesoscale (scale of RVE) or at microscale (scale of discontinuity) (see Lemaitre and Desmorat, 2005). As damage can be interpreted as the growth of micro-cavities or micro-cracks, the intrinsic variable was defined by Kachanov as

$$D = \frac{\delta S_D}{\delta S}, \tag{2.55}$$

where δS is the total area of cross section of an RVE, and δS_D is the total area of micro-voids in the cutting plane of the RVE which basically represents the surface density of microvoids (see fig. 2.4). In this thesis the damage is considered as isotropic phenomenon described by a scalar variable. For information regarding tensorial damage variables, Lemaitre (1996), Lemaitre and Desmorat (2005), Murakami (2012) are suggested. The internal variable D introduces a new quantity of interest, called the effective stress $\tilde{\boldsymbol{\sigma}}$, which is defined as

$$\tilde{\boldsymbol{\sigma}} = \frac{\boldsymbol{\sigma}}{1 - D}. \tag{2.56}$$

Equation (2.56) shows the increase in effective stress because of damage. The effect of damage can also be interpreted as the decrease in the modulus of elasticity. The effective modulus of elasticity $\tilde{E}$ is defined as

$$\tilde{E} = E(1 - D). \tag{2.57}$$

It is obvious that the scalar variable can take values between 0 and 1, with 0 being the virgin state and 1 indicates complete failure.

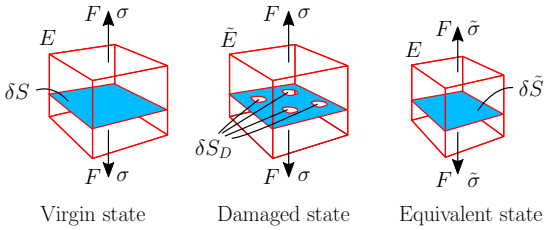

Figure 2.4: RVE showing virgin, damaged, and equivalent states

2.2.5 Damage with elasto-(visco)plasticity

The concept of damage being already formulated, the only thing remaining is to couple the scalar damage variable D with elasto-(visco)plasticity.

The first is to reformulate eq. (2.41), as

$$\rho\Psi^{*,e} = \frac{1+\nu}{2E}\frac{\sigma_{ij}\sigma_{ij}}{1-D} - \frac{\nu}{2E}\frac{\sigma_{kk}^2}{1-D}. \tag{2.58}$$

This gives the elastic state law as

$$\varepsilon_{ij} = \frac{1+\nu}{E}\frac{\sigma_{ij}}{1-D} - \frac{\nu}{E}\frac{\sigma_{kk}}{1-D}\delta_{ij}. \tag{2.59}$$

This also introduces a new variable Y which is the thermodynamic force conjugate to D. This variable can be obtained as

$$Y = \rho\frac{\partial\Psi^{*,e}}{\partial D} = \frac{1+\nu}{2E}\frac{\sigma_{ij}\sigma_{ij}}{(1-D)^2} - \frac{\nu}{2E}\frac{\sigma_{kk}^2}{(1-D)^2}. \tag{2.60}$$

For a loading that is cyclic, the damage law has to be modified. This is due to what is called "quasi-unilateral conditions of microdefects closure" (see Lemaitre and Desmorat, 2005), resulting in different material behaviour in tension and compression (see Ladevèze and Lemaitre, 1984). The difference in the elastic state equation during tension and compression is due to the fact that during compression the material regains some stiffness, as some of the micro-defects are closed (fig. 2.5), thereby increasing the effective area. This can be represented by the effective modulus of elasticity during tension $\tilde{E}^+$, which

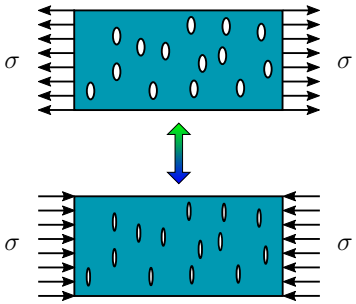

Figure 2.5: Closure of micro-defects during compression

is given by $\tilde{E}^+ = E(1-D)$, where E is the true modulus of elasticity, and by the effective elastic

modulus during compression $\tilde{E}^-$ given by $\tilde{E}^- = E\,(1 - hD)$. The closure parameter h has values between 0 (complete stiffness recovery) and 1 (no stiffness recovery). This phenomenon is described by modifying eq. (2.58) such that

$$\rho\Psi^{*,e} = \frac{1+\nu}{2E}\left[\frac{\langle\sigma\rangle^+_{ij}\,\langle\sigma\rangle^+_{ij}}{1-D} + \frac{\langle\sigma\rangle^-_{ij}\,\langle\sigma\rangle^-_{ij}}{1-hD}\right] - \frac{\nu}{2E}\left[\frac{\langle\sigma_{kk}\rangle^2}{1-D} + \frac{\langle-\sigma_{kk}\rangle^2}{1-hD}\right]. \tag{2.61}$$

Equations (2.59) to (2.60), therefore become

$$\varepsilon^e_{ij} = \frac{1+\nu}{E}\left[\frac{\langle\sigma\rangle^+_{ij}}{1-D} + \frac{\langle\sigma\rangle^-_{ij}}{1-hD}\right] - \frac{\nu}{E}\left[\frac{\langle\sigma_{kk}\rangle}{1-D} + \frac{\langle-\sigma_{kk}\rangle}{1-hD}\right]\delta_{ij}, \tag{2.62}$$

and

$$Y = \frac{1+\nu}{2E}\left[\frac{\langle\sigma\rangle^+_{ij}\,\langle\sigma\rangle^+_{ij}}{(1-D)^2} + h\frac{\langle\sigma\rangle^-_{ij}\,\langle\sigma\rangle^-_{ij}}{(1-hD)^2}\right] - \frac{\nu}{2E}\left[\frac{\langle\sigma_{kk}\rangle^2}{(1-D)^2} + h\frac{\langle-\sigma_{kk}\rangle^2}{(1-hD)^2}\right], \tag{2.63}$$

respectively. The term δ_{ij} in eq. (2.62) is the Kronecker delta, i.e. $\delta_{ij} = 1$ for $i = j$ and 0 otherwise. It should be mentioned that the decomposition of the stress tensor σ_{ij} into a positive part $\langle\sigma\rangle^+_{ij}$ and a negative part $\langle\sigma\rangle^-_{ij}$ is based on the information of the principal stresses and principal directions. The positive and negative principal stresses along with their corresponding normalised principal directions are used to build $\langle\sigma\rangle^+_{ij}$ and $\langle\sigma\rangle^-_{ij}$ respectively. Thereby, $\langle\sigma_{kk}\rangle$ and $\langle-\sigma_{kk}\rangle$ can be interpreted as traces of $\langle\sigma\rangle^+_{ij}$ and $\langle\sigma\rangle^-_{ij}$ respectively. Detailed information can be found in Lemaitre (1996), Lemaitre and Desmorat (2005).

The next is to update the evolution equation. Damage has a significant influence on the yield function f^p previously defined by eq. (2.47), which is henceforth modified as

$$f^p = \sqrt{\frac{3}{2}\left[\left(\frac{\boldsymbol{\sigma}^D}{1-D} - \boldsymbol{\beta}\right) : \left(\frac{\boldsymbol{\sigma}^D}{1-D} - \boldsymbol{\beta}\right)\right]} - R - \sigma_y. \tag{2.64}$$

To incorporate damage in the evolution equations, non-associative flow rules have to be considered. The potential F mentioned in eq. (2.31) is now written as

$$F = f^p + F_D, \tag{2.65}$$

where F_D is a non-linear function of Y. The most classical choice is to use (see Lemaitre and Desmorat, 2005)

$$F_D = \frac{S}{(1+s)\,(1-D)}\left(\frac{Y}{S}\right)^{s+1}, \tag{2.66}$$

with s and S being material parameters. Equation (2.48) can then be re-written as

$$\dot{\boldsymbol{\varepsilon}}^p = \frac{3}{2}\frac{\left(\frac{\boldsymbol{\sigma}^D}{1-D} - \boldsymbol{\beta}\right)}{\sqrt{\frac{3}{2}\left[\left(\frac{\boldsymbol{\sigma}^D}{1-D} - \boldsymbol{\beta}\right) : \left(\frac{\boldsymbol{\sigma}^D}{1-D} - \boldsymbol{\beta}\right)\right]}}\frac{\dot{\lambda}}{1-D}, \tag{2.67a}$$

$$\dot{\alpha} = \frac{3}{2} \frac{\left(\frac{\boldsymbol{\sigma}^D}{1-D} - \boldsymbol{\beta} \right)}{\sqrt{\frac{3}{2} \left[\left(\frac{\boldsymbol{\sigma}^D}{1-D} - \boldsymbol{\beta} \right) : \left(\frac{\boldsymbol{\sigma}^D}{1-D} - \boldsymbol{\beta} \right) \right]}} \dot{\lambda}, \tag{2.67b}$$

$$\dot{r} = \dot{\lambda}, \tag{2.67c}$$

where $\dot{\lambda}$ is the plastic or viscoplastic multiplier. Equation (2.50) becomes

$$\dot{r} = \dot{\lambda} = \dot{p}\,(1-D)\,. \tag{2.68}$$

The rate of growth of damage is then given by

$$\dot{D} = \frac{\partial F_D}{\partial Y} = \left(\frac{Y}{S} \right)^s \dot{p}. \tag{2.69}$$

The threshold of damage for damage law of the form of eq. (2.69) is generally given by a certain level of cumulative plastic strain p_D (see Lemaitre and Desmorat, 2005). Thereby, $\dot{D}$ is given by eq. (2.69) if $p > p_D$ and zero otherwise. The damage will continue to evolve till a critical damage level D_c is achieved, which marks the initiation of a macro-crack.

Apart from the particular damage model which has been illustrated here, several other damage models exist. The choice of the damage model depends not only on the material (e.g. ductile, brittle), but also on the type of loading (e.g. fatigue loading, creep loading). For different types of damage models, Lemaitre and Desmorat (2005) is suggested.

Another damage law formulation similar to Bellenger and Bussy (1998, 2000) can also been proposed. A viscous pseudo damage potential is proposed which is of the form

$$\Phi^{*,d} = \frac{k_d}{n_d + 1} \left\langle f^d \right\rangle_+^{n_d+1}, \tag{2.70}$$

where k_d and n_d are material parameters, f^d can be interpreted as damage function and in the most simplistic case is given by

$$f^d = Y - Y_{th}, \tag{2.71}$$

where Y_{th} describes the damage threshold. The evolution equation for damage is then given by

$$\dot{D} = \frac{\partial \phi^{*,d}}{\partial Y} = k_d \left\langle f^d \right\rangle_+^{n_d}. \tag{2.72}$$

Although damage mechanics is able to model the initiation point of a macro-crack, the drawback of this is the localisation of the quantities of interest. The solution is in most cases mesh dependent, and thereby localisation limiters are necessary. The earliest theories on this are to use constant mesh size or even use mesh size as a parameter. However, later on, a material internal length was introduced in the constitutive relations. This basically boils down to the fact that localised quantities, like plasticity or damage, for a material point also depend on a small domain around it (see Lemaitre and Desmorat, 2005). Therefore, non-local theories are proposed. One of the earliest ideas is to replace each variable by the corresponding averaged homogenised variable considering a small domain surrounding each material point (see Bažant and Pijaudier-Cabot, 1989). Another, alternate way is to introduce gradient theories (see Aifantis, 1987), where plasticity and damage at any material point depend on the corresponding thermodynamic variables and also on the first n derivatives in the Taylor expansion series. However using non-local or gradient-enhanced damage models are beyond the scope of the thesis and only localised damage parameters are used.

Although classical damage formulations encompass the damage variable between 0 and 1, there have been other formulations, for instance, in Bellenger and Bussy (1998, 2000), where a damage variable

ranging between 0 and ∞ has been used. However, in this thesis, classical definition of D between 0 and 1 will be used.

Another type of damage model which has been popular off late, is the Gurson-Tvergaard-Needleman (GTN) model. This type of model gives a physically improved formulation of micro-void nucleation, growth, and coalescence process. The damage variable in this case, defined by the void volume fraction, is considered to be evolving separately during void nucleation and void growth (see Acharyya and Dhar, 2008). Although, this gives an improved representation of the micro-mechanical process, it is not free from localisation problem. Hence, localisation limiters are used, e.g. Fish and Oskay (2005) uses a non-local GTN model. Although GTN model is beyond the scope of this thesis, it is worthwhile to mention it.

2.3 CDM approaches in fatigue

Different methodologies have been been adopted over the years to model as well as to simulate the fatigue mechanisms using continuum damage mechanics. A few most important approaches are presented here.

One of the most novel approaches used is the formulation of the "two-scale damage model" by Lemaitre (see Lemaitre et al., 1997). This is mainly used for high cycle fatigue. The global behaviour remains elastic, which is obtained through a macroscopic elastic structural calculation. After that the Gauss points with maximum stress concentrations are identified. Eshelby-Kroner scale transition law is then applied to get the micro-strain at chosen Gauss points from the macro-strain. Thereafter, elasto-plastic analysis coupled with damage is performed at the micro-scale. The final outcome of this is the damage variable D, which is considered to be equal in both the scales.

An important development in the solution framework of fatigue is the popular "jump cycle" approach (see Lemaitre and Desmorat, 2005). The basic idea here is confined to loads that are periodic or at least periodic by blocks, where calculations of full blocks of load cycles are skipped. The quantities of interest are calculated for a certain number of initial load cycles. The damage and accumulated plastic strain increments over the last computed cycle are then estimated. From this information, an estimation of the number of cycles that can be skipped is made with an assumption that damage and accumulated plastic strain are linear with respect to the number of cycles. After that the quantities of interest are again calculated for one cycle and an estimation is made for the number of cycles to skip. This continues till D_c is achieved. The "two-scale damage model" is generally used together with the "jump cycle" technique, e.g. in Bhamare et al. (2014), Lemaitre et al. (1997).

Another important approach is the time homogenisation technique initially proposed in Guennouni and Aubry (1986) for quasi-static elasto-viscoplastic problems. Later on Puel and Aubry extended this method for dynamics (see Puel and Aubry, 2012) and also for CDM (see Devulder et al., 2010). Fish and his co-workers, also proposed similar techniques for fatigue, using a viscoplasticity like damage model (see Oskay and Fish, 2004b) and also for GTN damage model (see Fish and Oskay, 2005). The main idea is to divide the time into two separate scales: a fast scale (micro-time scale) and a slow scale (macro-time scale). Thereafter, the quantities at each slow time scale are represented as homogenised quantities of the fast time scale. This solves the problem of numerical simulation of all the quantities of interest at the fast time.

2.4 Concluding remark

A review of classical material non-linearities in a continuum framework has been presented in this chapter, with damage being the primary quantity of interest. Although, a few methods of computing large number of cycles have been established, a novel approach using LATIN method and model reduction technique will be used. An introductory review of classical LATIN approach and different model reduction techniques will be given in the next chapter.

Chapter 3

Reduced order modelling and large time increment method

High degrees of fidelity in complex coupled multi-physics or multi-scale problems may result in large run-times and extreme memory consumption. Even with the availability of high performance computing platforms, such computations, in many industrial or academic cases can be rendered infeasible. Therefore, it is necessary to reduce these high-fidelity models, such that both memory-cost and run-time are reduced (see Cueto et al., 2014). The goal of model order reduction (MOR) methods or model reduction techniques is to extensively reduce computational cost and/or storage memory with a minimal loss of accuracy.

This chapter gives a brief overview of model reduction techniques for non-linear problems. The large time increment method in the light of material non-linearities is also introduced along with a succinct comparison with Newton-Raphson technique.

3.1 Classical incremental method

The classical or more popular approach to solve non-linear solid mechanics problems is to split the considered time domain $[0, T]$ into sufficiently small time intervals and then solve sequentially the boundary value problem at each time step. The equilibrium equation defined by eq. (2.6) for an incremental case can be written as a boundary value problem, which, after standard finite element discretisation, reduces to finding the nodal unknowns $\vec{u}_{n+1}$ such that the equilibrium equation represented by

$$\vec{r}(\vec{u}_{n+1}) \equiv \vec{F}^{\,int}(\vec{u}_{n+1}) - \vec{F}^{ext}_{n+1} = 0, \tag{3.1}$$

is satisfied, where $\vec{F}^{\,int}$ denotes the nodal forces arising from internal stresses, $\vec{F}^{ext}$ is obtained from the external applied body or/and surface forces, and $\vec{r}(\vec{u}_{n+1})$ is the residual vector (see de Souza Neto et al., 2011). Newton-Raphson method is a particularly attractive solution for this kind of equation. Each iteration of the Newton-Raphson method consists in solving the linearised version of eq. (3.1). Considering $\vec{u}^{\,k-1}_{n+1}$ being known at the $(k-1)^{\text{th}}$ iteration of the Newton-Raphson method, the goal at iteration k is to solve the linear system given by

$$\mathbf{K}_T \delta\vec{u}^{\,k} = -\vec{r}^{\,k-1}, \tag{3.2}$$

for $\delta\vec{u}^{k}$, where $\mathbf{K}_T$ is the global tangent stiffness matrix at $(k-1)^{\text{th}}$ iteration and the residual $\vec{r}^{\,k-1}$ is obtained as

$$\vec{r}^{\,k-1} = \vec{F}^{\,int}\left(\vec{u}^{\,k-1}_{n+1}\right) - \vec{F}^{ext}_{n+1}. \tag{3.3}$$

The nodal displacement $\vec{u}^{\,k}_{n+1}$ is then given as

$$\vec{u}^{\,k}_{n+1} = \vec{u}^{\,k-1}_{n+1} + \delta\vec{u}^{\,k}. \tag{3.4}$$

Generally the Newton-Raphson procedure is continued till the residual $\vec{r}^m$ at iteration m is low enough and satisfies a given convergence criterion. The schematic of the Newton-Raphson method is given in fig. 3.1.

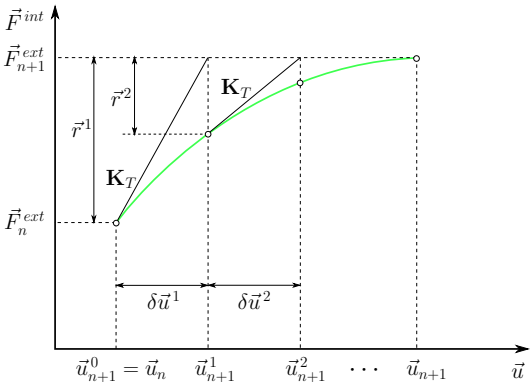

Figure 3.1: Newton-Raphson algorithm at time step $n + 1$ (de Souza Neto et al., 2011)

There are many varieties of Newton-Raphson methods which are the so-called modified Newton-Raphson methods. Some popular versions use the same tangent stiffness matrix for all the time increments, or use same stiffness matrix within each time increment and update only at the beginning of each increment, or update the stiffness matrix after certain iterations within each increment. For more details of classical incremental methods especially for material non-linearities, de Souza Neto et al. (2011), Reddy (2004), Wriggers (2008) are some of the recommended books. High fidelity-problems with large number of degrees of freedom and encompassing large number of time steps, invariably lead to extremely high numerical expense and memory consumption hence it is a practical necessity to reduce the high-fidelity problem.

3.2 Model reduction techniques

Model reduction techniques can be classified into *a posteriori* model reduction techniques where the reduced solution is obtained after a similar high-fidelity solution (known as the training stage) is computed, and *a priori* methods which compute the approximation without knowing any high-fidelity solution (see Chinesta et al., 2014b). Whatever the type of model reduction technique may be, the purpose is to yield low-dimensional approximations for the full high-dimensional system (see Pinnau, 2008).

For dynamic systems, especially for structural dynamics, the model reduction approaches are in general *a posteriori* as even though no high-fidelity pre-computations are needed, "basis vectors" are to be obtained before foregoing with any reduced computation. Some notable methods in this field are:

– Modal displacement method, where modal shape vectors are used as reduced basis. Eigenvalue analysis is performed for the structure in question and very few eigenvectors are extracted to build the reduced basis, on which the equation of motion is projected. Modal acceleration and modal truncation are varieties of modal superposition methods.

– Krylov subspace method, which reduces a system with higher degrees of freedom to a system with lower degrees of freedom but with similar input-output behaviour. A transfer function is calculated in the Laplacian domain from the time-invariant state-space system. Two bi-orthogonal projection matrices are calculated from the information of the moments of the transfer function, which are then used to reduce the original state-space system.

For a review of model reduction techniques in dynamics, Besselink et al. (2013) is suggested. In this thesis, however, the focus is on systems exhibiting material non-linearities.

3.2.1 Proper orthogonal decomposition (POD): *a posteriori* model reduction technique

The basic idea of POD is to compute certain full-order problems in order to extract relevant information which can then be used to calculate similar problems more efficiently. The first ideas of POD were developed in Karhunen (1946), Kosambi (1943), Loève (1946), Pearson (1901). The usage of POD in the field of mechanics deals with the creation of POD basis, from the snapshots obtained from the solution of the training phase, and then to use this basis to solve the intended problem in a reduced space (see Ryckelynck, 2009). Also known as principal component analysis (PCA), Karhunen Loève expansion (KLE) and singular value decomposition (SVD) (see Chatterjee, 2000), POD provides an optimally ordered set of basis functions in a least square sense for the full-order solution. These basis functions are called "proper orthogonal modes", "empirical eigenfunctions", or just "basis vectors". A reduced order model (ROM) or a surrogate model can then be generated by truncating the optimal basis (see Liang et al., 2002, Pinnau, 2008).

A full solution given by $\vec{u}(\vec{x},t)$ where $\vec{x}$ denotes the spatial coordinate and t being the temporal coordinate can be represented as

$$\vec{u}(\vec{x},t) = \sum_{i=1}^{\mathsf{r}} \mathcal{T}_i(t)\,\vec{\mathcal{X}}_i(\vec{x}) \tag{3.5}$$

such that the approximation becomes exact as $\mathsf{r} \to \infty$. The space functions $\vec{\mathcal{X}}_i(\vec{x})$ are chosen such that they are orthonormal and the determination of the time functions $\mathcal{T}_i(t)$ should only be depended on the corresponding space functions $\vec{\mathcal{X}}_i(\vec{x})$.

For a discretised case, if $\mathcal{U}$ are values at $\mathfrak{n}$ space and $\mathfrak{m}$ time points, the solution $\mathcal{U}$ will be an $\mathfrak{n} \times \mathfrak{m}$ matrix. One way to obtain the reduced basis is to perform a singular value decomposition (SVD) of the solution $\mathcal{U}$ such that

$$\mathcal{U} = \mathsf{U}\Sigma\mathsf{V}^T, \tag{3.6}$$

where U is an $\mathfrak{n} \times \mathfrak{n}$ orthogonal matrix, V is an $\mathfrak{m} \times \mathfrak{m}$ orthogonal matrix and Σ is an $\mathfrak{n} \times \mathfrak{m}$ diagonal matrix. The diagonal Σ_{ii} consists of $\mathfrak{r} = \min(\mathfrak{n},\mathfrak{m})$ non-negative numbers in decreasing order which are called the singular values of $\mathcal{U}$. To establish the equivalence of eq. (3.5) and eq. (3.6), it is assumed that $\mathsf{Q} = \Sigma\mathsf{V}^T$, where Q is an $\mathfrak{n} \times \mathfrak{m}$ matrix. Then eq. (3.6) can be written as

$$\mathcal{U} = \mathsf{U}\mathsf{Q} = \sum_{i=1}^{\mathfrak{n}} \mathsf{u}_i\mathsf{q}_i, \tag{3.7}$$

where u_i and q_i are ith column and ith row of the matrices U and Q respectively. Generally this summation needs not be for all $\mathfrak{n}$ but can be for $\mathfrak{s}$ columns and rows of U and Q respectively, with $\mathfrak{s} \ll \mathfrak{n}$. The value of $\mathfrak{s}$ can be determined from the magnitude of the singular values. Then $\mathcal{U}$ obtained from eq. (3.7) can be approximated as

$$\mathcal{U} \approx \sum_{i=1}^{\mathfrak{s}} \mathsf{u}_i\mathsf{q}_i. \tag{3.8}$$

u_i can be interpreted as function of space and q_i can be interpreted as function of time. It has to be noted that singular value decomposition is a generalisation of eigenvalue decomposition for non-square matrices. If $\mathcal{U}$ is a square symmetric positive definite matrix, then the singular values (diagonal elements of Σ) are the same as eigenvalues, and the matrix of singular vectors are the same (i.e $\mathsf{U} = \mathsf{V}$) and equal to the matrix of the eigenvectors (both right eigenvectors and left eigenvectors) (see Chatterjee,

2000). From eq. (3.8), the first $\mathfrak{s}$ columns of the U matrix (the $\{\mathsf{u}_i\}_{i=1}^{\mathfrak{s}}$ vectors) are used to construct a truncated matrix U_p called the projection matrix, where U is of size $\mathfrak{n} \times \mathfrak{s}$. Figure 3.2 shows an SVD approximation of a given solution field $\mathcal{U}_{ref}$. It is evident from fig. 3.2 that only four SVD modes are enough to get extremely low error (error $= \frac{\|\mathcal{U}_{ref} - \mathcal{U}_{apr}\|}{\|\mathcal{U}_{ref}\|}$, $\mathcal{U}_{ref}$ is the given reference field and $\mathcal{U}_{apr}$ is the approximate solution). This can also be quantified by the decrease in the magnitude of the singular

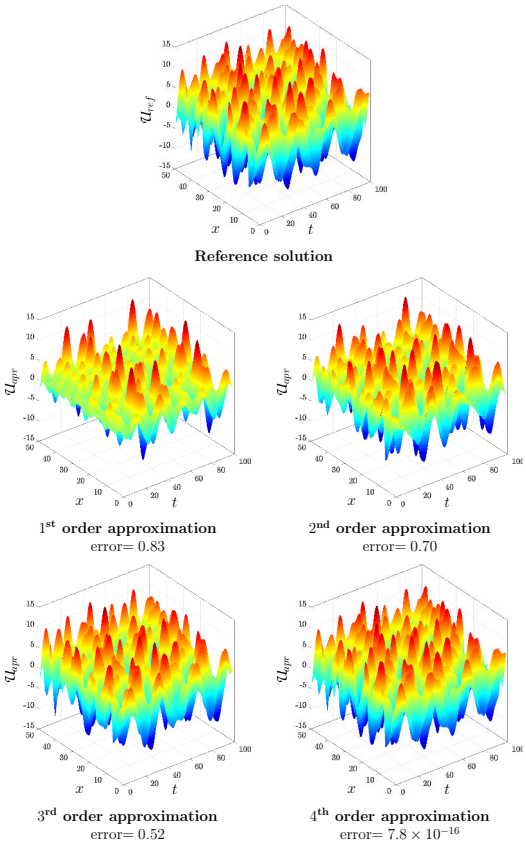

Figure 3.2: SVD approximations of a given solution field

value and the decrease of error as shown in fig. 3.3.

The construction of the projection matrix containing the basis vectors can also be achieved by PCA. Knowing a solution field $\mathcal{U}$, the covariance matrix C is calculated such that

$$\mathsf{C} = \mathcal{U}\mathcal{U}^T. \tag{3.9}$$

It is also advisable to have each column of $\mathcal{U}$ be distributed around zero, i.e the mean of each column should be subtracted from every element of that column (see Kerschen et al., 2005, Liang et al., 2002). It is obvious that C is an $\mathfrak{n} \times \mathfrak{n}$ matrix. Then the projection matrix U_p is obtained from the eigenvectors

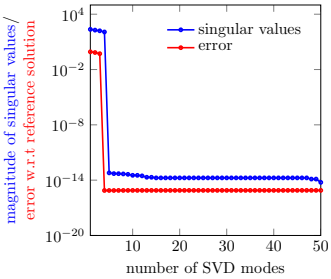

Figure 3.3: Decrease of error and singular values with SVD modes

of the covariance matrix C, where the columns $\{\mathsf{u}_i\}_{i=1}^{\mathfrak{s}}$ are the eigenvectors that serve as basis vectors (see Cueto et al., 2014). KLE on the other hand can be considered to be an extension of PCA for infinite-dimensional spaces (e.g. spaces of continuous time and/or space functions). Although, KLE is not discussed here, Liang et al. (2002) is suggested for more information and comparison between SVD, PCA, and KLE. It can be depicted that the spatial basis vectors obtained through SVD and PCA are identical, as for example the first four spatial basis vectors of the reference solution field $\mathcal{U}_{ref}$ of fig. 3.2 are shown in fig. 3.4.

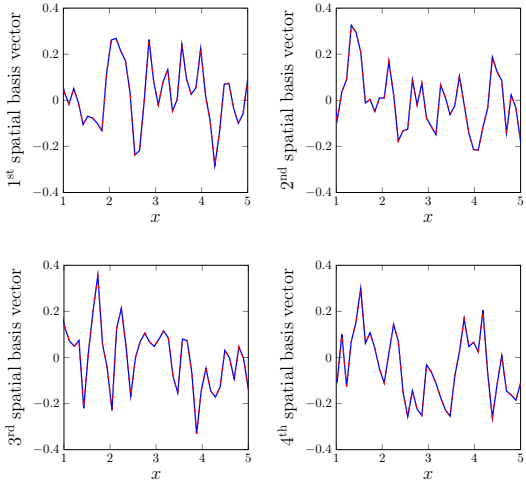

Figure 3.4: First four spatial basis vectors using SVD (—) and KLE (- -)

Once the projection matrix is built, it is used to solve the actual problem of interest in a reduced order space. If the non-linear problem defined by eq. (3.1), then at a particular time step $n+1$, the vector of nodal unknowns $\vec{u}_{n+1}$ being of size $\mathfrak{n} \times 1$ is projected in the reduced space by

$$\vec{u}_{n+1} = \mathsf{U}_p \vec{g}_{n+1}, \tag{3.10}$$

where $\vec{g}_{n+1}$ is the vector of the reduced degrees of freedom and is of size $\mathfrak{s} \times 1$. This definition is then

used in eq. (3.2), and the result is pre-multiplied by the transpose of the projection matrix,

$$\begin{aligned} \mathsf{U}_p^T \mathbf{K}_T \mathsf{U}_p \delta\vec{g} &= -\mathsf{U}_p^T \vec{r}, \\ \implies \mathbf{K}_{T,r} \delta\vec{g} &= -\vec{r}_r, \end{aligned} \tag{3.11}$$

where the reduced tangent stiffness matrix $\mathbf{K}_{T,r}$ is defined as

$$\mathbf{K}_{T,r} = \mathsf{U}_p^T \mathbf{K}_T \mathsf{U}_p, \tag{3.12}$$

and the reduced RHS $\vec{r}_r$ is defined as

$$\vec{r}_r = \mathsf{U}_p^T \vec{r}. \tag{3.13}$$

It might be noted that the iteration index k in eq. (3.2) has been dropped in eq. (3.11) just for convenience. The reduced system of equation is computationally much less expensive compared to the full system.

The problem however of classical POD-Galerkin formulation is that even if the global solution is computed in a reduced space, the computational effort to solve the non-linear constitutive relation at every local integration point remains high. To put that in perspective, the local computations are independent of the reduced model and the reduced approximation has no influence on the numerical expense with regard to the estimation of the internal variables that influence the tangent stiffness matrix. For linear problems this is not an issue as the stiffness matrix does not change and the time saving is directly proportional to the degree of reduction of the original finite element (FE) subspace to POD subspace.

To build an efficient ROM for non-linear problems, the hyper-reduction method has been proposed in Ryckelynck (2009), which tries to address this issue by introducing a reduced integration domain. The reduced integration domain is defined by choosing only a few elements of the complete mesh and considering the related balance condition. The internal variables are then not computed on the whole domain but only at the reduced integration domain, which are then extrapolated. This method gives robust computational time savings, and has been successfully used to simulate damage in Ryckelynck et al. (2011).

Another way of solving the issue of non-linear problems is to use discrete empirical interpolation methods as described in Radermacher and Reese (2016). The discrete empirical interpolation method is a discrete version of the classical empirical interpolation method used to solve parametrised partial differential equations (see e.g. Lass and Volkwein, 2013). The idea of empirical interpolation was used first in Barrault et al. (2004) in the context of partial differential equations, which was later modified as the discrete empirical interpolation method in Chaturantabut and Sorensen (2010). The main idea described in Radermacher and Reese (2016) is to split the internal force vector of eq. (3.1) into a linear and a non-linear part, where the linear part can be expressed with the help of a constant stiffness matrix. Two separate projection matrices are used, one for the nodal unknowns and one for the non-linear part of the internal force. The dependency of the total number of DOFs on the non-linear term is thereafter minimised by means of an empirical interpolation. This ultimately leads to the reduced tangent stiffness matrix that consists of a linear constant part (calculated only at the initial time step) and another non-linear part whose calculation time is reduced by empirical interpolation of the internal force vector.

Apart from these techniques that have introduced modification in the classical Galerkin-POD method to solve non-linear solid mechanics problems, there have been other methods to improve the usage of POD, such as the generalised empirical interpolation method proposed in Maday and Mula (2013) for data assimilation, or the missing point estimation procedure used in Astrid (2004) to reduce PDEs and applied in the process of heat transfer and computational fluid mechanics.

The usage of POD depends on the goal in hand. One usage may be to build the spatial basis by considering the training stage solution over a short time span and then use the reduced basis to calculate solution over a long time span. Another usage may be to calculate the reduced basis for a full-order problem for entire space-time domain in the training stage and then use the reduced basis to solve similar problems involving slight change in material properties or boundary conditions (see Cueto et al., 2014).

3.2.2 Proper generalised decomposition (PGD): *a priori* model reduction technique

It is desired, ideally to have a technique where a reduced order approximation can be built without relying on any training stage. One would then be able to assess the accuracy of the reduced order approximation, and enrich the reduced order basis if necessary. This leads to the proper generalised decomposition (PGD), which was first introduced as "radial loading approximation" in the context of LATIN method (see Cognard and Ladevèze, 1993, Ladevèze, 1989, 1999, and other works of Ladevèze) based on separated representation of the quantities of interest. For instance, the desired solution field $\mathcal{V}(\vec{x},t)$ is obtained in the separated form as (see Chinesta et al., 2014a)

$$\mathcal{V}(\vec{x},t)=\sum_{i=1}^{\mathsf{r}}\mathcal{T}_i(t)\,\mathcal{X}_i(\vec{x})\,. \tag{3.14}$$

Here the number of terms r needed for this finite sum decomposition is not known *a priori*. The functions $\mathcal{T}_i(t)$ and $\mathcal{X}_i(\vec{x})$ are constructed by successive enrichments. For a particular enrichment stage $\mathsf{v}+1$, the functions $\{\mathcal{T}_i\}_{i=1}^{\mathsf{v}}$ and $\{\mathcal{X}_i\}_{i=1}^{\mathsf{v}}$ being known from the previous steps, $\mathcal{T}_{\mathsf{v}+1}$ and $\mathcal{X}_{\mathsf{v}+1}$ are sought. This is achieved by invoking the weak form of the problem.

Considering a case where the problem is defined by

$$\mathcal{L}(\mathcal{V})=f(t,\vec{x})\,, \tag{3.15}$$

within the domain $\Omega\times[0,T]$. The right hand side f is the external input, and the operator $\mathcal{L}(\mathcal{V})$ can be defined as

$$\mathcal{L}(\mathcal{V})=\mathcal{L}_t(\mathcal{V})+\mathcal{L}_x(\mathcal{V})\,, \tag{3.16}$$

where, $\mathcal{L}_t=\dfrac{\partial}{\partial t}$ and $\mathcal{L}_x=\nabla^2$. The weak form corresponding to eq. (3.15) can be written as

$$\int_{\Omega\times[0,T]}\delta\mathcal{V}\cdot\left(\mathcal{L}(\mathcal{V})-f(t,\vec{x})\right)\mathrm{d}V\mathrm{d}t=0. \tag{3.17}$$

The separated form represented in eq. (3.14) can be used to decompose eq. (3.17) into a space problem,

$$\int_{\Omega}\delta\mathcal{X}_{\mathsf{v}+1}\cdot\left(a^x\cdot\mathcal{L}_x\left(\mathcal{X}_{\mathsf{v}+1}(\vec{x})\right)+b^x\cdot\mathcal{X}_{\mathsf{v}+1}(\vec{x})+w^x_{\mathsf{v}+1}(\vec{x})\right)\mathrm{d}V=0, \tag{3.18}$$

and into a time problem,

$$\int_{[0,T]}\delta\mathcal{T}_{\mathsf{v}+1}\cdot\left(a^t\cdot\mathcal{L}_t\left(\mathcal{T}_{\mathsf{v}+1}(t)\right)+b^t\cdot\mathcal{T}_{\mathsf{v}+1}(t)+w^t_{\mathsf{v}+1}(t)\right)\mathrm{d}t=0. \tag{3.19}$$

Here, a^x, b^x and a^t, b^t are constant terms. The terms $w^x_{\mathsf{v}+1}(\vec{x})$, and $w^t_{\mathsf{v}+1}(t)$ are obtained by integrating $f(t,\vec{x})$ and $\mathcal{L}\left(\sum_{i=1}^{\mathsf{v}}\mathcal{T}_i(t)\cdot\mathcal{X}_i(\vec{x})\right)$ over $[0,T]$ and Ω respectively.

The spatial problem can be solved by any discretisation technique for elliptic boundary value problems, and the temporal problem can be solved by any discretisation technique for initial value problems. These two problems are solved in a staggered manner, i.e. $\mathcal{X}_{\mathsf{v}+1}$ is calculated knowing $\mathcal{T}_{\mathsf{v}+1}$ and vice versa, till convergence is reached.

Apart from space-time separation, there are other forms of coordinate separation, e.g. fully separated decomposition for a three dimensional problems (fully separated PGD description has generally been used to address homogenisation problems in Chinesta et al., 2008, Prulière et al., 2013)

$$\mathcal{V}(x,y,z) = \sum_{i=1}^{\mathsf{r}} \mathcal{X}_i(x)\,\mathcal{Y}_i(y)\,\mathcal{Z}_i(z)\,, \tag{3.20}$$

or for parametric problems, the solution can be separated using the parameter c as a separate coordinate (see Ammar et al., 2010), i.e.

$$\mathcal{V}(\vec{x},t,c) = \sum_{i=1}^{\mathsf{r}} \mathcal{X}_i(\vec{x})\,\mathcal{T}_i(t)\,\mathcal{C}_i(c)\,. \tag{3.21}$$

Appropriate separated weak forms similar to eqs. (3.18) and (3.19) can be obtained.

Interested readers can consult Chinesta et al. (2014b) for an introduction to PGD technology, and Chinesta et al. (2013) which gives a detailed review on parametric PGD. PGD has been used extensively to solve many non-linear problems (see Chinesta and Cueto, 2014), for instance in fluid mechanics, the Fokker-Planck equation was solved using PGD in Ammar et al. (2006, 2007). PGD was also used to solve stochastic equation within the Brownian Configuration Field framework in Chinesta et al. (2007).

In the case of solid mechanics, PGD has been used generally in the context of LATIN method especially in LMT- Cachan, which was initially developed for small-displacement (infinitesimal strain) problems, and will be discussed in details in the next section. Extramural to LATIN method, space-parameter PGD separation for multi-scale problems can be found in El Halabi et al. (2016). Apart from that, two-dimensional space-space PGD separation has been used in Metoui et al. (2014) to simulate delamination using cohesive zone model, and in Vidal et al. (2012) to solve beam problems. These are just a few examples of PGD-based work on solid mechanics that are extraneous to LATIN-based PGD frameworks.

3.3 Large time increment (LATIN) method

Contrary to classical incremental technique, Ladevèze first proposed this new non-incremental method in the context of non-linear mechanical problems (see Ladevèze, 1985a,b) more than 30 years ago. The LATIN method being a non-incremental iterative technique, in contrary to the classical incremental technique (previously described in section 3.1), is not built on the notion that the interval $[0,T]$ needs to be partitioned into small steps. The method generally starts with an approximation of the quantities of interest for the whole spatial domain Ω and the whole temporal domain $[0,T]$. Thereafter, at each iteration, the quantities of interest are improved for the whole spatial and temporal domain till a convergence is reached. In general LATIN method is based on three basic principles (see Ladevèze, 1999).

- The first principle is the separation of difficulties. The governing equations are separated into two groups. A group of equations which are local in space, possibly non-linear; and a group of equations which are linear but possibly global in space.
- The second principle is a two-step iterative algorithm, where at each iteration the solution is constructed alternatively for the first group of equations and then for the second group of equations.
- The last principle is to solve the global problem defined on the entire space-time domain $\Omega \times [0,T]$ using PGD based reduced order approximation such that the numerical cost is drastically lowered.

A pictorial representation of the LATIN scheme is given in fig. 3.5.

Considering only the case of infinitesimal strain elasto-(visco)plasticity, the set of the quantities of interest is denoted by $\boldsymbol{s} = \left\{\dot{\varepsilon}^p, \dot{\boldsymbol{X}}, \boldsymbol{\sigma}, \boldsymbol{Z}\right\}$. For the time being, it is considered that the set of hardening variables follows a "normal formulation", i.e.

$$\boldsymbol{Z} = \boldsymbol{\Pi}\boldsymbol{X}, \tag{3.22}$$

with $\mathbf{\Pi}$ being a linear operator of material properties relating the internal hardening variables $\boldsymbol{X}$ with the corresponding thermodynamic forces $\boldsymbol{Z}$.

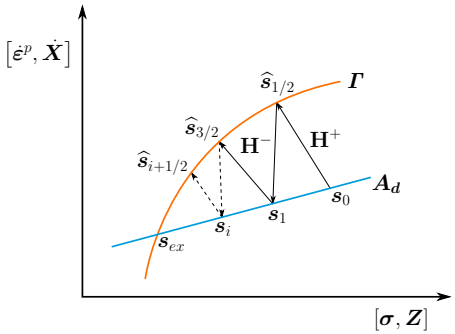

Figure 3.5: Schematic representation of LATIN method

3.3.1 First principle: separation of difficulties

To implement the first principle of LATIN method, two manifolds are introduced, based on a subdivision of the set of equations that must be solved.

- The first is the space $\boldsymbol{A_d}$ which belongs to the manifold of the admissibility conditions (eqs. (2.6) and (2.11)) and the linear state laws (eqs. (2.35) and (3.22)).
- The second is the space $\boldsymbol{\Gamma}$ which belongs to the manifold of the non-linear evolution equations (eq. (2.31), with $\Upsilon_i = \boldsymbol{X}$ and $\Lambda_i = \boldsymbol{Z}$ in eq. (2.31b)).

The exact solution is given by the intersection of these two manifolds, i.e.

$$\boldsymbol{s}_{ex} = \boldsymbol{A_d} \cap \boldsymbol{\Gamma}. \tag{3.23}$$

3.3.2 Second principle: two-step algorithm

The algorithm is initialised by a solution $\boldsymbol{s}_0 \in \boldsymbol{A_d}$ on the whole space-time domain, which is based on an elastic solution and $\dot{\varepsilon}^p, \dot{\boldsymbol{X}}, \boldsymbol{Z}$ are considered to be zero. The two-step algorithm is then initiated which includes a **local step**, an intermediate step which involves calculating $\hat{\boldsymbol{s}}_{i+1/2} \in \boldsymbol{\Gamma}$, knowing the solution set $\boldsymbol{s}_i \in \boldsymbol{A_d}$. This basically involves the solution of the evolution equations. The transfer of information from $\boldsymbol{s}_i$ to $\hat{\boldsymbol{s}}_{i+1/2}$ occurs through what is called the search direction operator. For the local step this equation is given by

$$\begin{bmatrix} \hat{\dot{\varepsilon}}^p_{i+1/2} - \dot{\varepsilon}^p_i \\ -\left(\hat{\dot{\boldsymbol{X}}}_{i+1/2} - \dot{\boldsymbol{X}}_i\right) \end{bmatrix} + \mathbf{H}^+ \begin{bmatrix} \hat{\boldsymbol{\sigma}}_{i+1/2} - \boldsymbol{\sigma}_i \\ \hat{\boldsymbol{Z}}_{i+1/2} - \boldsymbol{Z}_i \end{bmatrix} = 0, \tag{3.24}$$

where the search direction operator $\mathbf{H}^+$ represents the direction of ascent. The next step known as the **global step** is to calculate $\boldsymbol{s}_{i+1} \in \boldsymbol{A_d}$, knowing the solution set $\hat{\boldsymbol{s}}_{i+1/2} \in \boldsymbol{\Gamma}$ by solving the linear state laws and the admissibility conditions. Another search direction equation is introduced which transfers the information from $\hat{\boldsymbol{s}}_{i+1/2}$ to $\boldsymbol{s}_{i+1}$,

$$\begin{bmatrix} \dot{\varepsilon}^p_{i+1} - \hat{\dot{\varepsilon}}^p_{i+1/2} \\ -\left(\dot{\boldsymbol{X}}_{i+1} - \hat{\dot{\boldsymbol{X}}}_{i+1/2}\right) \end{bmatrix} - \mathbf{H}^- \begin{bmatrix} \boldsymbol{\sigma}_{i+1} - \hat{\boldsymbol{\sigma}}_{i+1/2} \\ \boldsymbol{Z}_{i+1} - \hat{\boldsymbol{Z}}_{i+1/2} \end{bmatrix} = 0, \tag{3.25}$$

where the search direction operator $\mathbf{H}^-$ signifies the direction of descent. This iterative algorithm continues till a convergence is reached. LATIN method inherently defines a LATIN error indicator which basically measures the distance between $\hat{\boldsymbol{s}}_{i+1/2}$ and $\boldsymbol{s}_{i+1}$. If this indicator is below a pre-defined tolerance, convergence is said to have reached. It has also to be noted that search direction operators $\mathbf{H}^+$ and $\mathbf{H}^-$ only affect the rate of convergence of the algorithm (see Néron and Ladevèze, 2010) but not the converged solution. Theoretically these operators can be any symmetric, positive definite operators that may vary during the iterations. For elasto-(visco)plastic problems, the direction of ascent is chosen as

$$\left(\mathbf{H}^+\right)^{-1} = 0, \tag{3.26}$$

i.e. the ascent direction is vertical (see Cognard and Ladevèze, 1993, Relun et al., 2013). For the direction of descent, the fastest way to convergence is the usage of an operator which is associated to the tangent space of $\boldsymbol{\Gamma}$, which is for viscoplastic problems the second derivative of the pseudo-potential Φ^* (see Cognard and Ladevèze, 1993, Relun et al., 2013). There can be other search directions that can be employed, readers are advised to consult Ladevèze (1999) for more information on search direction operators.

3.3.3 Third principle: model reduction method

Finally, the third principle essentially introduced a separation of variables, which was known back then as "radial loading approximation" (see Ladevèze, 1999). The idea is to solve the linear global stage (linear as all the non-linearities are dealt in the local stage) using certain space-time separated approximations which lead to the solution of the global admissibilities in a reduced space and generation of PGD-based ROM.

3.3.3.1 Galerkin formulation of the global stage

During the initial years of LATIN method (see Cognard and Ladevèze, 1993, Ladevèze, 1999, as for examples) the solution process of the linear global stage was based on Galerkin formulation. The quantities of interest are represented in terms of corrections, i.e.

$$\Delta\boldsymbol{s}_{i+1} = \boldsymbol{s}_{i+1} - \boldsymbol{s}_i. \tag{3.27}$$

The global stage then essentially involves solving for $\Delta\boldsymbol{\sigma}_{i+1}, \Delta\boldsymbol{Z}_{i+1}$ such that

$$\begin{aligned}
\int_{\Omega\times[0,T]} \left(\mathbf{C}^{-1}\Delta\dot{\boldsymbol{\sigma}}_{i+1} : \delta\boldsymbol{\sigma} + \mathbf{\Pi^{-1}}\Delta\dot{\boldsymbol{Z}}_{i+1} : \delta\boldsymbol{Z}\right) \mathrm{d}V\mathrm{d}t + \\
\int_{\Omega\times[0,T]} \mathbf{H}^- \left[\begin{array}{c} \Delta\boldsymbol{\sigma}_{i+1} \\ \Delta\boldsymbol{Z}_{i+1} \end{array}\right] : \left[\begin{array}{c} \delta\boldsymbol{\sigma} \\ \delta\boldsymbol{Z} \end{array}\right] \mathrm{d}V\mathrm{d}t = \\
\int_{\Omega\times[0,T]} \left[\begin{array}{c} \bar{\boldsymbol{\Delta}}^{\varepsilon} \\ \bar{\boldsymbol{\Delta}}^{X} \end{array}\right] : \left[\begin{array}{c} \delta\boldsymbol{\sigma} \\ \delta\boldsymbol{Z} \end{array}\right] \mathrm{d}V\mathrm{d}t,
\end{aligned} \tag{3.28}$$

with the term on the right hand side being

$$\left[\begin{array}{c} \bar{\boldsymbol{\Delta}}^{\varepsilon} \\ \bar{\boldsymbol{\Delta}}^{X} \end{array}\right] = \mathbf{H}^- \left[\begin{array}{c} \hat{\boldsymbol{\sigma}}_{i+1/2} - \boldsymbol{\sigma}_{i+1} \\ \hat{\boldsymbol{Z}}_{i+1/2} - \boldsymbol{Z}_{i+1} \end{array}\right] - \left[\begin{array}{c} \hat{\dot{\boldsymbol{\varepsilon}}}^p_{i+1/2} - \dot{\boldsymbol{\varepsilon}}^p_{i+1} \\ -\left(\hat{\dot{\boldsymbol{X}}}_{i+1/2} - \dot{\boldsymbol{X}}_{i+1}\right) \end{array}\right] \tag{3.29}$$

$\forall\, \delta\boldsymbol{\sigma}$ which is kinematically admissible for homogeneous equation and $\forall\, \delta\boldsymbol{Z}$ (see Ladevèze, 1999, for the origin of eq. (3.28)). The quantities of interest are thereby written in a separated variable form, i.e.

$$\Delta\boldsymbol{\sigma}_{i+1}\left(\vec{x},t\right)=\sum_{j=1}^{m}\lambda_j^{\sigma}\left(t\right)\bar{\boldsymbol{\sigma}}_j\left(\vec{x}\right), \tag{3.30a}$$

$$\Delta\boldsymbol{Z}_{i+1}\left(\vec{x},t\right)=\sum_{j=1}^{m'}\lambda_j^{Z}\left(t\right)\bar{\boldsymbol{Z}}_j\left(\vec{x}\right), \tag{3.30b}$$

where $\left\{\lambda_j^{\sigma}\right\}_{j=1}^{m}$ and $\left\{\lambda_j^{Z}\right\}_{j=1}^{m'}$ are the time functions, and $\{\bar{\boldsymbol{\sigma}}_j\}_{j=1}^{m}$ and $\left\{\bar{\boldsymbol{Z}}_j\right\}_{j=1}^{m'}$ are the space functions. The development thereafter is straightforward, i.e. this separable representation when introduced in the weak form eq. (3.28), yields separate equations for space and time which are solved iteratively. Detailed formulation can be found in Ladevèze (1999).

3.3.3.2 Minimisation formulation of the global stage

Apart from this Galerkin formulation, recently an alternative formulation has been developed to solve the global problem (see Ladevèze, 2014, Relun et al., 2011). This involves finding the solution set $\Delta\boldsymbol{s}_{i+1}$ which minimises over $\boldsymbol{A_d}$ the constitutive relation error e_{CE}^2. The constitutive relation error is associated with the search direction equation and is defined as

$$e_{CE}^2=\left\|\left[\begin{array}{c}\Delta\dot{\boldsymbol{\varepsilon}}_{i+1}^{p}\\-\Delta\dot{\boldsymbol{X}}_{i+1}\end{array}\right]-\mathbf{H}^{-}\left[\begin{array}{c}\Delta\boldsymbol{\sigma}_{i+1}\\\Delta\boldsymbol{Z}_{i+1}\end{array}\right]+\left[\begin{array}{c}\bar{\boldsymbol{\Delta}}^{\varepsilon}\\\bar{\boldsymbol{\Delta}}^{X}\end{array}\right]\right\|_{\mathbf{M}}^{2}, \tag{3.31}$$

where the norm is defined as

$$\|\square\|_{\mathbf{M}}^{2}=\int_{\Omega\times[0,T]}\square:\mathbf{M}\square\mathrm{d}V\mathrm{d}t, \tag{3.32}$$

and the operator $\mathbf{M}$ must be positive definite. The solution set $\Delta\boldsymbol{s}_{i+1}$ is then calculated such that

$$\Delta\boldsymbol{s}_{i+1}=\arg\min_{\Delta\boldsymbol{s}_{i+1}\in\boldsymbol{A_d}}\left\|\left[\begin{array}{c}\Delta\dot{\boldsymbol{\varepsilon}}_{i+1}^{p}\\-\Delta\dot{\boldsymbol{X}}_{i+1}\end{array}\right]-\mathbf{H}^{-}\left[\begin{array}{c}\Delta\boldsymbol{\sigma}_{i+1}\\\Delta\boldsymbol{Z}_{i+1}\end{array}\right]+\left[\begin{array}{c}\bar{\boldsymbol{\Delta}}^{\varepsilon}\\\bar{\boldsymbol{\Delta}}^{X}\end{array}\right]\right\|_{\mathbf{M}}^{2}. \tag{3.33}$$

The quantities of interest are also written in a separated variable form, i.e. along with eq. (3.30),

$$\Delta\dot{\boldsymbol{\varepsilon}}_{i+1}^{p}\left(\vec{x},t\right)=\sum_{j=1}^{m}\dot{\lambda}_j^{p}\left(t\right)\bar{\boldsymbol{\varepsilon}}_j^{p}\left(\vec{x}\right), \tag{3.34a}$$

$$\Delta\dot{\boldsymbol{X}}_{i+1}\left(\vec{x},t\right)=\sum_{j=1}^{m'}\dot{\lambda}_j^{X}\left(t\right)\bar{\boldsymbol{X}}_j\left(\vec{x}\right). \tag{3.34b}$$

It has to be noted that along with the minimisation problem, the admissibility conditions should also be satisfied in a weak sense (as constraints to the minimisation weak form). Ultimately, separate time and space equations are obtained which are solved iteratively. For detailed solution of the minimisation problem, Néron and Ladevèze (2010), Relun (2011) are suggested.

Generally, in the global stage of LATIN method, a combination of POD and PGD is used. At the beginning the reduced order basis is reused and only the time functions are updated, if the reduced order model hence formed is not satisfactory enough, the reduced basis is enriched by adding a space-time pair using the PGD technique (see Ladevèze, 2014). At each LATIN iteration, generally the reduced basis is enriched by a maximum of one space-time mode (see Néron and Ladevèze, 2010).

3.3.4 A note on "normal formulation"

At the beginning of section 3.3, it was considered that the hardening variables follow a "normal formulation" given by eq. (3.22). Indeed, the efficient usage of LATIN algorithm requires that the state equations are defined by linear operators (see Bhattacharyya et al., 2017, Cognard and Ladevèze, 1993, Ladevèze, 1989, 1999). The elastic state law (eq. (2.35)) and the kinematic state equation (eq. (2.45a)) introduced in chapter 2 already follow "normal formulations", however the isotropic state equation (eq. (2.45b)) does not. Henceforth, eq. (2.45b) is transformed into linear relations by a change of variable

$$\bar{R} = R_\infty \bar{r} \tag{3.35}$$

where, $\bar{R}$ and $\bar{r}$ are the new isotropic variables, such that

$$\begin{aligned} \bar{r} &= \int_0^r \left(\frac{\partial R}{\partial r} \frac{1}{R_\infty} \right)^{1/2} \mathrm{d}r, \\ \implies \bar{r} &= \frac{2}{\gamma^{1/2}} \left[1 - \exp\left(-\frac{\gamma r}{2} \right) \right]. \end{aligned} \tag{3.36}$$

This information of new isotropic internal variable along with eq. (2.45b) are used to establish the relation between R and $\bar{R}$, i.e.

$$R = R_\infty \left(\frac{\bar{R}}{R_\infty} \frac{\gamma^{1/2}}{2} \right) \left(2 - \frac{\bar{R}}{R_\infty} \frac{\gamma^{1/2}}{2} \right). \tag{3.37}$$

The new isotropic variables can be used to interpret eq. (3.22) as

$$\begin{bmatrix} \boldsymbol{\beta} \\ \bar{R} \end{bmatrix} = \begin{bmatrix} \mathbf{Q} & 0 \\ 0 & R_\infty \end{bmatrix} \begin{bmatrix} \boldsymbol{\alpha} \\ \bar{r} \end{bmatrix}, \tag{3.38}$$

such that

$$\boldsymbol{Z} = \begin{bmatrix} \boldsymbol{\beta} \\ \bar{R} \end{bmatrix}, \ \boldsymbol{\Pi} = \begin{bmatrix} \mathbf{Q} & 0 \\ 0 & R_\infty \end{bmatrix}, \ \boldsymbol{X} = \begin{bmatrix} \boldsymbol{\alpha} \\ \bar{r} \end{bmatrix}. \tag{3.39}$$

A state law following such a "normal formulation" can easily be incorporated in the linear global step of the LATIN method.

3.3.5 LATIN method in a heuristic nutshell

To summarise, LATIN method can be viewed as a linearisation scheme, with inherent fully discrete formulation. Instead of classical solution schemes that use time step by time step strategy, LATIN method gives an approximation of the quantities of interest for all time. Separate linearisation techniques are not necessary because of the separation of the linear and non-linear part which directly provides a linear formulation of the global equations. The local stage (or the solution of evolution equations) is extremely cheap as no time integration is needed and the primal quantities of interest are obtained in rate form by solving algebraic equations and the integration is done only in the global stage. The cost of solving the global equilibrium is reduced due to the separated representation with respect to space and time. The POD phase of the global stage, i.e. where the spatial basis is reused, is extremely cheap as there are no iterations involved and only the temporal weak form is solved. The choice of enriching the basis is governed by inherent criteria, and this being one of the most costly part of the algorithm, is performed if it is absolutely essential. The calculation of the direction of descent is also expensive and thereby is not calculated at every LATIN iteration but only if necessary. The choice of this operator may depend on the degree of non-linearity. For instance, if the problem involves low (visco)plasticity then even the inverse of Hooke's tensor may provide appreciable convergence however for high degree of plasticity the search direction operator should be close to the exact tangent operator.

The comparison of Galerkin-based PGD formulation and formulation based on residual minimisation including the respective benefits and drawbacks has been well explained in Nouy (2010). Although his model problem was based on advection diffusion reaction equation, Nouy has drawn excellent insight on the two formulations in a generic sense. Formulation based on minimal residual criterion can be considered to be more robust than Galerkin-based PGD formulation as there is a strict monotonic decrease of the residual and hence a guaranteed convergence. However, the convergence rate is depended on the construction of a suitable norm of the residual, which in many cases not being straightforward, renders the convergence rate much lower than Galerkin-based PGD formulation. The computational effort is dramatically increased in the case of minimal residual formulation because the separation order is higher compared to Galerkin-based formulation. The temporal problem in case of minimal residual formulation also is a second order ordinary differential equation (ODE) with initial and final boundary conditions compared to the first order ODE with initial condition obtained for Galerkin formulation. Although it is recommended in Nouy (2010) to avoid residual minimisation-based PGD for cases where Galerkin-based PGD works, the guaranteed convergence of the minimal residual-based PGD cannot be undermined. Henceforth, in this research a hybrid formulation will be used that benefits from both types of PGD formulation.

Although LATIN method has been introduced in this chapter in the context of small displacement (infinitesimal strain) problems, LATIN-PGD methods have been used to solve large displacement (finite strain) problems (see Ladevèze, 1999), in the case of buckling (see Boucard et al., 1997) and also for elastomers (see Aubard et al., 2002). LATIN-PGD has also been used in the field of parametric viscoplastic problems (see Relun et al., 2013) and also for multi-physics problems (see Néron and Dureisseix, 2008, Néron and Ladevèze, 2010). Computation of large frequency band in transient dynamics (see Barbarulo et al., 2014) and solution inverse problems (see Allix and Vidal, 2002) has also been performed using LATIN-PGD algorithm. It has also been used for structural domain decomposition (see Ladevèze and Nouy, 2003, Ladevèze et al., 2007) and to solve frictional contact problems (see Giacoma et al., 2015). A reference point method has also been introduced in Capaldo et al. (2017), where the idea of the hyper-reduction method has been used in a LATIN-PGD framework. As far as damage is concerned, LATIN has been used in Allix et al. (1989) for delamination in composite structures, in Bellenger and Bussy (1998, 2000) for metal forming processes. The main limitation of LATIN method, according to the author's point of view is its intrusive nature, especially when used in commercial finite element software or established finite element code. Most of the finite element software and academic finite element codes used in different academic and research institutions use classical time incremental schemes based on Newton-Raphson algorithms. Thereby, incorporation of LATIN method is not straightforward as the complete structure of the codes needs replacement and the complete notion of incremental finite element analysis needs to be re-structured. This according to the opinion of the author, is the reason behind the limited usage of the LATIN method in spite of its tremendous advantages. However, recently there have been works in LMT-Cachan to introduce LATIN in commercial finite element software.

3.3.6 Newton-Raphson technique in the light of LATIN method

With the background of LATIN method, the classical Newton-Raphson technique can be interpreted in the same perspective. In other words, Newton-Raphson methods can be viewed exactly as LATIN algorithms but not on whole space-time domain but at each time step (see Cognard and Ladevèze, 1993, Ladevèze, 1999, for details). If a solution set

$$s = \left[\boldsymbol{\varepsilon}\left(\vec{x}\right), \boldsymbol{\sigma}\left(\vec{x}\right)\right], \forall \vec{x} \in \Omega \tag{3.40}$$

is sought at time t_{n+1}, the goal is achieved iteratively similar to LATIN method. The iterations can be divided into,

– local stage: Seeking $\hat{s}_{n+1}^{k}$ from s_{n+1}^{k} such that constitutive material behaviour i.e. $\hat{\boldsymbol{\sigma}}_{n+1}^{k} = \mathcal{C}\left(\hat{\boldsymbol{\varepsilon}}_{n+1}^{k}\right)$ is satisfied. The solution set must also satisfy the "search direction" equation, given by $\hat{\boldsymbol{\varepsilon}}_{n+1}^{k} = \boldsymbol{\varepsilon}_{n+1}^{k}$.

– global stage: Seeking s_{n+1}^{k+1} from $\hat{s}_{n+1}^{k}$ such that the "search direction" equation $\boldsymbol{\sigma}_{n+1}^{k+1} - \hat{\boldsymbol{\sigma}}_{n+1}^{k} = \mathbf{C}_T \left(\boldsymbol{\sigma}_{n+1}^{k+1} - \hat{\boldsymbol{\sigma}}_{n+1}^{k} \right)$ is satisfied, where $\mathbf{C}_T$ can be the consistent tangent operator. The solution set s_{n+1}^{k+1} should also satisfy the global admissibility conditions, i.e. $\int_\Omega \left(\boldsymbol{\sigma}_{n+1}^{k+1} - \boldsymbol{\sigma}_{n+1}^{k} \right) : \delta\boldsymbol{\varepsilon} \mathrm{d}V = 0$, $\forall \delta\boldsymbol{\varepsilon}$ those are kinematically admissible to zero. It is quite evident that this will lead to the linearised form given in eq. (3.2). It is also needless to say that the starting point s_{n+1}^{0} is built from a converged solution of the previous time step t_n assuming an elastic solution which takes into account all the boundary conditions, hence the corrective solutions thereafter are admissible to zero.

The global manifold $\boldsymbol{A_d}|_{n+1}$ and the local manifold $\boldsymbol{\Gamma}|_{n+1}$ at time t_{n+1} along with the iterative scheme are shown in fig. 3.6.

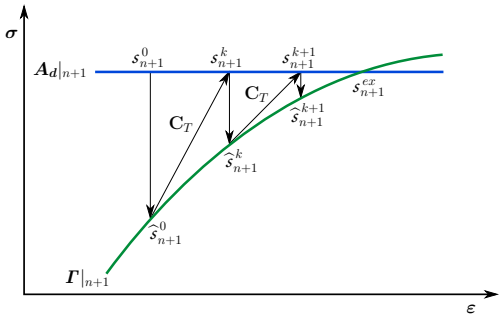

Figure 3.6: Similar iterative behaviour of Newton-Raphson algorithm as compared to LATIN method.

In a certain sense both these algorithms can be viewed in the same light, but the two nested loops are swapped. In Newton-Raphson algorithm, the external loop sweeps the temporal domain from the first time point to the last, and at each time point the inner loop consists of iterations between the global admissibilities and local constitutive behaviour. On the contrary, in LATIN algorithm, the external loop iterates between the global admissibilities and local constitutive behaviour for all the time points, whereas the inner loops sweep the temporal domain.

3.4 Concluding remark

To predict lifetime of structures under fatigue loading, model reduction strategies specific to LATIN method are important components in the solution philosophy, as the separated representation not only reduces the computation but also let the temporal part be treated separately. The strategy benefits from adaptive enrichment of the ROB and henceforth the ROM, dictated by the desired non-linear problem without any pre-computation.

In this research, the lifetime of a structure will be quantified by the evolution of damage variable, hence it is necessary to combine continuum damage mechanics and large time increment method to benefit from both of their advantages. Using damage as an extra internal variable in the context of LATIN algorithm is not straightforward as the elastic state law becomes non-linear. The detailed discussion regarding the inclusion of damage variable in LATIN framework will be carried out in the next chapter.

Chapter 4

LATIN-PGD technique for cyclic damage simulation

This chapter essentially deals with the strategy concerning the embodiment of damage as an internal variable in the LATIN framework. Unlike the usual elasto-(visco)plastic problems tackled by LATIN method as described in section 3.3, the elastic state law due to the presence of the damage variable is non-linear and hence cannot be solved in the linear stage. The proposed idea is to solve the non-linear elastic state law in the local stage. This chapter is based on Bhattacharyya et al. (2017) with certain elaboration wherever necessary.

The chapter begins with a summary of all the equations that need to be satisfied, thereby moves on to the solution strategies in the local and global steps of the LATIN method. An elaborative formulation of the global step that includes a hybrid technique to solve the PGD problem and the novel idea to solve the non-linear elastic state law are also detailed. The chapter ends with a few illustrative numerical examples to display the functionality of the method.

4.1 The proposed problem

The proposed problem to be solved is a quasi-static evolution of a structure that is described in chapter 2. The solution set $\boldsymbol{s}$ defined in chapter 3 must be expanded to encompass all the field variables that define the state of the structure, i.e. $\boldsymbol{s} = \left\{ \dot{\boldsymbol{\varepsilon}}^p, \boldsymbol{\varepsilon}^e, \dot{\boldsymbol{X}}, \dot{D}, \boldsymbol{\sigma}, \boldsymbol{Z}, Y \right\}$. The material chosen for this analysis is based on Marquis-Chaboche elasto-viscoplastic model with kinematic, isotropic hardening and coupled with damage. The set of all equations, with $\boldsymbol{\varrho} = \dfrac{\boldsymbol{\sigma}^D}{1-D} - \boldsymbol{\beta}$, that must be satisfied by the structure is summarised in table 4.1.

Table 4.1: The set of constitutive relations and admissibility conditions that need to be satisfied

viscoplastic yield function	$f^p = \sqrt{\frac{3}{2}\left[\boldsymbol{\varrho} : \boldsymbol{\varrho}\right]} + \frac{a}{2}\left[\boldsymbol{\beta} : \mathbf{Q}^{-1}\boldsymbol{\beta}\right] - R_\infty\left(\frac{\bar{R}}{R_\infty}\frac{\gamma^{1/2}}{2}\right)\left(2 - \frac{\bar{R}}{R_\infty}\frac{\gamma^{1/2}}{2}\right) - \sigma_y$
damage function	$f^d = Y - Y_{th}$
evolution equations	$\dot{\boldsymbol{\varepsilon}}^p = k\left\langle f^p\right\rangle_+^n \left[\frac{3}{2}\frac{\boldsymbol{\varrho}}{\sqrt{\frac{3}{2}\left[\boldsymbol{\varrho} : \boldsymbol{\varrho}\right]}}\right]\frac{1}{1-D}$
	$\dot{\alpha} = -k\left\langle f^p\right\rangle_+^n \left[-\frac{3}{2}\frac{\boldsymbol{\varrho}}{\sqrt{\frac{3}{2}\left[\boldsymbol{\varrho} : \boldsymbol{\varrho}\right]}} + a\mathbf{Q}^{-1}\boldsymbol{\beta}\right]$
	$\dot{\bar{r}} = -k\left\langle f^p\right\rangle_+^n \left[\frac{\bar{R}}{R_\infty}\frac{\gamma}{2} - \gamma^{1/2}\right]$
	$\dot{D} = k_d\left\langle f^d\right\rangle_+^{n_d}$
state laws	$\varepsilon^e_{ij} = \frac{1+\nu}{E}\left[\frac{\langle\sigma\rangle^+_{ij}}{1-D} + \frac{\langle\sigma\rangle^-_{ij}}{1-hD}\right] - \frac{\nu}{E}\left[\frac{\langle\sigma_{kk}\rangle}{1-D} + \frac{\langle-\sigma_{kk}\rangle}{1-hD}\right]\delta_{ij}$
	$\beta_{ij} = Q\alpha_{ij}$
	$\bar{R} = R_\infty \bar{r}$
	$Y = \frac{1+\nu}{2E}\left[\frac{\langle\sigma\rangle^+_{ij}\langle\sigma\rangle^+_{ij}}{(1-D)^2} + h\frac{\langle\sigma\rangle^-_{ij}\langle\sigma\rangle^-_{ij}}{(1-hD)^2}\right] - \frac{\nu}{2E}\left[\frac{\langle\sigma_{kk}\rangle^2}{(1-D)^2} + h\frac{\langle-\sigma_{kk}\rangle^2}{(1-hD)^2}\right]$
static admissibility	$\int\limits_{\Omega\times[0,T]} \boldsymbol{\sigma} : \delta\dot{\boldsymbol{\varepsilon}}\,\mathrm{d}V\mathrm{d}t + \int\limits_{\Omega\times[0,T]} \vec{f}_d \cdot \delta\dot{\vec{u}}\,\mathrm{d}V\mathrm{d}t + \int\limits_{\partial\Omega_2\times[0,T]} \vec{F}_d \cdot \delta\dot{\vec{u}}\,\mathrm{d}S\mathrm{d}t = 0$
kinematic admissibility	$-\int\limits_{\Omega\times[0,T]} \delta\boldsymbol{\sigma} : \dot{\boldsymbol{\varepsilon}}\,\mathrm{d}V\mathrm{d}t + \int\limits_{\partial\Omega_1\times[0,T]} \delta\boldsymbol{\sigma}\cdot\vec{n}\cdot\dot{\vec{U}}_d\,\mathrm{d}S\mathrm{d}t = 0$

4.2 Initialisation

The algorithm starts with the usual elastic initialisation. A solution set $\boldsymbol{s}_0 \in \boldsymbol{A_d}$ is calculated, considering the loading to be elastic. The elastic assumption ensures that all the internal variables $\boldsymbol{X}$, $\boldsymbol{Z}$, D and $\boldsymbol{\varepsilon}^p$ are set equal to zero. The displacement and/or force boundary conditions are taken into account in this phase, and each subsequent LATIN iteration will involve correction to the assumed linear elastic solution.

4.3 Local stage

The local stage essentially involves solution of all the local non-linear equations, i.e. the evolution equations and the non-linear elastic state law (see table 4.1). The objective thereby, is with the knowledge $\boldsymbol{s}_i \in \boldsymbol{A_d}$, to find $\hat{\boldsymbol{s}}_{i+1/2} \in \boldsymbol{\Gamma}$. The search direction equations that were introduced in eq. (3.24), are expanded to incorporate the ancillary variables of the solution set $\boldsymbol{s}$, i.e.

$$\begin{bmatrix} \hat{\boldsymbol{\varepsilon}}^p_{i+1/2} - \dot{\boldsymbol{\varepsilon}}^p_i \\ -\left(\hat{\boldsymbol{X}}_{i+1/2} - \dot{\boldsymbol{X}}_i\right) \\ \hat{\boldsymbol{\varepsilon}}^e_{i+1/2} - \boldsymbol{\varepsilon}^e_i \end{bmatrix} + \mathbf{B}^+ \begin{bmatrix} \hat{\boldsymbol{\sigma}}_{i+1/2} - \boldsymbol{\sigma}_i \\ \hat{\boldsymbol{Z}}_{i+1/2} - \boldsymbol{Z}_i \\ \hat{\boldsymbol{\sigma}}_{i+1/2} - \boldsymbol{\sigma}_i \end{bmatrix} = 0, \tag{4.1a}$$

$$\begin{bmatrix} \hat{D}_{i+1/2} - \dot{D}_i \end{bmatrix} + \mathbf{b}^+ \begin{bmatrix} \hat{Y}_{i+1/2} - Y_i \end{bmatrix} = 0. \tag{4.1b}$$

The new directions of ascent $\mathbf{B}^+$ and $\mathbf{b}^+$ are chosen based on eq. (3.26), i.e. to consider

$$\left(\mathbf{B}^+\right)^{-1} = 0, \text{ and } \left(\mathbf{b}^+\right)^{-1} = 0. \tag{4.2}$$

This choice of the search direction operators provides

$$\hat{\boldsymbol{\sigma}}_{i+1/2} = \boldsymbol{\sigma}_i,\ \hat{\boldsymbol{Z}}_{i+1/2} = \boldsymbol{Z}_i,\ \hat{Y}_{i+1/2} = Y_i. \tag{4.3}$$

The thermodynamic forces being obtained, the next step is to solve for the internal variables. The LATIN iteration index $i+1/2$ used for the local step is dropped henceforth for further formulations in this section to circumvent confusion and maintain clarity. The solution procedure begins with solving

$$\hat{D} = k_d \left\langle \hat{f}^{\,d} \right\rangle_+^{n_d}, \tag{4.4}$$

where

$$\hat{f}^{\,d} = \hat{Y} - Y_{th}, \tag{4.5}$$

to obtain $\hat{D}$. If, the time domain $[0, T]$ is discretised into $\tilde{n}+1$ time instances i.e. $[t_0 = 0, t_1, t_2, \cdots, t_n, \cdots, t_{\tilde{n}-1}, t_{\tilde{n}} = T]$, $\hat{D}^n$ at time instance t_n is obtained using a backward Euler rule, i.e.

$$\hat{D}^n = \hat{D}^{n-1} + k_d \left\langle \hat{Y}^n - Y_{th} \right\rangle_+^{n_d} \Delta t_n,\ \forall n = \{1, 2, \cdots, \tilde{n}-1\}, \tag{4.6}$$

with $\Delta t_n = t_n - t_{n-1}$. The quantity $\hat{D}^0$ is taken to be zero for virgin material, and contains the initial damage value for pre-damaged cases. The damage variable is calculated for all Gauss points. Thereafter, this information is used to calculate the elastic strain tensor, i.e.

$$\hat{\varepsilon}^e_{ij} = \frac{1+\nu}{E}\left[\frac{\langle\hat{\sigma}\rangle^+_{ij}}{1-\hat{D}} + \frac{\langle\hat{\sigma}\rangle^-_{ij}}{1-h\hat{D}}\right] - \frac{\nu}{E}\left[\frac{\langle\hat{\sigma}_{kk}\rangle}{1-\hat{D}} + \frac{\langle-\hat{\sigma}_{kk}\rangle}{1-h\hat{D}}\right]\delta_{ij}. \tag{4.7}$$

The algebraic formulation is solved to obtain $\hat{\boldsymbol{\varepsilon}}^e$ for every Gauss point at all time instances. The evolution equations

$$\hat{\dot{\boldsymbol{\varepsilon}}}^p = k \left\langle \hat{f}^p \right\rangle_+^n \left[\frac{\frac{3}{2}\frac{\hat{\boldsymbol{\varrho}}}{\sqrt{\frac{3}{2}\left[\hat{\boldsymbol{\varrho}} : \hat{\boldsymbol{\varrho}}\right]}}}\right] \frac{1}{1-\hat{D}} \tag{4.8a}$$

$$\hat{\dot{\alpha}} = -k \left\langle \hat{f}^p \right\rangle_+^n \left[-\frac{\frac{3}{2}\frac{\hat{\boldsymbol{\varrho}}}{\sqrt{\frac{3}{2}\left[\hat{\boldsymbol{\varrho}} : \hat{\boldsymbol{\varrho}}\right]}}} + a\mathbf{Q}^{-1}\hat{\beta}\right] \tag{4.8b}$$

$$\hat{\dot{\bar{r}}} = -k \left\langle \hat{f}^p \right\rangle_+^n \left[\frac{\hat{\bar{R}}}{R_\infty} \frac{\gamma}{2} - \gamma^{1/2} \right] \tag{4.8c}$$

with

$$\hat{\boldsymbol{\varrho}} = \frac{\hat{\boldsymbol{\sigma}}^D}{1-\hat{D}} - \hat{\boldsymbol{\beta}} \tag{4.9}$$

and the yield function

$$\hat{f}^p = \sqrt{\frac{3}{2}\left[\hat{\boldsymbol{\varrho}} : \hat{\boldsymbol{\varrho}}\right]} + \frac{a}{2}\left[\hat{\boldsymbol{\beta}} : \mathbf{Q}^{-1}\hat{\boldsymbol{\beta}}\right] - R_\infty \left(\frac{\hat{\bar{R}}}{R_\infty} \frac{\gamma^{1/2}}{2} \right) \left(2 - \frac{\hat{\bar{R}}}{R_\infty} \frac{\gamma^{1/2}}{2} \right) - \sigma_y \tag{4.10}$$

are also solved algebraically at each Gauss point for every time instance. It has to be noted that integration of the evolution equations (eq. (4.8)) is not needed in the local stage as the plastic strain and the hardening variables are obtained in rate form. This culminates into the complete solution set $\hat{\boldsymbol{s}}_{i+1/2}$, the knowledge of which is quintessential in obtaining the global solution set $\boldsymbol{s}_{i+1}$.

4.4 Search direction for global stage

The objective of the global stage is to construct a solution set $\boldsymbol{s}_{i+1} \in \boldsymbol{A_d}$. The first set of equations that needs to be considered is the search direction equations. Equation (3.25) is thereby modified as

$$\begin{bmatrix} \boldsymbol{\varepsilon}^p_{i+1} - \hat{\boldsymbol{\varepsilon}}^p_{i+1/2} \\ -\left(\boldsymbol{X}_{i+1} - \hat{\boldsymbol{X}}_{i+1/2} \right) \\ \boldsymbol{\varepsilon}^e_{i+1} - \hat{\boldsymbol{\varepsilon}}^e_{i+1/2} \end{bmatrix} - \mathbf{B}^- \begin{bmatrix} \boldsymbol{\sigma}_{i+1} - \hat{\boldsymbol{\sigma}}_{i+1/2} \\ \boldsymbol{Z}_{i+1} - \hat{\boldsymbol{Z}}_{i+1/2} \\ \boldsymbol{\sigma}_{i+1} - \hat{\boldsymbol{\sigma}}_{i+1/2} \end{bmatrix} = 0, \tag{4.11a}$$

$$\begin{bmatrix} \dot{D}_{i+1} - \hat{\dot{D}}_{i+1/2} \end{bmatrix} - \mathbf{b}^- \begin{bmatrix} Y_i - \hat{Y}_{i+1/2} \end{bmatrix} = 0, \tag{4.11b}$$

where $\mathbf{B}^- = \begin{bmatrix} \mathbf{H}^- & 0 \\ 0 & \mathbf{C}^{-1} \end{bmatrix}$. The operator $\mathbf{H}^-$ belongs to the tangent space associated with the solution set $\hat{\boldsymbol{s}}_{i+1/2}$ in the manifold $\boldsymbol{\Gamma}$. For mixed hardening, it is of the form

$$\mathbf{H}^- = \begin{bmatrix} \mathbf{H}_\sigma & \mathbf{H}_{\sigma\beta} & \mathbf{H}_{\sigma R} \\ \mathbf{H}_{\beta\sigma} & \mathbf{H}_\beta & \mathbf{H}_{\beta R} \\ \mathbf{H}_{R\sigma} & \mathbf{H}_{R\beta} & \mathbf{H}_R \end{bmatrix}. \tag{4.12}$$

To simplify the operator, only the diagonal terms are taken into account and the off-diagonal terms are considered to be zero, which results in

$$\mathbf{H}^- = \begin{bmatrix} \mathbf{H}_\sigma & 0 & 0 \\ 0 & \mathbf{H}_\beta & 0 \\ 0 & 0 & \mathbf{H}_R \end{bmatrix} = \begin{bmatrix} \mathbf{H}_\sigma & 0 \\ 0 & \mathbf{H}_Z \end{bmatrix}, \tag{4.13}$$

with,

$$\mathbf{H}_Z = \begin{bmatrix} \mathbf{H}_\beta & 0 \\ 0 & \mathbf{H}_R \end{bmatrix}. \tag{4.14}$$

The diagonal terms of $\mathbf{H}^-$ can be obtained from the pseudo-dissipation potential as

$$\mathbf{H}_\sigma = \frac{\partial}{\partial \boldsymbol{\sigma}} \left(\frac{\partial \Phi^*}{\partial \boldsymbol{\sigma}} \right) \Big|_{\boldsymbol{s}=\hat{\boldsymbol{s}}} = kn \left\langle \hat{f}^p \right\rangle^{n-1} \frac{1}{\left(1-\hat{D}\right)^2} \frac{3/2\hat{\boldsymbol{\varrho}}}{\hat{\varsigma}} \otimes \frac{3/2\hat{\boldsymbol{\varrho}}}{\hat{\varsigma}}$$

$$+ k \left\langle \hat{f}^p \right\rangle^n \frac{1}{\left(1-\hat{D}\right)^2} \frac{3/2 \left(\hat{\varsigma}\mathbb{I} - 3/2 \frac{\hat{\boldsymbol{\varrho}} \otimes \hat{\boldsymbol{\varrho}}}{\hat{\varsigma}} \right)}{\hat{\varsigma}^2}, \tag{4.15a}$$

$$\mathbf{H}_\beta = \frac{\partial}{\partial \boldsymbol{\beta}} \left(\frac{\partial \Phi^*}{\partial \boldsymbol{\beta}} \right) \Big|_{\boldsymbol{s}=\hat{\boldsymbol{s}}} = kn \left\langle \hat{f}^p \right\rangle^{n-1} \left(-\frac{3/2 \hat{\boldsymbol{\varrho}}}{\hat{\varsigma}} + \frac{a}{Q} \mathbb{I} \hat{\boldsymbol{\beta}} \right) \otimes \left(-\frac{3/2 \hat{\boldsymbol{\varrho}}}{\hat{\varsigma}} + \frac{a}{Q} \mathbb{I} \hat{\boldsymbol{\beta}} \right)$$
$$+ k \left\langle \hat{f}^p \right\rangle^n \frac{3/2 \left(\hat{\varsigma}\mathbb{I} - 3/2 \frac{\hat{\boldsymbol{\varrho}} \otimes \hat{\boldsymbol{\varrho}}}{\hat{\varsigma}} \right)}{\hat{\varsigma}^2} \frac{a}{Q} \mathbb{I}, \tag{4.15b}$$

$$\mathbf{H}_R = \frac{\partial}{\partial \bar{R}} \left(\frac{\partial \Phi^*}{\partial \bar{R}} \right) \Big|_{\boldsymbol{s}=\hat{\boldsymbol{s}}} = kn \left\langle \hat{f}^p \right\rangle^{n-1} \gamma \left(1 - \frac{\hat{\bar{R}} \gamma^{1/2}}{2R_\infty} \right)^2 + k \left\langle \hat{f}^p \right\rangle^n \frac{\gamma}{2R_\infty}, \tag{4.15c}$$

with $\hat{\varsigma} = \sqrt{\frac{3}{2} \hat{\boldsymbol{\varrho}} : \hat{\boldsymbol{\varrho}}}$ and $\mathbb{I}$ is identity matrix. It can be noted that the index $i+1/2$ is dropped in eq. (4.15) for convenience. The definitions of the search direction operators were established in Relun et al. (2013) for perfect viscoplasticity problems, and extended for hardening and damage in Bhattacharyya et al. (2017).

The operator $\mathbf{H}^-$ hence obtained is symmetric, positive and semi-definite. The inverse of this operator is not always defined, e.g. at the spatial and temporal points where the solution is elastic. Therefore it is regularised as

$$\mathbf{H}^- = \mathbf{H}^- + \varpi \mathbf{N}^{-1}, \tag{4.16}$$

with ϖ being the regularisation coefficient and

$$\mathbf{N} = \begin{bmatrix} \mathbf{C} & 0 & 0 \\ 0 & \mathbf{Q} & 0 \\ 0 & 0 & R_\infty \end{bmatrix}. \tag{4.17}$$

With these search direction operators being obtained, the quantities of interest can be calculated.

4.5 Internal variables at the global stage

The internal variables being local in space, are calculated without any PGD approximation, but by simply solving first order ODEs in time, locally at each Gauss point (GP). Some early versions of LATIN employed PGD-based technique to solve the internal variables as well (see Ladevèze, 1999, e.g.), however in this thesis PGD on internal variables is not used. The search direction equation for hardening variables eq. (4.11a) combined with the state equation can be written as

$$\begin{aligned} &-\left(\dot{\boldsymbol{X}}_{i+1} - \hat{\dot{\boldsymbol{X}}}_{i+1/2} \right) = \mathbf{H}_Z \left(\boldsymbol{Z}_{i+1} - \hat{\boldsymbol{Z}}_{i+1/2} \right) = \mathbf{H}_Z \left(\boldsymbol{\Pi} \boldsymbol{X}_{i+1} - \hat{\boldsymbol{Z}}_{i+1/2} \right), \\ &\implies \dot{\boldsymbol{X}}_{i+1} + \mathbf{H}_Z \boldsymbol{\Pi} \boldsymbol{X}_{i+1} = \hat{\dot{\boldsymbol{X}}}_{i+1/2} + \mathbf{H}_Z \hat{\boldsymbol{Z}}_{i+1/2}. \end{aligned} \tag{4.18}$$

This equation is solved using the same scheme as in eq. (4.6), i.e.

$$\boldsymbol{X}^n_{i+1} = \left(\frac{1}{\Delta t_n} \mathbb{I} + \mathbf{H}^n_Z \boldsymbol{\Pi} \right)^{-1} \left(\hat{\dot{\boldsymbol{X}}}^n_{i+1/2} + \mathbf{H}^n_Z \hat{\boldsymbol{Z}}^n_{i+1/2} + \frac{1}{\Delta t_n} \boldsymbol{X}^{n-1}_{i+1} \right), \quad \forall n = \{1, 2, \cdots, \tilde{n}\}. \tag{4.19}$$

The associated variables can then be simply calculated as

$$\boldsymbol{Z}^n_{i+1} = \boldsymbol{\Pi} \boldsymbol{X}^n_{i+1}, \ \forall n = \{0, 1, \cdots, \tilde{n}\}. \tag{4.20}$$

As far as the damage variables are concerned, the search direction operator $\mathbf{b}^-$ being considered to be zero,

$$\dot{D}_{i+1} = \hat{\dot{D}}_{i+1/2} \implies D_{i+1} = \hat{D}_{i+1/2}. \tag{4.21}$$

Finally, knowing $\boldsymbol{\sigma}_{i+1}$ and D_{i+1}, the energy release rate Y_{i+1} is estimated using

$$\begin{aligned} Y^n =& \frac{1+\nu}{2E}\left[\frac{\langle\sigma^n\rangle^+_{ij}\langle\sigma^n\rangle^+_{ij}}{(1-D^n)^2} + h\frac{\langle\sigma^n\rangle^-_{ij}\langle\sigma^n\rangle^-_{ij}}{(1-hD^n)^2}\right] \\ &- \frac{\nu}{2E}\left[\frac{\left\langle\sigma^n_{kk}\right\rangle^2}{(1-D^n)^2} + h\frac{\left\langle-\sigma^n_{kk}\right\rangle^2}{(1-hD^n)^2}\right],\ \forall n = \{0,1,\cdots,\tilde{n}-1\}. \end{aligned} \tag{4.22}$$

It can be noticed that the LATIN iteration index $i+1$ is dropped in eq. (4.22) to avoid confusion with the matrix indices. Although trivial, care should be taken to construct the positive and negative parts of the stress tensor at each time point t_n, as explained in section 2.2.5.

4.6 PGD formulation of the global stage

The idea here is to solve the global admissibilities using PGD-based model reduction methods, where the quantities of interest are represented in separated variable forms. The boundary conditions being taken into consideration in the elastic initialisation, the solution set which is searched here in terms of corrections has to be kinematically admissible to zero. The static admissibility condition can be expressed $\forall\delta\vec{u}$ which is kinematically admissible to zero as

$$\int_{[0,T]\times\Omega} \Delta\boldsymbol{\sigma}_{i+1} : \boldsymbol{\varepsilon}\left(\delta\vec{u}\right)\ \mathrm{d}V\ \mathrm{d}t = 0, \tag{4.23}$$

where $\Delta\boldsymbol{\sigma}_{i+1} = \boldsymbol{\sigma}_{i+1} - \boldsymbol{\sigma}_i$. In the presence of a linear elastic state law,

$$\Delta\boldsymbol{\sigma}_{i+1} = \mathbf{C}\left(\Delta\boldsymbol{\varepsilon}_{i+1} - \Delta\boldsymbol{\varepsilon}^p_{i+1}\right), \tag{4.24}$$

where $\Delta\boldsymbol{\varepsilon}_{i+1} = \boldsymbol{\varepsilon}_{i+1} - \boldsymbol{\varepsilon}_i$ and $\Delta\boldsymbol{\varepsilon}^p_{i+1} = \boldsymbol{\varepsilon}^p_{i+1} - \boldsymbol{\varepsilon}^p_i$. This allows the reformulation of eq. (4.23) into

$$\int_{[0,T]\times\Omega} \mathbf{C}\Delta\boldsymbol{\varepsilon}_{i+1} : \boldsymbol{\varepsilon}\left(\delta\vec{u}\right)\ \mathrm{d}V\ \mathrm{d}t = \int_{[0,T]\times\Omega} \mathbf{C}\Delta\boldsymbol{\varepsilon}^p_{i+1} : \boldsymbol{\varepsilon}\left(\delta\vec{u}\right)\ \mathrm{d}V\ \mathrm{d}t. \tag{4.25}$$

This weak form leads to a straightforward PGD representation of the stress and plastic strain corrections. The quantities of interest are described by a single temporal basis and by separate spatial bases related to each other through constant linear FE operators (see Relun et al., 2011, 2013, for details). In the presence of damage however the elastic state law is non-linear and the above formulations are not possible. To circumvent this difficulty, the following formulation is proposed.

The stress correction term $\Delta\boldsymbol{\sigma}_{i+1}$ is severed into $\Delta\boldsymbol{\sigma}'_{i+1}$ that relies on plastic deformation and $\Delta\tilde{\boldsymbol{\sigma}}_{i+1}$ that is procured from the non-linear elastic state law,

$$\Delta\boldsymbol{\sigma}_{i+1} = \Delta\boldsymbol{\sigma}'_{i+1} + \Delta\tilde{\boldsymbol{\sigma}}_{i+1}. \tag{4.26}$$

The total strain correction obeying the strain partition relation given by eq. (2.18) is also sundered into $\Delta\boldsymbol{\varepsilon}'_{i+1}$ depending on plasticity and $\Delta\tilde{\boldsymbol{\varepsilon}}_{i+1}$ relying on damage,

$$\Delta\boldsymbol{\varepsilon}_{i+1} = \Delta\boldsymbol{\varepsilon}'_{i+1} + \Delta\tilde{\boldsymbol{\varepsilon}}_{i+1}. \tag{4.27}$$

Now, the corrections to the quantities of interest are used to reformulate the search direction equation pertinent to the elastic strain tensor as

$$\Delta\boldsymbol{\sigma}_{i+1} = \mathbf{C}\Delta\boldsymbol{\varepsilon}^e_{i+1} - \Delta\mathbf{R}_{i+1}, \tag{4.28}$$

where $\Delta\boldsymbol{\varepsilon}^e_{i+1} = \boldsymbol{\varepsilon}^e_{i+1} - \boldsymbol{\varepsilon}^e_i$, and $\Delta\mathbf{R}_{i+1}$ given by

$$\Delta\mathbf{R}_{i+1} = \left(\boldsymbol{\sigma}_i - \hat{\boldsymbol{\sigma}}_{i+1/2}\right) - \mathbf{C}\left(\boldsymbol{\varepsilon}^e_i - \hat{\boldsymbol{\varepsilon}}^e_{i+1/2}\right), \tag{4.29}$$

represents a residual stress term at iteration $i+1$. Using eqs. (4.26) to (4.29), one can establish

$$\Delta\boldsymbol{\sigma}'_{i+1} + \Delta\tilde{\boldsymbol{\sigma}}_{i+1} = \mathbf{C}\left(\Delta\boldsymbol{\varepsilon}'_{i+1} - \Delta\boldsymbol{\varepsilon}^p_{i+1}\right) + \mathbf{C}\left(\Delta\tilde{\boldsymbol{\varepsilon}}_{i+1} - \Delta\boldsymbol{\varepsilon}^R_{i+1}\right), \tag{4.30}$$

where $\Delta\boldsymbol{\varepsilon}^R_{i+1}$ given by

$$\Delta\boldsymbol{\varepsilon}^R_{i+1} = \mathbf{C}^{-1}\Delta\mathbf{R}_{i+1}, \tag{4.31}$$

can be delineated as a residual strain obtained from non-linear state law.

This additive split of the stress and the total strain leads to separate satisfaction of the static admissibility condition. Equation (4.23) can thereby be split into two separated weak forms, the first one depending on the plastic deformations can be expressed $\forall\delta\vec{u}$ which is kinematically admissible to zero as

$$\int_{[0,T]\times\Omega} \Delta\boldsymbol{\sigma}'_{i+1} : \boldsymbol{\varepsilon}\left(\delta\vec{u}\right)\, \mathrm{d}V\, \mathrm{d}t = 0, \tag{4.32}$$

with

$$\Delta\boldsymbol{\sigma}'_{i+1} = \mathbf{C}\left(\Delta\boldsymbol{\varepsilon}'_{i+1} - \Delta\boldsymbol{\varepsilon}^p_{i+1}\right). \tag{4.33}$$

The second one that is related to damage can be expressed similarly $\forall\delta\vec{u}$ which is kinematically admissible to zero as

$$\int_{[0,T]\times\Omega} \Delta\tilde{\boldsymbol{\sigma}}_{i+1} : \boldsymbol{\varepsilon}\left(\delta\vec{u}\right)\, \mathrm{d}V\, \mathrm{d}t = 0, \tag{4.34}$$

with

$$\Delta\tilde{\boldsymbol{\sigma}}_{i+1} = \mathbf{C}\left(\Delta\tilde{\boldsymbol{\varepsilon}}_{i+1} - \Delta\boldsymbol{\varepsilon}^R_{i+1}\right). \tag{4.35}$$

Furthermore, considering only the plastic part of the search direction, eq. (4.11a) is re-formulated as

$$\Delta\dot{\boldsymbol{\varepsilon}}^p_{i+1} - \mathbf{H}_\sigma\Delta\boldsymbol{\sigma}_{i+1} + \bar{\boldsymbol{\Delta}}^\varepsilon_{i+1} = 0, \tag{4.36}$$

with

$$\bar{\boldsymbol{\Delta}}^\varepsilon_{i+1} = \mathbf{H}_\sigma\left(\hat{\boldsymbol{\sigma}}_{i+1/2} - \boldsymbol{\sigma}_i\right) - \left(\hat{\dot{\boldsymbol{\varepsilon}}}^p_{i+1/2} - \dot{\boldsymbol{\varepsilon}}^p_i\right). \tag{4.37}$$

As a result of the separation of the stress tensor, eq. (4.37) is rewritten using the quantities depending on plastic deformation, as

$$\Delta\dot{\boldsymbol{\varepsilon}}^p_{i+1} - \mathbf{H}_\sigma\Delta\boldsymbol{\sigma}'_{i+1} + \bar{\boldsymbol{\Delta}}^\varepsilon_{i+1} \approx 0. \tag{4.38}$$

The intention thereby is to solve for $\left(\Delta\dot{\boldsymbol{\varepsilon}}^p_{i+1}, \Delta\boldsymbol{\sigma}_{i+1}, \Delta\boldsymbol{\varepsilon}^e_{i+1}\right)$ with additional satisfaction of the admissibility conditions. It has to be noted, however, that the search direction equation given by eq. (4.38) is an exact equality only in the absence of damage, where $\Delta\boldsymbol{\sigma}_{i+1} = \Delta\boldsymbol{\sigma}'_{i+1}$. To obtain physically and mathematically viable solutions, it is necessary that the degree of inequality of eq. (4.38) is not too high, which basically hints that this approach is not feasible for high value of damage. However, for metals, the critical damage level being around 0.2 (see Lemaitre and Desmorat, 2005), the value of damage in general is low enough to render the equality approximation of eq. (4.38) reasonable.

A different strategy of addressing the non-linear elastic state law is presented in Appendix D by splitting the effective Hooke's tensor using singular value decomposition, which gives a complete satisfaction of the static admissibility for each of the snapshots iteratively at a given global stage. However the major limitation of the strategy as per Appendix D, is the fact that the Hooke's tensor can be decomposed in time and space only if the loading is proportional.

4.6.1 Separable representation of the quantities of interest

The quantities of interest are currently $\Delta\boldsymbol{\sigma}'_{i+1}$, $\Delta\tilde{\boldsymbol{\sigma}}_{i+1}$, $\Delta\dot{\boldsymbol{\varepsilon}}^p_{i+1}$, and $\Delta\boldsymbol{\varepsilon}^e_{i+1}$. The plastic strain can be written as

$$\Delta\boldsymbol{\varepsilon}^p_{i+1} = \boldsymbol{\lambda}^p(t)\,\bar{\boldsymbol{\varepsilon}}^p(\vec{x}) \;\Rightarrow \Delta\dot{\boldsymbol{\varepsilon}}^p_{i+1} = \dot{\boldsymbol{\lambda}}^p(t)\,\bar{\boldsymbol{\varepsilon}}^p(\vec{x})\,. \tag{4.39}$$

A similar separation on $\Delta\boldsymbol{\varepsilon}'_{i+1}$ and the corresponding displacement field lead to

$$\Delta\vec{u}_{i+1} = \boldsymbol{\lambda}^u(t)\,\bar{\vec{u}}(\vec{x}) \;\Rightarrow \Delta\boldsymbol{\varepsilon}'_{i+1} = \boldsymbol{\lambda}^u(t)\,\bar{\boldsymbol{\varepsilon}}(\vec{x})\,. \tag{4.40}$$

It needs to be mentioned that although only one space-time pair is used here to approximate each correction, it can easily be extended for more separated terms (see Néron and Ladevèze, 2010, for details). For the following development, the indices are dropped for simplicity and used if necessary. Introducing the PGD approximation, the variation in the displacement field in eq. (4.40) becomes $\delta(\Delta\vec{u}) = \delta\boldsymbol{\lambda}^u\bar{\vec{u}} + \boldsymbol{\lambda}^u\delta\bar{\vec{u}}$ with $\delta\bar{\vec{u}}$ being kinematically admissible to zero and $\delta\boldsymbol{\lambda}^u$ does not have any condition. The space-time problem defined by eq. (4.32) is thereby separated into a spatial problem and a temporal problem. The temporal problem consists in calculating $\boldsymbol{\lambda}^u$ such that $\forall\delta\boldsymbol{\lambda}^u$,

$$\int_{[0,T]} \boldsymbol{\lambda}^u\delta\boldsymbol{\lambda}^u\,\mathrm{d}t \int_\Omega \mathbf{C}\bar{\boldsymbol{\varepsilon}}\colon\boldsymbol{\varepsilon}\left(\bar{\vec{u}}\right)\,\mathrm{d}V = \int_{[0,T]} \boldsymbol{\lambda}^p\delta\boldsymbol{\lambda}^u\,\mathrm{d}t \int_\Omega \mathbf{C}\bar{\boldsymbol{\varepsilon}}^p\colon\boldsymbol{\varepsilon}\left(\bar{\vec{u}}\right)\,\mathrm{d}V. \tag{4.41}$$

The proportionality of $\boldsymbol{\lambda}^u$ and $\boldsymbol{\lambda}^p$ is a direct outcome of eq. (4.41), which lets, according to Relun et al. (2011), the most trivial assumption $\boldsymbol{\lambda}^u = \boldsymbol{\lambda}^p = \boldsymbol{\lambda}$. This preference of the temporal functions leads to the spatial problem be defined as

$$\int_{[0,T]} \boldsymbol{\lambda}\boldsymbol{\lambda}\,\mathrm{d}t \int_\Omega \mathbf{C}\bar{\boldsymbol{\varepsilon}}\colon\boldsymbol{\varepsilon}\left(\delta\bar{\vec{u}}\right)\,\mathrm{d}V = \int_{[0,T]} \boldsymbol{\lambda}\boldsymbol{\lambda}\,\mathrm{d}t \int_\Omega \mathbf{C}\bar{\boldsymbol{\varepsilon}}^p\colon\boldsymbol{\varepsilon}\left(\delta\bar{\vec{u}}\right)\,\mathrm{d}V, \tag{4.42}$$

$\forall\delta\bar{\vec{u}}$ which is kinematically admissible to zero. This can be further reduced to

$$\int_\Omega \mathbf{C}\bar{\boldsymbol{\varepsilon}}\colon\boldsymbol{\varepsilon}\left(\delta\bar{\vec{u}}\right)\,\mathrm{d}V = \int_\Omega \mathbf{C}\bar{\boldsymbol{\varepsilon}}^p\colon\boldsymbol{\varepsilon}\left(\delta\bar{\vec{u}}\right)\,\mathrm{d}V, \tag{4.43}$$

allowing the construction of an operator $\mathbb{E}$ in classical FE space such that

$$\bar{\boldsymbol{\varepsilon}} = \mathbb{E}\bar{\boldsymbol{\varepsilon}}^p. \tag{4.44}$$

Finally, $\Delta\boldsymbol{\sigma}'_{i+1}$ and $\Delta\dot{\boldsymbol{\varepsilon}}^p_{i+1}$, in a separated variable form can be represented as

$$\Delta\dot{\boldsymbol{\varepsilon}}^p_{i+1} = \dot{\boldsymbol{\lambda}}(t)\,\bar{\boldsymbol{\varepsilon}}^p(\vec{x})\,, \tag{4.45a}$$

$$\Delta\boldsymbol{\sigma}'_{i+1} = \boldsymbol{\lambda}(t)\,\mathbb{C}\bar{\boldsymbol{\varepsilon}}^p(\vec{x})\,. \tag{4.45b}$$

The construction of the FE operators $\mathbb{E}$ and $\mathbb{C}$ is explained in Appendix A.

The quantities $\Delta\tilde{\boldsymbol{\sigma}}_{i+1}$ and $\Delta\tilde{\boldsymbol{\varepsilon}}_{i+1}$ depending on damage are solved from the weak form eq. (4.34) together with eq. (4.35) providing

$$\int_{[0,T]\times\Omega} \mathbf{C}\left(\Delta\tilde{\boldsymbol{\varepsilon}}_{i+1} - \Delta\boldsymbol{\varepsilon}^R_{i+1}\right)\colon\tilde{\boldsymbol{\varepsilon}}(\delta\vec{u})\,\mathrm{d}V\,\mathrm{d}t = 0, \tag{4.46}$$

where $\Delta\varepsilon^R_{i+1}$ is a quantity already known from the local stage and $\delta\vec{u}$ is kinematically admissible to zero. $\Delta\tilde{\boldsymbol{\varepsilon}}_{i+1}$ can thereby be calculated using the same FE operator $\mathbb{E}$ as

$$\Delta\tilde{\boldsymbol{\varepsilon}}_{i+1} = \mathbb{E}\Delta\boldsymbol{\varepsilon}^R, \tag{4.47}$$

and $\Delta\tilde{\boldsymbol{\sigma}}_{i+1}$ is calculated as

$$\Delta\tilde{\boldsymbol{\sigma}}_{i+1} = \mathbb{C}\Delta\boldsymbol{\varepsilon}^R. \tag{4.48}$$

Lastly the corrections to the stress and elastic strain are given as

$$\Delta\boldsymbol{\sigma}_{i+1} = \Delta\boldsymbol{\sigma}'_{i+1} + \Delta\tilde{\boldsymbol{\sigma}}_{i+1}, \tag{4.49a}$$

$$\Delta\boldsymbol{\varepsilon}^e_{i+1} = \Delta\boldsymbol{\varepsilon}'_{i+1} + \Delta\tilde{\boldsymbol{\varepsilon}}_{i+1} - \Delta\boldsymbol{\varepsilon}^p_{i+1}. \tag{4.49b}$$

4.6.2 Hybrid method to construct the PGD reduced-order basis

As mentioned before, the calculation strategy of the separated forms involves both POD and PGD phases. The POD phase involving the update of the temporal functions by reusing the spatial basis, is relatively less expensive and performed at every global stage of the LATIN method. If the ROM hence obtained is not adequate enough, the ROB is enriched through the PGD phase by the addition of a new space-time mode. A hybrid strategy involving a Galerkin-based formulation to calculate the spatial problem and a formulation based on minimum residual to approximate the temporal problem is used.

4.6.2.1 Update of the reduced order basis

The idea of update stage at LATIN iteration $i+1$ is to reuse the m space functions that have already been generated from LATIN iteration i and update the corresponding time functions. The quantities of interest depending on plastic deformation are written as

$$\begin{aligned}
\Delta\dot{\boldsymbol{\varepsilon}}^p_{i+1} &= \sum_{j=1}^{m} \Delta\dot{\lambda}_j\,(t)\,\bar{\boldsymbol{\varepsilon}}^p_j\,(\vec{x})\,, \\
\Delta\boldsymbol{\sigma}'_{i+1} &= \sum_{j=1}^{m} \Delta\lambda_j\,(t)\,\mathbb{C}\bar{\boldsymbol{\varepsilon}}^p_j\,(\vec{x})\,,
\end{aligned} \tag{4.50}$$

where $\{\Delta\lambda_j\}_{j=1}^m$ represent the updates of the temporal functions. With the information of eq. (4.50), the constitutive relation error associated with eq. (4.38) is formulated as

$$\begin{aligned}
e^2_{CE} &= \left\|\Delta\dot{\boldsymbol{\varepsilon}}^p_{i+1} - \mathbf{H}_\sigma\Delta\boldsymbol{\sigma}'_{i+1} + \bar{\boldsymbol{\Delta}}^{\varepsilon}_{i+1}\right\|^2_{\mathbf{H}_\sigma^{-1}}, \\
&= \left\|\sum_{j=1}^{m}\Delta\dot{\lambda}_j\bar{\boldsymbol{\varepsilon}}^p_j - \mathbf{H}_\sigma\sum_{j=1}^{m}\Delta\lambda_j\mathbb{C}\bar{\boldsymbol{\varepsilon}}^p_j + \bar{\boldsymbol{\Delta}}^{\varepsilon}_{i+1}\right\|_{\mathbf{H}_\sigma^{-1}}.
\end{aligned} \tag{4.51}$$

Here $\{\Delta\lambda_j\}_{j=1}^m$ are the only unknowns and are approximated such that the constitutive relation is minimised, i.e.

$$\{\Delta\lambda_j\}_{j=1}^m = \underset{\{\Delta\lambda_i\}_{j=1}^m}{\arg\min}\left\|\sum_{j=1}^{m}\Delta\dot{\lambda}_j\bar{\boldsymbol{\varepsilon}}^p_j - \mathbf{H}_\sigma\sum_{j=1}^{m}\Delta\lambda_j\mathbb{C}\bar{\boldsymbol{\varepsilon}}^p_j + \bar{\boldsymbol{\Delta}}^{\varepsilon}_{i+1}\right\|_{\mathbf{H}_\sigma^{-1}}. \tag{4.52}$$

This results in multi-variable coupled differential equations. Zero-order discontinuous Galerkin method is used to solve this type of equations, as a better approximation compared to shooting method was obtained in Passieux (2008), Relun (2011). The method of solving the minimisation problem is detailed in

Appendix B. Thereafter, knowing $\{\Delta\lambda_j\}_{j=1}^{m}$, the total stress and elastic strain are approximated using eq. (4.49). This gives a ROM based on the same ROB. If this approximation is adequate, the particular global step is terminated and the algorithm moves to the next local step. The criterion to enrich the ROB is estimated by a saturation parameter ζ of the error indicator ξ (see section 4.7) which is similar to the criterion proposed in Heyberger et al. (2012),

$$\zeta = \frac{\xi_i - \xi_{i+1}}{\xi_i + \xi_{i+1}}. \tag{4.53}$$

If ζ is less than a tolerance level ζ^{tol} at a particular LATIN iteration, a space-time PGD pair needs to be added to enrich the reduced-order basis. On the contrary, if ζ is high enough, the ROM is considered to be effective.

4.6.2.2 Enrichment of the reduced-order basis

The enrichment of the ROB is performed using a hybrid strategy. The temporal functions are calculated using a minimisation of residual (as mentioned in section 4.6.2.1), and the spatial functions are computed using a Galerkin technique.

The search direction equation during the stage of enrichment becomes

$$\Delta\dot{\boldsymbol{\varepsilon}}^{p}_{i+1} - \mathbf{H}_{\sigma}\Delta\boldsymbol{\sigma}'_{i+1} + \bar{\boldsymbol{\Delta}}^{\varepsilon}_{i+1} = 0, \tag{4.54}$$

with

$$\bar{\boldsymbol{\Delta}}^{\varepsilon}_{i+1} = \mathbf{H}_{\sigma}\left(\hat{\boldsymbol{\sigma}}_{i+1/2} - \boldsymbol{\sigma}^{\mathsf{up}}_{i+1}\right) - \left(\hat{\dot{\boldsymbol{\varepsilon}}}^{p}_{i+1/2} - \dot{\boldsymbol{\varepsilon}}^{p\,,\,\mathsf{up}}_{i+1}\right), \tag{4.55}$$

where $\dot{\boldsymbol{\varepsilon}}^{p\,,\,\mathsf{up}}_{i+1}$ and $\boldsymbol{\sigma}^{\mathsf{up}}_{i+1}$ are the quantities obtained from the update stage. The quantities of interest thereafter are written in a separable form as

$$\Delta\dot{\boldsymbol{\varepsilon}}^{p}_{i+1} = \dot{\lambda}_{m+1}(t)\,\bar{\boldsymbol{\varepsilon}}^{p}_{m+1}(\vec{x}), \tag{4.56a}$$

$$\Delta\boldsymbol{\sigma}'_{i+1} = \lambda_{m+1}(t)\,\mathbb{C}\bar{\boldsymbol{\varepsilon}}^{p}_{m+1}(\vec{x}). \tag{4.56b}$$

This directly gives the constitutive relation error to be

$$e^2_{CE} = \left\|\dot{\lambda}_{m+1}\bar{\boldsymbol{\varepsilon}}^{p}_{m+1} - \mathbf{H}_{\sigma}\lambda_{m+1}\mathbb{C}\bar{\boldsymbol{\varepsilon}}^{p}_{m+1} + \bar{\boldsymbol{\Delta}}^{\varepsilon}_{i+1}\right\|_{\mathbf{H}_{\sigma}^{-1}}. \tag{4.57}$$

If the space function $\bar{\boldsymbol{\varepsilon}}^{p}_{m+1}$ is known, eq. (4.57) is minimised with respect to the time function to obtain λ_{m+1}, i.e.

$$\lambda_{m+1} = \underset{\lambda_{m+1}}{\arg\min}\left\|\dot{\lambda}_{m+1}\bar{\boldsymbol{\varepsilon}}^{p}_{m+1} - \mathbf{H}_{\sigma}\lambda_{m+1}\mathbb{C}\bar{\boldsymbol{\varepsilon}}^{p}_{m+1} + \bar{\boldsymbol{\Delta}}^{\varepsilon}_{i+1}\right\|_{\mathbf{H}_{\sigma}^{-1}}. \tag{4.58}$$

This equation is solved using similar strategy as section 4.6.2.1 and is detailed in Appendix B.

To calculate the spatial function, a Galerkin-based strategy is used. Equation (4.33) can be reformulated in a rate form as,

$$\Delta\dot{\boldsymbol{\varepsilon}}'_{i+1} = \Delta\dot{\boldsymbol{\varepsilon}}^{p}_{i+1} + \mathbf{C}^{-1}\Delta\dot{\boldsymbol{\sigma}}'_{i+1}, \tag{4.59}$$

such that $\Delta\dot{\boldsymbol{\varepsilon}}^{p}_{i+1}$ is obtained from eq. (4.54) and $\Delta\boldsymbol{\sigma}'_{i+1}$ from eq. (4.56b). For convenience, all the indices indicating the number of modes and number of LATIN iteration are dropped for convenience. The kinematic admissibility condition is written $\forall\delta\boldsymbol{\sigma}$ which is statically admissible to zero, as

$$\int_{[0,T]\times\Omega} \Delta\dot{\boldsymbol{\varepsilon}}' : \delta\boldsymbol{\sigma}\;\mathrm{d}V\;\mathrm{d}t = 0. \tag{4.60}$$

Considering $\delta\boldsymbol{\sigma} = \boldsymbol{\lambda}\delta\bar{\boldsymbol{\sigma}}$, eq. (4.60) can be written as

$$\int_{\Omega} \left\langle \Delta\dot{\boldsymbol{\varepsilon}}'\boldsymbol{\lambda} \right\rangle : \delta\bar{\boldsymbol{\sigma}} \, \mathrm{d}V = 0, \tag{4.61}$$

$\forall\, \delta\bar{\boldsymbol{\sigma}}$ which is statically admissible to zero, where $\langle\square\rangle = \int_{[0,T]} \square \, \mathrm{d}t$ and $\boldsymbol{\lambda}$ being the known function of time. Using eqs. (4.54) and (4.59), eq. (4.61) can be written as

$$\int_{\Omega} \left[\left\langle \mathbf{H}_{\sigma}\boldsymbol{\lambda}^2 \right\rangle \bar{\boldsymbol{\sigma}} + \left\langle \dot{\boldsymbol{\lambda}}\boldsymbol{\lambda} \right\rangle \mathbf{C}^{-1}\bar{\boldsymbol{\sigma}} - \left\langle \bar{\boldsymbol{\Delta}}^{\varepsilon}\boldsymbol{\lambda} \right\rangle \right] : \delta\bar{\boldsymbol{\sigma}} \, \mathrm{d}V = 0, \tag{4.62}$$

A pseudo-strain $\bar{\bar{\boldsymbol{\varepsilon}}}$ is defined thereafter such that

$$\bar{\bar{\boldsymbol{\varepsilon}}} = \left\langle \Delta\dot{\boldsymbol{\varepsilon}}'\boldsymbol{\lambda} \right\rangle = \mathbf{W}^{-1}\bar{\boldsymbol{\sigma}} - \bar{\boldsymbol{\delta}}, \tag{4.63}$$

with $\mathbf{W}^{-1} = \left\langle \mathbf{H}_{\sigma}\boldsymbol{\lambda}^2 \right\rangle + \left\langle \dot{\boldsymbol{\lambda}}\boldsymbol{\lambda} \right\rangle \mathbf{C}^{-1}$ and $\bar{\boldsymbol{\delta}} = \left\langle \bar{\boldsymbol{\Delta}}^{\varepsilon}\boldsymbol{\lambda} \right\rangle$. Using the introduced definition of the pseudo-strain, eq. (4.62) can be rewritten as

$$\int_{\Omega} \bar{\bar{\boldsymbol{\varepsilon}}} : \delta\bar{\boldsymbol{\sigma}} \, \mathrm{d}V = 0. \tag{4.64}$$

Considering now the static admissibility condition, i.e

$$\int_{\Omega} \bar{\boldsymbol{\sigma}} : \boldsymbol{\varepsilon}\left(\delta\bar{\vec{u}}\right) \, \mathrm{d}V = 0, \tag{4.65}$$

$\forall\delta\bar{\vec{u}}$ that is kinematically admissible to zero and $\bar{\boldsymbol{\sigma}}$ that is statically admissible to zero. This static admissibility condition is re-written with respect to the pseudo-strain, i.e. using eq. (4.59) and by introducing a pseudo-displacement field $\bar{\bar{\vec{u}}}$ which is kinematically admissible to zero, such that $\boldsymbol{\varepsilon}\left(\bar{\bar{\vec{u}}}\right) = \bar{\bar{\boldsymbol{\varepsilon}}}$,

$$\int_{\Omega} \mathbf{W}\boldsymbol{\varepsilon}\left(\bar{\bar{\vec{u}}}\right) : \boldsymbol{\varepsilon}\left(\delta\bar{\bar{\vec{u}}}\right) \, \mathrm{d}V = -\int_{\Omega} \mathbf{W}\bar{\boldsymbol{\delta}} : \boldsymbol{\varepsilon}\left(\delta\bar{\bar{\vec{u}}}\right) \, \mathrm{d}V = 0, \tag{4.66}$$

$\forall\delta\bar{\bar{\vec{u}}}$ that is kinematically admissible to zero. This spatial problem is solved using classical FE scheme to obtain the pseudo-displacement $\bar{\bar{\vec{u}}}$. The associated pseudo-strain $\bar{\bar{\boldsymbol{\varepsilon}}}$ can then be easily calculated using the corresponding derivatives of the shape functions. Knowing $\bar{\bar{\boldsymbol{\varepsilon}}}$, eqs. (4.59) and (4.63) can be used to calculate the space function $\bar{\boldsymbol{\varepsilon}}^{p}_{m+1}$ as

$$\bar{\boldsymbol{\varepsilon}}^{p}_{m+1} = \frac{1}{\left\langle \boldsymbol{\lambda}\dot{\boldsymbol{\lambda}} \right\rangle} \left[\bar{\bar{\boldsymbol{\varepsilon}}} - \left\langle \boldsymbol{\lambda}\dot{\boldsymbol{\lambda}} \right\rangle \mathbf{C}^{-1}\mathbf{W}\left(\bar{\bar{\boldsymbol{\varepsilon}}} + \bar{\boldsymbol{\delta}}\right) \right]. \tag{4.67}$$

A fixed-point iteration is used to approximate $\bar{\boldsymbol{\varepsilon}}^{p}_{m+1}\left(\vec{x}\right)$ and $\boldsymbol{\lambda}_{m+1}\left(t\right)$ which is summarised in algorithm 1, with the number of sub-iterations s_{it} taken to be five.

The new space function $\bar{\boldsymbol{\varepsilon}}^{p}_{m+1}$ is orthonormalised with respect to the previously existing spatial basis $\left\{\bar{\boldsymbol{\varepsilon}}^{p}_{j}\right\}_{j=1}^{m}$ using Gram-Schmidt algorithm (see Ruhe, 1983). In the numerical process all the former time functions $\{\boldsymbol{\lambda}_j\}_{j=1}^{m}$ are updated along with the new time function $\boldsymbol{\lambda}_{m+1}$. If the modified time function $\boldsymbol{\lambda}_{m+1}$ has an insignificant norm the corresponding space-time pair may be rejected (see Appendix C).

Algorithm 1: Fixed-point iterative algorithm

Initialise

$$\lambda_{m+1}(t) = \frac{t}{T}.$$

for $j = \{1, \ldots, s_{it}\}$ **do**

Calculate $\bar{\varepsilon}^p_{m+1}$

Normalise $\bar{\varepsilon}^p_{m+1}$, i.e.

$$\bar{\varepsilon}^p_{m+1} = \frac{\bar{\varepsilon}^p_{m+1}}{\left\langle \bar{\varepsilon}^p_{m+1}, \bar{\varepsilon}^p_{m+1} \right\rangle^{1/2}}$$

with

$$\left\langle \bar{\varepsilon}^p_{m+1}, \bar{\varepsilon}^p_{m+1} \right\rangle = \int_\Omega \bar{\varepsilon}^p_{m+1} : \mathbf{C}\, \bar{\varepsilon}^p_{m+1}\, \mathrm{d}V$$

Calculate $\lambda_{m+1}(t)$

end

Result: $\lambda_{m+1}(t)$, $\bar{\varepsilon}^p_{m+1}$

4.7 Relaxation of the solution field and convergence criterion

To secure convergence of the LATIN-PGD algorithm, the global step needs to be relaxed. Represented by $\breve{\boldsymbol{s}}_{i+1}$, the solution set obtained at the end of the global step $i+1$, which was previously being denoted by $\boldsymbol{s}_{i+1}$, the new solution set $\boldsymbol{s}_{i+1}$ can be formulated as

$$\boldsymbol{s}_{i+1} = \varphi \breve{\boldsymbol{s}}_{i+1} + (1-\varphi)\, \boldsymbol{s}_i, \tag{4.68}$$

where φ is a relaxation parameter. The convergence of the iterative algorithm is determined by a relative LATIN indicator. This indicator is basically the distance between the local solution and the global solution, given by

$$\xi = \frac{\|\hat{\boldsymbol{s}}^p_{i+1/2} - \boldsymbol{s}^p_{i+1}\|}{\|\hat{\boldsymbol{s}}^p_{i+1/2}\| + \|\boldsymbol{s}^p_{i+1}\|}, \tag{4.69}$$

with

$$\begin{aligned} \|\boldsymbol{s}^p\|^2 = \int_{[0,T]\times\Omega} \Big(& \boldsymbol{\sigma} : \mathbf{H}_\sigma \boldsymbol{\sigma} + \boldsymbol{Z} : \mathbf{H}_Z \boldsymbol{Z} + \dot{\boldsymbol{\varepsilon}}^p : \mathbf{H}_\sigma^{-1} \dot{\boldsymbol{\varepsilon}}^p + \boldsymbol{\varepsilon}^e : \mathbf{C} \boldsymbol{\varepsilon}^e \\ & + \dot{\boldsymbol{X}} : \mathbf{H}_Z^{-1} \dot{\boldsymbol{X}} \Big)\, \mathrm{d}V\, \mathrm{d}t. \end{aligned} \tag{4.70}$$

It has to be noted that the relaxation parameter φ, the regularisation coefficient ϖ, and the error saturation tolerance ζ^{tol} mostly affect the rate of convergence and not the convergence itself.

4.8 Numerical examples

The innovative algorithm has been tested on academic examples in one-dimensional and two-dimensional cases. The relaxation parameter φ and regularisation coefficient ϖ are valued to be 0.8 and 0.15 respectively (from Relun et al., 2011).

4.8.1 Bar under traction

The one-dimensional test problem considered is a bar with length $L = 1000$ mm and area of cross section $A = 100$ mm^2 as depicted in fig. 4.1. The bar is constrained at $x = 0$ and a sinusoidal prescribed displacement loading of amplitude $1.2 \times 10^{-3}\, L$ is applied at $x = L$ with a time period $\Delta T = 10$ s for 20 cycles.

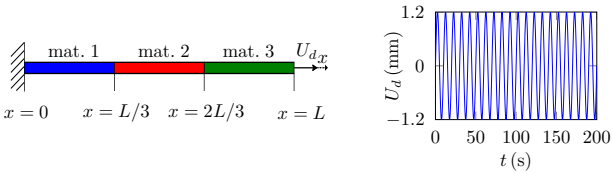

Figure 4.1: A bar in traction

The structure is composed of three different materials designated by mat. 1, mat. 2 and mat. 3, which have different yield stresses σ_y. The material considered is a Cr-Mo steel at $580°$C with the properties given in table 4.2 (from Lemaitre and Desmorat, 2005).

Table 4.2: Material properties for Cr-Mo steel at $580°$C

Material parameter	Value		
E	134000 MPa		
ν	0.3		
R_∞	30 MPa		
γ	2 MPa		
Q	5500 MPa		
a	250 MPa		
k_D	2.778 MPa$^{-n_d}$s^{-1}		
n_D	2		
K	1220 MPa s$^{1/n}$		
n	2.5		
k	K^{-n}		
h	0.2		
σ_y	mat. 1	mat. 2	mat. 3
	80 MPa	82.5 MPa	85 MPa

The structure is discretised in space using 90 linear bar elements such that each part has the same number of elements. A time step size of 0.1 s is chosen for temporal discretisation, which results in 100 time elements per cycle and in total 2000 time elements. In the computational model, the criterion ζ^{tol} to enrich the reduced-order basis is taken to be 0.01. The algorithm is stopped if the saturation parameter ζ is lower than 10^{-4}. For one-dimensional problems, the search direction operators defined in eq. (4.15) become

$$\mathbf{H}_\sigma = kn \left\langle f^p \right\rangle^{n-1} \frac{1}{(1-D)^2}, \tag{4.71a}$$

$$\mathbf{H}_\beta = kn \left\langle f^p \right\rangle^{n-1} \left(-\mathrm{sign}\left(\frac{\sigma}{1-D} - \beta \right) + \frac{a}{C}\beta \right)^2 + k \left\langle f^p \right\rangle^{n} \frac{a}{C}, \tag{4.71b}$$

$$\mathbf{H}_R = kn \left\langle f^p \right\rangle^{n-1} \gamma \left(1 - \frac{\bar{R}\gamma^{1/2}}{2R_\infty} \right)^2 + k \left\langle f^p \right\rangle^n \frac{\gamma}{2R_\infty}. \tag{4.71c}$$

The convergence of the algorithm is measured by the LATIN error indicator ξ depicted in fig. 4.2. Towards the end of the algorithm the LATIN indicator ξ shows a stagnating phenomenon, and neither updating the reduced basis or its enrichment will improve the solution significantly. The orthonormalisation procedure presented in Appendix C results in generation of a total of three PGD pairs due to rejection of insignificant modes. The quantity of interest $\dot{\varepsilon}^p$ obtained as the sum of products of space-time modes after convergence is shown in fig. 4.3.

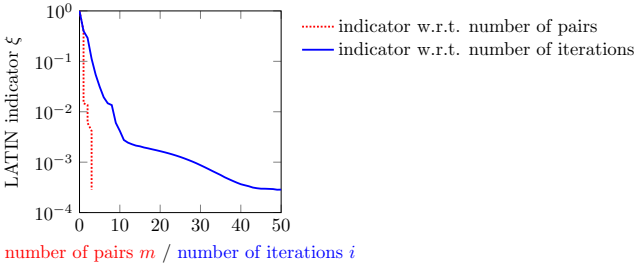

Figure 4.2: Evolution of the LATIN indicator with respect to the number of PGD pairs or LATIN iterations for the bar problem

The internal variables in rate form and the corresponding associated variables for the three sections of the bar are depicted in fig. 4.4. The isotropic hardening variables $\bar{R}$ and $\bar{r}$ are referred here as growth stress and growth strain respectively, as they represent the growth of the yield surface. Due to the prescribed boundary conditions, the stress is constant for a given time all over the bar, with decreasing amplitude with time, which basically represents material weakening due to damage. For mat. 1, the plastic strain rate and kinematic hardening variables in rate form show increasing amplitude with respect to time. The amplitudes however decrease for mat. 2 and mat. 3. For mat. 1 there is a monotonic increase in the amplitude of $\dot{\bar{r}}$, and for mat. 2 and mat. 3, the amplitude of $\dot{\bar{r}}$ decreases. The associated variable $\bar{R}$ increases for all the three materials.

The quantities of interest that directly indicate the influence of unilateral condition of micro-defect closure effects are depicted in fig. 4.5. The damage variable D remains practically constant during the compressive part of the loading and increases during the tensile part of the loading. The energy release rate Y also illustrates the difference in behaviour during compression and tension, i.e. very high in tension and extremely low during compression. The elastic strain ε^e also shows a higher value during tension than in compression. The values of D at the end of loading for mat. 1, mat. 2 and mat. 3 are 0.22, 0.18 and 0.15 respectively.

General practical engineering problems invariably portray high localisation for both plastic deformation and damage. The presence of stress raisers (e.g. notches, holes, defects and such others) in most engineering components, concentrates the effect of plasticity and damage to a very limited region, while the rest of the structure remains undamaged and elastic. Classical two-dimensional mechanical problems are considered in section 4.8.2 and section 4.8.3 to depict this phenomenon.

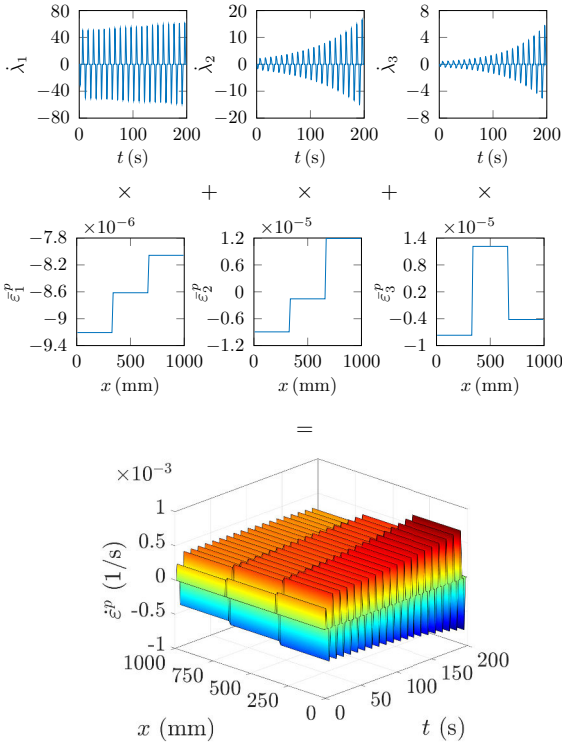

Figure 4.3: Space-time modes needed to approximate $\dot{\varepsilon}^p(x,t)$ in the bar under cyclic loading at convergence

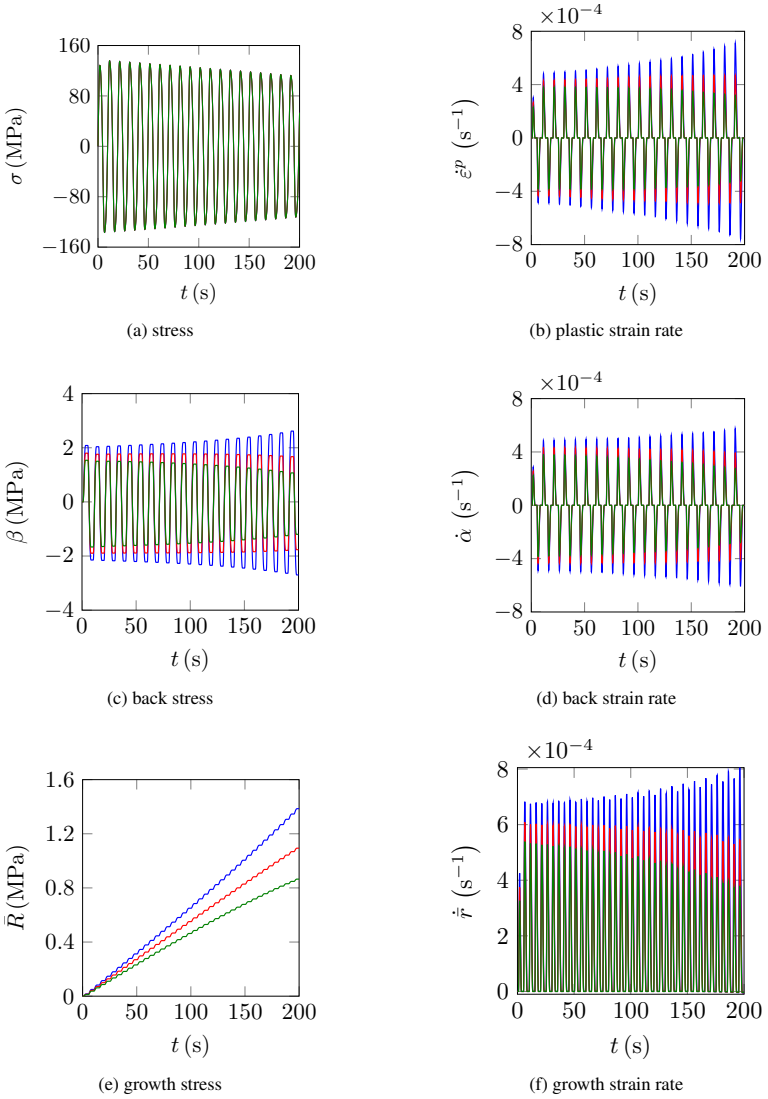

(a) stress

(b) plastic strain rate

(c) back stress

(d) back strain rate

(e) growth stress

(f) growth strain rate

Figure 4.4: Evolution of internal and associated variables in mat. 1 (–), mat. 2 (–) and mat. 3 (–) for the bar under cyclic loading

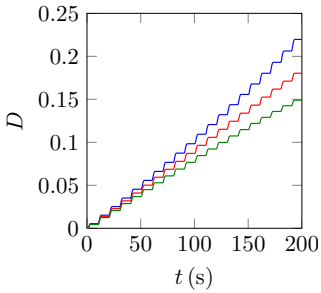

(a) damage

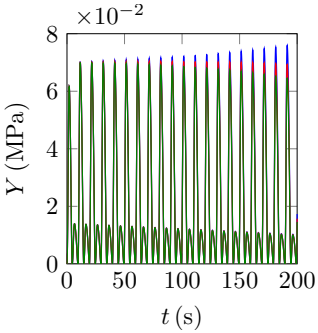

(b) strain energy release rate

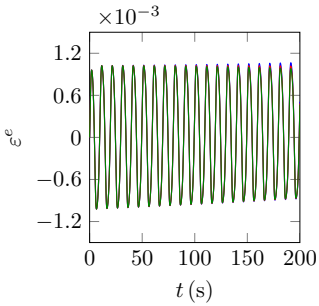

(c) elastic strain

Figure 4.5: Evolution of quantities describing loss of stiffness in mat. 1 (–), mat. 2 (–) and mat. 3 (–) for the bar under cyclic loading

4.8.2 "L" shaped structure

An "L" shaped structure subjected to a concentrated load represented in fig. 4.6 is considered as a two-dimensional test problem. The structural geometry is defined by length $L = 120$ mm, and width $W = 20$ mm. The structure is filleted at the inside corner with fillet radius $r = 5$ mm to avoid singularity. The thickness of the structure is taken to be 1 mm. A sinusoidal displacement $U_d(t)$ of amplitude 1.5 mm is prescribed with a time period $\Delta T = 10$ s, for 5 cycles.

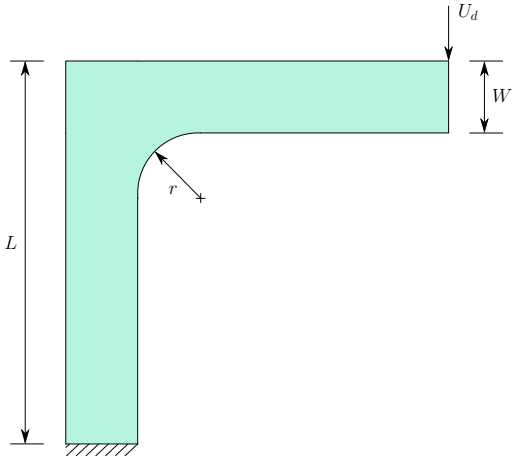

Figure 4.6: An "L" shaped structure subjected to a concentrated load

The material properties used are the same as given in table 4.1, with $\sigma_y = 85$ MPa. A total of 277 linear two-dimensional quadrilateral isoparametric plane stress elements with 4 Gauss points per element are used to discretise the structure, which generates 337 nodes. A time step size of 0.2 s is chosen for the temporal discretisation. The criterion to enrich the ROB ζ^{tol} is taken to be 10^{-2}. Compared to the one-dimensional problem of section 4.8.1, the calculation of the search direction operators for high dimensional cases is considerably expensive. These operators are thereby not calculated at every iteration, but are only updated if there is a saturation of the LATIN error indicator. It is quantitatively measured by the criterion ζ with the tolerance being 10^{-2}. The decrease in the LATIN indicator ξ is shown in fig. 4.7. After the first iteration, the indicator reads 5×10^{-2}. After 21 iterations, the LATIN indicator becomes 9×10^{-3} with 8 PGD modes being generated. The saturation of the indicator is at $\xi = 8 \times 10^{-4}$, with a total of 40 modes being generated. This saturation of LATIN indicator at a relatively high value, compared to fig. 4.2 is due to the fact that a coarse temporal mesh has been used. In case of a finer temporal mesh this LATIN indicator can be lowered even for two-dimensional problems, as shown in the next numerical example (section 4.8.3).

The distribution of the cumulative plastic strain at the end of loading is depicted in fig. 4.8. It is distributed on both sides of the vertical web, with the inner side being predominant and the maximum at the filleted corner of the structure, whereas most part of the structure shows no plastic deformation.

The residual von Mises stress is distributed in a similar manner as the accumulated plastic strain, as shown in fig. 4.9. It is concentrated at the filleted corner with lower valued distribution on both sides of the web.

The distribution of damage variable D, the main quantity of interest, at the end of the loading ($t = T$) is represented in fig. 4.10. The distribution is similar to the one of the accumulated plastic strain and residual von Mises stress, i.e. maximum at the filleted corner. The span of damage in the filleted corner, which is the region of interest, after certain load cycles is also represented in fig. 4.10. The damage

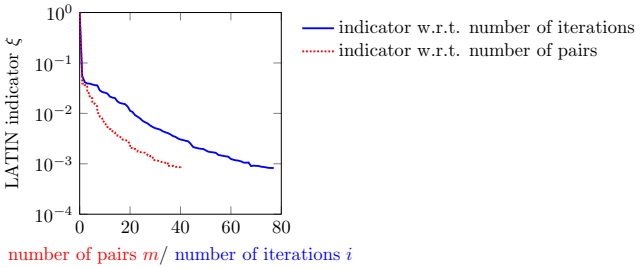

Figure 4.7: Evolution of the LATIN indicator with respect to the number of PGD pairs or LATIN iterations for the "L" shaped structure

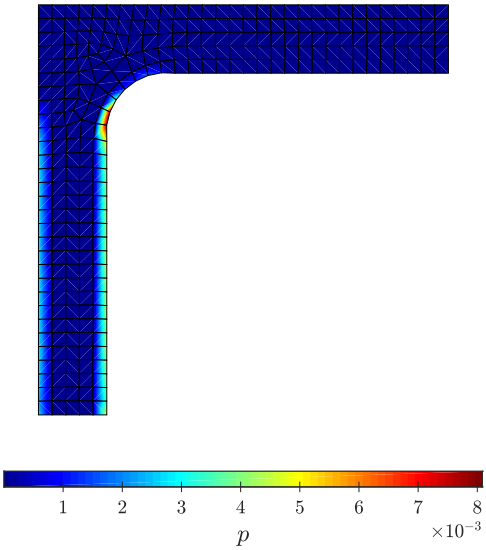

Figure 4.8: Distribution of accumulated plastic strain in the "L" shaped structure at $t = T$

evolution with respect to time for the weakest GP of this region of interest is shown in fig. 4.11 with the maximum value being 0.049 at the end of loading.

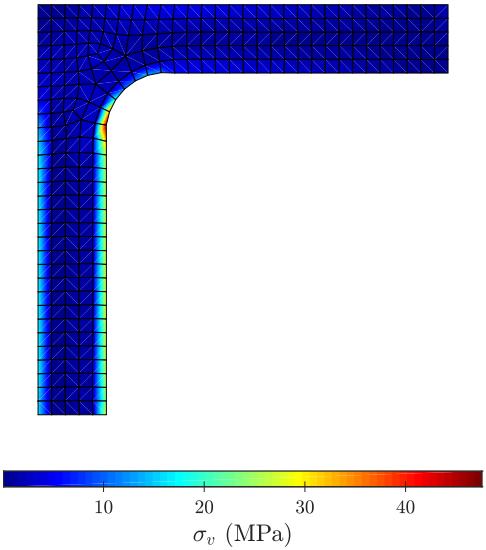

Figure 4.9: Distribution of residual von Mises stress in the “L” shaped structure at $t = T$

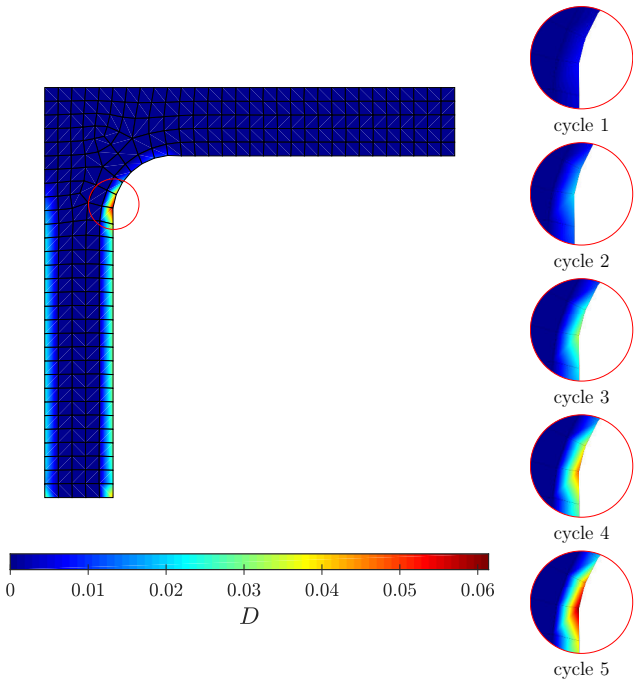

Figure 4.10: Damage distribution in the "L" shaped structure at $t = T$ and the spread of damage in the region of interest after certain load cycles

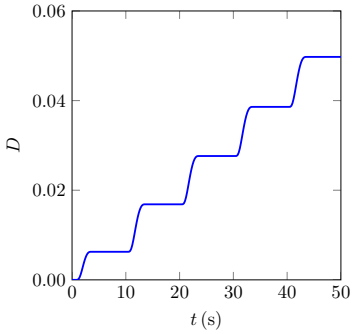

Figure 4.11: Damage evolution at the weakest GP of the "L" shaped structure

4.8.3 Plate with a hole

The goal of this example is to depict a comparative study for virgin and pre-damaged structures and also to present the influence of lower time step size on the LATIN error indicator ξ for two-dimensional structures. The test problem considered is a classic plate with a hole. The rectangular plate of length $L = 40$ mm, width $W = 60$ mm and thickness of 1 mm is considered, with a central circular hole of diameter $\phi = 20$ mm. Uniformly distributed sinusoidal displacements of amplitude 0.012 mm and time period $\Delta T = 10$ s are applied on both ends of the plate, as shown in fig. 4.12, for 10 cycles. The symmetry of the structure enables only a quarter of the plate to be considered for the analysis (see fig. 4.12).

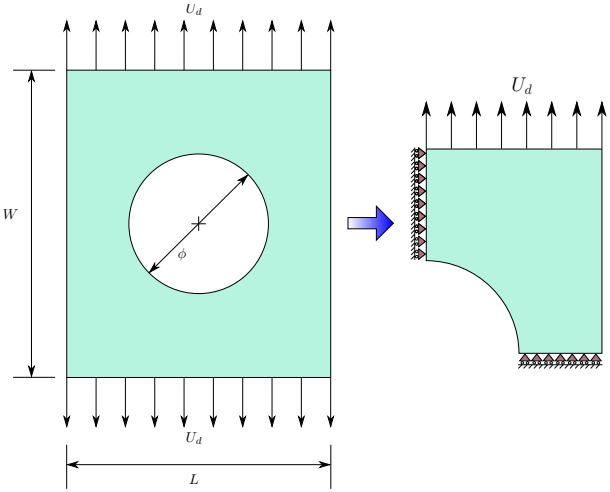

Figure 4.12: A plate with a hole subjected to distributed loads and the symmetric part considered for analysis

The material properties are the same as used in section 4.8.2. The structure is discretised using 129 linear two-dimensional quadrilateral isoparametric plane stress elements with 4 Gauss points per element, generating 154 nodes. A finer time step size of 0.1 s is chosen for the temporal discretisation.

The first numerical test is to solve the problem considering all the GPs to be virgin, which is followed by solving the problem considering the GPs which are indicated by $*$ in fig. 4.13 to be pre-damaged and the virgin GPs are marked in $\bullet$. The decrease in the LATIN indicator ξ for the virgin structure is shown in fig. 4.14. A total of 34 modes are generated to obtain $\xi = 9 \times 10^{-5}$ in 75 iterations. Expectedly, the indicator is much lower compared to fig. 4.7, because of finer temporal discretisation (see Ladevèze, 1999, for explanation). For the pre-damaged structure, 38 PGD modes are generated in 83 iterations to obtain $\xi = 9 \times 10^{-5}$ (see fig. 4.15).

The distribution of damage variable D along with the damage spread in the respective regions of interest, for both the cases, at the end of the loading ($t = T$) is represented in fig. 4.16. It is obvious from fig. 4.16, that there is a shift of the maximum damaged point in the pre-damaged case, compared to the virgin case. The weakest Gauss point for the virgin structure is GP 1 (see fig. 4.13) and GP 2 (see fig. 4.13) for the pre-damaged structure. The evolution of damage for both of these GPs is represented in fig. 4.17.

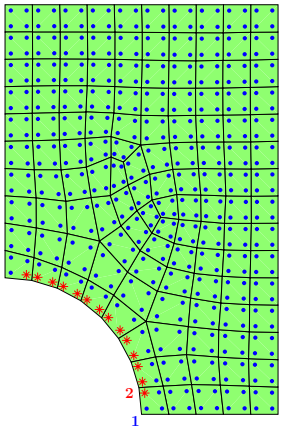

Figure 4.13: FE mesh depicting the virgin (•) and pre-damaged (∗) Gauss points

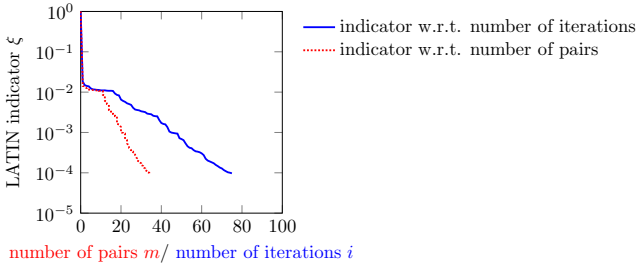

Figure 4.14: Evolution of the LATIN indicator with respect to the number of PGD pairs or LATIN iterations for the virgin structure

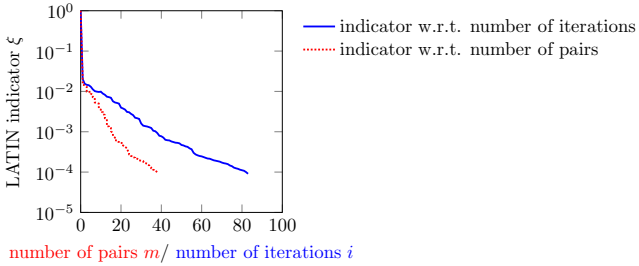

Figure 4.15: Evolution of the LATIN indicator with respect to the number of PGD pairs or LATIN iterations for the pre-damaged structure

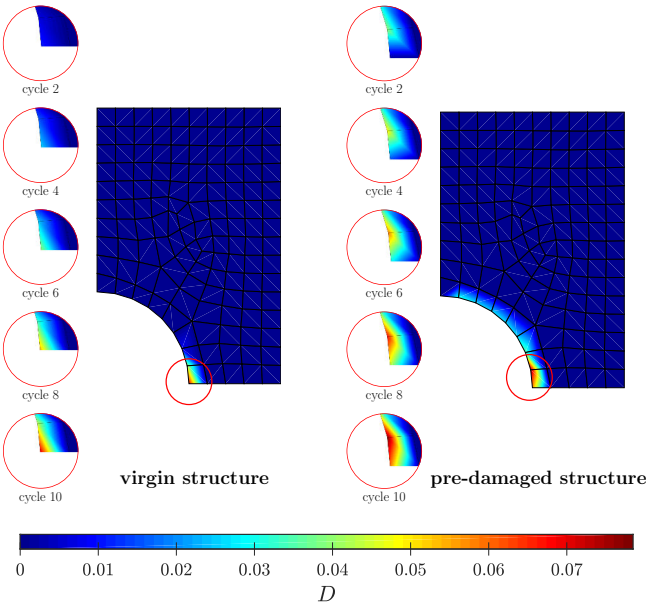

Figure 4.16: Comparison of damage distribution at $t = T$ and the spread of damage in the region of interest after certain load cycles

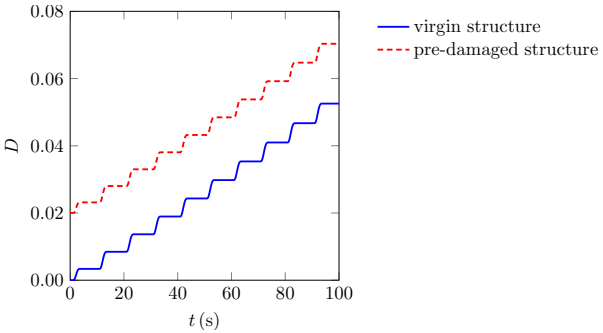

Figure 4.17: Damage evolution at the weakest GP of the plate with hole, i.e. GP 1 for the virgin structure, and GP 2 for the pre-damaged structure

4.9 Concluding remarks

This is a novel attempt to include unilateral condition of micro-defect closure effect in a LATIN-PGD framework. The algorithm is able to provide appreciable accuracy and robustness as illustrated in the academic examples. In case of high value of damage, on the other hand, this framework will perhaps be not as accurate, however as the focus is on metals, where the maximum damage is not high, this apparent problem is rendered insignificant. This chapter also depicts a hybrid PGD formulation, which according to the knowledge of the author is one of the first in a LATIN framework. However it still does not address the issue at hand which is to tackle large number of cycles. The usage of PGD-based model reduction approach presented here is not enough to reduce numerical cost when large number of cycles is simulated. Therefore a multi-temporal discretisation is needed to effectively simulate fatigue behaviour with less CPU cost which will be detailed in the next chapter.

Chapter 5

Multi-scale temporal discretisation approach

The strategy to compute damage as presented in chapter 4, when applied for cycle by cycle simulations can be extremely time consuming if the problem involves large number of cycles, e.g. 10^5 cycles will have 10^7 time points if 100 time points per cycle are considered and the total computation is unreasonably expensive. To circumvent this problem, a multi-temporal approach is used. The range of problems encompassed here are those where the applied forces or displacements are periodic with a constant time period ΔT, but with amplitudes that may vary with time (see Cognard and Ladevèze, 1993, Ladevèze, 1999). To reduce the cost of the mechanical problem, the temporal dependency of the different quantities on the whole time domain $[0, T]$, which may include several thousands of cycles, is described in parallel by two time scale discretisations:

– a coarse temporal discretisation $\tilde{\theta}$ defined on the complete temporal domain $[0, T]$ representing the beginning of every cycle,

– a fine temporal discretisation τ_i defined within cycle i.

Any instant of interest t can be discretised by the pair $\left(\tilde{\theta}_i, \tau_i\right)$ as

$$t = \tilde{\theta}_i + \tau_i, \text{with } i \in [0, N-1] \text{ and } \tau_i \in [0, \Delta T]\,,\ \forall t \in [0, T]\,, \tag{5.1}$$

where N is the number of cycles included in the temporal domain.

The two scales allow to represent in parallel, the slow evolution along the cycles using the coarse temporal discretisation and the rapid evolution within a specific cycle by the fine temporal discretisation. This type of description allows the definition of "nodal cycles" where the quantities of interest are calculated in the fine temporal scale. Two successive "nodal cycles" bound what is called a "time element", where the evolution of the quantities of interest is considered to be slow allowing a finite element like interpolation on the coarse scale of the temporal quantities. The chapter starts with the description of the finite element like interpolation scheme in time. Thereafter, the calculation of a "nodal cycle" is detailed and is followed by various academic test cases, including numerical verification and comparison with mono-scale LATIN-PGD method.

5.1 Finite element like time interpolation scheme

Using the two-time scale description, the constitutive relation and the admissibility condition are solved using LATIN-PGD technique (as described in chapter 4) only on the "nodal cycles". The time element $\tilde{m}+1$ is bounded by two "nodal cycles" defined by their initial times $\Theta_{\tilde{m}}$ and $\Theta_{\tilde{m}+1}$ respectively. For the sake of clarity a change of variables is introduced for each "time element" containing $\tilde{p}$ cycles through $\theta_k, \forall k \in [0, \tilde{p}-1]$ which represents the coarse discretisation for the given "time element" locally. This representation provides the time t to be defined as

$$t = \theta_k + \tau_k, \text{ with } k \in [0, \tilde{p}-1] \text{ and } \tau_k \in [0, \Delta T]\,,\ \forall t \in [\Theta_{\tilde{m}}, \Theta_{\tilde{m}+1} + \Delta T]\,. \tag{5.2}$$

Once the successive "nodal cycles" $\tilde{m}$ and $\tilde{m}+1$ have been computed, a one-dimensional interpolation is used to estimate the quantities of interest on $[\Theta_{\tilde{m}}, \Theta_{\tilde{m}+1}]$ based on temporal shape functions (see Cognard and Ladevèze, 1993). Linear one-dimensional temporal shape functions $\nu_{\tilde{m}}$ and $\nu_{\tilde{m}+1}$ for the time element $[\Theta_{\tilde{m}}, \Theta_{\tilde{m}+1}]$ are defined as

$$\nu_{\tilde{m}}(\theta_k) = \frac{\Theta_{\tilde{m}+1} - \theta_k}{\Theta_{\tilde{m}+1} - \Theta_{\tilde{m}}},\ \nu_{\tilde{m}+1}(\theta_k) = \frac{\theta_k - \Theta_{\tilde{m}}}{\Theta_{\tilde{m}+1} - \Theta_{\tilde{m}}},\ \forall t \in [\Theta_{\tilde{m}}, \Theta_{\tilde{m}+1} + \Delta T]\,. \tag{5.3}$$

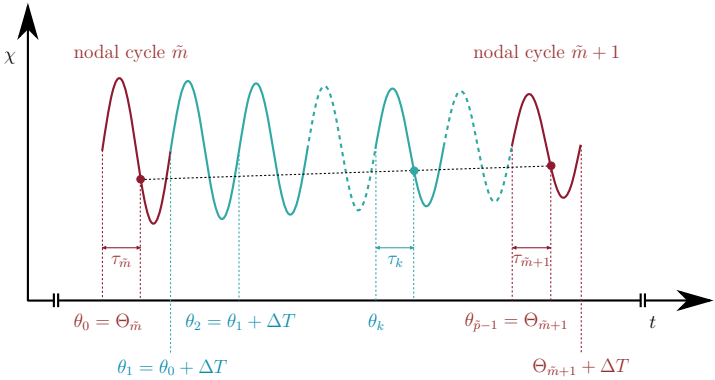

Figure 5.1: Discretisation of the time domain using two time scale discretisations: θ along the cycles and τ within a cycle, $\tilde{p}$ being the number of cycles for the time element $[\Theta_{\tilde{m}}, \Theta_{\tilde{m}+1}]$

Then, for any temporal quantity of interest χ, its approximation within the time element $[\Theta_{\tilde{m}}, \Theta_{\tilde{m}+1}]$ is written as a polynomial expansion based on pre-defined temporal shape functions $\{\nu_{\tilde{m}}, \nu_{\tilde{m}+1}\}$ and on the knowledge of the quantity for the two "nodal cycles" denoted as $\chi(\Theta_{\tilde{m}} + \tau_{\tilde{m}})$ and $\chi(\Theta_{\tilde{m}+1} + \tau_{\tilde{m}+1})$. Similarly to conventional finite elements, the interpolation reads

$$\begin{aligned}\chi(t = \theta_k + \tau_k) = \nu_{\tilde{m}}(\theta_k)\,\chi(\Theta_{\tilde{m}} + \tau_{\tilde{m}}) + \nu_{\tilde{m}+1}(\theta_k)\,\chi(\Theta_{\tilde{m}+1} + \tau_{\tilde{m}+1})\,,\\ \forall t \in [\Theta_{\tilde{m}}, \Theta_{\tilde{m}+1} + \Delta T]\,,\end{aligned} \tag{5.4}$$

with $\tau_{\tilde{m}} = \tau_{\tilde{m}+1} = \tau_k$ belonging to $[0, \Delta T]$ as the period is constant. The interpolation is more tedious than with conventional finite element as the nodes describe no more some single points but some sub-domains. It can be noted that the benefit of the fine time discretisation is transferred to the whole element by the interpolation process.

The finite element like description in time of the quantities of interest lies in a set of time elements which spans the time domain (see fig. 5.1). However, it can be noted that this scheme does not include a Galerkin form of the problem on the whole time domain, but only an *a posteriori* time interpolation scheme is considered.

The idea is first to calculate initial few cycles classically as given in chapter 4, which can be interpreted as a "training stage" as the ROB obtained will be re-used for the two-scale computation. In details, the first element is built from the "nodal cycle" 0, which is the last classically computed cycle defined over $[\Theta_0, \Theta_0 + \Delta T]$. Then, from "nodal cycle" 0, the goal is to calculate "nodal cycle" 1 defined over $[\Theta_1, \Theta_1 + \Delta T]$, and successively from knowing "nodal cycle" 1, computing "nodal cycle" 2 and so on (see fig. 5.2). The computation is pursued for the different "nodal cycles" in succession until the ultimate "nodal cycle" concluding the time domain of interest is achieved, or until the critical damage has been reached. The computation of each "nodal cycle" involves solution of the global admissibility and the local equations using the LATIN-PGD algorithm only in the corresponding temporal domain.

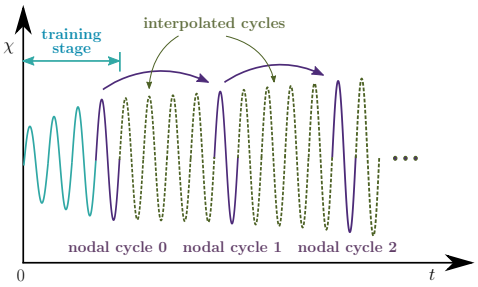

Figure 5.2: Pictorial representation of the two-time scale scheme

As far the material model is considered, the same model as given in table 4.1 is chosen but now only with kinematic hardening. The constitutive relations are rewritten in table 5.1, the global admissibilities are the same as given in table 4.1.

Table 5.1: Constitutive relations for only kinematic hardening

viscoplastic yield function	$f^p = \sqrt{\frac{3}{2}\left[\boldsymbol{\varrho} : \boldsymbol{\varrho}\right]} + \frac{a}{2}\left[\boldsymbol{\beta} : \mathbf{Q}^{-1}\boldsymbol{\beta}\right] - \sigma_y$
damage function	$f^d = Y - Y_{th}$
evolution equations	$\dot{\boldsymbol{\varepsilon}}^p = k\left\langle f^p\right\rangle_+^n \left[\frac{3}{2}\frac{\boldsymbol{\varrho}}{\sqrt{\frac{3}{2}\left[\boldsymbol{\varrho} : \boldsymbol{\varrho}\right]}}\right]\frac{1}{1-D}$
	$\dot{\boldsymbol{\alpha}} = -k\left\langle f^p\right\rangle_+^n \left[-\frac{3}{2}\frac{\boldsymbol{\varrho}}{\sqrt{\frac{3}{2}\left[\boldsymbol{\varrho} : \boldsymbol{\varrho}\right]}} + a\mathbf{Q}^{-1}\boldsymbol{\beta}\right]$
	$\dot{D} = k_d\left\langle f^d\right\rangle_+^{n_d}$
state laws	$\varepsilon_{ij}^e = \frac{1+\nu}{E}\left[\frac{\langle\sigma\rangle_{ij}^+}{1-D} + \frac{\langle\sigma\rangle_{ij}^-}{1-hD}\right] - \frac{\nu}{E}\left[\frac{\langle\sigma_{kk}\rangle}{1-D} + \frac{\langle-\sigma_{kk}\rangle}{1-hD}\right]\delta_{ij}$
	$\beta_{ij} = Q\alpha_{ij}$
	$Y = \frac{1+\nu}{2E}\left[\frac{\langle\sigma\rangle_{ij}^+\langle\sigma\rangle_{ij}^+}{(1-D)^2} + h\frac{\langle\sigma\rangle_{ij}^-\langle\sigma\rangle_{ij}^-}{(1-hD)^2}\right] - \frac{\nu}{2E}\left[\frac{\langle\sigma_{kk}\rangle^2}{(1-D)^2} + h\frac{\langle-\sigma_{kk}\rangle^2}{(1-hD)^2}\right]$

5.2 Computation of one "nodal cycle"

Each "nodal cycle" is computed using the LATIN-PGD framework as an independent problem. Therefore, a LATIN initialisation is first handled on this sub-domain. Then, the LATIN iterative scheme is processed, i.e. successive computations of a linear global stage and a non-linear local stage are done.

5.2.1 Initialisation

Contrary to classical LATIN strategy in which the initialisation originates from an elastic computation, using the two-time scale approach, the initialisation for each "nodal cycle" benefits from the knowledge of the previous "nodal cycle".

Some quantities of interest, such as the stress, the elastic strain, the internal variables for kinematic hardening, and the time functions representing the plastic strain $\{\lambda_j\}_{j=1}^{\mu}$ exhibit cyclic behaviour. Therefore, their initialisation for "nodal cycle" $\tilde{m}+1$ is based on the duplication of their estimation at "nodal cycle" $\tilde{m}$. Even if the global tendency of these variables is cyclic, due to the influence of increasing damage, they are not perfectly periodic. Thereby, as it is necessary to avoid any non-physical discontinuity at the transition between successive cycles, the initialisation for any cyclic quantity $\vartheta\left(\Theta_{\tilde{m}+1}+\tau_{\tilde{m}+1}\right)$ defined $\forall\tau_{\tilde{m}+1}\in[0,\Delta T]$ and for a particular $\Theta_{\tilde{m}+1}$ is based on a transformation of the quantity of interest $\vartheta\left(\Theta_{\tilde{m}}+\tau_{\tilde{m}}\right)$ defined $\forall\tau_{\tilde{m}}\in[0,\Delta T]$ and at $\Theta_{\tilde{m}}$, such that the continuity is preserved. A linear transformation between $\vartheta\left(\Theta_{\tilde{m}}+\tau_{\tilde{m}}\right)$ and $\tilde{\vartheta}\left(\Theta_{\tilde{m}}+\tau_{\tilde{m}}\right)$ is considered as

$$\tilde{\vartheta}\left(\Theta_{\tilde{m}}+\tau_{\tilde{m}}\right)=\vartheta\left(\Theta_{\tilde{m}}+\tau_{\tilde{m}}\right)+a_{\vartheta}\cdot\left(\Theta_{\tilde{m}}+\tau_{\tilde{m}}\right)+b_{\vartheta}, \tag{5.5}$$

where a_{ϑ} and b_{ϑ} are some parameters defined for every quantity of interest such that the periodicity of the transformed quantity of interest is guaranteed, i.e.

$$\tilde{\vartheta}\left(\Theta_{\tilde{m}}\right)=\tilde{\vartheta}\left(\Theta_{\tilde{m}}+\Delta T\right)=\vartheta\left(\Theta_{\tilde{m}}+\Delta T\right). \tag{5.6}$$

The initialisation $\vartheta^0\left(\tau_{\tilde{m}+1}\right)$ for the "nodal cycle" $\tilde{m}+1$ is thus based on the transformed quantity computed for the "nodal cycle" $\tilde{m}$ as

$$\begin{aligned}\vartheta^0\left(\Theta_{\tilde{m}+1}+\tau_{\tilde{m}+1}\right)=\tilde{\vartheta}\left(\Theta_{\tilde{m}}+\tau_{\tilde{m}}\right)=\vartheta\left(\Theta_{\tilde{m}}+\tau_{\tilde{m}}\right)+\frac{\vartheta\left(\Theta_{\tilde{m}}\right)-\vartheta\left(\Theta_{\tilde{m}}+\Delta T\right)}{\Delta T}\cdot\left(\tau_{\tilde{m}}\right)\\+\vartheta\left(\Theta_{\tilde{m}}+\Delta T\right)-\vartheta\left(\Theta_{\tilde{m}}\right).\end{aligned} \tag{5.7}$$

On another hand, the damage variable which is non-cyclic but a non-decreasing function of time, is initialised as constant over the whole "nodal cycle" $\tilde{m}+1$, with the magnitude being the one obtained at $\Theta_{\tilde{m}}+\Delta T$. The initialisation of the strain energy release rate Y is calculated from the damage and the stress tensor.

Thereafter, the quantities of interest are estimated iteratively using the two-step LATIN algorithm over "nodal cycle" $\tilde{m}+1$.

5.2.2 Local stage

The main difficulty in the local stage is the evaluation of damage at every Gauss point which needs a time integration scheme. To proceed the integration of the damage evolution equation over "nodal cycle" $\tilde{m}+1$, the value of the damage at the beginning of this "nodal cycle", i.e. at $\Theta_{\tilde{m}+1}$ is required.

Therefore, it is required to calculate $\chi\left(\Theta_{\tilde{m}+1}\right)$ from $\chi\left(\Theta_{\tilde{m}}\right)$. Assume a temporal evolution of any quantity of interest χ defined by a general first order ODE

$$\frac{\mathrm{d}\chi}{\mathrm{d}t}+\kappa\chi=\upsilon, \tag{5.8}$$

over a time domain with κ and υ being some time-dependent known parameters. For application for damage, these parameters are material-dependent. From the knowledge of an initial value of the quantity of interest $\chi(t_k)$, the solution of the ODE at a further time t_l can be determined as (see Ladevèze, 1999)

$$\chi(t_l) = \check{\chi}(t_l, t_k) + \Re(t_l, t_k)\,\chi(t_k), \tag{5.9}$$

with $\check{\chi}(t_k, t_l)$ being the solution of the ODE at time t_l considering zero initial condition at time t_k, and $\Re$ the "resolvent" operator defined as

$$\Re(t_l, t_k) = \exp\left(\int_{t_k}^{t_l} -\kappa(\tau)\, d\tau\right). \tag{5.10}$$

To compute the solution with zero initial condition and the resolvent operator with the minimum numerical cost, the proposed strategy is to compute these quantities only at the "nodal cycle" $\tilde{m}+1$, and then to propagate the information using a discretisation based on the instants θ_k representing the beginning of the loading cycles within the time element $[\Theta_{\tilde{m}}, \Theta_{\tilde{m}+1}]$. Considering a time element comprising $\tilde{p}$ cycles, the discretisation is defined such that $\theta_k = \Theta_{\tilde{m}} + k\Delta T$, where k is a natural number comprised in the interval $[0, \tilde{p}-2]$. Therefore, it is established that $\theta_0 = \Theta_{\tilde{m}}$ and $\theta_{\tilde{p}-1} = \Theta_{\tilde{m}+1}$.

The linear interpolation introduced in section 5.1 allows to obtain $\check{\chi}(\theta_{k+1}, \theta_k)$ and $\Re(\theta_{k+1}, \theta_k)$ from the knowledge of the two "nodal cycles" $\tilde{m}$ and $\tilde{m}+1$ delimiting the time element as

$$\check{\chi}(\theta_{k+1}, \theta_k) = \nu_{\tilde{m}}(\theta_k)\,\check{\chi}(\Theta_{\tilde{m}} + \Delta T, \Theta_{\tilde{m}}) + \nu_{\tilde{m}+1}(\theta_k)\,\check{\chi}(\Theta_{\tilde{m}+1} + \Delta T, \Theta_{\tilde{m}+1}), \tag{5.11a}$$

$$\Re(\theta_{k+1}, \theta_k) = \nu_{\tilde{m}}(\theta_k)\,\Re(\Theta_{\tilde{m}} + \Delta T, \Theta_{\tilde{m}}) + \nu_{\tilde{m}+1}(\theta_k)\,\Re(\Theta_{\tilde{m}+1} + \Delta T, \Theta_{\tilde{m}+1}). \tag{5.11b}$$

These interpolated values can be used for approximating the solution of the ODE (eq. (5.8)) as

$$\begin{aligned}\chi(\theta_{k+1}) = {} & \nu_{\tilde{m}}(\theta_k)\left[\check{\chi}(\Theta_{\tilde{m}} + \Delta T, \Theta_{\tilde{m}}) + \Re(\Theta_{\tilde{m}} + \Delta T, \Theta_{\tilde{m}})\,\chi(\theta_k)\right] \\ & + \nu_{\tilde{m}+1}(\theta_k)\left[\check{\chi}(\Theta_{\tilde{m}+1} + \Delta T, \Theta_{\tilde{m}+1}) + \Re(\Theta_{\tilde{m}+1} + \Delta T, \Theta_{\tilde{m}+1})\,\chi(\theta_k)\right].\end{aligned} \tag{5.12}$$

In the specific case of the evolution equation for damage, the "resolvent" operator $\Re$ is equal to one. Considering the solution $D(\tau_{\tilde{m}})$ is known $\forall \tau_{\tilde{m}} \in [0, \Delta T]$, for the first "nodal cycle", $\check{D}$ may be easily evaluated as $D(\Theta_0 + \Delta T) - D(\Theta_0)$. Otherwise it is computed only for the second "nodal cycle" $\check{D}(\Theta_{\tilde{m}} + \Delta T, \Theta_{\tilde{m}})$ by solving the evolution equation using zero initial condition. Thereby, eq. (5.12) is solved at each θ_{k+1} till $D(\theta_{\tilde{p}-1})$ is calculated. This process can also be represented as

$$D(\theta_{\tilde{p}-1}) = D(\theta_0) + \Delta D_{ini} + \sum_{k=1}^{\tilde{p}-2} \Delta D_k, \tag{5.13}$$

as illustrated in fig. 5.3

Using the interpolation scheme defined by eq. (5.12), the initial value of damage for the "nodal cycle" $\tilde{m}+1$ can be written as

$$D(\Theta_{\tilde{m}+1}) = D(\Theta_{\tilde{m}}) + \sum_{k=0}^{\tilde{p}-2}\left(\frac{\theta_{\tilde{m}+1} - \theta_k}{\Theta_{\tilde{m}+1} - \Theta_{\tilde{m}}}\Delta D_{ini} + \frac{\theta_k - \Theta_{\tilde{m}}}{\Theta_{\tilde{m}+1} - \Theta_{\tilde{m}}}\Delta D_{fin}\right), \tag{5.14}$$

where ΔD_{ini} and ΔD_{fin} are the damage increments for the initial and final cycles of the time element respectively.

All the other quantities of interest do not require any time integration. They can be calculated from the non-linear material behaviour in rate form independently for every Gauss point before tackling the admissibility conditions at the global stage.

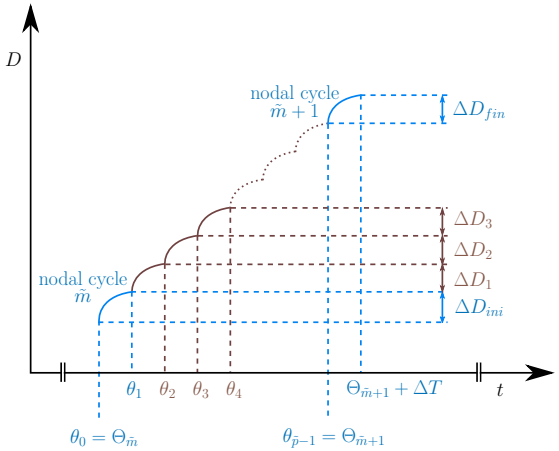

Figure 5.3: Calculating $D\left(\Theta_{\tilde{m}+1}\right)$, knowing $D\left(\Theta_{\tilde{m}}\right)$

5.2.3 Global stage

The global admissibility conditions are calculated for the whole space domain but only for a sub-domain in time, which is the "nodal cycle" $\tilde{m}+1$. The idea is exactly similar to section 4.6, the only difference being the temporal domain includes only the "nodal cycle" of interest.

Mainly, the global stage is used only for updating the already built ROB, and enrichment is done if there is an absolute necessity. For simple structures with simple boundary conditions that induce no localisation (see e.g. fig. 5.4), the ROB obtained from the "training stage" is considered sufficient, and any new space-time mode added will be rejected after the orthonormalisation procedure as explained in Appendix C. Thereby the enrichment step is skipped completely to save CPU cost. For structures that may induce localisations (see e.g. figs. 5.14 and 5.17), however, a maximum of one space-time pair is added per "nodal cycle" to enrich the reduced order basis. The enrichment condition is the same as explained in section 4.6.

If $\{\lambda_j^{\tilde{m}+1}\}_{j=1}^m$ are the time functions used to describe "nodal cycle" $\tilde{m}+1$ at LATIN iteration i with the space functions being $\{\bar{\varepsilon}_j^{p,\,\tilde{m}+1}\}_{j=1}^m$, the objective at LATIN iteration $i+1$ is to calculate $\{\Delta\lambda_j^{\tilde{m}+1}\}_{j=1}^m$ which are the corrections of $\{\lambda_j^{\tilde{m}+1}\}_{j=1}^m$. The process is exactly as described in section 4.6.2.1, the only difference being the temporal domain, which is now $[\Theta_{\tilde{m}+1}, \Theta_{\tilde{m}+1}+\Delta T]$.

If enrichment of the ROB is necessary, a new space-time mode $\bar{\varepsilon}_{m+1}^{p,\,\tilde{m}+1}$, $\lambda_{m+1}^{\tilde{m}+1}$ is added according to the process described in section 4.6.2.2.

As far as the kinematic hardening variables are concerned, eq. (4.18) is rewritten over the "nodal cycle" $\tilde{m}+1$ as

$$\Delta\dot{\boldsymbol{\alpha}}_{i+1}^{\tilde{m}+1} + \mathbf{H}_\beta^{\tilde{m}+1}\boldsymbol{\Pi}\Delta\boldsymbol{\alpha}_{i+1}^{\tilde{m}+1} + \bar{\boldsymbol{\Delta}}_{i+1}^{\alpha,\,\tilde{m}+1} = 0 \tag{5.15}$$

with

$$\bar{\boldsymbol{\Delta}}_{i+1}^{\alpha,\,\tilde{m}+1} = \mathbf{H}_\beta^{\tilde{m}+1}\left(\boldsymbol{\Pi}\boldsymbol{\alpha}_i^{\tilde{m}+1} - \hat{\boldsymbol{\beta}}_{i+1/2}^{\tilde{m}+1}\right) + \dot{\boldsymbol{\alpha}}_i^{\tilde{m}+1} - \hat{\dot{\boldsymbol{\alpha}}}_{i+1/2}^{\tilde{m}+1}, \tag{5.16}$$

and

$$\Delta\boldsymbol{\alpha}_{i+1}^{\tilde{m}+1} = \boldsymbol{\alpha}_{i+1}^{\tilde{m}+1} - \boldsymbol{\alpha}_i^{\tilde{m}+1},\ \Delta\dot{\boldsymbol{\alpha}}_{i+1}^{\tilde{m}+1} = \dot{\boldsymbol{\alpha}}_{i+1}^{\tilde{m}+1} - \dot{\boldsymbol{\alpha}}_i^{\tilde{m}+1}. \tag{5.17}$$

Equation (5.15) is solved to obtain the corrective terms over the "nodal cycle" $\tilde{m}+1$ using zero initial condition as described in section 4.5.

The relaxation of the solution and the convergence indicator for "nodal cycle" $\bar{m}+1$ is the same as given in section 4.7.

5.3 Numerical examples

Two-dimensional classical mechanical problems subjected to cyclic loadings are considered to investigate the abilities and the robustness of the proposed numerical scheme. All the two-dimensional structures mentioned herein are discretised in space using linear four-noded isoparametric quadrilateral elements with four Gauss points per element. A one-dimensional problem has also been solved to build virtual ε-N curves.

5.3.1 Verification with mono-scale LATIN method

The first set of analysis is performed for a material behaviour characterised by viscoplasticity and kinematic hardening without any contribution of damage. A rectangular plate described by its length $L = 50$ mm and width $W = 100$ mm which is constrained on three sides as shown in fig. 5.4 is considered. The unconstrained side of the plate is loaded with a uniformly distributed sinusoidal displacement of the form $U_d = U_0 \sin \frac{2\pi t}{\Delta T}$ with the time period $\Delta T = 1$ s for 1000 cycles. The goal is to compare the results obtained using two-time scale algorithm with the results obtained from the mono-scale method described in chapter 4.

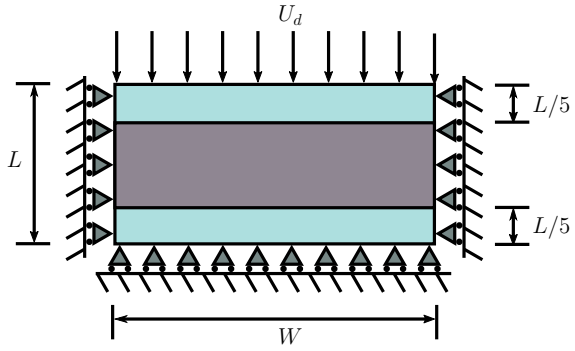

Figure 5.4: Rectangular plate with different yield stresses

The material considered is Cr-Mo steel at 25°C with properties given in table 5.2. The yield stress σ_y considered for the central part is 188 MPa and for the peripheral material is 189 MPa.

The problem is initially solved for $U_0 = 0.073$ mm. Four separate temporal discretisations are examined using the two-scale computation, with a minimum of 50 cycles to a maximum of 500 cycles per time element (see table 5.3). The result of this analysis, compared to a mono-scale solution is given in fig. 5.5. Plasticity being the defining phenomenon in the process, the relative error is based on the plastic strain rate, i.e.

$$er^2 = \frac{\int\limits_{\Omega\times[0,T]} \left(\dot{\varepsilon}^p_{ref} - \dot{\varepsilon}^p_{ob}\right) : \left(\dot{\varepsilon}^p_{ref} - \dot{\varepsilon}^p_{ob}\right) \, \mathrm{d}V \, \mathrm{d}t}{\int\limits_{\Omega\times[0,T]} \dot{\varepsilon}^p_{ref} : \dot{\varepsilon}^p_{ref} \, \mathrm{d}V \, \mathrm{d}t + \int\limits_{\Omega\times[0,T]} \dot{\varepsilon}^p_{ob} : \dot{\varepsilon}^p_{ob} \, \mathrm{d}V \, \mathrm{d}t}, \tag{5.18}$$

where $\dot{\varepsilon}^p_{ref}$ is the mono-scale reference solution and $\dot{\varepsilon}^p_{ob}$ is the solution obtained from the two-time scale computations. Increasing the size of time elements decreases the accuracy of the approximation, i.e.

Table 5.2: Material properties for Cr-Mo steel at $25^\circ\mathrm{C}$

Material parameter	Value
E	199740 MPa
ν	0.3
Q	20602 MPa
a	141.4 MPa
k_D	$0.128\ \mathrm{MPa}^{-n_d}\mathrm{s}^{-1}$
n_D	2
K	$195\ \mathrm{MPa\,s}^{1/n}$
n	12.5
k	K^{-n}
h	0.2
σ_y	189 MPa

Table 5.3: Different temporal discretisations

Temporal discretisation	Number of cycles per time element	Total number of time elements
I	50	20
II	100	10
III	200	5
IV	500	2

increases er, although this increase is very less and even 500 cycles per time element provides results of appreciable accuracy (see fig. 5.5). The relative CPU time is estimated using $t_{ob}^{cal}/t_{ref}^{cal}$, where t_{ref}^{cal} is the reference mono-scale computation time and t_{ob}^{cal} is the time required to obtain the solution using the two-time scale computations. This relative CPU time expectedly decreases with increase in number of cycles per time element. It should also be noted from fig. 5.5 that there is a drastic drop in the calculation time for two-time scale computation, compared to the mono-scale computational time, even if 50 cycles per time element are used.

Similar tests are performed for material that is susceptible to damage along with visco-plasticity and kinematic hardening with the damage threshold considered to be $\frac{(1.4\sigma_y)^2}{2E}$. The problem is solved for $U_0 = 0.070$ mm using the four temporal discretisations explained previously. The relative error estimation with respect to a reference mono-scale solution is now based on the damage variable and is given by

$$er_d^2 = \frac{\int\limits_{\Omega\times[0,T]} \left(D_{ref} - D_{ob}\right)\cdot\left(D_{ref} - D_{ob}\right)\ \mathrm{d}V\ \mathrm{d}t}{\int\limits_{\Omega\times[0,T]} D_{ref}\cdot D_{ref}\ \mathrm{d}V\ \mathrm{d}t + \int\limits_{\Omega\times[0,T]} D_{ob}\cdot D_{ob}\ \mathrm{d}V\ \mathrm{d}t}, \tag{5.19}$$

where D_{ref} and D_{ob} are obtained from a reference mono-scale and a two-time scale LATIN-PGD algorithms respectively. The relative error, which is plotted in fig. 5.6, strongly increases with respect to the size of time elements. Although it is much higher than the one of the visco-plastic case shown in fig. 5.5, it is still in the acceptable range, i.e. a minimum of $2.6\,\%$ and a maximum of $4.2\,\%$ is observed. On an other hand, the reduction in CPU time is here even more drastic compared to the case without damage.

Further tests are conducted to analyse the effect of the load level on the accuracy of different temporal discretisations represented in fig. 5.7a. These comparisons are with respect to the results obtained using

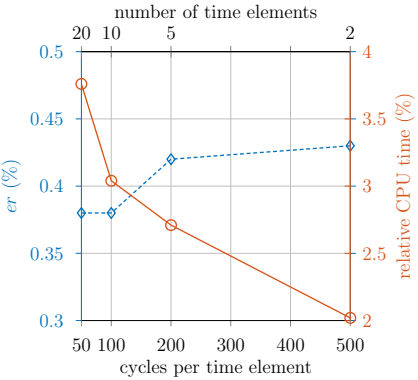

Figure 5.5: Relative accuracy and saved time for different temporal meshes for the structure without damage

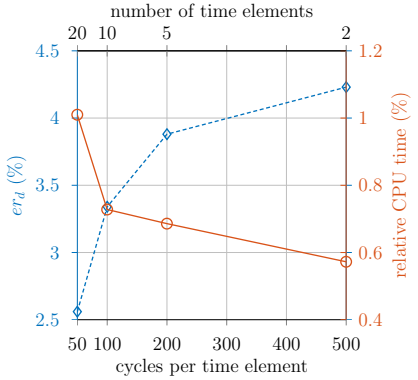

Figure 5.6: Relative accuracy and saved time for different temporal meshes for isotropic damage

50 cycles per time element. It is seen that with increase in load level, the coarser temporal discretisation results in higher inaccuracy as the damage behaviour becomes non-linear (see fig. 5.8). However for low damage level, the damage evolution is comparatively linear and coarse temporal mesh provides relatively acceptable accuracy.

As far as the computational time is concerned (see fig. 5.7b), there are two aspects that should be explained. First of all, for a given load level, finer temporal mesh will be computationally expensive as the number of "nodal cycles" computed is higher. Secondly, for a given temporal discretisation, increasing the load level will increase the CPU cost as higher load induces higher degree of non-linearity and more LATIN iterations are needed at each "nodal cycle" for convergence. It should be noted that the comparisons depicted in fig. 5.7 are with respect to a two-time scale solution using 50 cycles per time element and not a mono-scale solution.

These observations lead to a conclusion that the magnitude of damage is a defining factor in the choice of the type of temporal discretisation. For low damage level, coarse temporal mesh can be used for reasonable accuracy while improving the CPU cost. However, for higher damage level, a fine temporal

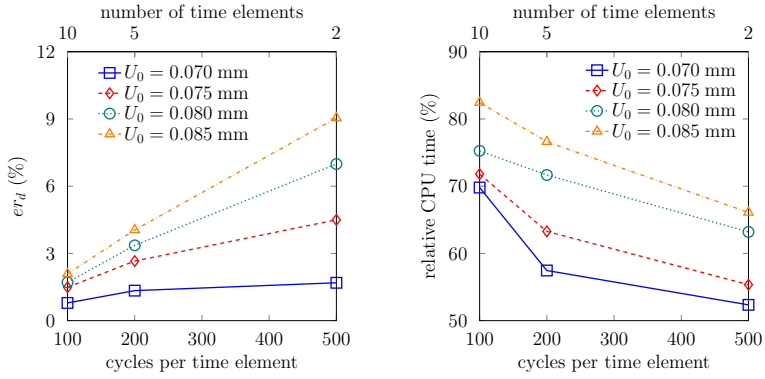

(a) relative error

(b) relative computational time

Figure 5.7: Comparison with the size of time elements relative to 50 cycles per time element solution

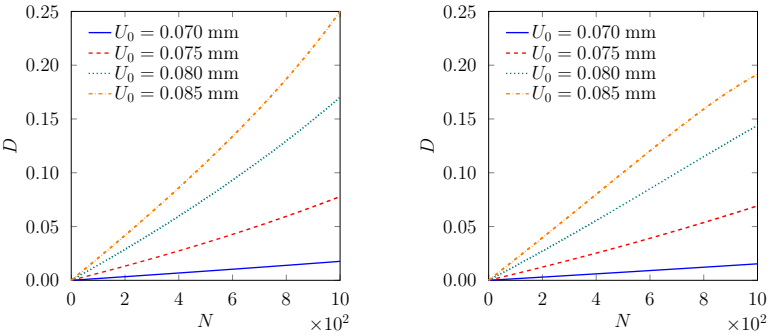

(a) for the central part

(b) for the peripheral part

Figure 5.8: Damage evolution in the plate for different load levels

mesh must be used which will give adequate accuracy in the expense of calculation time. Therefore, an adaptive temporal discretisation scheme based on the damage level should be used .

5.3.2 Influence of the "training stage"

Before using the adaptive scheme, it should also be checked if the number of cycles those are initially calculated for the generation of the ROB has any influence in the solution. Four separate tests are conducted on the same structure given in fig. 5.4 using $U_0 = 0.063$ mm for 1×10^5 cycles with 50, 20, 10, and 5 cycles for the "training stage". A uniform temporal mesh of 100 cycles per time element is considered thereafter. Considering the solution obtained using 50 cycles in the "training stage" as the reference, the solutions of the other cases are compared using the error criterion of eq. (5.19). The error criterion, given in fig. 5.9, shows that with the decrease in number of cycles of the training phase, the final

solution deviates further from the reference solution. However the amount of inaccuracy is very low and it is not necessary to include high number of cycles in the "training stage", as it will drastically increase the numerical cost. Hence for the next analyses described henceforth will include a "training phase" of 10 cycles.

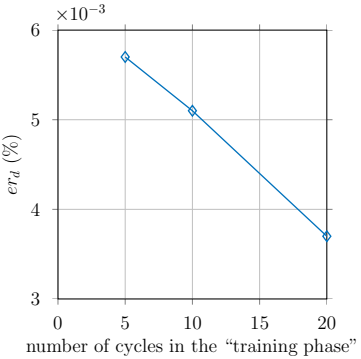

Figure 5.9: Variation of accuracy with respect to the number of cycles of the "training stage"

The distribution of damage obtained after the end of loading using 50 cycles in the "training stage" is shown in fig. 5.10, with maximum damage at the central part and minimum at the periphery. The corresponding evolutions of damage for these two regions are given in fig. 5.11.

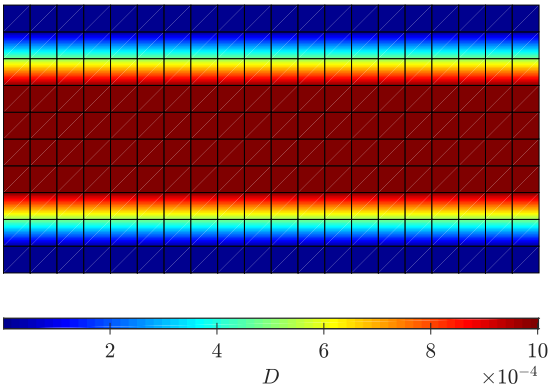

Figure 5.10: Distribution of damage after end of loading, i.e. after 1×10^5 cycles

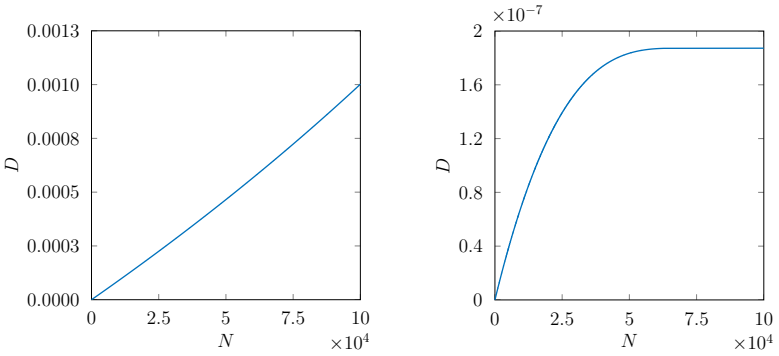

(a) for the central part

(b) for the peripheral part

Figure 5.11: Damage evolution in the plate for a total of 1×10^5 cycles

5.3.3 Simulation of large number of cycles

Now the aim is to observe the damage behaviour involving large number of cycles. An adaptive temporal meshing scheme given in table 5.4 is tested on the simple structure given in fig. 5.4, which is chosen to avoid any localisation and stress raisers which may lead to regional concentration of damage.

Table 5.4: Adaptive temporal discretisation based on damage level

Damage range	Number of cycles per time element
$D_{\tilde{m}}^{\max} < 0.001$	500
$0.001 < D_{\tilde{m}}^{\max} \leq 0.01$	200
$0.01 < D_{\tilde{m}}^{\max} \leq 0.1$	100
$D_{\tilde{m}}^{\max} > 0.1$	50

Using term $D_{\tilde{m}}^{\max}$ that describes the maximum damage value at the end of "nodal cycle" m, the size of the time element $[\Theta_{\tilde{m}}, \Theta_{\tilde{m}+1}]$ i.e. the value of $\Theta_{\tilde{m}+1}$ is determined based on table 5.4.

A total of 5×10^5 cycles are simulated with the load amplitude $U_0 = 0.060$ mm. The "training stage" is based on the calculation of initial 10 cycles, after which the reduced order basis is reused to calculate every "nodal cycle". The adaptive numerical scheme computes only 2185 "nodal cycles" and the rest is interpolated. The search direction operators are calculated only once for each "nodal cycle", and then reused during the subsequent LATIN iterations. A total of three PGD modes are obtained during the training phase of the problem, and these basis functions are not enriched during the calculation of the "nodal cycles".

The distribution of damage at the end of loading is depicted in fig. 5.12. The central region of the plate consists of a weaker material, hence the damage evolution is much higher as displayed in fig. 5.13a. For the peripheral region, the damage evolution is much lower and it also shows saturation after certain load cycles (see fig. 5.13b).

The tests performed till now is based on fig. 5.4 where the basis generated from the "training stage" is considered to be optimal and is later on re-used for the "nodal cycles" without enrichments. However the examples provided in sections 5.3.4 to 5.3.5 are on structures that induce localisation, hence the basis

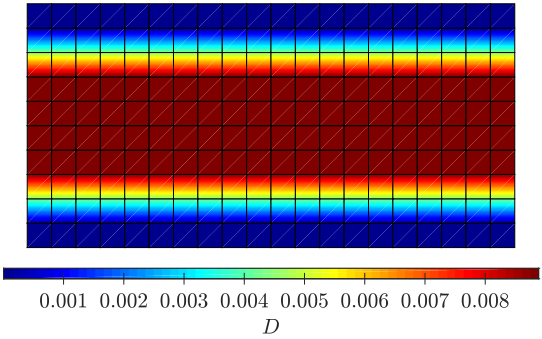

Figure 5.12: Damage distribution at the end of loading, i.e. after 5×10^5 cycles

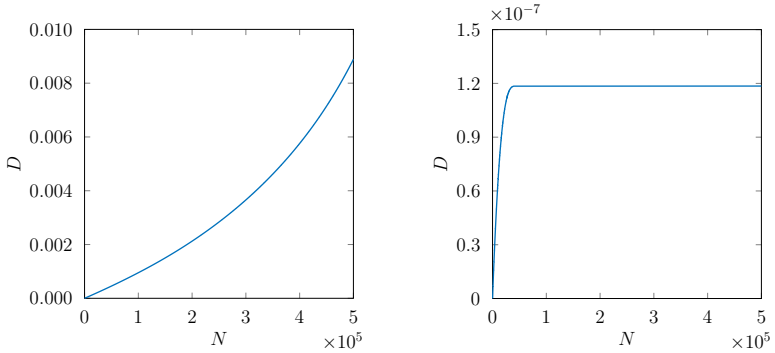

(a) for the central part

(b) for the peripheral part

Figure 5.13: Damage evolution in the plate for a total of 5×10^5 cycles

obtained from “training stage” is not considered to be optimal, and the ROB is enriched by a maximum of one PGD mode per “nodal cycle”.

5.3.4 Pre-damaged structure

The idea of this analysis is to simulate and compare the behaviour of virgin and pre-damaged materials, for which a two-dimensional notched plate is considered. The structure consists of a rectangular plate of length $L = 20$ mm, width $W = 10$ mm, and two semicircular notches of equal radii $\phi = 4$ mm as illustrated in fig. 5.14. The structure is loaded with uniformly distributed sinusoidal displacements of the form $U_d = U_0 \sin \frac{2\pi t}{\Delta T}$ with time period $\Delta T = 1$ s on the longitudinal ends for 20000 cycles. The quarter of the plate generated out of symmetry for the numerical analysis is also shown in fig. 5.14, along with the region of interest where damage localisation is anticipated.

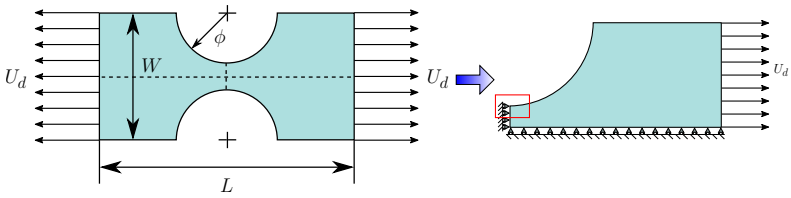

Figure 5.14: A plate with semicircular notches subjected to distributed loads

For a given load amplitude $U_0 = 0.0057$ mm, the first analysis considered is to assume the complete structure to be virgin. A total of 7 PGD modes are calculated during the "training stage" which are then used to approximate the "nodal cycles". A total of 171 "nodal cycles" and 11 PGD modes are calculated to simulate 20000 cycles. Thereafter the Gauss points marked in red in fig. 5.15 are assigned an initial damage value of 0.005, and the problem is recalculated. A total of 186 "nodal cycles" and 13 PGD modes are needed to simulate the total behaviour, with a "training stage" of 10 cycles and 7 PGD modes.

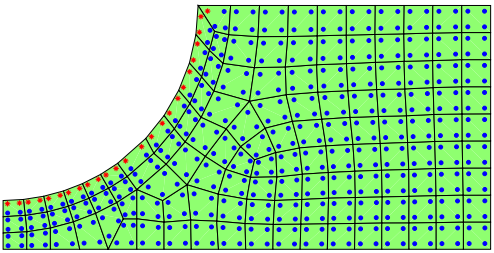

Figure 5.15: FE discretisation showing virgin (•) and pre-damaged (∗) Gauss points

The spread of damage after certain specific cycles in the region of interest for both virgin and pre-damaged structures is shown in fig. 5.16. The most affected Gauss point for both cases is the same, with the respective damage evolution given in fig. 5.17.

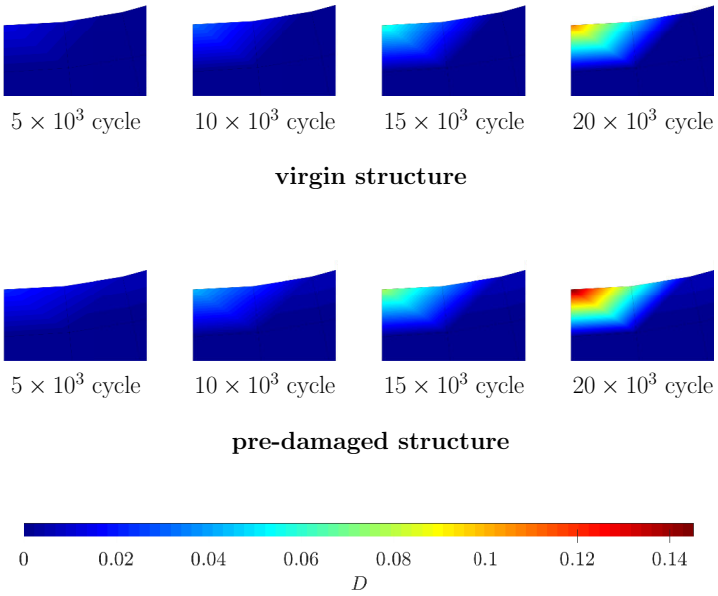

Figure 5.16: Damage distribution at the end of loading

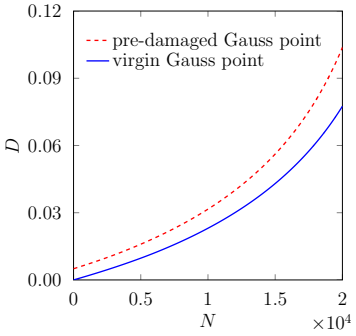

Figure 5.17: Damage evolution at the most weak Gauss point

5.3.5 Variable amplitude loading

The intent herein is to simulate the difference in behaviour of a given structure subjected to constant amplitude (CA) load and variable amplitude (VA) load. The effect of sequence in case VA load, i.e. low-to-high (L-H) or high-to-low (H-L) is also studied. The structure used for this analysis is a square plate of length $L = 40$ mm. This plate consists of an elliptical hole with semi-major axis $a = 10$ mm and semi-minor axis $b = 5$ mm. The plate is subjected to uniformly distributed sinusoidal displacements of the form $U_d = U_0 \sin \frac{2\pi t}{\Delta T}$ with time period $\Delta T = 1$ s on the ends, as shown in fig. 5.18 for 10000 cycles. The quarter of the plate, with the symmetric boundary conditions, along with the anticipated region of interest, is also shown in fig. 5.18.

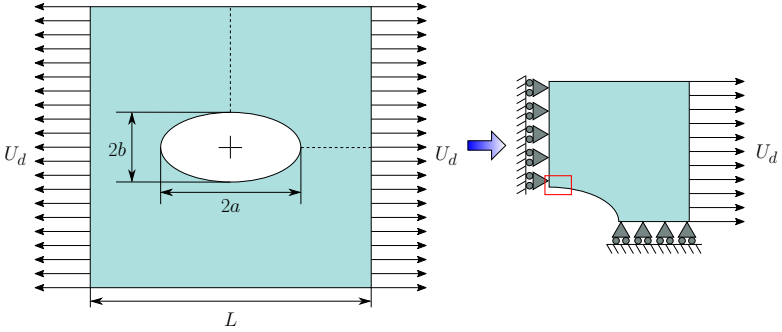

Figure 5.18: A square plate with an elliptical hole subjected to distributed loads

With the same material properties as before, the first part of the analysis is to simulate the complete loading using constant amplitude. The "training stage" consists of 10 cycles, which yields 8 PGD pairs. Using the adaptive temporal scheme, a total of 95 "nodal cycles" are simulated by generating 19 PGD pairs.

In the next part of the analysis, the load amplitude U_0 is considered to be uniformly increasing as shown in fig. 5.19. The "training stage" similar to the constant amplitude case consists of 10 load cycles generating 7 PGD modes. A total of 90 "nodal cycles" are generated with a total of 18 PGD modes at the end of the last "nodal cycle".

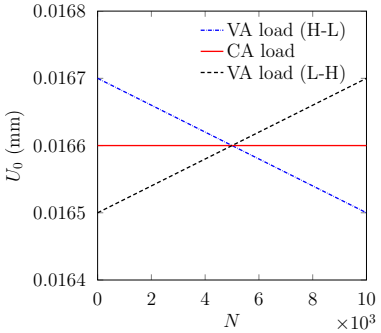

Figure 5.19: Variation of amplitude with number of load cycles for three different load cases

The last part of the analysis consists of the load amplitude U_0 to be uniformly decreasing as shown

in fig. 5.19. The "training stage" similar to the constant amplitude case consists of 10 load cycles but generates 8 PGD modes. A total of 98 "nodal cycles" are generated with a total of 19 PGD modes at the end of the last "nodal cycle".

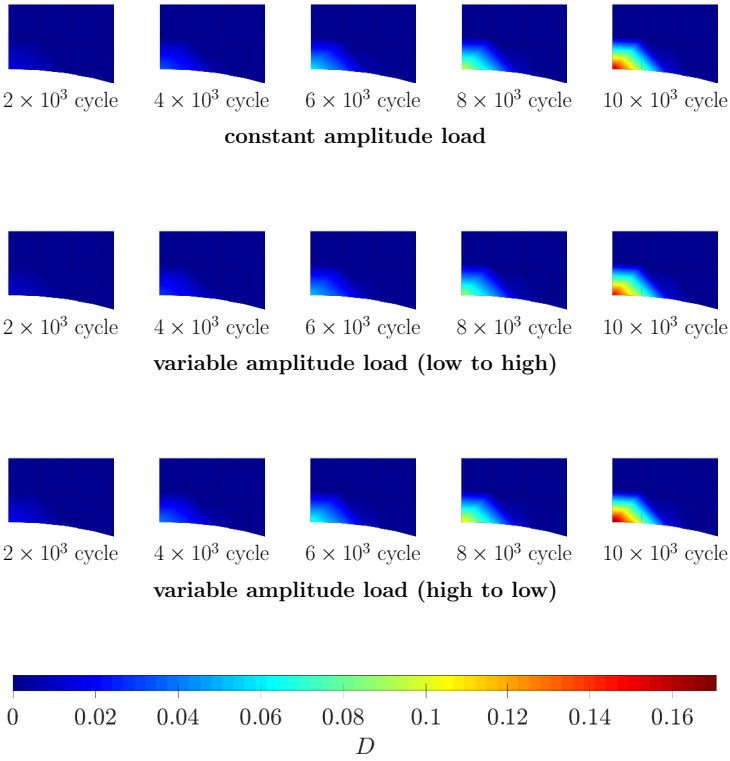

Figure 5.20: Spread of damage at certain load cycles in the region of interest for the plate with elliptical hole

It has to be mentioned that the mean value of the load amplitude for the three cases is considered to be the same. The spread of damage for these three loading cases, at certain cycles, in the region of interest is shown in fig. 5.20. Damage is obtained to be lower for constant amplitude loading as compared to the H-L loading but higher that L-H loading. The effect of sequence can be observed if the evolution of damage is plotted for the weakest GP for the three load cases (fig. 5.21). The evolution of damage for H-L loading is found to be higher than for L-H loading.

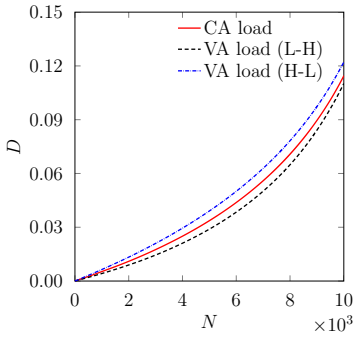

Figure 5.21: Evolution of damage with respect to number of load cycles for the weakest GP

5.3.6 Virtual ε-N curves

To develop virtual ε-N curves, a one-dimensional structure as shown in fig. 4.1 is considered. The bar is considered to be made of a single material with the material properties given in table 5.2. A verification study is done at the beginning, which involves comparing the solutions obtained using different uniform temporal meshes with the mono-scale reference solution. A total of 2000 cycles are simulated using the mono-scale LATIN-PGD method. Thereafter the same problem is solved using different uniform temporal meshes and the comparative solution is depicted in fig. 5.22a. As the temporal mesh gets finer the solution approaches the reference solution. A more quantitative description of this fact is presented in fig. 5.22b, where the error, defined by eq. (5.18), increases with increase in number of cycles per time element. The CPU time however shows a drastic decrease as compared to the reference CPU time, and the relative CPU cost decreases with increase in number of cycles per time element.

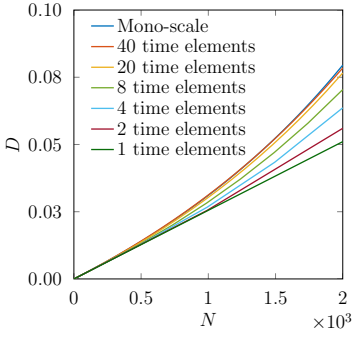

(a) damage

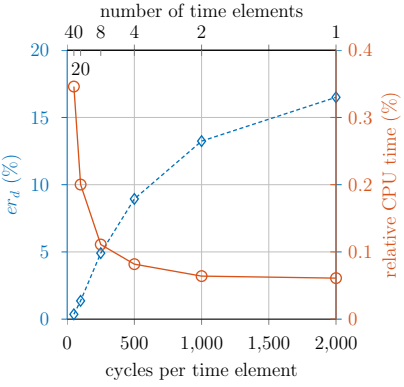

(b) relative error and CPU time

Figure 5.22: Comparison with different sizes of time elements relative to mono-scale solution

To build an ε-N curve, a critical damage level of 0.2 is chosen and the structure is loaded at a given strain amplitude ε_a. The structure is assumed to have failed when the damage value reaches 0.2 and the number of cycles needed is noted. This ordeal gives one point of the ε-N curve, which is thereby repeated

for approximately 20 times with different strain amplitudes to obtain other points, which are then joined to obtain one particular ε-N curve. As far as the temporal discretisation is considered, each virtual point is obtained using a uniform temporal mesh which varies for different strain amplitudes, the lowest being 10 cycles per time element and the highest being 200 cycles per time element.

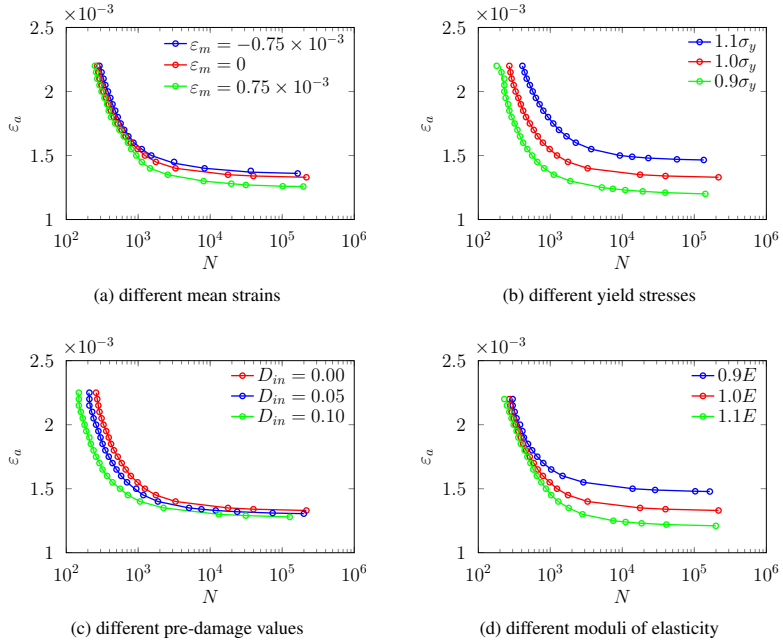

(a) different mean strains

(b) different yield stresses

(c) different pre-damage values

(d) different moduli of elasticity

Figure 5.23: ε-N curves

Different ε-N curves are plotted by varying different material or structural properties (see fig. 5.23). The mean-strain effect on the ε-N curve is depicted in fig. 5.23a. For a negative mean strain ε_m, the evolution of damage will be less as the compressive part will be more than the tensile part, thereby for a given amplitude ε_a, more cycles will be needed to achieve a critical damage level, as compared to a zero mean-strain case. For a positive mean-strain, however, the effect is reversed, with a higher tensile part, the number of cycles needed to reach the critical damage value is less compared to a zero mean-strain-case. The effect of different yield stresses is shown in fig. 5.23b, where, with decrease in yield stress the material becomes more susceptible to damage and less cycles are needed to reach the critical damage value for a given strain amplitude. Also the damage threshold considered here is directly proportional to the yield stress, hence higher σ_y induces lower damage. The effect of different values of initial damage D_{in} is shown in fig. 5.23c, where with higher initial damage value, the number of cycles needed to reach the critical damage becomes less for a given strain amplitude. The effect of various moduli of elasticity is displayed in fig. 5.23d. For a higher value of the modulus of elasticity, the stress becomes higher at a given ε_a and generates lesser number of cycles to obtain the critical damage. Also the damage threshold chosen here is inversely proportional to the modulus of elasticity, hence higher E induces higher damage.

5.4 Concluding remark

An approach has been proposed in this chapter that can effectively handle large number of cycles. Verification studies that were performed, showed confirmation with the mono-scale LATIN method, with finer temporal discretisation providing more accuracy but consuming more CPU time. Adaptive temporal discretisation has thereby been used to obtain optimal compromise between numerical cost and accuracy. This method is effective to deal with various types of loading and initial conditions and also been used to simulate virtual ε-N curves.

In a way this method can be compared to the classical jump-cycle approach. Indeed, the "nodal cycles" used in this non-incremental framework can be compared to the cycle computed after the jumps used in an incremental framework. The finite element time description is however novel in this approach and can effectively approximate the intermediate cycles in a time element, i.e. the jumped cycles. The choice of the initial conditions for the cyclic quantities at each "nodal cycle" is similar to the jump cycle method. However, the initial condition for damage is linearly approximated in jump cycle, whereas here, a "resolvent" technique was used, which is more accurate.

Chapter 6

Conclusion and future perspective

A novel technique has been developed to include damage as an internal variable in a classical LATIN-PGD framework. The main difficulty that arose herein was the elastic state law which was no longer linear. To circumvent this difficulty, the elastic state law was solved in the local stage of the LATIN method and the stress and total strain tensor were separated into parts depending on plasticity and parts depending on damage. The separated parts should also be admissible and PGD was applied to the plastic part only. The unilateral condition of micro-defect closure effect was used in the damage description, which provided the difference between tension and compression. An on the fly PGD technique based on a greedy algorithm was used to build the ROM which satisfied the global admissibilities. A hybrid PGD method was used to solve the global step where the temporal approximations were calculated though the minimisation of a mechanical residual and the spatial approximations were obtained from classical Galerkin method. PGD-based approximation was used to approximate the quantities depending on plastic deformation and quantities depending on damage were already known from the local stage of the LATIN algorithm. For the hardening terms, no model reduction approach was utilised as they are obtained from cheap local first order ODEs. This technique was tested in simple academic examples subjected to cyclic loading and the results were qualitatively satisfactory. The test results also showed that the technique was able to handle non-proportional loading quite efficiently.

This approach was thereafter extended so that a large number of cycles could be simulated. A two-scale temporal discretisation approach was adopted, which took into account the slow evolution of the quantities of interest along the load cycles and their fast evolution within a cycle. The quantities of interest were calculated only at certain "nodal cycles" and finite element like temporal interpolation allowed to approximate the intermediate cycles. The first few cycles were calculated using mono-scale LATIN technique to obtain the ROB ("training stage" of the two-scale method), which were then utilised to obtain the approximations at each "nodal cycle". Every "nodal cycle" was subjected to a separate LATIN algorithm where the ROB of the previous "nodal cycle" was updated and enriched only if necessary. A "resolvent" technique introduced in Cognard and Ladevèze (1993) for visco-plasticity was used to calculate the initial conditions for damage at each "nodal cycle". This method was compared with the solution of mono-scale LATIN-PGD method and acceptable accuracy was obtained with drastic reduction in numerical expense. It was thereafter used to simulate large number of cycles and also to obtain virtual ε-N curves. An adaptive temporal scheme was also used where the sizes of the time elements are not considered to be equal but adapted according to the damage evolution. This adaptive temporal scheme was used to simulate pre-damaged structure and structure subjected to variable amplitude load.

Although, non-proportional loading can be handled, the limitation of the proposed method to include damage in a LATIN-PGD clearly is the fact that high value of damage will lead to inaccuracy. Although for metals where the critical damage is relatively low, this is not a problem, for damage computations in materials like rubber, the damage may be much higher compared to metals. Therefore, a formulation that is able to tackle high values of damage with acceptable accuracy should be developed in the future. Other

sophisticated damage models, for instance the 2-scale damage model can also be included, if the objective is to perform HCF simulations. Inertia effects, although excluded in the current work, can be introduced if the intent is to calculate dynamic fatigue.

As far as the two-scale discretisation is concerned, a better criterion for the adaptive temporal meshes may also be included in the future. Although, simple cyclic loading has been tested, the challenge of simulation of block loadings, or narrow-band random loading should also be explored.

Lastly, all these problems were tested in simple academic problems, and trials should be done if this concept can be utilised in practical engineering problems.

Appendices

Appendix A

Calculation of the finite element operators

The objective herein is provide a brief methodology for the construction of the FE operators $\mathbb{E}$ and $\mathbb{C}$ defined in section 4.6.1.

To derive the finite element operator $\mathbb{E}$ introduced in eq. (4.44), consider the spatial problem eq. (4.43), i.e.

$$\int_{\Omega} \mathbf{C}\bar{\varepsilon} : \varepsilon\left(\delta\vec{\bar{u}}\right) \, \mathrm{d}V = \int_{\Omega} \mathbf{C}\bar{\varepsilon}^{p} : \varepsilon\left(\delta\vec{\bar{u}}\right) \, \mathrm{d}V. \tag{A.1}$$

Let the spatial discretisation be done with classical FE scheme. Then the discretised form for one elemental domain Ω_{el} will be

$$\left[\int_{\Omega_{el}} \mathbf{B}\mathbf{C}\mathbf{B}^{T} \mathrm{d}\Omega\right] \{\bar{u}_{el}\}, \tag{A.2}$$

for the left hand side, and

$$\left[\int_{\Omega_{el}} \mathbf{B}\mathbf{C} \mathrm{d}\Omega\right] \left\{\bar{\varepsilon}^{p}_{el}\right\}, \tag{A.3}$$

for the right hand side. $\mathbf{B}$ is the matrix containing the derivatives of the shape functions, $\{\bar{u}_{el}\}$ are nodal unknowns for one element and $\left\{\bar{\varepsilon}^{p}_{el}\right\}$ are the unknowns at all Gauss points for one element. These elemental equations need to be assembled, and the global equation reads

$$\mathbf{K}_{tot} \{\bar{u}_{tot}\} = \mathbf{L}_{tot} \left\{\bar{\varepsilon}^{p}_{tot}\right\}, \tag{A.4}$$

where $\mathbf{K}_{tot}$ and $\mathbf{L}_{tot}$ are the assembled matrices, $\{\bar{u}_{tot}\}$ and $\left\{\bar{\varepsilon}^{p}_{tot}\right\}$ are the total number of nodal unknowns and Gauss point quantities respectively. It is needless to mention that although the stiffness matrix $\mathbf{K}_{tot}$ depends on the total number of nodal degrees of freedom, $\mathbf{L}_{tot}$ depends also on the total number of Gauss points. The right hand side of eq. (A.4) can be viewed as a "pseudo nodal force vector", hence care should be taken to include contribution of all the Gauss points to the "pseudo nodal force vector" at each element while building $\mathbf{L}_{tot}$. Thereafter the procedure is quite straightforward. An operator

$$\mathbf{O}^{red}_{tot} = \left(\mathbf{K}^{red}_{tot}\right)^{-1} \mathbf{L}^{red}_{tot} \tag{A.5}$$

is calculated, where removal of the corresponding rows and columns of $\mathbf{K}_{tot}$ and the corresponding rows of $\mathbf{L}_{tot}$ where the nodal degrees of freedom are known, results in $\mathbf{K}^{red}_{tot}$ and $\mathbf{L}^{red}_{tot}$ respectively. The

corresponding rows of $\mathbf{O}_{tot}^{red}$ are thereby filled with zeros to obtain $\mathbf{O}_{tot}$. Equation (A.4) can thereby be written as

$$\{\bar{u}_{tot}\} = \mathbf{O}_{tot} \left\{\bar{\varepsilon}_{tot}^{p}\right\}. \tag{A.6}$$

The total assembled matrix containing the derivatives of the shape functions can then be used to rewrite eq. (A.6) as

$$\mathbf{B}_{tot}^{T} \{\bar{u}_{tot}\} = \mathbf{B}_{tot}^{T} \mathbf{O}_{tot} \left\{\bar{\varepsilon}_{tot}^{p}\right\} \implies \{\bar{\varepsilon}_{tot}\} = \mathbb{E} \left\{\bar{\varepsilon}_{tot}^{p}\right\}, \tag{A.7}$$

where $\mathbb{E}$ is the FE operator relating the space function of plastic strain $\left\{\bar{\varepsilon}_{tot}^{p}\right\}$ and total strain $\{\bar{\varepsilon}_{tot}\}$.

Now to find the FE operator $\mathbb{C}$, the strain partition relationship is used, i.e.

$$\begin{aligned} &\{\bar{\varepsilon}_{tot}^{e}\} = \{\bar{\varepsilon}_{tot}\} - \left\{\bar{\varepsilon}_{tot}^{p}\right\} \\ &\implies \{\bar{\boldsymbol{\sigma}}_{tot}\} = \mathbf{C}_{tot} \left(\{\bar{\varepsilon}_{tot}\} - \left\{\bar{\varepsilon}_{tot}^{p}\right\}\right) \\ &\implies \{\bar{\boldsymbol{\sigma}}_{tot}\} = \mathbf{C}_{tot} \left(\mathbb{E} - \mathbb{I}\right) \left\{\bar{\varepsilon}_{tot}^{p}\right\} \\ &\implies \{\bar{\boldsymbol{\sigma}}_{tot}\} = \mathbb{C} \left\{\bar{\varepsilon}_{tot}^{p}\right\}, \end{aligned} \tag{A.8}$$

where $\mathbf{C}_{tot}$ is the complete elasticity matrix for all the Gauss points, and $\mathbb{C}$ is the FE operator which relates the space function of plastic strain $\left\{\bar{\varepsilon}_{tot}^{p}\right\}$ and stress $\{\bar{\boldsymbol{\sigma}}_{tot}\}$.

Appendix B

Solution technique of the temporal problem

The purpose herein is to elaborate the methodology of solving the temporal problem that is defined as a minimisation of a mechanical residual in chapter 4.

The residual is defined in terms of the constitutive relation error defined in eq. (3.31). As the separated representation is only for the stress and plastic strain, only the first part of eq. (3.31) is rewritten as

$$e_{CE}^2 = \left\| \Delta\dot{\boldsymbol{\varepsilon}}^p - \mathbf{H}_\sigma \Delta\boldsymbol{\sigma}' + \bar{\boldsymbol{\Delta}}^\varepsilon \right\|_{\mathbf{M}}^2, \tag{B.1}$$

with

$$\mathbf{M} = \mathbf{H}_\sigma^{-1}. \tag{B.2}$$

The LATIN indices $i+1$ are dropped for clarity and will be sustained for the complete appendix. Considering the case where a new mode is added, i.e.

$$\Delta\dot{\boldsymbol{\varepsilon}}^p = \dot{\lambda}\bar{\boldsymbol{\varepsilon}}^p, \tag{B.3a}$$

$$\Delta\boldsymbol{\sigma}' = \lambda\mathbb{C}\bar{\boldsymbol{\varepsilon}}^p, \tag{B.3b}$$

with the index of the number of modes being dropped for convenience. Equations (B.2) and (B.3) can be used to rewrite eq. (B.1) as

$$\begin{aligned} e_{CE}^2 &= \left\| \dot{\lambda}\bar{\boldsymbol{\varepsilon}}^p - \mathbf{H}_\sigma \lambda\mathbb{C}\bar{\boldsymbol{\varepsilon}}^p + \bar{\boldsymbol{\Delta}}^\varepsilon \right\|_{\mathbf{H}_\sigma^{-1}}^2, \\ &= \int_{\Omega\times[0,T]} \left(\dot{\lambda}\bar{\boldsymbol{\varepsilon}}^p - \mathbf{H}_\sigma \lambda\mathbb{C}\bar{\boldsymbol{\varepsilon}}^p + \bar{\boldsymbol{\Delta}}^\varepsilon\right) : \mathbf{H}_\sigma^{-1} \left(\dot{\lambda}\bar{\boldsymbol{\varepsilon}}^p - \mathbf{H}_\sigma \lambda\mathbb{C}\bar{\boldsymbol{\varepsilon}}^p + \bar{\boldsymbol{\Delta}}^\varepsilon\right) \mathrm{d}V\mathrm{d}t, \end{aligned} \tag{B.4}$$

with $\bar{\boldsymbol{\varepsilon}}^p$ being the known space function. Equation (B.4) needs to be minimised with respect to the time function λ, which gives the following weak form,

$$\int_{[0,T]} \delta\dot{\lambda} \left(a_{11}\dot{\lambda} - a_{10}\lambda + d_1\right) \mathrm{d}t - \int_{[0,T]} \delta\lambda \left(a_{10}\dot{\lambda} - a_{00}\lambda + d_0\right) \mathrm{d}t = 0, \tag{B.5}$$

with

$$a_{11} = \int_\Omega \bar{\boldsymbol{\varepsilon}}^p : \mathbf{H}_\sigma^{-1} \bar{\boldsymbol{\varepsilon}}^p \mathrm{d}V, \tag{B.6a}$$

$$a_{10} = \int_{\Omega} \bar{\varepsilon}^p : \mathbb{C}\bar{\varepsilon}^p \mathrm{d}V, \tag{B.6b}$$

$$a_{00} = \int_{\Omega} \mathbf{H}_\sigma \mathbb{C}\bar{\varepsilon}^p : \mathbb{C}\bar{\varepsilon}^p \mathrm{d}V, \tag{B.6c}$$

$$d_1 = \int_{\Omega} \bar{\varepsilon}^p : \mathbf{H}_\sigma^{-1} \bar{\Delta}^\varepsilon \mathrm{d}V, \tag{B.6d}$$

$$d_0 = \int_{\Omega} \mathbf{H}_\sigma \mathbb{C}\bar{\varepsilon}^p : \mathbf{H}_\sigma^{-1} \bar{\Delta}^\varepsilon \mathrm{d}V. \tag{B.6e}$$

Equation (B.5) leads to a strong form consisting of a second order ODE with mixed boundary conditions (see Passieux, 2008). However, solution of eq. (B.5) is calculated in a weak sense. A discontinuous Galerkin scheme of order zero is used to solve eq. (B.5), the detail of which can be found in Passieux (2008), Relun (2011). The main idea is to have piecewise constant functions for every time element and at each node there is a jump or discontinuity in the nodal unknowns (see fig. B.1 for a particular temporal quantity $\boldsymbol{\lambda}$).

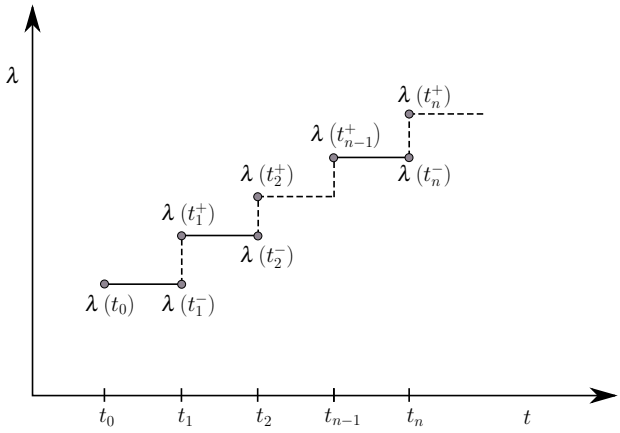

Figure B.1: Discontinuous Galerkin scheme of order zero

For any time element $[t_{n-1}, t_n]$, $\boldsymbol{\lambda}\left(t_{n-1}^+\right) = \boldsymbol{\lambda}\left(t_n^-\right)$, and the derivative $\dot{\boldsymbol{\lambda}}$ is approximated as

$$\dot{\boldsymbol{\lambda}} = \check{\boldsymbol{\lambda}}\left(t_n^+\right) = \frac{\boldsymbol{\lambda}\left(t_n^+\right) - \boldsymbol{\lambda}\left(t_n^-\right)}{\Delta t_n}, \tag{B.7}$$

with $\Delta t_n = t_n - t_{n-1}$.

To derive the elemental equation for a particular time element $[t_{n-1}, t_n]$, the domain of integration is only for $[t_{n-1}, t_n]$ in eq. (B.5), i.e.

$$\int_{t_{n-1}}^{t_n} \delta\dot{\boldsymbol{\lambda}}\left(a_{11}\dot{\boldsymbol{\lambda}} - a_{10}\boldsymbol{\lambda} + d_1\right) \mathrm{d}t - \int_{t_{n-1}}^{t_n} \delta\boldsymbol{\lambda}\left(a_{10}\dot{\boldsymbol{\lambda}} - a_{00}\boldsymbol{\lambda} + d_0\right) \mathrm{d}t. \tag{B.8}$$

Using the discontinuous Galerkin formulation, eq. (B.8) is rewritten as

$$\begin{aligned}\delta\boldsymbol{\lambda}\left(t_n^+\right)\left[\left(\frac{a_{11}}{(\Delta t_n)^2}-\frac{a_{10}}{\Delta t_n}-\frac{a_{10}}{\Delta t_n}+a_{00}\right)\boldsymbol{\lambda}\left(t_n^+\right)+\left(-\frac{a_{11}}{(\Delta t_n)^2}+\frac{a_{10}}{\Delta t_n}\right)\boldsymbol{\lambda}\left(t_n^-\right)\right.\\ \left.+\frac{d_1}{\Delta t_n}-d_0\right]-\delta\boldsymbol{\lambda}\left(t_n^-\right)\left[\left(\frac{a_{11}}{(\Delta t_n)^2}-\frac{a_{10}}{\Delta t_n}\right)\boldsymbol{\lambda}\left(t_n^+\right)-\frac{a_{11}}{(\Delta t_n)^2}\boldsymbol{\lambda}\left(t_n^-\right)+\frac{d_1}{\Delta t_n}\right]=0\end{aligned} \tag{B.9}$$

which gives the following linear system of equations

$$\mathrm{T}_{el}\mathrm{q}_{el}=\mathrm{b}_{el}, \tag{B.10}$$

with

$$\mathrm{q}_{el}=\begin{bmatrix}\boldsymbol{\lambda}\left(t_n^-\right)\\ \boldsymbol{\lambda}\left(t_n^+\right)\end{bmatrix}=\begin{bmatrix}\boldsymbol{\lambda}\left(t_{n-1}^+\right)\\ \boldsymbol{\lambda}\left(t_n^+\right)\end{bmatrix}, \tag{B.11}$$

$$\mathrm{b}_{el}=\begin{bmatrix}\dfrac{d_1}{\Delta t_n}\\ -\dfrac{d_1}{\Delta t_n}+d_0\end{bmatrix}, \tag{B.12}$$

and

$$\mathrm{T}_{el}=\begin{bmatrix}\dfrac{a_{11}}{(\Delta t_n)^2} & -\dfrac{a_{11}}{(\Delta t_n)^2}+\dfrac{a_{10}}{\Delta t_n}\\ -\dfrac{a_{11}}{(\Delta t_n)^2}+\dfrac{a_{10}}{\Delta t_n} & \dfrac{a_{11}}{(\Delta t_n)^2}-\dfrac{a_{10}}{\Delta t_n}-\dfrac{a_{10}}{\Delta t_n}+a_{00}\end{bmatrix}. \tag{B.13}$$

It must be mentioned that, the quantities a_{11}, a_{10}, a_{00} can be time-dependent and the quantities d_1, d_0 are most definitely time-dependent. Therefore, in eq. (B.10) average values of these quantities are used, which obviously vary for different time elements.

It is needless to say that this formulation is exactly similar to first-order finite difference method, where the nodal unknowns can be expressed as

$$\mathrm{q}_{el}=\begin{bmatrix}\boldsymbol{\lambda}_{n-1}\\ \boldsymbol{\lambda}_n\end{bmatrix}, \tag{B.14}$$

where $\boldsymbol{\lambda}_{n-1}$ and $\boldsymbol{\lambda}_n$ represent the nodal unknowns at time points (or nodes) t_{n-1} and t_n respectively. The elemental equation, i.e. eq. (B.10) must be assembled for all the time elements resulting in the system of linear equations

$$\mathrm{T}_{tot}\mathrm{q}_{tot}=\mathrm{b}_{tot}, \tag{B.15}$$

where, T_{tot} is obtained from the assembly of T_{el}, b_{tot} from the assembly of b_{el}, and q_{tot} will contain all the nodal unknowns. Generally, this problem is solved with the knowledge of $\boldsymbol{\lambda}_0$, i.e. $\boldsymbol{\lambda}$ at t_0, which basically shows that the boundary value problem has been transformed into an initial value problem.

Now, if the minimisation problem is for the update of the time functions, the linearised form invariably includes more than one degree of freedom per node. The number of degree of freedom per node is exactly the same as the number of modes that are being updated. If m represents the number of modes that are present, the corrections of the stress and the plastic strain rate can be written as,

$$\Delta\boldsymbol{\varepsilon}^p=\sum_{i=1}^{m}\Delta\dot{\lambda}_i\bar{\boldsymbol{\varepsilon}}_i^p, \tag{B.16a}$$

$$\Delta\boldsymbol{\sigma}' = \sum_{i=1}^{m} \Delta\lambda_i \mathbb{C}\bar{\boldsymbol{\varepsilon}}_i^p. \tag{B.16b}$$

The constitutive relation error will thereby be written as

$$e_{CE}^2 = \left\| \sum_{i=1}^{m} \Delta\dot{\lambda}_i \bar{\boldsymbol{\varepsilon}}_i^p - \mathbf{H}_\sigma \sum_{i=1}^{m} \Delta\lambda_i \mathbb{C}\bar{\boldsymbol{\varepsilon}}_i^p + \bar{\boldsymbol{\Delta}}^\varepsilon \right\|_{\mathbf{H}_\sigma^{-1}}^2. \tag{B.17}$$

The minimisation will henceforth be on all the m time functions, which generates the element matrix of the form

$$\mathrm{b}_{el} = \begin{bmatrix} \dfrac{d_1^1}{\Delta t_n} \\ \dfrac{d_1^2}{\Delta t_n} \\ \vdots \\ \dfrac{d_1^m}{\Delta t_n} \\ -\dfrac{d_1^1}{\Delta t_n} + d_0^1 \\ -\dfrac{d_1^2}{\Delta t_n} + d_0^2 \\ \vdots \\ -\dfrac{d_1^m}{\Delta t_n} + d_0^m \end{bmatrix}, \quad \begin{array}{l} \text{with } d_1^i = \displaystyle\int_\Omega \bar{\boldsymbol{\varepsilon}}_i^p : \mathbf{H}_\sigma^{-1} \bar{\boldsymbol{\Delta}}^\varepsilon \mathrm{d}V, \\ \text{and } d_0^i = \displaystyle\int_\Omega \mathbf{H}_\sigma \mathbb{C}\bar{\boldsymbol{\varepsilon}}_i^p : \mathbf{H}_\sigma^{-1} \bar{\boldsymbol{\Delta}}^\varepsilon \mathrm{d}V, \\ \forall i \in \{1, \cdots, m\}, \end{array} \tag{B.18}$$

$$\mathrm{q}_{el} = \begin{bmatrix} \Delta\lambda_{1,\,n-1} \\ \Delta\lambda_{2,\,n-1} \\ \vdots \\ \Delta\lambda_{m,\,n-1} \\ \Delta\lambda_{1,\,n} \\ \Delta\lambda_{2,\,n} \\ \vdots \\ \Delta\lambda_{m,\,n} \end{bmatrix}, \tag{B.19}$$

and

$$\mathrm{T}_{el} = \begin{bmatrix} \mathcal{P}^{1,1} & \mathcal{P}^{1,2} & \dots & \mathcal{P}^{1,m} & \mathcal{Q}^{1,1} & \mathcal{Q}^{1,2} & \dots & \mathcal{Q}^{1,m} \\ \mathcal{P}^{2,1} & \mathcal{P}^{2,2} & \dots & \mathcal{P}^{2,m} & \mathcal{Q}^{2,1} & \mathcal{Q}^{2,2} & \dots & \mathcal{Q}^{2,m} \\ \vdots & \vdots & \dots & \vdots & \vdots & \vdots & \dots & \vdots \\ \mathcal{P}^{m,1} & \mathcal{P}^{m,2} & \dots & \mathcal{P}^{m,m} & \mathcal{Q}^{m,1} & \mathcal{Q}^{m,2} & \dots & \mathcal{Q}^{m,m} \\ \mathcal{Q}^{1,1} & \mathcal{Q}^{1,2} & \dots & \mathcal{Q}^{1,m} & \mathcal{R}^{1,1} & \mathcal{R}^{1,2} & \dots & \mathcal{R}^{1,m} \\ \mathcal{Q}^{2,1} & \mathcal{Q}^{2,2} & \dots & \mathcal{Q}^{2,m} & \mathcal{R}^{2,1} & \mathcal{R}^{2,2} & \dots & \mathcal{R}^{2,m} \\ \vdots & \vdots & \dots & \vdots & \vdots & \vdots & \dots & \vdots \\ \mathcal{Q}^{m,1} & \mathcal{Q}^{m,2} & \dots & \mathcal{Q}^{m,m} & \mathcal{R}^{m,1} & \mathcal{R}^{m,2} & \dots & \mathcal{R}^{m,m} \end{bmatrix}, \tag{B.20}$$

with $\mathcal{P}^{i,j} = \dfrac{a_{11}^{i,j}}{(\Delta t_n)^2}$, $\mathcal{Q}^{i,j} = -\dfrac{a_{11}^{i,j}}{(\Delta t_n)^2} + \dfrac{a_{10}^{i,j}}{\Delta t_n}$,

$\mathcal{R}^{i,j} = \dfrac{a_{11}^{i,j}}{(\Delta t_n)^2} - \dfrac{a_{10}^{i,j}}{\Delta t_n} - \dfrac{a_{10}^{i,j}}{\Delta t_n} + a_{00}^{i,j}$, where $a_{11}^{i,j} = \displaystyle\int_\Omega \bar{\varepsilon}_i^p : \mathbf{H}_\sigma^{-1} \bar{\varepsilon}_j^p \mathrm{d}V$,

$a_{10}^{i,j} = \displaystyle\int_\Omega \bar{\varepsilon}_i^p : \mathbb{C}\bar{\varepsilon}_j^p \mathrm{d}V, a_{00} = \int_\Omega \mathbf{H}_\sigma \mathbb{C}\bar{\varepsilon}_i^p : \mathbb{C}\bar{\varepsilon}_j^p \mathrm{d}V,\ \forall i,j \in \{1, \cdots, m\}$.

This elemental form needs to be assembled to achieve the form of eq. (B.15) which can then be solved using the initial values $\{\Delta\lambda_{1,\,0}, \Delta\lambda_{2,\,0}, \cdots \Delta\lambda_{m,\,0}\}$, to obtain q_{tot}.

Appendix C

Orthonormalisation of the space functions

The spatial basis functions obtained through the PGD-based technique as described in section 4.6.2.2 must be orthonormal to each other. The most common method to orthonormalise the spatial basis vectors is to use a Gram-Schmidt algorithm.

Considering $\dot{\varepsilon}_0^p$ be the elastic initialisation, at any LATIN iteration i, m is the number of modes used to approximate the plastic strain rate, i.e.

$$\dot{\varepsilon}_{i-1}^p = \dot{\varepsilon}_0^p + \sum_{j=1}^{m} \dot{\lambda}_j \bar{\varepsilon}_j^p \ . \tag{C.1}$$

Considering the case where a space-time mode is added to describe the plastic strain rate

$$\dot{\varepsilon}_i^p = \dot{\varepsilon}_0^p + \sum_{j=1}^{m} \dot{\lambda}_j \bar{\varepsilon}_j^p + \dot{\lambda}_{m+1} \bar{\varepsilon}_{m+1}^p \ , \tag{C.2}$$

where $\{\bar{\varepsilon}^p\}_{j=1}^m$ are orthonormal basis vectors but $\bar{\varepsilon}_{m+1}^p$ is not orthonormal to $\{\bar{\varepsilon}^p\}_{j=1}^m$. The spatial vector $\bar{\varepsilon}_{m+1}^p$ is orthonormalised by algorithm 2, with respect to the existing basis. To maintain equality of the solution, the temporal functions are also modified. The number of modes m is updated depending on the contribution of the new but modified temporal function and the plastic strain rate can be written as

$$\dot{\varepsilon}_i^p = \dot{\varepsilon}_0^p + \sum_{j=1}^{m} \dot{\lambda}_j \bar{\varepsilon}_j^p \ . \tag{C.3}$$

This process allows to compare the contribution of the different modes. All the modes that are generated are not considered, depending on the norm of the time functions corresponding to the orthonormal spatial basis. However, because of the Gram-Schmidt projection, useful information pertaining to the rejected modes is still taken into account.

Algorithm 2: Orthonormalisation of space functions

Write

$$\dot{\varepsilon}_i^p = \dot{\varepsilon}_0^p + \sum_{j=1}^{m} \dot{\lambda}_j \bar{\varepsilon}_j^p + \dot{\lambda}_{m+1} \left[\bar{\varepsilon}_{m+1}^p - \sum_{j=1}^{m} \frac{\left\langle \bar{\varepsilon}_{m+1}^p, \bar{\varepsilon}_j^p \right\rangle}{\left\langle \bar{\varepsilon}_j^p, \bar{\varepsilon}_j^p \right\rangle} \bar{\varepsilon}_j^p \right] + \dot{\lambda}_{m+1} \sum_{j=1}^{m} \frac{\left\langle \bar{\varepsilon}_{m+1}^p, \bar{\varepsilon}_j^p \right\rangle}{\left\langle \bar{\varepsilon}_j^p, \bar{\varepsilon}_j^p \right\rangle} \bar{\varepsilon}_{j'}^p$$

with

$$\langle \mathbf{a}, \mathbf{b} \rangle = \int_{\Omega} \mathbf{a} : \mathbf{C}\,\mathbf{b}\, \mathrm{d}V$$

for $j = \{1, \ldots, m\}$ **do**

Calculate

$$\dot{\lambda}_j = \dot{\lambda}_j + \dot{\lambda}_{m+1} \frac{\left\langle \bar{\varepsilon}_{m+1}^p, \bar{\varepsilon}_j^p \right\rangle}{\left\langle \bar{\varepsilon}_j^p, \bar{\varepsilon}_j^p \right\rangle}$$

end

Calculate

$$\bar{\varepsilon}_{m+1}^p = \frac{\left[\bar{\varepsilon}_{m+1}^p - \sum_{j=1}^{m} \frac{\left\langle \bar{\varepsilon}_{m+1}^p, \bar{\varepsilon}_j^p \right\rangle}{\left\langle \bar{\varepsilon}_j^p, \bar{\varepsilon}_j^p \right\rangle} \bar{\varepsilon}_j^p \right]}{\left\langle \left[\bar{\varepsilon}_{m+1}^p - \sum_{j=1}^{m} \frac{\left\langle \bar{\varepsilon}_{m+1}^p, \bar{\varepsilon}_j^p \right\rangle}{\left\langle \bar{\varepsilon}_j^p, \bar{\varepsilon}_j^p \right\rangle} \bar{\varepsilon}_j^p \right], \left[\bar{\varepsilon}_{m+1}^p - \sum_{j=1}^{m} \frac{\left\langle \bar{\varepsilon}_{m+1}^p, \bar{\varepsilon}_j^p \right\rangle}{\left\langle \bar{\varepsilon}_j^p, \bar{\varepsilon}_j^p \right\rangle} \bar{\varepsilon}_j^p \right] \right\rangle^{1/2}}$$

and

$$\dot{\lambda}_{m+1} = \dot{\lambda}_{m+1} \left\langle \left[\bar{\varepsilon}_{m+1}^p - \sum_{j=1}^{m} \frac{\left\langle \bar{\varepsilon}_{m+1}^p, \bar{\varepsilon}_j^p \right\rangle}{\left\langle \bar{\varepsilon}_j^p, \bar{\varepsilon}_j^p \right\rangle} \bar{\varepsilon}_j^p \right], \left[\bar{\varepsilon}_{m+1}^p - \sum_{j=1}^{m} \frac{\left\langle \bar{\varepsilon}_{m+1}^p, \bar{\varepsilon}_j^p \right\rangle}{\left\langle \bar{\varepsilon}_j^p, \bar{\varepsilon}_j^p \right\rangle} \bar{\varepsilon}_j^p \right] \right\rangle^{1/2}$$

if $\int_{[0,T]} \lambda_{m+1}^2 \, \mathrm{d}t / \int_{[0,T]} \lambda_1^2 \, \mathrm{d}t > \mu^{\mathrm{tol}}$ **then**

Update

$m = m + 1$

end

Result: $\dot{\varepsilon}_i^p = \varepsilon_0^p + \sum_{j=1}^{m} \dot{\lambda}_j \bar{\varepsilon}_j^p$

Appendix D

Alternative method of incorporating non-linear elastic state law

In chapter 4, the incorporation of damage in LATIN-PGD has been performed by including the non-linear elastic state equation in the local stage. However it is also possible to incorporate the state law in the global stage.

In the local stage, the search direction equations are

$$\begin{bmatrix} \hat{\dot{\boldsymbol{\varepsilon}}}^p_{i+1/2} - \dot{\boldsymbol{\varepsilon}}^p_i \\ -\left(\hat{\dot{\boldsymbol{X}}}_{i+1/2} - \dot{\boldsymbol{X}}_i\right) \end{bmatrix} + \mathbf{H}^+ \begin{bmatrix} \hat{\boldsymbol{\sigma}}_{i+1/2} - \boldsymbol{\sigma}_i \\ \hat{\boldsymbol{Z}}_{i+1/2} - \boldsymbol{Z}_i \end{bmatrix} = 0 \,, \tag{D.1a}$$

$$\begin{bmatrix} \hat{\dot{D}}_{i+1/2} - \dot{D}_i \end{bmatrix} + \mathbf{h}^+ \begin{bmatrix} \hat{Y}_{i+1/2} - Y_i \end{bmatrix} = 0 \,. \tag{D.1b}$$

Along with these, the evolution equations are solved.

In the global stage, the static admissibility condition can be written $\forall \delta\vec{u}$ which is kinematically admissible to zero, as

$$\int_{[0,T]\times\Omega} \Delta\boldsymbol{\sigma}_{i+1} : \boldsymbol{\varepsilon}\left(\delta\vec{u}\right) \, \mathrm{d}V \, \mathrm{d}t = 0, \tag{D.2}$$

with

$$\Delta\boldsymbol{\sigma}_{i+1} = \tilde{\mathbf{C}}_{i+1} \left(\Delta\boldsymbol{\varepsilon}_{i+1} - \Delta\boldsymbol{\varepsilon}^p_{i+1}\right). \tag{D.3}$$

$\tilde{\mathbf{C}}$ is the effective Hooke's tensor that depends on the damage variable. To separate the static admissibility condition into space and time, the effective Hooke's tensor needs to be represented in a separable form.

D.1 Series expansion of non-linear elastic law

At any LATIN iteration $i+1$, the effective Hooke's tensor $\tilde{\mathbf{C}}_{i+1}$ is expressed in the form of series of linear state laws. As per the definition of proportional loading

$$\mathrm{sign}\left(\sigma_{ij}\left(t,\vec{x}\right)\right) = \mathrm{sign}\left(tr\left[\boldsymbol{\sigma}\left(t,\vec{x}\right)\right]\right) = \mathrm{sg}\left(t,\vec{x}\right), \quad \forall\, i,j \in \{1,2,3\}\,. \tag{D.4}$$

Hooke's tensor in compliance form ($\tilde{\mathbf{K}}_{i+1} = \tilde{\mathbf{C}}_{i+1}^{-1}$) at each space-time point is calculated as

$$\tilde{\mathbf{K}}_{i+1}(t,\vec{x}) = \tilde{G}_{i+1}(t,\vec{x}) \begin{bmatrix} 1 & -\nu & -\nu & 0 & 0 & 0 \\ -\nu & 1 & -\nu & 0 & 0 & 0 \\ -\nu & -\nu & 1 & 0 & 0 & 0 \\ 0 & 0 & 0 & 1+\nu & 0 & 0 \\ 0 & 0 & 0 & 0 & 1+\nu & 0 \\ 0 & 0 & 0 & 0 & 0 & 1+\nu \end{bmatrix}, \tag{D.5}$$

with

$$\begin{aligned} \tilde{G}_{i+1}(t,\vec{x}) &= \frac{1}{E\left(1 - D_{i+1}(t,\vec{x})\right)} \text{ if } \mathrm{sg}(t,\vec{x}) \geq 0 \\ &= \frac{1}{E\left(1 - hD_{i+1}(t,\vec{x})\right)} \text{ if } \mathrm{sg}(t,\vec{x}) < 0. \end{aligned} \tag{D.6}$$

A singular value decomposition is performed on $\tilde{G}_{i+1}$ such that it is represented as

$$\tilde{G}_{i+1}(t,\vec{x}) \approx \sum_{l=1}^{q} g_{i+1}^{l}(t)\, \bar{G}_{i+1}^{l}(\vec{x}), \tag{D.7}$$

where q is the number of pre-selected modes. From this representation of $\tilde{G}_{i+1}(t,\vec{x})$, the Hooke's tensor can be written as

$$\tilde{\mathbf{K}}_{i+1}(t,\vec{x}) \approx \sum_{l=1}^{q} k_{i+1}^{l}(t)\, \bar{\mathbf{K}}_{i+1}^{l}(\vec{x}), \tag{D.8}$$

where

$$\bar{\mathbf{K}}_{i+1}^{l}(\vec{x}) = \bar{G}_{i+1}^{l}(\vec{x}) \begin{bmatrix} 1 & -\nu & -\nu & 0 & 0 & 0 \\ -\nu & 1 & -\nu & 0 & 0 & 0 \\ -\nu & -\nu & 1 & 0 & 0 & 0 \\ 0 & 0 & 0 & 1+\nu & 0 & 0 \\ 0 & 0 & 0 & 0 & 1+\nu & 0 \\ 0 & 0 & 0 & 0 & 0 & 1+\nu \end{bmatrix}, \tag{D.9}$$

and $k_{i+1}^{l}(t) = g_{i+1}^{l}(t)$.

As far as the Hooke tensor in stiffness form $\tilde{\mathbf{C}}_{i+1}(t,\vec{x})$ is concerned, it is easily represented in a similar space-time separable form as

$$\tilde{\mathbf{C}}_{i+1}(t,\vec{x}) \approx \sum_{l=1}^{q} c_{i+1}^{l}(t)\, \bar{\mathbf{C}}_{i+1}^{l}(\vec{x}), \tag{D.10}$$

where

$$c_{i+1}^{l}(t) = \frac{1}{k_{i+1}^{l}(t)}, \bar{\mathbf{C}}_{i+1}^{l}(\vec{x}) = \bar{\mathbf{K}}_{i+1}^{l}(\vec{x})^{-1}, \ \forall\, l \leq q. \tag{D.11}$$

D.2 Separable representation of the quantities of interest

The corrective terms at LATIN iteration $i+1$ are now written as

$$\Delta\boldsymbol{\sigma}_{i+1} = \sum_{l=1}^{q} \Delta\boldsymbol{\sigma}_{i+1}^{l} \quad \text{and} \quad \Delta\bar{\boldsymbol{\varepsilon}}_{i+1}^{p} = \sum_{l=1}^{q} \Delta\bar{\boldsymbol{\varepsilon}}_{i+1}^{p\,,\,l}, \tag{D.12}$$

where q is the number of SVD modes used to describe the non-linear state equation as series of linear state laws. Then each sub-corrective term is written in terms of separable form of space and time.

The development of the PGD formulation starts from the static admissibility condition defined by eq. (D.2) and is similar to the development in section 4.6.1. The only thing to be noted is because of eq. (D.10), the Hooke tensor is also represented in a separable form.

For any sub-iteration l, using the same approximation as that of section section 4.6.1 gives

$$\Delta\bar{\boldsymbol{\varepsilon}}_{i+1}^{p\,,\,l} = \dot{\lambda}\,(t)\,\bar{\boldsymbol{\varepsilon}}^{p}\,(\vec{x})\,, \tag{D.13a}$$

$$\Delta\boldsymbol{\sigma}_{i+1}^{l} = \eta\,(t)\,\bar{\boldsymbol{\sigma}}\,(\vec{x})\,, \tag{D.13b}$$

with $\eta = c_{i+1}^{l}\lambda$ and $\bar{\boldsymbol{\sigma}} = \mathbb{C}_{i+1}^{l}\bar{\boldsymbol{\varepsilon}}^{p}$. The linear operators $\mathbb{E}_{i+1}^{l}$ and $\mathbb{C}_{i+1}^{l}$ are calculated the same way as described in Appendix A. The only difference is they will not be constant but change at each sub-iteration l. Subsequently, the space-time modes are calculated using the methods described in section 4.6.2. It is evident that the time functions for space and plastic strain are no longer equal. As far as the two spatial bases are concerned, the relation between them is not consistent, and orthonormalisation of one basis does not necessarily guarantee orthonormality of the other, hence both bases need separate orthonormalisation.

The limitation of this method lies on the fact that the Hooke's tensor needs to be separated, which is not possible for non-proportional loading. However, for the case of proportional loading this method shows appreciable accuracy compared to the method described in chapter 4. This method has been tested in the same one-dimensional problem (classic example of proportional loading) as given in section 4.8.1 for 5 cycles. For simplicity, the bar has been considered to be made of a single material with $\sigma_y = 85$ MPa. Considering the solution obtained using the method described in chapter 4 as reference, the solution obtained through the method involving separation of Hooke's tensor furnished an error of 1%, where the error is defined by eq. (5.19)). This particular method, although opens a new portal in solving damage mechanics using LATIN-PGD algorithm, is not advisable. The reason is not only the limitation in solving non-proportional loading, but also the higher numerical expense due to sub-iterations as compared to the method described in chapter 4.

Appendix E

Extended summary in French

E.1 Introduction

Le phénomène de fatigue est d'une grande importance dans le dimensionnement des pièces mécaniques ainsi que des structures de génie civil. La fatigue dans un sens général peut être définie comme le changement de propriétés d'une structure soumise à un chargement répété. Ces travaux s'intéressent à la fatigue mécanique, c'est-à-dire aux fluctuations créant des contraintes dans le maté- riau. La nature du chargement peut être parfaitement périodique, non-périodique ou aléatoire. Quelle que soit la nature de la fatigue, la rupture de la structure a lieu suite à trois phases (voir Suresh, 2001) :

– la nucléation et croissance de micro-vides qui amorce une fissure macroscopique,

– la propagation stable de la fissure macroscopique,

– la propagation instable de la fissure qui mène à la rupture totale du matériau.

Trois approches sont principalement utilisées par les ingénieurs pour garantir la sécurité d'une structure (voir Suresh, 2001). L'approche dite ≪ safe-life ≫ vise à assure que la structure demeure sûre durant un certain nombre de cycles de chargement. L'approche dite ≪ fail-safe ≫ requiert que la structure soit capable de supporter un certain niveau d'endommagement sans mener immédiatement à sa rupture totale, qui serait catastrophique. Le dimensionnement en ≪ tolérance à l'endommagement ≫ s'intéresse à la capacité d'une structure à survivre à la présence d'endommagement dans l'attente d'une réparation. La vie totale en fatigue est la somme du nombre de cycles correspondant à l'initialisation de la macro-fissure et du nombre de cycles correspondant à la propagation menant à la rupture catastrophique. Les philosophies de dimensionnement parmi les ingénieurs varient selon le stade de la rupture qui est étudié, mais également selon les propriétés du matériau, le chargement, la géométrie de la structure, etc.

Quel que soit l'objectif de l'ingénieur, de nombreux développements en recherche ont lieu pour représenter les phénomènes complexes mis en jeu durant la fatigue cyclique ou aléatoire avec des modèles flexibles et pertinents.

E.1.1 Différentes modélisations proposées pour l'analyse de la fatigue

Les approches historiques pour l'analyse de la fatigue sont basées sur l'exploitation de courbes empiriques introduites par Wöhler (voir Wöhler, 1860). La représentation du niveau de contraintes imposées à la structure en fonction du nombre de cycles durant lesquels la structure survit, observé durant les expériences, produit des courbes dites courbes S-N. Ceci peut être un outil efficace pour une analyse directe de type ≪ safe-life ≫ si un chargement parfaitement périodique et de même contrainte moyenne que celle de la courbe S-N est considéré. À partir du comportement asymptotique de la courbe, une limite d'endurance, niveau de chargement en dessous duquel le matériau n'atteindra théoriquement jamais la rupture, peut être définie. Pour des chargements conduisant à des déformations plastiques conséquentes

e.g. en fatigue à faible nombre de cycles, il est plutôt recommendé de considérer une approche de type ≪ strain-life ≫ comme proposé dans Coffin (1954) et Manson (1954) pour des matériaux métalliques. Similairement aux courbes S-N qui sont utilisées pour des approches de type ≪ stress-life ≫, les courbes $\Delta\varepsilon$-N ou ε_a-N utilisées pour les approches ≪ strain-life ≫ (voir Lemaitre and Desmorat, 2005) sont des représentations des déformations totales $\Delta\varepsilon$ ou de leur amplitude ε_a ou en fonction du nombre de cycles de survie à la fatigue. Les méthodes empiriques peuvent être étendues pour traiter des cas plus sophistiqués. Par exemple, l'effet dû à la contrainte moyenne peut être pris en compte (voir Gerber, 1874, Goodman, 1899, Soderberg, 1939), ainsi que celui lié aux concentrations de contraintes dues à des entailles en utilisant la règle de Neuber (voir Neuber, 1937). La durée de vie en fatigue d'une structure soumise à des blocs de chargements de différentes amplitudes peut être étudiée en utilisant une loi d'endommagement cumulative couplée avec une courbe S-N. La loi d'accumulation peut être linéaire comme celle de Palmgren-Miner (voir Miner, 1945, Palmgren, 1924) ou non-linéaires comme la loi d'endommagement proposée par Marco and Starkey (1954).

Les méthodes pré-citées sont phénoménologiques par nature et basées sur l'utilisation de relations empiriques provenant de résultats expérimentaux. Par exemple, elles n'offrent pas la flexibilité nécessaire pour analyser les effets dus à l'ordre dans lequel les différents niveaux de chargement sont appliqués à la structure. Pour dépasser cette limitation, les changements observés dans la structure durant le chargement cyclique peuvent être décrits par des variables internes dans le cadre de la mécanique des milieux continus. L'endommagement défini en tant que variable interne est utilisé pour quantifier la phase d'initiation de fissures macroscopiques qui visent à réduire la capacité portante du matériau (voir Lemaitre and Desmorat, 2005). L'utilisation de cette approche pour prédire l'espérance de vie à la fatigue d'une structure ou d'un matériau fut introduite par Chaboche and Lesne (1988), ils utilisèrent ainsi un modèle d'endommagement continu non-linéaire pour décrire les différentes phases du procédé de détérioration du matériau. Diverses modifications et développements ont été réalisés au fil des années pour améliorer la modélisation de l'endommagement par fatigue et incorporer les différents phénomènes physiques aussi précisément que possible. Par exemple, quand le chargement est important, la structure subit d'importantes déformations plastiques, menant à une durée de vie restreinte, en général inférieure à 10^5 cycles, ce cas est dénommé fatigue oligocycliques ou à faible nombre de cycles. Au contraire, lors de cas de fatigue à grand nombre de cycles, le chargement est beaucoup plus faible que la limite d'élasticité. Donc, aucune déformation plastique macroscopique n'est mise en jeu, la structure peut supporter un très grand nombre de cycles. Le modèle d'endommagement à deux échelles (voir Lemaitre et al., 1997) est un développement majeur pour la modélisation de la fatigue à grand nombre de cycles, il représente le comportement macroscopique élastique alors que l'endommagement est évalué seulement à l'échelle microscopique.

Pour étudier la propagation d'une macro-fissure, le cadre de la mécanique de la fracture est utilisé connaissant la pré-existence d'une fissure dans le matériau. La loi la plus traditionnelle pour décrire la croissance des fissures est la loi de Paris-Erdogan (voir Paris and Erdogan, 1963).

Plus d'informations sur les techniques classiques et les développements récents au sujet de la modélisation et des simulations pour des cas de fatigue peuvent être trouvées par exemple dans Cui (2002). Une approche de description continue de l'endommagement est ici utilisée pour modéliser le comportement à la fatigue de manière flexible. Ceci permet de considérer la chronologie des différents cycles ou les effets d'inertie dus à des cycles à hautes fréquences. Cependant, cette approche peut mener à des coûts de calcul prohibitifs. Des développements ont été réalisés dans le cadre de techniques numériques nouvelles et robustes pour réduire le coût de calcul. Par exemple, ce problème peut être surmonté en utilisant des techniques de réduction d'ordre de modèles.

E.1.2 Techniques de réduction de modèles pour des calculs en fatigue

La réduction d'ordre de modèle est une famille de stratégies numériques qui a montré son efficacité pour de nombreux problèmes à grande dimension tels que les études paramétriques ou les calculs en temps réel (voir Cueto et al., 2014). La solution est recherchée en résolvant le problème de Galerkin dans une base d'ordre réduit, c'est-à-dire dont la dimension est beaucoup plus faible que la taille du modèle originel à grande dimension. L'utilisation d'une décomposition orthogonale aux valeurs propres

(Proper orthogonal decomposition : POD) dans le champ de la mécanique est basée sur la construction initiale d'une base réduite désignée ici comme base POD, à partir des snapshots de la solution de l'étape d'apprentissage. Ensuite, cette base est utilisée pour résoudre le problème d'intérêt à coût réduit (Néron and Ladevèze, 2010, Ryckelynck, 2009). La POD fournit une base réduite optimale au sens des moindres carrés pour la solution du problème d'ordre complet. En utilisant une décomposition propre généralisée (Proper Generalised Decomposition : PGD), le problème est également résolu sur une base réduite, mais cette base est définie au cours du calcul en fonction du problème considéré par un algorithme glouton Chinesta et al. (2013, 2014b), Ladevèze (1999). Cette technique ne requiert aucune phase d'apprentissage et évalue la qualité du modèle réduit au cours des itérations enrichissant la base réduite si besoin.

La méthode LATIN (voir Ladevèze, 1999) est une approche numérique dans laquelle une approximation de la solution est recherchée sur l'ensemble du domaine spatio-temporel à chaque itération, l'équilibre global traité en tant que problème linéarisé et le comportement non-linéaire du matériau sont considérés séparément. Donc, cette approche offre un cadre approprié pour inclure des techniques de réduction d'ordre de modèle même pour des problèmes a priori non linéaires. Elle a été développée initialement pour résoudre des problèmes plastiques et visco-plastiques et a montré une réduction drastique du coût numérique en comparaison aux approches traditionnelles aussi bien dans son cadre initial que dans de nombreuses applications dans les dernières décennies (voir Ladevèze, 2014, Relun et al., 2013). Une nouvelle version est proposée dans ces travaux de thèse pour étudier des problèmes (visco-)plastiques avec endommagement par fatigue prenant en compte l'effet de fermeture des micro-défauts.

Pour des simulations des fatigue appliquées à un grand nombre de cycles, des stratégies numéri- ques particulières sont nécessaires pour éviter le coût numérique dû à l'étendue du domaine temporel, il peut être remarqué que dans le cadre de simulations de fatigue, ce n'est pas un calcul en temps réel qui est recherché, mais un calcul à temps réduit.

E.1.3 Schémas temporaux efficaces pour des calculs de fatigue

Pour des cas de chargements de fatigue à grand ou très grand nombre de cycles ou dans des cas de fatigue combinée, c'est-à-dire pour lesquels le chargement est une combinaison de chargement à large amplitude-basse fréquence et faible amplitude-haute fréquence (voir Suresh, 2001), le coût numérique dû aux schémas d'intégration temporelle peut être extrêmement élevé. Ce coût peut être réduit en bénéficiant de la nature cyclique du chargement pour ne pas calculer explicitement l'ensemble des cycles.

La procédure par saut de cycles est une technique très robuste (voir Lemaitre and Desmorat, 2005) qui évite le calcul de blocs entiers de cycles. Après avoir calculé en détail un ensemble de cycles, le résultat est utilisé pour établir une tendance d'évolution et extrapoler les quantités d'intérêt durant la suite du chargement. Ainsi, un état initial extrapolé est utilisé pour calculer un cycle futur et extrapoler un bloc de cycles suivants, ainsi de suite jusqu'à ce que l'ensemble du domaine temporel soit simulé. Une fonction de contrôle a été proposée de sorte que la longueur des sauts de cycles soit adaptée pour garantir une qualité d'approximation acceptable (voir Cojocaru and Karlsson, 2006). Cette méthode est très appropriée et effiace pour des systèmes aux comportement quasi-linéaires. Cependant, la fonction de contrôle permet également de considérer des comportements non-linéaires, les sauts de cycles sont alors automatiquement raccourcis voire abandonnés.

Pour les cas de fatigue combinée, les techniques d'homogénéisation temporelles peuvent être utilisées. Elles sont basées sur une hypothèse de séparation d'échelle de temps entre une échelle de temps large associée avec le chargement à basse fréquence et une échelle de temps court associée avec le chargement à haute fréquence. Le rapport entre ces deux temps est supposé suffisamment faible pour considérer que les deux échelles sont indépendantes. Ainsi, le comportement dû à la fréquence élevée est homogénéisé et le problème est résolu pour une discrétisation temporelle adaptée au chargement à basses fréquences. Développée initialement pour des cas quasi-statiques et des comportement plastiques (voir Guennouni and Aubry, 1986), cette méthode a été étendue plus récemment pour des cas avec endommagement ou effets dynamiques (voir Oskay and Fish, 2004b).

Dans le cadre de la méthode LATIN, comme l'ensemble du domaine temporel est étudié à chaque itération, une double échelle temporelle dans le cadre d'une discrétisation de type ≪ éléments finis ≫ a

été proposée pour des problèmes de visco-plasticité (voir Cognard and Ladevèze, 1993, Ladevèze, 1999). Seulement quelques cycles d'intérêt, appelés ≪ nœuds temporels ≫ ou ≪ cycles nodaux ≫, sont calculés en utilisant un schéma temporel traditionnel. L'évolution des quantités d'intérêt entre deux nœuds est interpolée en utilisant des fonctions de forme de manière similaire à la méthode des éléments finis spaciaux.

Les méthodes empiriques étant basées sur des expériences complexes et coûteuses, le but de ce projet est de développer une approche numérique permettant de prévoir le comportement en fatigue basé sur la mécanique des milieux continus. Pour faire face au coût numérique induit par ces modèles, un schéma numérique basé sur une réduction d'ordre de modèle approprié est proposé qui permet de simuler des tests virtuels pour de très grands nombres de cycles avec un coût raisonnable. Le schéma numérique proposé est flexible quant au modèle phénoménologique d'endommagement considéré. Le cadre général ainsi que les équations considérées sont résumées dans la section E.2. Ensuite, la réduction d'ordre de modèle basée sur la méthode LATIN-PGD est introduite dans la section E.3. Finalement, le traitement numérique du problème temporel qui permet de réduire le coût numérique est détaillé dans la section E.4.

E.2 Approche basée sur la mécanique des milieux continus

L'intérêt se porte ici sur les méthodes qui traitent de la simulation de structures soumises à des chargements par fatigue en utilisant une variable interne d'endommagement dans le cadre de la mécanique des milieux continues. Une structure de référence continue est considérée pour des analyses quasi-statiques

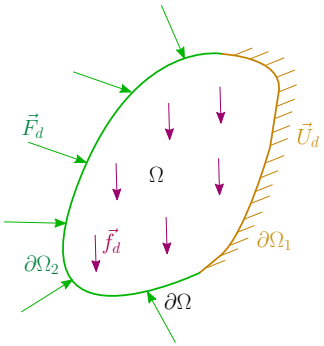

Figure E.1: Problème de référence dans le domaine Ω

sur une domaine spatial Ω (voir fig. E.1). Dans un cadre simplifié, l'évolution de l'état des structures peut être considérée pour être isotherme sur le domaine temporel $[0, T]$. Une telle structure en général est soumise à des forces volumiques $\vec{f}_d$, des forces de traction $\vec{F}_d$ sur la partie $\partial_2\Omega$ de la frontière $\partial\Omega$, et à des déplacements imposés $\vec{u}_d$ sur la partie complémentaire $\partial_1\Omega$. Ainsi, la compatibilité des forces appliquées avec les contraintes internes est assurée par la condition statique d'admissibilité, qui est définie telle que

$$-\int_{\Omega\times[0,T]} \boldsymbol{\sigma} : \delta\dot{\boldsymbol{\varepsilon}}\mathrm{d}V\mathrm{d}t + \int_{\Omega\times[0,T]} \vec{f}_d \cdot \delta\dot{\vec{u}}\,\mathrm{d}V\mathrm{d}t + \int_{\partial\Omega_2\times[0,T]} \vec{F}_d \cdot \delta\dot{\vec{u}}\,\mathrm{d}S\mathrm{d}t = 0, \qquad \text{(E.1)}$$

avec le tenseur des contraintes $\boldsymbol{\sigma}$ statiquement admissible, et $\delta\vec{u}$ qui est un champ cinématiquement admissible. D'autre part, la compatibilité des déplacement prescrits avec la déformation générée dans la

structure est établie à partir de la condition cinématique d'admissibilité, qui est définie telle que

$$-\int_{\Omega\times[0,T]} \delta\boldsymbol{\sigma} : \dot{\boldsymbol{\varepsilon}}\, \mathrm{d}V\mathrm{d}t + \int_{\partial\Omega_1\times[0,T]} \delta\boldsymbol{\sigma}\cdot\vec{n}\cdot\dot{\vec{U}}_d\, \mathrm{d}S\mathrm{d}t = 0, \tag{E.2}$$

où $\boldsymbol{\varepsilon}$ est le tenseur de déformations totales qui est cinématiquement admissible et peut être séparé en une partie élastique $\boldsymbol{\varepsilon}^e$ et une partie plastique $\boldsymbol{\varepsilon}^p$ additivement. $\delta\boldsymbol{\sigma}$ est un champ statiquement admissible.

Les propriétés mécaniques des matériaux sont décrites par un ensemble de relations constitutives. Les équations d'état pour les matériaux élasto-plastiques soumis à un endommagement unilatéral sont obtenues à partir de la fonction d'énergie libre (voir Lemaitre and Desmorat, 2005)

$$\varepsilon^e_{ij} = \frac{1+\nu}{E}\left[\frac{\langle\sigma\rangle^+_{ij}}{1-D} + \frac{\langle\sigma\rangle^-_{ij}}{1-hD}\right] - \frac{\nu}{E}\left[\frac{\langle\sigma_{kk}\rangle}{1-D} + \frac{\langle-\sigma_{kk}\rangle}{1-hD}\right]\delta_{ij}, \tag{E.3a}$$

$$\beta_{ij} = Q\alpha_{ij}, \tag{E.3b}$$

$$R = R_\infty\left(1-\exp\left(-\gamma r\right)\right), \tag{E.3c}$$

$$Y = \frac{1+\nu}{2E}\left[\frac{\langle\sigma\rangle^+_{ij}\langle\sigma\rangle^+_{ij}}{(1-D)^2} + h\frac{\langle\sigma\rangle^-_{ij}\langle\sigma\rangle^-_{ij}}{(1-hD)^2}\right] - \frac{\nu}{2E}\left[\frac{\langle\sigma_{kk}\rangle^2}{(1-D)^2} + h\frac{\langle-\sigma_{kk}\rangle^2}{(1-hD)^2}\right]. \tag{E.3d}$$

Ici, l'éq. (E.3a) représente la loi d'état élastique, qui à cause de l'endommagement est non-linéaire par nature, et n'est donc pas décrite par un opérateur linéaire. E et ν sont le module d'élasticité et le coefficient de Poisson respectivement. D est la variable d'endommagement isotropique et h le paramètre de fermeture représentant l'effet de fermeture des micro-défauts, il indique que l'endommagement a un effet plus important lors d'un chargement en tension qu'en compression. Durant la compression, une partie des micro-défauts sont refermés, ainsi la surface effective du matériau soutenant la charge est augmentée, le matériau regagne de la rigidité en apparence. Cet effet peut être représenté par un module d'élasticité effectif durant la tension $\tilde{E}^+$, défini comme $\tilde{E}^+ = E\left(1-D\right)$, alors que le module effectif d'élasticité durant la compression $\tilde{E}^-$ est donné par $\tilde{E}^- = E\left(1-hD\right)$. Ce paramètre de fermeture a des valeurs comprises entre 0 (regain complet de la rigidité) et 1 (aucun regain de rigidité). Les éq. (E.3b) et (E.3c) fournissent les relations entre les variables internes α_{ij} et r décrivant l'écrouissage cinématique et isotropique des matériaux et les forces thermodynamiques relatives β_{ij} et R, en utilisant le paramètre matériau Q pour l'écrouissage cinématique et les paramètres matériaux R_∞ et γ pour l'écrouissage isotropique. L'éq. (E.3d) définit le taux d'énergie libérée Y, qui est la force thermodynamique correspondant à l'endommagement, c'est une fonction non-linéaire du tenseur des contraintes et de la variable d'endommagement.

Les équations d'évolution sont obtenues à partir des potentiels basés sur le modèle de Marquis-Chaboche :

$$\dot{\boldsymbol{\varepsilon}}^p = k\left\langle f^p\right\rangle^n_+\left[\frac{\frac{3}{2}\dfrac{\boldsymbol{\varrho}}{\sqrt{\frac{3}{2}\left[\boldsymbol{\varrho}:\boldsymbol{\varrho}\right]}}}\right]\frac{1}{1-D}, \tag{E.4a}$$

$$\dot{\alpha} = -k\left\langle f^p\right\rangle^n_+\left[-\frac{3}{2}\frac{\boldsymbol{\varrho}}{\sqrt{\frac{3}{2}\left[\boldsymbol{\varrho}:\boldsymbol{\varrho}\right]}} + a\mathbf{Q}^{-1}\boldsymbol{\beta}\right], \tag{E.4b}$$

$$\dot{r} = k\left\langle f^p\right\rangle^n_+, \tag{E.4c}$$

$$\dot{D} = k_d\left\langle f^d\right\rangle^{n_d}_+, \tag{E.4d}$$

avec $\boldsymbol{\varrho} = \dfrac{\boldsymbol{\sigma}^D}{1-D} - \boldsymbol{\beta}$ et $\boldsymbol{\sigma}^D$ étant la partie déviatorique du tenseur des contraintes. La limite d'élasticité est définie également par le modèle de Marquis-Chaboche :

$$f^p = \sqrt{\frac{3}{2}\left[\boldsymbol{\varrho} : \boldsymbol{\varrho}\right]} + \frac{a}{2}\left[\boldsymbol{\beta} : \mathbf{Q}^{-1}\boldsymbol{\beta}\right] - R - \sigma_y. \tag{E.5}$$

Les paramètres relatifs aux matériaux k et n décrivent le comportement visqueux. La fonction limite relative à l'endommagement est donnée par

$$f^d = Y - Y_{th} \tag{E.6}$$

avec Y_{th} la valeur limite, n_d et k_d des paramètres spécifiques au matériau considéré.

L'initiation d'une fissure macroscopique est indiquée par l'endommagement critique D_c, valeur pour laquelle la rupture du matériau est considérée atteinte.

E.3 Approche par réduction d'ordre de modèle basée sur la méthode LATIN pour les calculs d'endommagement

L'approche LATIN cherche à résoudre les équations définissant le problème sur l'ensemble du domaine spatio-temporel à chaque itération. Les équations sont traitées itérativement, à savoir l'équilibre global de la structure d'une part, la loi élastique et les équations d'évolution non linéaires d'autre part. Une réduction de modèle est utilisée par l'intermédiaire d'une séparation des dépendances en temps et en espace. L'approche LATIN-PGD permet pour les structures ayant un comportement visco-plastique de définir les deux quantités d'intérêt, qui sont les contraintes et les déformations plastiques, en utilisant une unique base temporelle. Pour examiner des cas incluant de l'endommagement, une nouvelle quantité d'intérêt, la déformation élastique, est introduite. Le champ solution est noté $\boldsymbol{s} = \left\{\dot{\boldsymbol{\varepsilon}}^p, \dot{\boldsymbol{\varepsilon}}^e, \dot{\boldsymbol{X}}, \dot{D}, \dot{\boldsymbol{\sigma}}, \dot{\boldsymbol{Z}}, \dot{Y}\right\}$ où $\boldsymbol{X}$ représente l'ensemble des variables d'écrouissage (cinématique et isotropique) et $\boldsymbol{Z}$ est la variable conjuguée à $\boldsymbol{X}$. La loi d'état non-linéaire peut être incluse dans l'étape globale conduisant à une séparation de variables utilisant différentes fonctions temporelles pour les contraintes et les déformations. Sinon, comme présenté ici, la non-linéarité due à la loi d'état peut être considérée à l'étape locale et les contraintes peuvent être séparées en deux contributions, l'une définie à l'étape locale et l'autre écrite en tant que décomposition en formes dépendant indépendemment du temps et de l'espace utilisant les mêmes fonctions temporelles que pour la déformation plastique.

L'algorithme est initialisé par la résolution d'un problème considérant les conditions aux limites du problème d'intérêt mais un comportement du matériau parfaitement élastique quelles que soient les conditions de chargement. Puis, des corrections liées à la plasticité et à l'endommagement sont ajoutées successivement à la solution élastique à chaque itération. L'ensemble des équations est divisé en deux sous-groupes, l'un comprenant les équations globales et linéaires alors que le second comprend les équations locales et non-linéaires. Une itération LATIN se compose de deux étapes :

- le problème global et linéaire est résolu dans l'espace $\boldsymbol{A_d}$ qui appartient à la variété des conditions d'admissibilité éq. (E.1) et éq. (E.2), des lois d'état linéaires éq. (E.3b) et éq. (E.3c), et de la loi d'état non-linéaire pour l'endommagement éq. (E.3d) ;
- le problème local et non-linéaire est résolu dans l'espace $\boldsymbol{\Gamma}$ qui appartient à la variété des équations d'évolution éq. (E.4) et de la loi d'état élastique éq. (E.3a) qui n'est pas linéarisable à cause de l'endommagement.

Il peut être remarqué que l'éq. (E.3d) bien que non linéaire est abordée avec le groupe des équations linéaires comme une étape de post-traitement à partir de la connaissance du tenseur des contraintes et de la variable d'endommagement à la fin de chaque itération. La solution exacte du problème $\boldsymbol{s}_{ex}$ est définie comme l'intersection des deux variétés par

$$\boldsymbol{s}_{ex} \in \boldsymbol{A_d} \cap \boldsymbol{\Gamma}. \tag{E.7}$$

L'estimation de la solution est recherchée alternativement dans les deux variétés jusqu'à atteindre la convergence. À partir de l'estimation de la solution dans une étape, l'approximation est recherchée dans la variété suivante en utilisant certains opérateurs linéaires appelés opérateurs de direction de recherche.

E.3.1 Étape locale

À l'étape locale, les équations d'évolution pour les variables internes sont résolues, elles sont locales en espace et non-linéaires. La loi d'état élastique étant non-linéaire est également traitée durant cette étape. À partir de la solution $\boldsymbol{s}_i \in \boldsymbol{A_d}$ à l'itération LATIN i, l'estimation $\hat{\boldsymbol{s}}_{i+1/2} \in \boldsymbol{\Gamma}$ est réalisée de telle sorte que les directions de recherche locale soient satisfaites

$$\begin{bmatrix} \hat{\boldsymbol{\varepsilon}}^p_{i+1/2} - \dot{\boldsymbol{\varepsilon}}^p_i \\ -\left(\hat{\boldsymbol{X}}_{i+1/2} - \dot{\boldsymbol{X}}_i\right) \\ \hat{\boldsymbol{\varepsilon}}^e_{i+1/2} - \dot{\boldsymbol{\varepsilon}}^e_i \\ \hat{D}_{i+1/2} - \dot{D}_i \end{bmatrix} + \mathbf{B}^+ \begin{bmatrix} \hat{\boldsymbol{\sigma}}_{i+1/2} - \boldsymbol{\sigma}_i \\ \hat{\boldsymbol{Z}}_{i+1/2} - \boldsymbol{Z}_i \\ \hat{\boldsymbol{\sigma}}_{i+1/2} - \boldsymbol{\sigma}_i \\ \hat{Y}_{i+1/2} - Y_i \end{bmatrix} = 0. \tag{E.8}$$

Ici, la direction de descente est notée $\mathbf{B}^+$. En suivant l'idée proposée par Ladevèze (1999), la direction de recherche est considérée verticale de telle manière que

$$\left(\mathbf{B}^+\right)^{-1} = 0. \tag{E.9}$$

La solution de l'équation définissant la direction de recherche éq. (E.8) ainsi que des équations d'évolution éq. (E.4) et de la loi élastique non-linéaire éq. (E.3a) constitue l'estimation $\hat{\boldsymbol{s}}_{i+1/2}$. À partir de cette approximation, la solution de l'étape globale $\boldsymbol{s}_{i+1}$ est recherchée.

E.3.2 Étape globale incluant une réduction d'ordre de modèle

À l'étape globale, la solution $\boldsymbol{s}_{i+1} \in \boldsymbol{A_d}$ satisfait les lois d'état, les conditions d'admissibilité et les directions de recherche descendantes :

$$\begin{bmatrix} \dot{\boldsymbol{\varepsilon}}^p_{i+1} - \hat{\boldsymbol{\varepsilon}}^p_{i+1/2} \\ -\left(\dot{\boldsymbol{X}}_{i+1} - \hat{\dot{\boldsymbol{X}}}_{i+1/2}\right) \\ \boldsymbol{\varepsilon}^e_{i+1} - \hat{\boldsymbol{\varepsilon}}^e_{i+1/2} \end{bmatrix} - \mathbf{B}^- \begin{bmatrix} \boldsymbol{\sigma}_{i+1} - \hat{\boldsymbol{\sigma}}_{i+1/2} \\ \boldsymbol{Z}_{i+1} - \hat{\boldsymbol{Z}}_{i+1/2} \\ \boldsymbol{\sigma}_{i+1} - \hat{\boldsymbol{\sigma}}_{i+1/2} \end{bmatrix} = 0 \tag{E.10a}$$

$$\begin{bmatrix} \dot{D}_{i+1} - \hat{D}_{i+1/2} \end{bmatrix} - \mathbf{b}^- \begin{bmatrix} Y_i - \hat{Y}_{i+1/2} \end{bmatrix} = 0, \tag{E.10b}$$

où $\mathbf{B}^- = \begin{bmatrix} \mathbf{H}^- & 0 \\ 0 & \mathbf{C}^{-1} \end{bmatrix}$. L'opérateur $\mathbf{H}^-$ appartient à l'espace tangent associé à la solution $\hat{\boldsymbol{s}}_{i+1/2}$ dans la variété $\boldsymbol{\Gamma}$ et $\mathbf{C}$ est le tenseur de Hooke pour le matériau non endommagé. En considérant que la variable d'endommagement n'est pas actualisée durant l'étape linéaire, l'opérateur de direction de recherche $\mathbf{b}^-$ est défini comme nul.

La première étape étant le calcul des variables d'écrouissage, les équations d'état sont combinées sous la forme

$$\boldsymbol{Z}_{i+1} = \boldsymbol{\Pi} \boldsymbol{X}_{i+1} \tag{E.11}$$

où $\boldsymbol{\Pi}$ est un opérateur linéaire incluant les paramètres relatifs aux lois d'état. L'équation de direction de recherche pour les variables d'écrouissage éq. (E.10a) combinée avec l'équation d'état éq. (E.11) peut être écrite

$$-(\dot{\boldsymbol{X}}_{i+1} - \hat{\dot{\boldsymbol{X}}}_{i+1/2}) = \mathbf{H}_Z(\boldsymbol{\Pi} \boldsymbol{X}_{i+1} - \hat{\boldsymbol{Z}}_{i+1/2}), \tag{E.12}$$

avec $\mathbf{H}_Z$ étant la part découplée de $\mathbf{H}^-$ qui relie les variables internes à leurs variables associées. Les variables d'écrouissage sont ainsi obtenues en résolvant l'éq. (E.10a) en temps à chaque point de Gauss. Il peut être mentionné que la validité de l'éq. (E.11) présuppose que les variables d'écrouissage isotropique aient été transformées de telle sorte que l'équation d'état devienne linéaire, c'est-à-dire qu'elle suivent une ≪ formulation normale ≫ (voir Bhattacharyya et al., 2017, Cognard and Ladevèze, 1993, pour plus de détails).

La difficulté pour calculer les contraintes et déformations par rapport aux travaux précédents également basés sur la méthode LATIN est que loi d'état élastique éq. (E.3a) est ici potentiellement non-linéaire à cause de la possibilité d'endommagement. La présence d'un problème non-linéaire s'oppose a priori à l'utilisation d'une technique de réduction de modèle. L'idée proposée ici vise à transformer ce problème non-linéaire en deux équations indépendantes en décomposant les contraintes et les déformations totales en un partie dépendant de la déformation plastique d'une part, et une partie dépendant du niveau d'endommagement d'autre part.

Les quantités d'intérêt à ce point $\boldsymbol{\sigma}_{i+1}$, $\boldsymbol{\varepsilon}^e_{i+1}$ et $\dot{\varepsilon}^p_{i+1}$ sont représentées en forme corrective à l'itération $i+1$, c'est-à-dire

$$\Delta\boldsymbol{\sigma}_{i+1} = \boldsymbol{\sigma}_{i+1} - \boldsymbol{\sigma}_i, \quad \Delta\boldsymbol{\varepsilon}^e_{i+1} = \boldsymbol{\varepsilon}^e_{i+1} - \boldsymbol{\varepsilon}^e_i \quad \text{et} \quad \Delta\dot{\varepsilon}^p_{i+1} = \dot{\varepsilon}^p_{i+1} - \dot{\varepsilon}^p_i. \tag{E.13}$$

Les corrections en termes de contraintes et de déformations totales à l'étape globale de l'itération $i+1$ sont ainsi séparées en parties dépendant de la déformation plastique ($\Delta\boldsymbol{\sigma}'_{i+1}$, $\Delta\boldsymbol{\varepsilon}'_{i+1}$) et de l'endommagement ($\Delta\tilde{\boldsymbol{\sigma}}_{i+1}$, $\Delta\tilde{\boldsymbol{\varepsilon}}_{i+1}$) de telle sorte que

$$\Delta\boldsymbol{\sigma}_{i+1} = \Delta\boldsymbol{\sigma}'_{i+1} + \Delta\tilde{\boldsymbol{\sigma}}_{i+1}, \tag{E.14a}$$

$$\Delta\boldsymbol{\varepsilon}_{i+1} = \Delta\boldsymbol{\varepsilon}'_{i+1} + \Delta\tilde{\boldsymbol{\varepsilon}}_{i+1}. \tag{E.14b}$$

À partir de ces séparations et de l'équation de direction de recherche ainsi que de la relation additive de décomposition des déformations, il peut être établi que

$$\Delta\boldsymbol{\sigma}'_{i+1} + \Delta\tilde{\boldsymbol{\sigma}}_{i+1} = \mathbf{C}\left(\Delta\boldsymbol{\varepsilon}'_{i+1} - \Delta\boldsymbol{\varepsilon}^p_{i+1}\right) + \mathbf{C}\left(\Delta\tilde{\boldsymbol{\varepsilon}}_{i+1} - \Delta\boldsymbol{\varepsilon}^R_{i+1}\right), \tag{E.15}$$

où $\Delta\boldsymbol{\varepsilon}^R_{i+1}$ peut être interprété comme une déformation résiduelle provenant de la loi d'état non-linéaire à l'itération $i+1$. Les termes correctifs $\Delta\tilde{\boldsymbol{\sigma}}_{i+1}$ et $\Delta\tilde{\boldsymbol{\varepsilon}}_{i+1}$ sont ainsi obtenus à partir de l'équation d'équilibre, directement.

D'autre part, si seulement la partie plastique est considérée, la direction de recherche peut être écrite

$$\Delta\boldsymbol{\varepsilon}^p_{i+1} - \mathbf{H}_\sigma\Delta\boldsymbol{\sigma}'_{i+1} + \bar{\boldsymbol{\Delta}}_{i+1} = 0, \tag{E.16}$$

où $\bar{\boldsymbol{\Delta}}_{i+1}$ est un terme correctif plastique provenant de l'étape locale et $\mathbf{H}_\sigma$ représente la partie découplée de $\mathbf{H}^-$ qui rellie la contrainte aux taux de déformation plastique.

Les termes de correction relatifs au comportement plastique $\Delta\sigma'_{i+1}$ et $\Delta\varepsilon'_{i+1}$ sont alors écrits dans une forme séparable en utilisant la PGD.

E.3.2.1 Séparation de variables

La Décomposition Propre Généralisée (PGD) est une technique de réduction d'ordre de modèles flexible, qui n'est pas basée sur une phase d'entraînement. Étant donné qu'à chaque itération LATIN, les quantités d'intérêt sont approximées sur l'ensemble du domaine spatio-temporel par une forme linéaire de l'équilibre mécanique, l'utilisation de la PGD couplée avec la méthode LATIN est opportune. Toute fonction dépendant de plusieurs variables indépendantes peut s'écrire sous la forme d'une somme infinie de produits de fonctions dépendantes d'une seule variable (voir Ladevèze, 1999, 2014), la PGD recherche des approximations des quantités d'intérêt sous la forme de sommes finies de produits de fonctions définies dans des espaces de plus petite dimension que la fonction originelle en utilisant un algorithme glouton.

Donc, cette approximation inclut une erreur due à la troncature de la série de formes séparables. Ici la déformation plastique et la part des contraintes relatives à la déformation plastique sont approximées par

$$\begin{aligned}\dot{\boldsymbol{\varepsilon}}^p(\vec{x},t) &= \sum_{j=1}^{m} \dot{\lambda}_j(t)\,\bar{\boldsymbol{\varepsilon}}_j^p(\vec{x}),\\ \boldsymbol{\sigma}'(\vec{x},t) &= \sum_{j=1}^{m} \lambda_j(t)\,\mathbb{C}\bar{\boldsymbol{\varepsilon}}_j^p(\vec{x}),\end{aligned} \tag{E.17}$$

où m est le nombre de paires considérées dans la décomposition, et $\mathbb{C}$ est un opérateur linéaire qui lie les fonctions spatiales relatives aux contraintes et aux déformations plastiques.

E.3.2.2 Mise à jour de la base réduite

L'algorithme glouton est tel qu'après avoir défini une première paire de fonctions d'espace et de temps à la volée, à chaque itération une première décomposition est recherchée en réutilisant les fonctions spatiales prédéfinies et en actualisant les fonctions temporelles. Cette étape est équivalente à une décomposition orthogonale aux valeurs propres (POD) sur la base spatiale établie. En considérant que m modes spatiaux-temporels ont été générés pour approximer les contraintes et les déformations plastiques à l'itération i, les termes correctifs des contraintes et des taux de déformation plastique à l'itération $i+1$ sont donnés par

$$\begin{aligned}\Delta\dot{\boldsymbol{\varepsilon}}_{i+1}^p(\vec{x},t) &= \sum_{j=1}^{m} \Delta\dot{\lambda}_j(t)\,\bar{\boldsymbol{\varepsilon}}_j^p(\vec{x}),\\ \Delta\boldsymbol{\sigma}'_{i+1}(\vec{x},t) &= \sum_{j=1}^{m} \Delta\lambda_j(t)\,\mathbb{C}\bar{\boldsymbol{\varepsilon}}_j^p(\vec{x}).\end{aligned} \tag{E.18}$$

Les fonctions temporelles mises à jour sont calculées par minimisation d'un résidu mécanique qui est défini comme la norme de l'opérateur définissant la direction de recherche, c'est-à-dire

$$\{\Delta\lambda_j\}_{j=1}^m = \underset{\{\Delta\lambda_i\}_{j=1}^m}{\arg\min} \left\| \sum_{j=1}^{m} \Delta\dot{\lambda}_j\bar{\boldsymbol{\varepsilon}}_j^p - \mathbf{H}_\sigma \sum_{j=1}^{m} \Delta\lambda_j\mathbb{C}\bar{\boldsymbol{\varepsilon}}_j^p + \bar{\boldsymbol{\Delta}} \right\|_{\mathbf{H}_\sigma^{-1}}. \tag{E.19}$$

Puis, si l'amélioration de l'approximnation n'est pas suffisamment importante, une nouvelle paire est ajoutée à la décomposition.

E.3.2.3 Enrichissement de la base spatio-temporelle

L'objectif de la phase d'enrichissement est d'ajouter une nouvelle paire de fonctions spatio-temporelles. Les corrections des contraintes et déformation plastiques sont écrites comme

$$\begin{aligned}\Delta\dot{\boldsymbol{\varepsilon}}_{i+1}^p(\vec{x},t) &= \dot{\lambda}_{m+1}(t)\,\bar{\boldsymbol{\varepsilon}}_{m+1}^p(\vec{x}),\\ \Delta\boldsymbol{\sigma}'_{i+1}(\vec{x},t) &= \lambda_{m+1}(t)\,\mathbb{C}\bar{\boldsymbol{\varepsilon}}_{m+1}^p(\vec{x}),\end{aligned} \tag{E.20}$$

avec l'intention de calculer les quantités séparables $\dot{\lambda}_{m+1}$ et $\bar{\boldsymbol{\varepsilon}}_{m+1}^p$.

Une stratégie hybride est utilisée, la fonction spatiale $\bar{\boldsymbol{\varepsilon}}_{m+1}^p$ est calculée à partir d'une formulation de Galerkin, en utilisant la condition d'admissibilité cinématique éq.E.2, tel que $\forall\delta\boldsymbol{\sigma}$ statiquement admissible à zéro

$$\int_{[0,T]\times\Omega} \Delta\boldsymbol{\varepsilon}' : \delta\boldsymbol{\sigma}\,\mathrm{d}\Omega\,\mathrm{d}t = 0, \tag{E.21}$$

et la condition d'admissibilité statique définie par l'éq. (E.1) telle que $\forall \delta\vec{u}$ cinématiquement admissible à zéro

$$\int_{[0,T]\times\Omega} \Delta\boldsymbol{\sigma}'_{i+1} : \boldsymbol{\varepsilon}\left(\delta\vec{u}\right) \, \mathrm{d}\Omega \, \mathrm{d}t = 0 \tag{E.22}$$

avec

$$\Delta\boldsymbol{\sigma}'_{i+1} = \mathbf{C}\left(\Delta\boldsymbol{\varepsilon}'_{i+1} - \Delta\boldsymbol{\varepsilon}^p_{i+1}\right). \tag{E.23}$$

Puis la fonction temporelle $\boldsymbol{\lambda}_{m+1}$ est résolue similairement à l'étape d'apprentissage par minimisation d'un résidu mécanique

$$\boldsymbol{\lambda}_{m+1} = \underset{\boldsymbol{\lambda}_{m+1}}{\arg\min} \left\| \dot{\boldsymbol{\lambda}}_{m+1}\bar{\boldsymbol{\varepsilon}}^p_{m+1} - \mathbf{H}_\sigma \boldsymbol{\lambda}_{m+1}\mathbb{C}\bar{\boldsymbol{\varepsilon}}^p_{m+1} + \bar{\boldsymbol{\Delta}} \right\|_{\mathbf{H}_\sigma^{-1}}. \tag{E.24}$$

Cet algorithme par point fixe entre les problèmes spaciaux et temporels converge rapidement.

Une fois le tenseur des contraintes connu à l'itération $i+1$, le taux de libération d'énergie de déformation élastique relative à l'endommagement est calculée à partir de l'éq (E.3d).

E.3.3 Relaxation du champ solution et critère de convergence

Pour garantir la convergence de l'algorithme LATIN-PGD, l'étape globale requiert l'utilisation d'une relaxation. Soit $\breve{\boldsymbol{s}}_{i+1}$ la solution obtenue à la fin de l'étape globale $i+1$, préalablement notée $\boldsymbol{s}_{i+1}$, une nouvelle solution $\boldsymbol{s}_{i+1}$ est calculée

$$\boldsymbol{s}_{i+1} = \varphi\breve{\boldsymbol{s}}_{i+1} + (1-\varphi)\,\boldsymbol{s}_i \tag{E.25}$$

où φ est un paramètre de relaxation. La convergence de l'algorithme itératif est déterminée par un indicateur LATIN relatif. Cet indicateur représente intrinsèquement la distance entre les solutions locale et globale, c'est-à-dire

$$\xi = \frac{\|\hat{\boldsymbol{s}}^p_{i+1/2} - \boldsymbol{s}^p_{i+1}\|}{\|\hat{\boldsymbol{s}}^p_{i+1/2}\| + \|\boldsymbol{s}^p_{i+1}\|} \tag{E.26}$$

avec

$$\|\boldsymbol{s}^p\|^2 = \int_{[0,T]\times\Omega} \Big(\boldsymbol{\sigma} : \mathbf{H}_\sigma\boldsymbol{\sigma} + \boldsymbol{Z} : \mathbf{H}_Z\boldsymbol{Z} + \dot{\boldsymbol{\varepsilon}}^p : \mathbf{H}_\sigma^{-1}\dot{\boldsymbol{\varepsilon}}^p + \boldsymbol{\varepsilon}^e : \mathbf{C}\boldsymbol{\varepsilon}^e + \dot{\boldsymbol{X}} : \mathbf{H}_Z^{-1}\dot{\boldsymbol{X}}\Big) \, \mathrm{d}V \, \mathrm{d}t. \tag{E.27}$$

E.3.4 Exemple numérique

La structure en L étudiée est soumise à une charge concentrée comme représenté par la fig. E.2. La géométrie de la structure est définie par sa longueur $L = 120$ mm et sa largeur $W = 20$ mm. La structure est arrondie à l'angle intérieur avec un rayon de filetage $r = 5$ mm pour éviter l'apparition de singularités. Son épaisseur est de 1 mm. Le matériau considéré est de l'acier Cr-Mo à $580°\mathrm{C}$ (voir Bhattacharyya et al., 2017, pour les propriétés du matériau). Un déplacement sinusoïdal $U_d\,(t)$ d'amplitude 1.5 mm avec une période $\Delta T = 10$ s est appppliqué à la structure durant cinq cycles.

La distribution de l'endommagement D, quantité d'intérêt principale, à la fin du chargement ($t = T$) est représentée dans la fig. E.3. Il est réparti sur les deux côtés de la pièce verticale, de manière prédominante du côté intérieur avec un maximum au niveau de l'angle arrondi alors que la majeure partie de la structure reste vierge d'endommagement. L'étendue de l'endommagement au niveau de l'angle intérieur qui est la région d'intérêt, après certains cycles de chargement, est également représentée dans la fig. E.3. L'évolution de l'endommagement en fonction du temps pour le point de Gauss le plus vulnérable

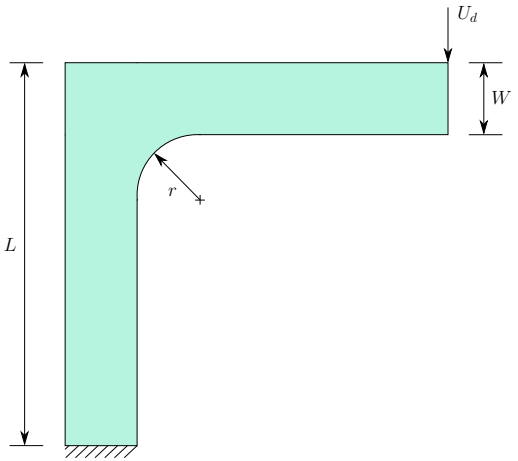

Figure E.2: Une structure en L soumise à une charge ponctuelle

de cette région d'intérêt est illustrée dans la fig. E.3 avec une valeur maximale de l'endommagement de 0.073 à la fin du chargement.

La diminution de l'indicateur LATIN ξ est présentée dans la fig. E.4. Après la première itération, l'indicateur a une valeur de 5×10^{-2}. Après 21 itérations, la valeur de l'indicateur LATIN devient 9×10^{-3} et 8 modes PGD ont été générés. La saturation de l'indicateur a lieu pour une valeur de $\xi = 8 \times 10^{-4}$ avec un total de 40 modes PGD.

Cet exemple montre que cette approche est efficace pour un nombre de cycles moindre. Toutefois, pour des calculs en fatigue, le coût numérique des fonctions temporelles devient important voire prohibitif. Par exemple, 10^5 cycles discrétisés par 100 points par cycle conduisent à un calcul comprenant 10^7 points de discrésation en temps. Il est donc nécessaire de réduire le coût numérique des calculs dépendant du temps.

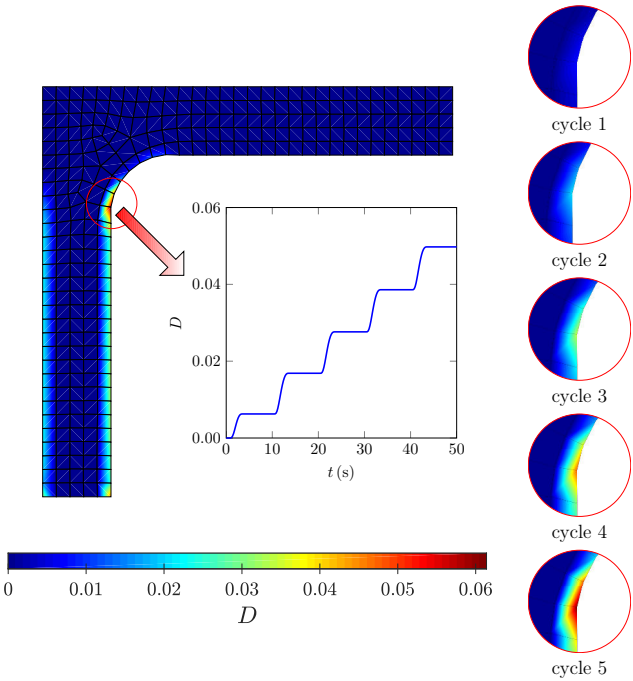

Figure E.3: Distribution de l'endommagement dans la structure en L et évolution de l'endommagement au point de Gauss le plus vulnérable

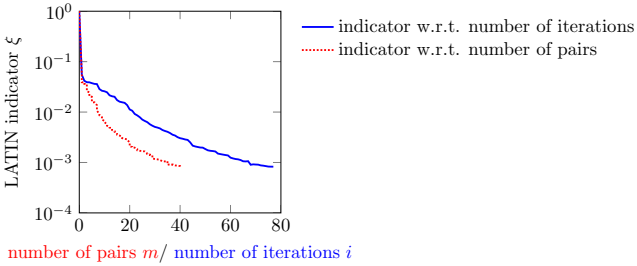

Figure E.4: Évolution de l'indicateur LATIN en fonction du nombre de paires PGD ou des itérations LATIN pour la structure en L

E.4 Une approche à deux échelles de temps

Dans le cas d'un grand nombre de cycles, la stratégie précédente peut être améliorée en utilisant une multi-échelle temporelle. Toute quantité définie sur l'ensemble du domaine $[0, T]$ peut ainsi être décrite en utilisant deux échelles temporelles,

– la discrétisation θ liée aux temps longs définie sur l'intervalle $[0, T]$ qui représente l'évolution lente avec les cycles de chargement,
– la discrétisation τ_i liée aux temps courts décrivant l'évolution rapide des quantités d'intérêt au cours d'un cycle i.

Il peut être remarqué que les chargements considérés ici sont à période constante notée ΔT.

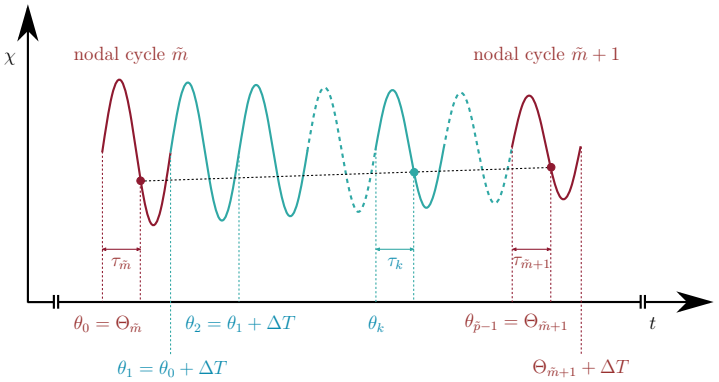

Figure E.5: Discrétisation du domaine temporel utilisant deux discrétisations en temps : θ le long des cycles et τ au cours d'un cycle, $\tilde{p}$ étant le nombre de cycles pour l'élément temporel $[\Theta_{\tilde{m}}, \Theta_{\tilde{m}+1}]$

L'approche proposée consiste à introduire une description type éléments finis des quantités temporelles qui sont ainsi calculées uniquement pour certains cycles choisis appelés nœuds temporels ou cycles nodaux (voir fig. E.5). Pour tout élément temporel $[\Theta_{\tilde{m}}, \Theta_{\tilde{m}+1}]$, une fois les cycles nodaux $\tilde{m}$ et $\tilde{m}+1$ connus, une interpolation uni-dimensionnelle linéaire est utilisée (voir Cognard and Ladevèze, 1993). L'interpolation temporelle de la quantité χ sur l'élément temporel $[\Theta_{\tilde{m}}, \Theta_{\tilde{m}+1}]$ s'écrit

$$\chi\left(t = \theta_k + \tau_k\right) = \frac{\Theta_{\tilde{m}+1} - \theta_k}{\Theta_{\tilde{m}+1} - \Theta_{\tilde{m}}} \chi\left(\Theta_{\tilde{m}} + \tau_{\tilde{m}}\right) + \frac{\theta_k - \Theta_{\tilde{m}}}{\Theta_{\tilde{m}+1} - \Theta_{\tilde{m}}} \chi\left(\Theta_{\tilde{m}+1} + \tau_{\tilde{m}+1}\right), \quad \forall t \in \left[\Theta_{\tilde{m}}, \Theta_{\tilde{m}+1} + \Delta T\right], \tag{E.28}$$

avec $\tau_{\tilde{m}} = \tau_{\tilde{m}+1} = \tau_k$ appartenant à $[0, \Delta T]$, la période étant constante.

Les quelques premiers cycles sont calculés classiquement pour construire une base réduite initiale (cette phase peut également être interprétée comme une ≪ étape d'apprentissage ≫). Ensuite, les cycles nodaux sont calculés progressivement. Le dernier cycle calculé classiquement défini sur le domaine $[\Theta_0, \Theta_0 + \Delta T]$ devient le cycle nodal 0 et à partir de sa connaissance, l'idée est de calculer le cycle nodal 1 défini sur $[\Theta_1, \Theta_1 + \Delta T]$. Ensuite, connaissant le cycle nodal 1, le cycle nodal 2 est calculé, et ainsi de suite. Cette procédure est suivie jusqu'à ce que le dernier cycle nodal soit calculé.

E.4.1 Initialisation

L'initialisation des quantités d'intérêt au cycle nodal $\tilde{m}+1$ à partir de leurs valeurs au cycle nodal $\tilde{m}$ dépend des quantités qui sont considérées. La contributon de l'écrouissage isotropique est ici négligée. Les quantités qui sont cycliques, à savoir les contraintes, les déformations élastiques et les variables cinématiques, sont dupliquées à partir du cycle nodal $\tilde{m}$. Une transformation est considérée de telle sorte qu'elles deviennent périodiques et que la continuité avec le cycle $\tilde{m}$ soit ainsi préservée. Les fonctions temporelles représentant les déformations plastiques $\{\lambda_j\}_{j=1}^m$ sont également dupliquées de manière similaire. Les quantités non-cycliques, à savoir ici uniquement l'endommagement, sont initialisées comme

constantes sur le cycle nodal $\tilde{m}+1$ avec la valeur obtenue à $\Theta_{\tilde{m}}+\Delta T$. Le taux de restitution de l'énergie de déformation liée à l'endommagement est calculé à partir de l'endommagement et du tenseur des contraintes. Le champ solution pour le cycle nodal $\tilde{m}+1$ est calculé ultérieurement en utilisant les deux étapes de l'algorithme LATIN-PGD jusqu'à convergence.

E.4.2 Étape locale

Durant l'étape locale, toutes les quantités d'intérêt excepté l'endommagement ne nécessitent aucune intégration temporelle et peuvent être estimées directement. L'unique difficulé réside dans l'intégration de $\dot{D}$ pour obtenir la variable d'endommagement. Pour intégrer l'éq. (E.4d) sur le cycle nodal $\tilde{m}+1$, il est nécessaire de connaître la condition initiale à θ_m. Considérons une équation générale ordinaire de premier ordre (voir Ladevèze, 1999)

$$\frac{\mathrm{d}\chi}{\mathrm{d}t}+\kappa\chi=\upsilon \tag{E.29}$$

définie sur l'ensemble du domaine temporel avec κ et υ des quantités temporelles connues. L'idée est de calculer $\chi\left(\Theta_{\tilde{m}+1}\right)$ à partir de $\chi\left(\Theta_{\tilde{m}}\right)$. L'élément temporel $[\Theta_{\tilde{m}},\theta_{\tilde{m}+1}]$ est discrétisé en certaines instances θ_k de telle sorte que $\theta_k=\Theta_{\tilde{m}}+k\Delta T$, avec $k=0,1,2,\cdots,\tilde{p}-2$, où $\tilde{p}$ est le nombre de cycles dans l'élément temporel $[\theta_{m-1},\theta_m]$. Ainsi, on obtient $\theta_0=\Theta_{\tilde{m}}$ et $\theta_{\tilde{p}-1}=\Theta_{\tilde{m}+1}$. Connaissant $\chi\left(\theta_k\right)$, l'éq. (E.29) peut être résolue pour obtenir $\chi\left(\theta_{k+1}\right)$ sous la forme

$$\chi\left(\theta_{k+1}\right)=\check{\chi}\left(\theta_{k+1},\theta_k\right)+\Re\left(\theta_{k+1},\theta_k\right)\chi\left(\theta_k\right) \tag{E.30}$$

où $\check{\chi}$ représente la solution homogène de l'ODE et $\Re$ représente l'opérateur $\ll$ résolvant $\gg$ (voir Bhattacharyya et al., 2018, Ladevèze, 1999).

Le défi désormais est de calculer $\check{\chi}$ et $\Re$ avec un coût numérique réduit. La manière la plus simple consiste à évaluer les quantités seulement aux cycles nodaux $\tilde{m}$ et $\tilde{m}+1$ puis à utiliser une interpolation linéaire pour estimer $\check{\chi}\left(\theta_{k+1},\theta_k\right)$ et $\Re\left(\theta_{k+1},\theta_k\right)$, c'est-à-dire

$$\check{\chi}\left(\theta_{k+1},\theta_k\right)=\frac{\Theta_{\tilde{m}+1}-\theta_k}{\Theta_{\tilde{m}+1}-\Theta_{\tilde{m}}}\check{\chi}\left(\Theta_{\tilde{m}}+\Delta T,\Theta_{\tilde{m}}\right)+\frac{\theta_k-\Theta_{\tilde{m}}}{\Theta_{\tilde{m}+1}-\Theta_{\tilde{m}}}\check{\chi}\left(\Theta_{\tilde{m}+1}+\Delta T,\Theta_{\tilde{m}+1}\right), \tag{E.31a}$$

$$\Re\left(\theta_{k+1},\theta_k\right)=\frac{\Theta_{\tilde{m}+1}-\theta_k}{\Theta_{\tilde{m}+1}-\Theta_{\tilde{m}}}\Re\left(\Theta_{\tilde{m}}+\Delta T,\Theta_{\tilde{m}}\right)+\frac{\theta_k-\Theta_{\tilde{m}}}{\Theta_{\tilde{m}+1}-\Theta_{\tilde{m}}}\Re\left(\Theta_{\tilde{m}+1}+\Delta T.\Theta_{\tilde{m}+1}\right). \tag{E.31b}$$

Ces valeurs interpolées peuvent être utilisées pour écrire l'éq. (E.30) comme

$$\begin{aligned}\chi\left(\theta_{k+1}\right)=&\,\nu_{\tilde{m}}\left(\theta_k\right)\left[\check{\chi}\left(\Theta_{\tilde{m}}+\Delta T,\Theta_{\tilde{m}}\right)+\Re\left(\Theta_{\tilde{m}}+\Delta T,\Theta_{\tilde{m}}\right)\chi\left(\theta_k\right)\right]\\&+\nu_{\tilde{m}+1}\left(\theta_k\right)\left[\check{\chi}\left(\Theta_{\tilde{m}+1}+\Delta T,\Theta_{\tilde{m}+1}\right)+\Re\left(\Theta_{\tilde{m}+1}+\Delta T,\Theta_{\tilde{m}+1}\right)\chi\left(\theta_k\right)\right].\end{aligned} \tag{E.32}$$

À partir de $\chi\left(\theta_0=\Theta_{\tilde{m}}\right)$, $\chi\left(\theta_{\tilde{p}-1}=\Theta_{\tilde{m}+1}\right)$ est calculé progressivement, et l'éq. (E.29) est résolue pour le cycle nodal $\tilde{m}+1$.

L'évolution de l'endommagement définie par l'éq. (E.4d) est estimée pour le cycle $\tilde{m}+1$ en utilisant la technique précédemment définie.

E.4.3 Étape globale

Les modes spatiaux calculés pour les cycles initiaux sont réutilisés alors que les fonctions temporelles des modes PGD sont recalculées pour le cycle nodal $\tilde{m}+1$. L'initialisation des fonctions temporelles $\{\lambda_j\}_{j=1}^m$ est telle qu'elle assure la continuité des quantités à la transition entre les cycles nodaux $\tilde{m}$ et $\tilde{m}+1$. Puis, les corrections des fonctions temporelles $\{\Delta\lambda_j\}_{j=1}^m$ sont calculées en résolvant l'éq. (E.19)

avec des conditions initiales nulles. Si nécessaire, les bases PGD peuvent également être enrichies comme détaillé dans la section E.3.2.3.

Concernant les variables cinématiques, qui sont également cycliques, elles peuvent être traitées de manière similaire. Leur initialisation est pareillement réalisée de manière à garantir la continuité vis-à-vis du cycle nodal $\tilde{m}$, et l'éq. (E.12) est résolue sur le cycle nodal $\tilde{m}+1$. Ainsi les quantités sont calculées en termes de correction en résolvant l'équation différentielle ordinaire éq. (E.11) avec des conditions initiales nulles.

Cette approche LATIN-PGD à deux échelles de temps permet de bénéficier d'une réduction drastique de coût numérique en comparaison avec la technique LATIN-PGD traditionnelle.

E.4.4 Exemples numériques

L'approche bi-échelle est vérifiée par comparaison avec la méthode LATIN-PGD mono-échelle. Une plaque rectangulaire décrite par sa longueur $L = 50$ mm et sa largeur $W = 100$ mm est considérée. Des liaisons glissières sont imposées sur trois côtés comme illustré sur la fig. E.6. Sur le quatrième côté un déplacement sinusoïdal de la forme $U_d = U_0 \sin \frac{2\pi t}{T}$ est appliqué uniformément pendant 1000 cycles.

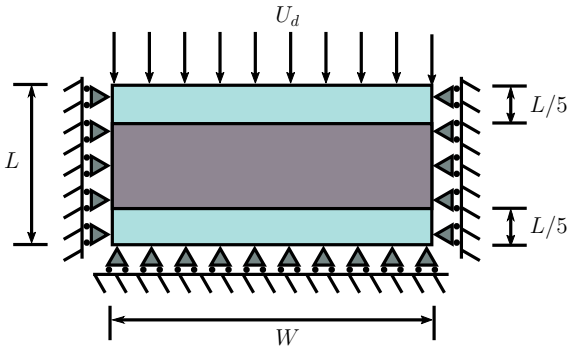

Figure E.6: Plaque rectangulaire avec différentes limites d'élasticité

La plaque est composée de trois parties ayant différentes limites d'élasticité, la partie centrale ayant une limite d'élastité plus faible que les deux parties périphériques. Le matériau considéré est de l'acier Cr-Mo à $25°\mathrm{C}$.

Table E.1: Différentes discrétisations temporelles

Discrétisation temporelle	Nombre de cycles par élément temporel	Nombre total d'éléments temporels
I	50	20
II	100	10
III	200	5
IV	500	2

Le problème est résolu pour $U_0 = 0.070$ mm en considérant d'une part l'approche mono-échelle et d'autre part l'approche bi-échelle avec les différents maillages temporels détaillés dans la table E.1.

L'erreur relative est basée sur l'endommagement et est définie comme suit

$$er_d^2 = \frac{\int_{\Omega\times[0,T]} (D_{ms} - D_{ts}) \cdot (D_{ms} - D_{ts}) \ \mathrm{d}\Omega \, \mathrm{d}t}{\int_{\Omega\times[0,T]} D_{ms} \cdot D_{ms} \ \mathrm{d}\Omega \, \mathrm{d}t + \int_{\Omega\times[0,T]} D_{ts} \cdot D_{ts} \ \mathrm{d}\Omega \, \mathrm{d}t}, \tag{E.33}$$

où D_{ms} et D_{ts} sont les endommagements obtenus en utilisant les algorithmes LATIN-PGD mono-échelle et bi-échelle respectivement. L'erreur relative qui est représentée dans la fig. E.7, croît grandement avec la taille des éléments. Le temps de calcul relatif est estimé par la formule $t_{ts}^{cal}/t_{ms}^{cal}$ où t_{ms}^{cal} est le temps de calcul en utilisant l'algorithme mono-échelle et t_{ts}^{cal} le temps requis pour le calcul bi-échelle. Ce temps relatif, comme prévu, diminue lorsque le nombre de cycles par élément temporel augmente.

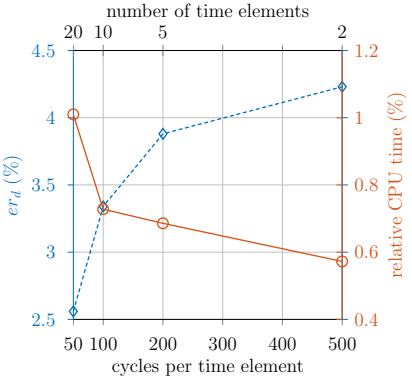

Figure E.7: Erreur et temps de calculs relatifs pour différents maillages temporels en comparaison avec un calcul LATIN mono-échelle

Plusieurs autres tests sont conduits pour différents niveaux de chargement et différents maillages temporels. Les résultats sont comparés avec ceux obtenus en utilisant la dicrétisation I dans la fig. E.8.

Plus le niveau de chargement est élevé, plus l'endommagement est important ainsi que l'erreur relative due aux maillages grossiers. Ainsi, il apparaît qu'un maillage adaptatif serait approprié pour optimiser le temps de calcul sans sacrifier la qualité de l'approximation numérique, comme proposé dans la table E.2.

Table E.2: Discrétisation temporelle adaptative basée sur le niveau d'endommagement

Niveau d'endommagement	Nombre de cycles par élément temporel
$D_m^{\max} < 0.001$	500
$0.001 < D_m^{\max} \leq 0.01$	200
$0.01 < D_m^{\max} \leq 0.1$	100
$D_m^{\max} > 0.1$	50

Le schéma adaptatif est utilisé pour simuler un grand nombre de cycles ici 5×10^5. Seulement 2185 cycles nodaux sont calculés. Trois modes PGD sont générés durant l'étape d'entraînement, qui sont ensuite réutilisés durant la suite des calculs sans enrichissement de la base réduite. La distribution de l'endommagement à la fin du chargement est représentée dans la fig. E.9, avec un maximum au centre et un minimum à la périphérie. L'évolution de l'endommagement dans ces deux régions est présentée

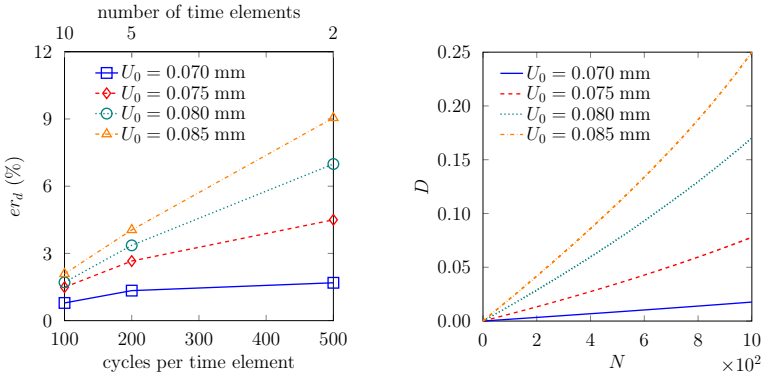

(a) Erreur relative par rapport à la discrétisation I

(b) Évolution de l'endommagement dans la partie centrale de la plaque en utilisant la discrétisation I

Figure E.8: Calculs pour différents niveaux de chargement

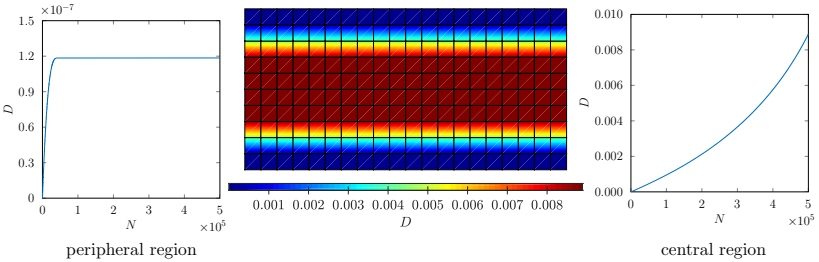

Figure E.9: Distribution et évolution de l'endommagement

dans la fig. E.9, l'endommagement présente une saturation pour la partie périphérique alors qu'il croît perpétuellement dans la partie centrale.

L'étude suivante consiste à analyser la différence de comportement pour une structure soumise à une amplitude constante (CA) ou àune amplitude variable (VA). L'effet de la séquence pour la charge variable, c'est-à-dire faible à grande amplitude (low to high : L-H) ou grande à faible amplitude (high to low : H-L) est également analysé. La structure considérée est une plaque carrée de côté $L = 40$ mm comportant un trou elliptique de demi-grand axe $a = 10$ mm et demi-petit axe $b = 5$ mm. La plaque est soumise à des déplacements sinusoïdaux de la forme $U_d = U_0 \sin \frac{2\pi t}{T}$ durant 10 000 cycles avec une période $T = 1$ s uniformément distribués sur les deux extrémités comme illustré sur la fig. E.10. Au vu des conditions de symétrie, seulement le comportement d'un quart de plaque est calculé avec les conditions aux limites représentées sur la fig. E.10, dans laquelle est également précisée la région d'intérêt attendue. La base réduite peut être enrichie d'un maximum d'une nouvelle paire par cycle nodal.

L'analyse vise à simuler le comportement de la structure soumise à trois types de chargement : à amplitude constante, uniformémement croissante ou uniformément décroissante. Dans les trois cas, l'étape d'apprentissage considère les 10 premiers cycles. Elle conduit à une base réduite comportant sept paires PGD pour le chargement à amplitude constante ou croissante et huit modes pour une amplitude décroissante. En utilisant le schéma temporel adaptatif prédéfini, 95 cycles nodaux sont calculés pour le

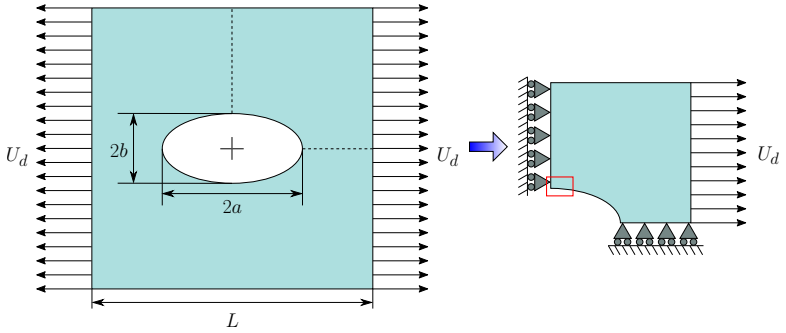

Figure E.10: Une plaque carrée avec un trou elliptique soumise à des chargements répartis

chargement à amplitude constante, 90 cycles nodaux pour le cas à amplitude croissante et 98 pour le cas à amplitude décroissante. La base réduite est enrichie de 11 modes pour les chargements à amplitude constante ou décroissante, et 10 modes pour le chargement L-H.

La distribution de l'endommagement pour ces trois cas de chargement, à certain cycles, dans la région d'intérêt est representée dans la fig. E.11. L'endommagement obtenu est beaucoup plus faible pour le chargement à amplitude constante que pour ceux à amplitude variable. L'effet de la séquence de chargement peut être observé dans la fig. E.12 où sont représentées les évolutions de l'endommagement pour le point de Gauss le plus vulnérable dans les trois cas de chargement. L'endommagement augmente beaucoup plus drastiquement pour le chargement H-L que pour le chargement L-H.

La dernière analyse considère un exemple numérique uni-dimensionnel, en particulier une barre soumise à un chargement cyclique en traction pour établir des courbes ε_a-N virtuelles. La structure est encastrée à une extrémité et soumise à un déplacement sinusoïdal de la forme $U_d\left(t\right) = U_0 \sin\left(\frac{2\pi t}{T}\right)$ à l'autre extrémité. Pour les tests numériques cités ci-après, une valeur d'endommagement critique de 0.2 est considérée comme point de rupture. Plusieurs tests numériques sont réalisés en variant ε_a ce qui conduit à différents nombres de cycles N supportables par la structure avant d'atteindre le niveau d'endommagement critique. Le domaine temporel pour chaque test numérique est discrétisé uniformément, avec un plus faible nombre de cycles par élément pour les plus grandes valeurs de ε_a. La taille des éléments est comprise entre 10 et 200 cycles. Le calcul d'une courbe (voir fig. E.13) nécessite approximativement une heure.

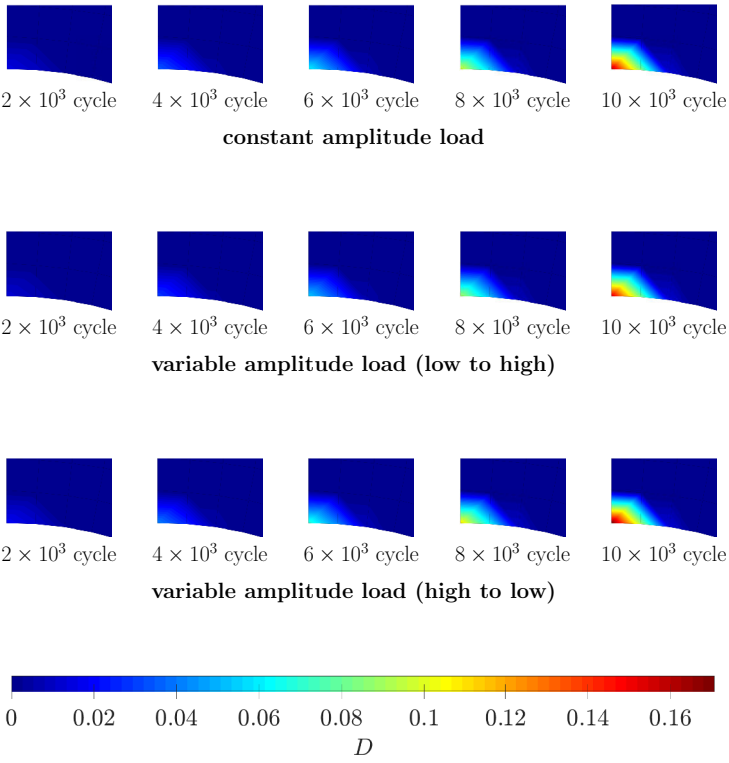

Figure E.11: Distribution de l'endommagement pour certains cycles de chargement dans la région d'intérêt pour la plaque avec un trou elliptique

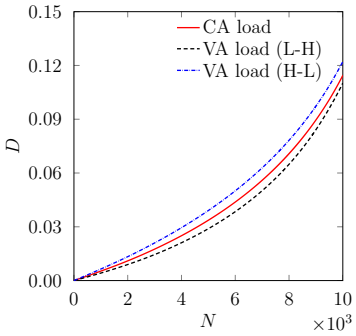

Figure E.12: Évolution de l'endommagement en fonction du nombre de cycles de chargement pour le point de Gauss le plus vulnérable

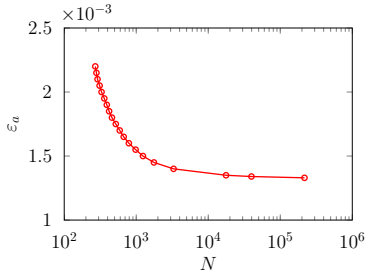

Figure E.13: Courbe ε-N virtuelle

E.5 Conclusion

Une approche numérique innovante a été introduite ici pour le calcul de l'endommagement par fatigue. Une technique non-incrémentale a été utilisée comme cadre numérique et le coût numérique a été réduit par l'utilisation de la PGD qui transforme le problème à grande dimension en un problème à dimension réduite. Une approche multi-échelle en temps a été proposée pour étendre la méthode LATIN-PGD à la simulation de l'évolution de l'endommagement lors de chargement de fatigue. Son efficacité numérique a été démontrée et ouvre une voie pour des simulations complexes basées sur la mécanique des milieux continus pour la fatigue à très grand nombre de cycles.

References

S. Acharyya and S. Dhar. A complete GTN model for prediction of ductile failure of pipe. *Journal of Material Science*, 43:1897–1909, 2008.

E. C. Aifantis. The physics of plastic deformation. *International Journal of Plasticity*, 3(3):211 – 247, 1987.

W. A. J. Albert. Über Treibseile am Harz. *Archiv für Mineralogie, Geognosie, Bergbau und Hüttenkunde*, 10:215–234, 1838.

O. Allix, P. Ladevèze, D. Gilleta, and R. Ohayon. A damage prediction method for composite structures. *International Journal for Numerical Methods in Engineering*, 27:271–283, 1989.

O. Allix and P. Vidal. A new multi-solution approach suitable for structural identification problems. *Computer Methods in Applied Mechanics and Engineering*, 191(25):2727 – 2758, 2002.

A. Ammar, B. Mokdad, F. Chinesta, and R. Keunings. A new family of solvers for some classes of multidimensional partial differential equations encountered in kinetic theory modeling of complex fluids. *Journal of Non-Newtonian Fluid Mechanics*, 139(3):153 – 176, 2006.

A. Ammar, B. Mokdad, F. Chinesta, and R. Keunings. A new family of solvers for some classes of multidimensional partial differential equations encountered in kinetic theory modelling of complex fluids: Part II: Transient simulation using space-time separated representations. *Journal of Non-Newtonian Fluid Mechanics*, 144(2):98 – 121, 2007.

A. Ammar, M. Normandin, and F. Chinesta. Solving parametric complex fluids models in rheometric flows. *Journal of Non-Newtonian Fluid Mechanics*, 165(23):1588 – 1601, 2010.

P. Astrid. *Reduction of process simulation models: a proper orthogonal decomposition approach*. PhD thesis, Technische Universiteit Eindhoven, 2004.

X. Aubard, P.-A. Boucard, P. Ladevèze, and S. Michel. Modeling and simulation of damage in elastomer structures at high strains. *Computers and Structures*, 80(27):2289 – 2298, 2002.

A. Barbarulo, P. Ladevèze, H. Riou, and L. Kovalevsky. Proper Generalized Decomposition applied to linear acoustic: A new tool for broad band calculation. *Journal of Sound Vibration*, 333:2422–2431, May 2014.

M. Barrault, N. Nguyen, Y. Maday, and A. Patera. An "empirical interpolation" method: Application to efficient reduced-basis discretization of partial differential equation (in French). *C. R. Acad. Sci. Paris*, 339:667–672, 2004.

O. H. Basquin. The exponential law of endurance tests. *American Society for Testing Materials Proceedings*, 10:625–630, 1910.

J. Bauschinger. Über die Veränderungen der Elastizitätsgrenze und der Festigkeit des Eisens und Stahls durch Strecken, Quetschen, Erwärmen Abkühlen und durch oftmals wiederholte Belastung. *Mitt. Mech. Tech. Lab. München*, 13:1–115, 1886.

Z. P. Bažant and G. Pijaudier-Cabot. Measurement of characteristic length of nonlocal continuum. *Journal of Engineering Mechanics*, 115(4):755–767, 1989.

E. Bellenger and P. Bussy. Plastic and viscoplastic damage models with numerical treatment for metal forming processes. *Journal of Materials Processing Technology*, 80–81:591 – 596, 1998.

E. Bellenger and P. Bussy. Numerical simulation of creep damage evolutions with the latin method. In *European Congress on Computational Methods in Applied Sciences and Engineering ECCOMAS*, 2000. Barcelona.

B. Besselink, U. Tabak, A. Lutowska, N. van de Wouw, H. Nijmeijer, D. Rixen, M. Hochstenbach, and W. Schilders. A comparison of model reduction techniques from structural dynamics, numerical mathematics and systems and control. *Journal of Sound and Vibration*, 332(19):4403 – 4422, 2013.

S. Bhamare, T. Eason, S. Spottswood, S. R. Mannava, V. K. Vasudevan, and D. Qian. A multi-temporal scale approach to high cycle fatigue simulation. *Computational Mechanics*, 53(2):387–400, Feb 2014.

M. Bhattacharyya, A. Fau, U. Nackenhorst, D. Néron, and P. Ladevèze. A LATIN-based model reduction approach for the simulation of cycling damage. *Computational Mechanics*, 2017.

M. Bhattacharyya, A. Fau, U. Nackenhorst, D. Néron, and P. Ladevèze. A model reduction technique in space and time for fatigue simulation. In J. Sorić, P. Wriggers, and O. Allix, editors, *Multiscale Modeling of Heterogeneous Structures*, pages 183–203. Springer International Publishing, Cham, 2018.

P.-A. Boucard, P. Ladevèze, M. Poss, and P. Rougée. A nonincremental approach for large displacement problems. *Computers and Structures*, 64(1):499 – 508, 1997. Computational Structures Technology.

F. Braithwaite. On the fatigue and consequent fracture of metals. *Institution of Civil Engineers, Minutes of Proceedings*, 13:463–474, 1854.

M. Capaldo, P.-A. Guidault, D. Néron, and P. Ladevèze. The Reference Point Method, a hyperreduction technique: Application to PGD-based nonlinear model reduction. *Computer Methods in Applied Mechanics and Engineering*, 322(Supplement C):483 – 514, 2017.

J. L. Chaboche and P. M. Lesne. A non-linear continuous fatigue damage model. *Fatigue and Fracture of Engineering Materials and Structures*, 11(1):1–17, 1988.

A. Chatterjee. An introduction to the proper orthogonal decomposition. *Current Science*, 78:808–817, 2000.

S. Chaturantabut and D. C. Sorensen. Nonlinear model reduction via discrete empirical interpolation. *SIAM Journal on Scientific Computing*, 32(5):2737–2764, 2010.

F. Chinesta, A. Ammar, A. Falco, and M. Laso. On the reduction of stochastic kinetic theory models of complex fluids. *Modelling and Simulation in Materials Science and Engineering*, 15(6):639, 2007.

F. Chinesta, A. Ammar, F. Lemarchand, P. Beauchene, and F. Boust. Alleviating mesh constraints: Model reduction, parallel time integration and high resolution homogenization. *Computer Methods in Applied Mechanics and Engineering*, 197(5):400 – 413, 2008.

F. Chinesta, A. Leygue, F. Bordeu, J. V. Aguado, E. Cueto, D. Gonzalez, I. Alfaro, A. Ammar, and A. Huerta. PGD-based computational vademecum for efficient design, optimization and control. *Archives of Computational Methods in Engineering*, 20(1):31–59, Mar 2013.

F. Chinesta and E. Cueto. *PGD-Based Modeling of Materials, Structures and Processes*. Springer International Publishing, Cham, 2014.

F. Chinesta, E. Cueto, and A. Huerta. PGD for solving multidimensional and parametric models. In F. Chinesta and P. Ladevèze, editors, *Separated Representations and PGD-Based Model Reduction: Fundamentals and Applications*, pages 27–89. Springer Vienna, Vienna, 2014a.

F. Chinesta, R. Keunings, and A. Leygue. *The proper generalized decomposition for advanced numerical simulations. A primer.* Cham: Springer, 2014b.

L. F. Coffin. A study of the effects of cyclic thermal stresses on a ductile metal. *Transactions of the American Society of Mechanical Engineers*, 76:931–950, 1954.

J.-Y. Cognard and P. Ladevèze. A large time increment approach for cyclic viscoplasticity . *International Journal of Plasticity*, 9(2):141–157, 1993.

D. Cojocaru and A. Karlsson. A simple numerical method of cycle jumps for cyclically loaded structures. *Internation Journal of Fatigue*, 28:1677–1689, 2006.

B. Crossland. Effect of large hydrostatic pressure on the torsional fatigue strength of an alloy steel. In *Proceedings of the international conference on fatigue of metals, IME London*, pages 138–149, 1956.

E. Cueto, F. Chinesta, and A. Huerta. Model order reduction based on proper orthogonal decomposition. In F. Chinesta and P. Ladevèze, editors, *Separated Representations and PGD-Based Model Reduction: Fundamentals and Applications*, pages 1–26. Springer Vienna, Vienna, 2014.

W. Cui. A state-of-the-art review on fatigue life prediction methods for metal structures. *Journal of Marine Science and Technology*, 7(1):43–56, 2002.

K. Dang Van. Sur la résistance à la fatigue des métaux. *Sciences Technique Armement*, 47, 1973.

P. Davoli. Principles of current methodologies in high-cycle fatigue design of metallic structures. In K. Dang Van and I. V. Papadopoulos, editors, *High-Cycle Metal Fatigue: From Theory to Applications*, pages 1–56. Springer Vienna, Vienna, 1999.

E. A. de Souza Neto, D. Perić, and D. R. J. Owen. *Computational Methods for Plasticity: Theory and Applications*. John Wiley & Sons Ltd., 2011.

A. Devulder, D. Aubry, and G. Puel. Two-time scale fatigue modelling: application to damage. *Computational Mechanics*, 45:637–646, 2010.

R. J. Donahue, H. M. Clark, P. Atanmo, R. Kumble, and A. J. McEvily. Crack opening displacement and the rate of fatigue crack growth. *International Journal of Fracture Mechanics*, 8(2):209–219, Jun 1972.

K. Donald and P. C. Paris. An evaluation of ΔK_{eff} estimation procedure on 6061-T6 and 2024-T3 aluminum alloys. *International Journal of Fatigue*, 21:47–57, 1999.

F. El Halabi, D. González, J. Sanz-Herrera, and M. Doblaré. A PGD-based multiscale formulation for non-linear solid mechanics under small deformations. 2016.

W. Elber. *Fatigue crack propagation: some effects of crack closure on the mechanisms of fatigue crack propagation under cyclic tensile loading*. PhD thesis, University of New South Wales, 1968.

W. Elber. Fatigue crack closure under cyclic tension. *Engineering Fracture Mechanics*, 2:37–45, 1970.

J. A. Ewing and J. C. Humfrey. The fracture of metals under rapid alterations of stress. *Philosophical Transactions of the Royal Society, London*, A200:241–250, 1903.

J. A. Ewing and W. Rosenhain. Experiments in micro-metallurgy- effects of strain. preliminary notice. *Philosophical Transactions of the Royal Society, London*, A199:85–90, 1900.

A. Fatemi and L. Yang. Cumulative fatigue damage and life prediction theories: a survey of the state of the art for homogeneous materials. *International Journal of Fatigue*, 20(1):9–34, 1998.

J. Fish and C. Oskay. A nonlocal multiscale fatigue model. *Mechanics of Advanced Materials and Structures*, 12(6):485–500, 2005.

R. G. Forman and R. M. Kearney, V. E. Engle. Numerical analysis of crack propagation in cyclic-loaded structures. *Journal of Basic Engineering*, 89(3):459–463, 1967.

E. Gassner. Auswirkung betriebsähnlicher Belastungsfolgen auf die Festigkeit von Flugzeugbauteilen. *Jahrbuch 1941 der deutschen Luftfahrtforschung*, pages 472–483, 1941.

H. Gerber. Bestimmung der zulässigen Spannungen in Eisen-constructionen. *Zeitschrift des Bayerischen Architekten- und Ingenieur-Vereins*, 6:101–110, 1874.

A. Giacoma, D. Dureisseix, A. Gravouil, and M. Rochette. Toward an optimal a priori reduced basis strategy for frictional contact problems with latin solver. *Computer Methods in Applied Mechanics and Engineering*, 283(Supplement C):1357 – 1381, 2015.

K. Golos and F. Ellyin. A total strain energy density theory for cumulative fatigue damage. *ASME Journal of Pressure Vessel Technology*, 110:36–41, 1988.

J. Goodman. *Mechanics Applied to Engineering*. Longman, Green and Company, London, 1899.

H. J. Gough. *The Fatigue of Metals*. London, Scott, Greenwood, 1924.

A. A. Griffith. The phenomena of rupture and flow in solids. *Philosophical Transactions of the Royal Society*, 221A:163, 1920.

H. J. Grover. An observation concerning the cycle ratio in cumulative damage. In *Symposium of Fatigue of Aircraft Structures*, pages 120–124. ASTM STP 274. American Society for Testing and Materials, 1960.

T. Guennouni and D. Aubry. Réponse homogénéisée en temps de structures sous chargements cycliques. *Comptes rendus de l'Académie des sciences. Série 2, Mécanique, Physique, Chimie, Sciences de l'univers, Sciences de la Terre*, 303(20):1765–1768, 1986.

B. P. Haigh. A new machine for alternating load tests. *Engineering*, 24:721–723, 1912.

R. Hertzberg, C. Newton, and R. Jaccard. Crack closure: Correlation and confusion. In J. Newman and W. Elber, editors, *Mechanics of Fatigue Crack Closure*, pages 139–148. ASTM International, West Conshohocken, PA, 1988.

C. Heyberger, P.-A. Boucard, and D. Néron. Multiparametric analysis within the proper generalized decomposition framework. *Computational Mechanics*, 49(3):277–289, 2012.

D. Hobson, M. Brown, and E. de los Rios. Two phases of short crack growth in a medium carbon steel. In J. Miller and E. de los Rios, editors, *The Behaviour of Short Fatigue Cracks, EGF Pub. Sheffield, U.K.*, pages 441–459. Mechanical Engineering Publications, London, 1986.

P. D. Hobson. *The growth of short fatigue cracks in a medium carbon steel*. PhD thesis, University of Sheffield, Sheffield, 1986.

C. E. Inglis. Stresses in a plate due to the presence of cracks and sharp corners. *Trans. Institution of Naval Architects*, 55:219–242, 1913.

N. P. Inglis. Hysteresis and fatigue of Wöhler rotating cantilever specimen. *The Metallurgist*, pages 23–27, 1927.

G. R. Irwin. Analysis of stresses ans strains near the end of a crack traversing a plate. *Journal of Applied Mechanics*, 24:361–364, 1957.

L. M. Kachanov. In time to rupture in creep conditions (in Russian). *Izviestia Akademii Nauk SSSR, Otdelenie Tekhnicheskikh Nauk*, 8:26–31, 1958.

L. M. Kachanov. *Introduction to continuum damage mechanics*. Mechanics of Elastic Stability. Springer Netherlands, 1986.

K. Karhunen. Zur Spektraltheorie stochastischer Prozesse. *Annales Academiae Scientarum Fennicae. Ser. A. I. Math.-Phys.*, 34, 1946.

V. Kazymyrovych. Very high cycle fatigue of engineering materials : A literature review. Technical Report 2009:22, Karlstad University, Department of Mechanical and Materials Enineering, 2009.

G. Kerschen, J.-C. Golinval, A. F. Vakakis, and L. A. Bergman. The method of proper orthogonal decomposition for dynamical characterization and order reduction of mechanical systems: An overview. *Nonlinear Dynamics*, 41(1):147–169, Aug 2005.

V. Kliman. Fatigue life prediction for a material under programmable loading using the cyclic stress-strain properties. *Materia1 Science and Engineering*, 68(1):1–10, 1984.

J. Kohout and S. Vechet. New functions for a description of fatigue curves and their advantages. In X. R. Wu and Z. G. Wang, editors, *Proceedings of the 7th International Fatigue Congress (Fatigue '99)*, pages 783–788. Higher Education Press, 1999.

J. B. Kommers. Repeated stress tests of steel. *Amer. Mach.*, 42:551–553, 1915.

D. D. Kosambi. Statistics in function space. *Journal of Indian Mathematical Society*, 7:76–88, 1943.

D. Kujawski. Enhanced model of partial crack closure for correlation of R-ratio effects in aluminum alloys. *International Journal of Fatigue*, 23:95–102, 2001.

D. Kujawski and F. Ellyin. A cumulative damage theory of fatigue crack initiation and propagation. *International Journal of Fatigue*, 6(2):83–88, 1984.

P. Ladevèze. The large time increment method for the analyse of structures with nonlinear constitutive relation described by internal variables. *Comptes Rendus de l'Académie des Sciences*, 309(II):1095–1099, 1989.

P. Ladevèze. *Nonlinear Computational Structural Mechanics - new approaches and non-incremental methods of calculation*. Mechanical Engineering Series. Springer New York, 1999.

P. Ladevèze and J. Lemaitre. Damage effective stress in quasi unilateral conditions. The 16th International Congress of Theoretical and Applied Mechanics, Lyngby, Denmark, 1984.

P. Ladevèze. New algorithms: mechanical framework and development (in French). Technical Report 57, LMT-Cachan, 1985a.

P. Ladevèze. On a family of algorithms for structural mechanics (in French). *Comptes Rendus de l'Académie des Sciences*, 300(2):41 – 44, 1985b.

P. Ladevèze. PGD in linear and nonlinear computational solid mechanics. In F. Chinesta and P. Ladevèze, editors, *Separated Representations and PGD-Based Model Reduction: Fundamentals and Applications*, pages 91–152. Springer Vienna, Vienna, 2014.

P. Ladevèze and A. Nouy. On a multiscale computational strategy with time and space homogenization for structural mechanics. *Computer Methods in Applied Mechanics and Engineering*, 192(28):3061 – 3087, 2003.

P. Ladevèze, D. Néron, and P. Gosselet. On a mixed and multiscale domain decomposition method. *Computer Methods in Applied Mechanics and Engineering*, 196(8):1526 – 1540, 2007. Domain Decomposition Methods: recent advances and new challenges in engineering.

B. F. Langer. Fatigue failure from stress cycles of varying amplitude. *ASME Journal of Applied Mechanics*, 59:A160–A162, 1937.

O. Lass and S. Volkwein. Pod galerkin schemes for nonlinear elliptic-parabolic systems. *SIAM Journal on Scientific Computing*, 35(3):A1271–A1298, 2013.

B. N. Leis. A nonlinear history-dependent damage model for low cycle fatigue. In H. D. Solomon, G. R. Halford, L. R. Kaisand, and B. N. Leis, editors, *Low Cycle Fatigue, ASTM STP 519*, pages 143–159. American Society for Testing and Materials, Philadelphia, PA, 1988.

J. Lemaitre. Coupled elasto-plasticity and damage constitutive equations. *Computer Methods in Applied Mechanics and Engineering*, 51(1):31 – 49, 1985.

J. Lemaitre. *A course on damage mechanics*. Springer, Berlin, 1996.

J. Lemaitre and J. Chaboche. *Mechanics of Solid Materials*. Cambridge University Press, 1990.

J. Lemaitre and R. Desmorat. *Engineering Damage Mechanics: Ductile, Creep, Fatigue and Brittle Failures*. Springer, 2005.

J. Lemaitre, J. P. Sermage, and R. Desmorat. A two scale damage concept applied to fatigue. *International Journal of Fracture*, 97:67 – 81, 1997.

J. Lemaitre and I. Doghri. Damage 90: a post processor for crack initiation. *Computer Methods in Applied Mechanics and Engineering*, 115(3):197 – 232, 1994.

M. P. Lesne and S. Savalle. An efficient cycles jump technique for viscoplastic structure calculations involving large number of cycles. In D. R. J. Owen, E. Oñate, and E. Hinton, editors, *Proceedings of the 2nd International Conference on Computational Plasticity*, pages 591–602. Pineridge Press, Ltd., Swansea, 1989.

Y. Liang, H. Lee, S. Lim, W. Lin, K. Lee, and C. Wu. Proper orthogonal decomposition and its applications - part I: Theory. *Journal of Sound and Vibration*, 252(3):527 – 544, 2002.

M. Loève. Fonctions aléatoires de second ordre. *Rev. Sci.*, 84:195–206, 1946.

Y. Maday and O. Mula. A generalized empirical interpolation method: Application of reduced basis techniques to data assimilation. In F. Brezzi, P. Colli Franzone, U. Gianazza, and G. Gilardi, editors, *Analysis and Numerics of Partial Differential Equations*, pages 221–235. Springer Milan, Milan, 2013.

S. S. Manson. Behaviour of materials under conditions of thermal stress. Technical report, National Advisory Commission on Aeronautics: report 1170. Cleveland: Lewis Flight Propulsion Laboratory, 1954.

S. S. Manson. Fatigue: a complex subject-some simple approximations. *Exp Mech J Soc Exp Stress Anal*, 5(7):193–226, 1965.

S. M. Marco and W. L. Starkey. A concept of fatigue damage. *Transaction ASME*, 32(76):627, 1954.

M. Matsuishi and T. Endo. Fatigue of metals subjected to varying stress. In *Journal of Basic Engineering*. Presented to Kyushu District Meeting, 1968.

G. Maugin. *The Thermomechanics of Plasticity and Fracture*. Cambridge Texts in Applied Mathematics. Cambridge University Press, 1992.

A. J. McEvily, H. Bao, and S. Ishihara. A modified constitutive relation for fatigue crack growth. In X. R. Wu and Z. G. Wang, editors, *Proceedings of the 7th International Fatigue Congress (Fatigue99)*, pages 329–336. Higher Education Press, Beijing, 1999.

S. Metoui, E. Pruliere, A. Ammar, F. Dau, and I. Iordanoff. The proper generalized decomposition for the simulation of delamination using cohesive zone model. *International Journal for Numerical Methods in Engineering*, 99(13):1000–1022, 2014.

K. J. Miller. Metal fatigue-a new perspective. In A. S. Argon, editor, *Topics in Fracture and Fatigue*, pages 309–330. Springer-Verlag. Berlin, 1992.

M. A. Miner. Cumulative damage in fatigue. *Journal of Applied Mechanics*, 12:159–164, 1945.

H. F. Moore. The fatigue of metals. *J. Engrs CI. Phil.*, 36:138–143, 1919.

A. Morin. *Leçons de mécanique pratique—résistance des matériaux*. Librairie de L. Hachette et Cie, Paris, 1853.

J. Morrow. Fatigue properties of metals. In *Section 3.2 of Fatigue Design Handbook*. Pub. No. AE-4, Society of Automotive Engineers, Warrendale, PA, 1964.

S. Murakami. *Continuum Damage Mechanics: A Continuum Mechanics Approach to the Analysis of Damage and Fracture*. Solid Mechanics and Its Applications. Springer, 2012.

S. Murakami and N. Ohno. A constitutive equation of creep damage in polycrystalline metals. In *IUTAM Colloquium Euromech 111*, 1978. Marienbad.

M. A. Nasri. *Dimensional reduction for the simulation of metal fatigue (in French)*. PhD thesis, Ecole nationale supérieure d'arts et métiers - ENSAM, May 2017.

A. Navarro and E. R. de los Rios. A microstructurally short fatigue crack growth equation. *Fatigue and Fracture of Engineering Materials and Structures*, 11:383–396, 1988.

D. Néron and D. Dureisseix. A computational strategy for poroelastic problems with a time interface between coupled physics. *International Journal for Numerical Methods in Engineering*, 73(6):783–804, 2008.

D. Néron and P. Ladevèze. Proper generalized decomposition for multiscale and multiphysics problems. *Archives of Computational Methods in Engineering*, 17(4):351–372, Dec 2010.

H. Neuber. *Kerbspannungslehre, Grundlage für eine genaue Spannungsrechnung*. Springer-Verlag Berlin, 1937.

X. Niu, G. X. Li, and H. Lee. Hardening law and fatigue damage of a cyclic hardening metal. *Engineering Fracture Mechanics*, 26(2):163–170, 1987.

A. Nouy. A priori model reduction through proper generalized decomposition for solving time-dependent partial differential equations. *Computer Methods in Applied Mechanics and Engineering*, 199(23): 1603 – 1626, 2010.

S. Oller, O. Salomón, and E. Oñate. A continuum mechanics model for mechanical fatigue analysis. *Computational Materials Science*, 32(2):175 – 195, 2005.

C. Oskay and J. Fish. Multiscale modeling of fatigue for ductile materials. *International Journal for Multiscale Computational Engineering*, 2(3), 2004a.

C. Oskay and J. Fish. Fatigue life prediction using two-scale temporal asymptotic homogenization. *International Journal for Numerical Methods in Engineering*, 61:329–359, 2004b.

N. S. Ottosen, R. Stenström, and M. Ristinmaa. Continuum approach to high-cycle fatigue modeling. *International Journal of Fatigue*, 30(6):996–1006, 2008.

A. Palmgren. Die Lebensdauer von Kugellagern. *Zeitschrift des Vereins Deutscher Ingenieure*, 68:339–341, 1924.

I. V. Papadopoulos, P. Davoli, C. Gorla, M. Filippini, and A. Bernasconi. A comparative study of multiaxial high-cycle fatigue criteria for metals. *International Journal of Fatigue*, 19:219–235, 1997.

P. C. Paris and F. Erdogan. A critical analysis of crack propagation laws. *Journal of Basic Engineering*, 85:528–34, 1963.

P. C. Paris, M. P. Gomez, and W. P. Anderson. A rational analytic theory of fatigue. *The Trend in Engineering*, 13:9–14, 1961.

J.-C. Passieux. *Time-space radial approximation and multiscale LATIN method (in French)*. PhD thesis, École normale supérieure de Cachan - ENS Cachan, 2008.

K. Pearson. On lines and planes of closest to points in space. *Philosophical Magazine*, 2:609–629, 1901.

S. Pearson. Initiation of fatigue cracks in commercial aluminium allys and the subsequent propagation of very short cracks. *Engineering Fracture Mechanics*, 7:235–247, 1975.

R. Pinnau. Model reduction via proper orthogonal decomposition. In W. H. A. Schilders, H. A. van der Vorst, and J. Rommes, editors, *Model Order Reduction: Theory, Research Aspects and Applications*, pages 95–109. Springer Berlin Heidelberg, Berlin, Heidelberg, 2008.

B. Pommier. *Détermination de la réponse asymptotique d'une structure anélastique soumise à un chargement thermomécanique cyclique*. PhD thesis, Ecole Polytechnique X, October 2003.

L. P. Pook. *Metal Fatigue: What It Is, Why It Matters*. Solid Mechanics and Its Applications. Springer Netherlands, 2007.

E. Prulière, F. Chinesta, A. Ammar, A. Leygue, and A. Poitou. On the solution of the heat equation in very thin tapes. *International Journal of Thermal Sciences*, 65(Supplement C):148 – 157, 2013.

G. Puel and D. Aubry. Material fatigue simulation using a periodic time-homogenisation method. *European Journal of Computational Mechanics*, 21(3-6):312–324, 2012.

B. Pyttel, D. Schwerdt, and C. Berger. Very high cycle fatigue - Is there a fatigue limit? *International Journal of Fatigue*, 33(1):49 – 58, 2011. Advances in Very High Cycle Fatigue.

A. Radermacher and S. Reese. Pod-based model reduction with empirical interpolation applied to nonlinear elasticity. *International Journal for Numerical Methods in Engineering*, 107:477 – 495, 2016.

W. Ramberg and W. R. Osgood. Description of stress-strain curves by three parameters. Technical note no. 902, National Advisory Committee For Aeronautics, Washington DC, 1943.

W. J. M. Rankine. On the causes of the unexpected breakage of the journals of railway axles, and on the means of preventing such accidents by observing the law of continuity in their construction. *Institution of Civil Engineers, Minutes of Proceedings*, 2:105–108, 1842.

J. Reddy. *An Introduction to Nonlinear Finite Element Analysis*. OUP Oxford, 2004.

N. Relun, D. Néron, and P.-A. Boucard. Multiscale elastic-viscoplastic computational analysis. *European Journal of Computational Mechanics*, 20(7-8):379–409, 2011.

N. Relun, D. Néron, and P.-A. Boucard. A model reduction technique based on the PGD for elastic-viscoplastic computational analysis. *Computational Mechanics*, 51:83–92, 2013.

N. Relun. *Multiparametric strategy for robust design in fatigue (in French)*. PhD thesis, École normale supérieure de Cachan - ENS Cachan, 2011.

H. A. Richard and M. Sander. *Fatigue Crack Growth: Detect - Assess - Avoid*. Solid Mechanics and Its Applications. Springer International Publishing, 2016.

R. O. Ritchie, S. Suresh, and C. M. Moss. Near-threshold fatigue crack growth in 2 1/4 Cr-1 Mo pressure vessel steel in air and hydrogen. *Journal of Engineering Materials and Technology*, 102:293–299, 1980.

M. L. Roessle and A. Fatemi. Strain-controlled fatigue properties of steels and some simple approximations. *International Journal of Fatigue*, 22:495–511, 2000.

A. Ruhe. Numerical aspects of Gram-Schmidt orthogonalization of vectors. *Linear Algebra and its Applications*, 52:591 – 601, 1983.

D. Ryckelynck. Hyper-reduction of mechanical models involving internal variables. *International Journal for Numerical Methods in Engineering*, 77(1):75–89, 2009.

D. Ryckelynck, D. M. Benziane, S. Cartel, and J. Besson. A robust adaptive model reduction method for damage simulations. *Computational Materials Science*, 50(5):1597 – 1605, 2011.

K. Saï. *Modèles à grand nombre de variables internes et méthodes numériques associées*. PhD thesis, Ecole Nationale Supérieure des Mines de Paris, 1993.

J. Schijve. *Fatigue of Structures and Materials*. Springer Netherlands, 2008.

J. Schijve and D. Brock. Crack propagation tests based on a gust spectrum with variable amplitude loading. *Aircraft Engineering*, 34:314–316, 1962.

J. Schijve and A. H. W. Hoeymakers. Fatigue crack growth in lugs and the stress intensity factor. *Fatigue of Engineering Materials and Structures*, 1:185–201, 1971.

J. Schijve. Fatigue under variable-amplitude loading. In J. Schijve, editor, *Fatigue of Structures and Materials*, pages 295–328. Springer Netherlands, Dordrecht, 2009.

W. Schütz. A history of fatigue. *Engineering Fracture Mechanics*, 54(2):263–300, 1996.

G. Sines. Behavior of metals under complex static and alternating stresses. In G. Sines and J. L. Waisman, editors, *Metal Fatigue*, pages 145–169. New York McGraw-Hill, 1959.

J. Skrzypek and A. Ganczarski. *Modeling of material damage and failure of structures: theory and applications*. Springer-Verlag Berlin Heidelberg, 1999.

J. H. Smith. A fatigue testing machine. *Engineering*, 88:105–107, 1908.

K. N. Smith, P. Watson, and T. H. Topper. A stress-strain function for the fatigue of metals. *J Mater*, 5: 767–778, 1970.

K. Sobczyk and B. F. Spencer. *Random Fatigue: From Data to Theory*. Academic Press, 1992.

C. R. Soderberg. Factor of safety and working stress. *Transactions of the American Society of Mechanical Engineers*, 52:13–28, 1939.

L. Spangenberg. Über die Festigkeitsversuche mit Eisen und Stahl. *Glasers Ann. Gew.*, 5:6–15, 1879.

S. Suresh. *Fatigue of materials*. Cambridge University Press, Cambridge, 2 edition, 2001.

S. Suresh and R. O. Ritchie. A geometrical model for fatigue crack closure induced by fracture surface morphology. *Metallurgical Transactions*, 13A:1627–1631, 1982.

K. Tanaka, Y. Kanagawa, and S. Murakami. Study on Evolution of Internal Damage in CFRP in Fatigue Process. *Journal of the Society of Materials Science, Japan*, 47(5):440–445, 1998.

A. Thum. *Festigkeitsprüfung bei schwingender Beanspruchung. Siebel, Handbuch der Werkstoffprüfung*. 175/231. Verlag Springer Berlin, 2 edition, 1939.

B. Tomkins. Fatigue crack propagation-an analysis. *Philosophical Magazine*, 18(155):1041, 1968.

A. K. Vasudevan, K. Sadananda, and N. Louat. A review of crack closure, fatigue crack threshold and related phenomena. *Material Science and Engineering*, A188:1–22, 1994.

P. Vidal, L. Gallimard, and O. Polit. Composite beam finite element based on the proper generalized decomposition. *Computers & Structures*, 102-103(Supplement C):76 – 86, 2012.

W. Weibull. *A Statistical Theory of the Strength of Materials*. Ingeniörs Vetenskaps Akademiens Handlingar No. 151 Generalstabens Litografisky Anstalts Förlag, Stockholm, 1939.

E. Weiß, B. Postberg, T. Nicak, and J. Rudolph. Simulation of ratcheting and low cycle fatigue. *International Journal of Pressure Vessels and Piping*, 81(3):235 – 242, 2004.

A. Wöhler. Versuche zur Ermittlung der auf die Eisenbahnwagenachsen einwirkenden Kräfte und die Widerstandsfähigkeit der Wagen-Achsen. *Zeitschrift für Bauwesen*, 10:583–616, 1860.

A. Wöhler. Über die Festigkeitsversuche mit Eisen und Stahl. *Zeitschrift für Bauwesen*, 20:73–106, 1870.

P. Wriggers. *Nonlinear Finite Element Methods*. Springer Berlin Heidelberg, 2008.

W. Wunderlich and W. D. Pilkey. *Mechanics of Structures: Variational and Computational Methods*. CRC Press, 2 edition, 2002.

L. Xue. A unified expression for low cycle fatigue and extremely low cycle fatigue and its implication for monotonic loading. *International Journal of Fatigue*, 30:1691–1698, 2008.

J. Zarka and J. Caiser. Elastic-plastic response of a structure subjected to cyclic loading: practical rules. *Mechanics Today*, 6:93 – 198, 1979.

List of publications in IBNM

Institut für Baumechanik und Numerische Mechanik
Gottfried Wilhelm Leibniz Universität Hannover

Reports published so far in this series:

S 73/1 Seminar über Thermodynamik und Kontinuumsmechanik, Hannover 1973

F 75/1 "Die Spannungsberechnung im Rahmen der Finite–Element–Methode",
R. Ahmad, Dissertation, April 1975

F 76/1 "Zur Theorie und Anwendung der Stoffgleichungen elastisch–plastisch–viskoser Werkstoffe",
H. Mentlein, Dissertation, April 1976

S 77/1 Seminar über lineare und geometrisch nichtlineare Schalentheorie einschließlich Stabilitätstheorie, Hannover 1977

F 77/2 "Beitrag zur Berechnung von Gründungsplatten mit Hilfe der Finite–Element–Methode",
H. Meyer, Dissertation, July 1977

F 77/3 "Zur Berechnung der Eigenfrequenzen und Eigenschwingungsformen räumlich vorgekrümmter und vorverwundener Stäbe",
J. Möhlenkamp, Dissertation, December 1977

F 77/4 "Zur Theorie und Berechnung geometrisch und physikalisch nicht-linearer Kontinua mit Anwendung der Methode der finiten Elemente",
J. Paulun, Dissertation, December 1977

S 78/1 2. Seminar über Thermodynamik und Kontinuumsmechanik,
Hannover 1978

F 79/1 "Theoretische und numerische Behandlung geometrisch nichtlinearer viskoplastischer Kontinua",
K.–D. Klee, Dissertation, February 1979

F 79/2 "Zur Konstruierbarkeit von Variationsfunktionalen für nichtlineare Probleme der Kontinuumsmechanik",
J. Siefer, Dissertation, October 1979

F 80/1 "Theoretische und numerische Behandlung gerader Stäbe mit endlichen Drehungen",
M. Kessel, Dissertation, February 1980

F 81/1 "Zur Berechnung von Kontakt– und Stoßproblemen elastischer Körper mit Hilfe der Finite–Element–Methode",
P. Wriggers, Dissertation, January 1981

F 81/2 "Stoffgleichungen für Steinsalze unter mechanischer und thermischer Beanspruchung",
J. Olschewski, E. Stein, W. Wagner, D. Wetjen, geänderte Fassung eines Zwischenberichtes zum BMFT–Forschungsvorhaben KWA 1608/5

F 82/1 "Konvergenz und Fehlerabschätzung bei der Methode der Finiten Elemente",
R. Rohrbach, E. Stein, Abschlußbericht eines VW–Forschungsvorhabens, February 1982

F 82/2 "Alternative Spannungsberechnung in Finite–Element–Verschiebungsmodellen",
C. Klöhn, Dissertation, November 1982

F 83/1 Seminar über nichtlineare Stabtheorie, Hannover 1983

F 83/2 "Beiträge zur nichtlinearen Theorie und inkrementellen Finite–Element– Berechnung dünner elastischer Schalen",
A. Berg, Dissertation, July 1983

F 83/3 "Elastoplastische Plattenbiegung bei kleinen Verzerrungen und großen Drehungen",
J. Paulun, Habilitation, September 1983

F 83/4 "Geometrisch nichtlineare FE–Berechnung von Faltwerken mit plastisch / viskoplastischem Deformationsverhalten",
M. Krog, Dissertation, December 1983

F 85/1 Verleihung der Ehrendoktorwürde des Fachbereichs Bauingenieur– und Vermessungswesen der Universität Hannover an die Herren Prof. Dr. Drs. h.c. J.H. Argyris, Dr.–Ing. H.Wittmeyer

F 85/2 "Eine geometrisch nichtlineare Theorie schubelastischer Schalen mit Anwendung auf Finite–Element–Berechnungen von Durchschlag– und Kontaktproblemen",
W. Wagner, Dissertation, March 1985

F 85/3 “Geometrisch/physikalisch nichtlineare Probleme — Struktur und Algorithmen — ”, GAMM–Seminar im February 1985 in Hannover

F 87/1 “Finite–Elemente–Berechnungen ebener Stabtragwerke mit Fließgelenken und großen Verschiebungen”, R.Kahn, Dissertation, October 1987

F 88/1 “Theorie und Numerik schubelastischer Schalen mit endlichen Drehungen unter Verwendung der Biot–Spannungen”, F. Gruttmann, Dissertation, June 1988

F 88/2 “Optimale Formgebung von Stabtragwerken mit Nichtlinearitäten in der Zielfunktion und in den Restriktionen unter Verwendung der Finite-Element-Methode”, V. Berkhahn, Dissertation, October 1988

F 88/3 “Beiträge zur Theorie und Numerik großer plastischer und kleiner elastischer Deformationen mit Schädigungseinfluß”, R. Lammering, Dissertation, November 1988

F 88/4 “Konsistente Linearisierungen in der Kontinuumsmechanik und ihrer Anwendung auf die Finite–Elemente–Methode”, P. Wriggers, Habilitation, November 1988

F 88/5 “Mathematische Formulierung und numerische Methoden für Kontaktprobleme auf der Grundlage von Extremalprinzipien”, D. Bischoff, Habilitation, December 1988

F 88/6 “Zur numerischen Behandlung thermomechanischer Prozesse”, C. Miehe, Dissertation, December 1988

F 89/1 “Zur Stabilität und Konvergenz gemischter finiter Elemente in der linearen Elastizitätstheorie”, R. Rolfes, Dissertation, June 1989

F 89/2 “Traglastberechnungen von Faltwerken mit elastoplastischen Deformationen”, K.-H. Lambertz, Dissertation, October 1989

F 89/3 “Transientes Kriechen und Kriechbruch im Steinsalz”, U. Heemann, Dissertation, November 1989

F 89/4 “Materialgesetze zum Verhalten von Betonkonstruktionen bei harten Stößen”, E. Stein, P. Wriggers, T. Vu Van & T. Wedemeier, December 1989

F 89/5 “Lineare Konstruktion und Anwendungen von Begleitmatrizen”, C. Carstensen, Dissertation, December 1989

F 90/1 “Zur Berechnung prismatischer Stahlbetonbalken mit verschiedenen Querschnittsformen für allgemeine Beanspruchungen”, H. N. Lucero–Cimas, Dissertation, April 1990

F 90/2 “Zur Behandlung von Stoß- Kontaktproblemen mit Reibung unter Verwendung der Finite–Element–Methode”, T. Vu Van, Dissertation, June 1990

F 90/3 “Netzadaption und Mehrgitterverfahren für die numerische Behandlung von Faltwerken”, L. Plank, Dissertation, September 1990

F 90/4 “Beiträge zur Theorie und Numerik finiter inelastischer Deformationen”, N. Müller–Hoeppe, Dissertation, October 1990

F 90/5 “Beiträge zur Theorie und Numerik von Materialien mit innerer Reibung am Beispiel des Werkstoffes Beton”, T. Wedemeier, Dissertation, October 1990

F 91/1 “Zur Behandlung von Stabilitätsproblemen der Elastostatik mit der Methode der Finiten Elemente”, W. Wagner, Habilitation, April 1991

F 91/2 “Mehrgitterverfahren und Netzadaption für lineare und nichtlineare statische Finite–Elemente–Berechnungen von Flächentragwerken”, W. Rust, Dissertation, October 1991

F 91/3 “Finite Elemente Formulierungen im Trefftzschen Sinne für dreidimensionale anisotrop–elastische Faserverbundstrukturen”, K. Peters, Dissertation, December 1991

F 92/1 “Einspielen und dessen numerische Behandlung von Flächentragwerken aus ideal plastischem bzw. kinematisch verfestigendem Material”, G. Zhang, Dissertation, February 1992

F 92/2 “Strukturoptimierung stabilitätsgefährdeter Systeme mittels analytischer Gradientenermittlung”, A. Becker, Dissertation, April 1992

F 92/3 “Duale Methoden für nichtlineare Optimierungsprobleme in der Strukturmechanik”, R. Mahnken, Dissertation, April 1992

F 93/1 “Kanonische Modelle multiplikativer Elasto–Plastizität. Thermodynamische Formulierung und numerische Implementation”, C. Miehe, Habilitation, December 1993

F 93/2 “Theorie und Numerik zur Berechnung und Optimierung von Strukturen aus isotropen, hyperelastischen Materialien”, F.–J. Barthold, Dissertation, December 1993

F 94/1 “Adaptive Verfeinerung von Finite-Element-Netzen für Stabilitätsprobleme von Flächentragwerken”, E. Stein, B. Seifert, W. Rust, Forschungsbericht, October 1994

F 95/1 “Adaptive Verfahren für die Formoptimierung von Flächentragwerken unter Berücksichtigung der CAD–FEM–Kopplung”,
A. Falk, Dissertation, June 1995

F 96/1 “Theorie und Numerik dünnwandiger Faserverbundstrukturen”,
F. Gruttmann, Habilitation, January 1996

F 96/2 “Zur Theorie und Numerik finiter elastoplastischer Deformationen von Schalenstrukturen”,
B. Seifert, Dissertation, March 1996

F 96/3 “Theoretische und algorithmische Konzepte zur phänomenologischen Beschreibung anisotropen Materialverhaltens”,
J. Schröder, Dissertation, March 1996

F 96/4 “Statische und dynamische Berechnungen von Schalen endlicher elastischer Deformationen mit gemischten finiten Elementen”,
P. Betsch, Dissertation, March 1996

F 96/5 “Kopplung von Finiten Elementen und Randelementen für ebene Elastoplastizität mit Implementierung auf Parallelrechnern”,
M. Kreienmeyer, Dissertation, March 1996

F 96/6 “Theorie und Numerik dimensions- und modelladaptiver Finite-Elemente-Methoden von Flächentragwerken”,
S. Ohnimus, Dissertation, June 1996

F 96/7 “Adaptive Finite Elemente Methoden für MIMD-Parallelrechner zur Behandlung von Strukturproblemen mit Anwendung auf Stabilitätsprobleme”,
O. Klaas, Dissertation, July 1996

F 96/8 “Institutsbericht 1971–1996 aus Anlaß des 25-jährigen Dienstjubiläums von Prof. Dr.-Ing. Dr.-Ing. E.h. Dr. h.c. mult. Erwin Stein, December 1996

F 97/1 “Modellierung und Numerik duktiler kristalliner Werkstoffe”,
P. Steinmann, Habilitation, August 1997

F 97/2 “Formoptimierung in der Strukturdynamik”,
L. Meyer, Dissertation, September 1997

F 97/3 “Modellbildung und Numerik für Versagensprozesse in Gründungen von Caisonwellenbrechern”,
M. Lengnick, Dissertation, November 1997

F 98/1 “Adaptive gemischte finite Elemente in der nichtlinearen Elastostatik und deren Kopplung mit Randelementen”,
U. Brink, Dissertation, February 1998

F 98/2 “Theoretische und numerische Aspekte zur Parameteridentifikation und Modellierung bei metallischen Werkstoffen”,
R. Mahnken, Habilitation, July 1998

F 98/3 “Lokalisierung und Stabilität der Deformation wassergesättigter bindiger und granularer Böden”,
J. M. Panesso, Dissertation, August 1998

F 98/4 “Theoretische und numerische Methoden in der angewandten Mechanik mit Praxisbeispielen”,
R. Mahnken (Hrsg.), Festschrift anlässlich der Emeritierung von Prof. Dr.–Ing. Dr.–Ing. E.h. h.c. mult. Erwin Stein, November 1998

F 99/1 “Eine h-adaptive Finite–Element–Methode für elasto–plastische Schalenprobleme in unilateralem Kontakt”,
C.-S. Han, Dissertation, July 1999

F 00/1 “Ein diskontinuierliches Finite–Element–Modell für Lokalisierungsversagen in metallischen und granularen Materialien”,
C. Leppin, Dissertation, March 2000

F 00/2 “Untersuchungen von Strömungen in zeitlich veränderlichen Gebieten mit der Methode der Finiten Elemente”,
H. Braess, Dissertation, March 2000

F 00/3 “Theoretische und algorithmische Beiträge zur Berechnung von Faserverbundschalen”,
J. Tessmer, Dissertation, March 2000

F 00/4 “Theorie und Finite-Element-Methode für die Schädigungsbeschreibung in Beton und Stahlbeton”,
D. Tikhomirov, Dissertation, August 2000

F 01/1 “A C1 - continuous formulation for finite deformation contact”,
L. Krstulovic-Opara, Dissertation, January 2001

F 01/2 “Strain Localisation Analysis for Fully and Partially Saturated Geomaterials”,
H. Zhang, Dissertation, January 2001

F 01/3 “Meso-makromechanische Modellierung von Faserverbundwerkstoffen mit Schädigung”,
C. Döbert, Dissertation, April 2001

F 01/4 “Thermomechanische Modellierung gummiartiger Polymerstrukturen”,
S. Reese, Habilitation, April 2001

F 01/5 “Thermomechanisches Verhalten von Gummimaterialien während der Vulkanisation – Theorie und Numerik –”,
M. André, Dissertation, April 2001

F 01/6 “Adaptive FEM für elastoplastische Deformationen – Algorithmen und Visualisierung”,
M. Schmidt, Dissertation, June 2001

F 01/7 “Verteilte Algorithmen für h-, p- und d-adaptive Berechnungen in der nichtlinearen Strukturmechanik ”,
R. Niekamp, Dissertation, June 2001

F 01/8 “Theorie und Numerik zur Berechnung und Optimierung von Strukturen mit elastoplastischen Deformationen”,
K. Wiechmann, Dissertation, July 2001

F 01/9 “Direct Computation of Instability Points with Inequality Contraints using the Finite Element Method”,
H. Tschöpe, Dissertation, September 2001

F 01/10 “Theorie und Numerik residualer Fehlerschätzer für die Finite-Elemente-Methode unter Verwendung äquilibrierter Randspannungen”,
S. Ohnimus, Habilitation, September 2001

F 02/1 “Adaptive Algorithmen für thermo-mechanisch gekoppelte Kontaktprobleme”,
A. Rieger, Dissertation, August 2002

F 02/2 “Consistent coupling of shell- and beam-models for thermo-elastic problems”,
K. Chavan, Dissertation, September 2002

F 03/1 “Error-controlled adaptive finite element methods in large strain hyperelasticity and fracture mechanics”,
M. Rüter, Dissertation, May 2003

F 03/2 “Formulierung und Simulation der Kontaktvorgänge in der Baugrund-Tragwerks-Interaktion”,
A. Haraldsson, Dissertation, June 2003

F 03/3 “Concepts for Nonlinear Orthotropic Material Modeling with Applications to Membrane Structures”,
T. Raible, Dissertation, June 2003

F 04/1 “On Single- and Multi-Material arbitrary Lagrangian-Eulerian Approaches with Application to Micromechanical Problems at Finite Deformations”,
D. Freßmann, Dissertation, October 2004

F 04/2 “Computational Homogenization of Microheterogeneous Materials at Finite Strains Including Damage”,
S. Löhnert, Dissertation, October 2004

F 05/1 “Numerical Micro-Meso Modeling of Mechanosensation driven Osteonal Remodeling in Cortical Bone”,
C. Lenz, Dissertation, July 2005

F 05/2 “Mortar Type Methods Applied to Nonlinear Contact Mechanics”,
K.A. Fischer, Dissertation, July 2005

F 05/3 “Models, Algorithms and Software Concepts for Contact and Fragmentation in Computational Solid Mechanics”,
C. Hahn, Dissertation, November 2005

F 06/1 “Computational Homogenization of Concrete”,
S. Moftah, Dissertation, January 2006

F 06/2 “Reduction Methods in Finite Element Analysis of Nonlinear Structural Dynamics”,
H. Spiess, Dissertation, February 2006

F 06/3 “Theoretische und algorithmische Konzepte zur Beschreibung des beanspruchungsadaptiven Knochenwachstums”,
B. Ebbecke, Dissertation, March 2006

F 06/4 “Experimentelle Untersuchungen an elastomeren Werkstoffen”,
M. Dämgen, Dissertation, December 2006

F 07/1 “Numerische Konzepte zur Behandlung inelastischer Effekte beim reibungsbehafteten Rollkontakt”,
M. Ziefle, Dissertation, February 2007

F 07/2 “Begleitbuch zur Leibniz-Ausstellung”,
Hrsg: E. Stein, P. Wriggers, 2007

F 07/3 “Modellierung und Simulation der hochfrequenten Dynamik rollender Reifen”,
M. Brinkmeier, Dissertation, June 2007

F 07/4 “Computational Homogenization of micro-structural Damage due to Frost in Hardened Cement Paste”,
M. Hain, Dissertation, July 2007

F 07/5 “Elektromechanisch gekoppelte Kontaktmodellierung auf Mikroebene”,
T. Helmich, Dissertation, August 2007

F 07/6 “Dreidimensionales Diskrete Elemente Modell für Superellipsoide”,
C. Lillie, Dissertation, October 2007

F 07/7 “Adaptive Methods for Continuous and Discontinuous Damage Modeling in Fracturing Solids”,
S.H. Reese, Dissertation, October 2007

F 08/1 “Student Projects of Micromechanics”,
Hrsg: U. Nackenhorst, August 2008

F 09/1 “Theory and Computation of Mono- and Poly- crystalline Cyclic Martensitic Phase Transformations”,
G. Sagar, Dissertation, August 2009

F 09/2 “Student projects of Micromechanics”,
D. Balzani and U. Nackenhorst, Course Volume, October 2009

F 09/3 “Multiscale Coupling based on the Quasicontinuum Framework, with Application to Contact Problems”,
W. Shan, Dissertation, November 2009

F 10/1 “A Multiscale Computational Approach for Microcrack Evolution in Cortical Bone and Related Mechanical Stimulation of Bone Cells”,
D. Kardas, Dissertation, September 2010

F 11/1 “Ein integrales Modellierungskonzept zur numerischen Simulation der Osseointegration und Langzeitstabilität von Endoprothesen”,
A. Lutz, Dissertation, October 2011

F 12/1 “Ein physikalisch motiviertes Reifen-Fahrbahnmodell für die Gesamtfahrzeugsimulation”,
R. Chiarello, Dissertation, February 2012

F 13/1 “Thermomechanical Analysis of Tire Rubber Compounds in Rolling Contact”,
A. Suwannachit, Dissertation, September 2012

F 13/2 “Towards a Finite Element Model for Fluid Flow in the Human Hip Joint”,
K. Fietz, Dissertation, September 2013

F 14/1 “Micro-Mechanically Based Damage Analysis of Ultra High Performance Fibre Reinforced Concrete Structures with Uncertainties”,
A. Hürkamp, Dissertation, December 2013

F 14/2 “Numerical Solution of High-Dimensional Fokker-Planck Equations with Discontinuous Galerkin Methods”,
F. Loerke, Dissertation, December 2013

F 14/3 “Numerische Simulation probabilistischer Schädigungsmodelle mit der Stochastischen Finite Elemente Methode”,
P.-P. Jablonski, Dissertation, September 2014

F 15/1 “On a Finite Element Approach for the Solution of a mechanically Stimulated Biochemical Fracture Healing Model”,
A. Sapotnick, Dissertation, February 2015

F 15/2 “Stimulation of Elastic-Plastic Material Behavior with Uncertain Material Parameters. A Spectral Stochastic Finite Element method Approach”,
S. Fink, Dissertation, February 2015

F 15/3 “A Fully Micro-mechanically Motivated Material Law for Filled Elastomer”,
O. Stegen, Dissertation, March 2015

F 16/1 “A modified adaptive harmony search algorithm approach on structural identification and damage detection”,
M. Jahjouh, Dissertation, January 2016

F 17/1 “Computational Simulation of Piezo-electrically Stimulated Bone Adaption Surrounding Activated Teeth Implants”,
S. Shirazibeheshtiha, Dissertation, January 2017

F 17/2 “A Constitutive Contact Model for Homogenized Tread-Road Interaction in Rolling Resistance Computations”,
R. Beyer, Dissertation, February 2017

F 17/3 “A Posteriori Error Estimates for Advanced Galerkin Methods”,
M.O. Rüter, Habilitation, November 2017

F 17/4 “Probabilistische Finite Element Modellierung des mechanischen Materialverhaltens von Salzgestein”,
M. Grehn, Dissertation, December 2017

F 18/1 “Modeling and numerical simulation for the prediction of the Fatigue strength of Airsprings”,
N.K. Jha, Dissertation, February 2018

Title: A model reduction approach in space and time for fatigue damage simulation

An innovative numerical scheme is proposed to predict the life time of mechanical components under fatigue loading, using classical continuum damage mechanics based models. The large time increment (LATIN) method, which is a non-incremental solution technique and builds the solution iteratively for the complete space-time domain, along with proper generalised decomposition (PGD) that separates the quantities of interest with respect to space and time, is used as a numerical framework. The first goal of the research is to introduce damage as an internal variable in the LATIN-PGD framework in a reasonable computational time. The PGD-based model reduction is however not enough to solve problems involving large number of load cycles. The second part of the research is to overcome this bottleneck by using a multi-time scale approach, that takes into account the rapid evolution of the quantities of interest within a load cycle and their slow evolution along the load cycles.

Keywords: LATIN method, damage, fatigue, PGD, multi-temporal scale

Titre : Une approche de réduction de modèles en temps et espace pour le calcul de lendommagement par fatigue

Un schéma numérique original est proposé pour prédire la durée de vie de pièces mécaniques sous des chargements de fatigue, en utilisant des modèles basés sur la mécanique de l'endommagement de milieux continus. La méthode LATIN, qui est une méthode de résolution non-incrémentale construisant la solution itérativement sur l'ensemble du domaine spatio-temporel est utilisée, munie d'une décomposition propre généralisée (PGD) qui sépare les quantités d'intérêt par rapport à leur dépendance en temps et en espace. Le premier objectif de ces travaux est d'introduire l'endommagement en tant que variable interne dans le cadre de résolution de la LATIN-PGD pour permettre de réduire les temps de calcul. Cependant la réduction de modèle basée sur la PGD n'est pas suffisante pour résoudre des problèmes comportant un grand nombre de cycles. La seconde partie des ces travaux vise à réduire le temps de calcul en utilisant une échelle multi-temporelle, qui considère d'une part l'évolution rapide des quantités d'intérêt au cours d'un cycle et leur évolution lente le long des cycles de chargement.

Mots-clés : méthode LATIN, endommagement, fatigue, PGD, échelle multi-temporelle

Titel: Ein Modellreduktionsverfahren in Raum und Zeit für die Ermüdungs-Schädigungs Simulation

Um die Lebensdauer mechanischer Komponenten unter Ermüdungsbelastung vorherzusagen, wird ein innovatives numerisches Schema, auf Grundlage von klassischen Modellen der Schädigungsmechanik, vorgeschlagen. Verwendet werden hierbei die LATIN (Large Time Increment) Methode, ein nicht-inkrementelles, iteratives Lösungsverfahren, welches die Lösung simultan in Raum und Zeit erstellt und die Proper Generalised Decomposition (PGD), eine Methode zur Dimensionsreduktion, welche eine Separation der Zielgrößen in Raum und Zeit erlaubt. Das erste Forschungsziel ist Schädigung als interne Variable in das LATIN-PGD Framework in einer angemessenen Rechenzeit einzubringen. Die PGD-basierte Modellreduktion reicht jedoch nicht aus, um Simulationen mit einer großen Anzahl von Lastzyklen berechenbar zu machen. Um dieses Problem zu lösen, wird im zweiten Teil dieser Forschungsarbeit ein mehrskaliger Zeitansatz verwendet, der die schnelle Entwicklung der Bezugsgrößen innerhalb eines Lastzyklus und ihre langsame Entwicklung entlang der Lastzyklen berücksichtigt.

Stichworte: LATIN Methode, Schädigung, Ermüdung, PGD, Mehrskalenansatz in der Zeit

ISBN 978-3-935732-47-5 **NNT 2018SACLN019**